AFCRL-64-970
JANUARY 1964
SPECIAL REPORTS, NO. 20

AIR FORCE CAMBRIDGE RESEARCH LABORATORIES
L. G. HANSCOM FIELD, BEDFORD, MASSACHUSETTS

Studies of the Characteristics of Probable Lunar Surface Materials

JOHN W. SALISBURY
PETER E. GLASER
Editors

OFFICE OF AEROSPACE RESEARCH
United States Air Force

AFCRL-64-970
JANUARY 1964
SPECIAL REPORTS, NO. 20

SPACE PHYSICS LABORATORY PROJECT 8602

AIR FORCE CAMBRIDGE RESEARCH LABORATORIES

L. G. HANSCOM FIELD, BEDFORD, MASSACHUSETTS

Studies of the Characteristics of Probable Lunar Surface Materials

JOHN W. SALISBURY

PETER E. GLASER*

Editors

*Arthur D. Little Inc., Cambridge, Mass.

(Prepared cooperatively under Contract No. AF 19(628)-421
by the Air Force Cambridge Research Laboratories and
Arthur D. Little, Inc.)

OFFICE OF AEROSPACE RESEARCH
United States Air Force

FOREWORD

The research program of which this is a progress report was conceived and directed by John W. Salisbury, Chief of the Lunar Planetary Research Branch, Air Force Cambridge Research Laboratories. Project Director for Arthur D. Little, Inc., was Peter E. Glaser.

This report is the result of the cooperative efforts of the staffs of both of the above groups. Contributions were made by the following individuals:

Air Force Cambridge Research Laboratories

John W. Salisbury, Joel E. M. Adler, Roger A. Van Tassel, Graham R. Hunt, Vern G. Smalley, and R. T. Dodd.

Arthur D. Little, Inc.

Peter E. Glaser, Ronald V. Allen, Edward J. Boudreau, Richard S. Davis, John L. Engelke, Philip C. Johnson, Robert K. McConnell, Raymond W. Moore, Jr., David M. Rostoker, Ivan Simon, Barry A. Stein, Bernard Vonnegut, and Alfred E. Wechsler.

ABSTRACT

This report presents the findings of a cooperative effort by scientists of the Lunar Planetary Research Branch of the Air Force Cambridge Research Laboratories and of Arthur D. Little, Inc., on theoretical and experimental studies to determine the nature and most probable physical form of materials on the lunar surface. To accomplish these goals, the following efforts were performed: (1) installation of an ultra-high-vacuum system to simulate the probable lunar environment, (2) selection of material samples to simulate the probable lunar surface, (3) experimentation on and analysis of these materials in a high vacuum, (4) studies of the behavior of clean surfaces in a high vacuum, (5) measurements of electrostatic phenomena in a high vacuum, (6) measurement of thermal properties in a high vacuum, and (7) spectroscopic studies.

BLANK PAGE

TABLE OF CONTENTS

TABLE OF CONTENTS (cont'd)

TABLE OF CONTENTS (cont'd)

TABLE OF CONTENTS (cont'd)

LIST OF APPENDICES

LIST OF APPENDICES (cont'd)

LIST OF ILLUSTRATIONS

LIST OF ILLUSTRATIONS (Cont'd)

LIST OF ILLUSTRATIONS (Cont'd)

LIST OF ILLUSTRATIONS (Cont'd)

LIST OF TABLES

BLANK PAGE

SECTION I

INTRODUCTION

When conducting lunar simulation research, it is necessary to comply with two requirements: 1) the environment within the simulation chamber must approximate that of the moon in all significant respects; and 2) experiments conducted within the chamber must be designed so that the effects of pertinent variables may be isolated and measured.

The first requirement demands a knowledge of both the lunar environment, and the aspects of that environment which affect the experiments to be performed. Fortunately, the absence of an appreciable lunar atmosphere is well-established, and all lunar simulation research can begin with an ultra-high-vacuum chamber. However, the choice of materials used, their preparation, and kinds of experiments performed, all depend to a very high degree upon aspects of the lunar environment which are clearly in the realm of speculation. Thus, behind every such research program must lie a partially theoretical model of the lunar environment which may bias the results of experiments or, in fact, result in the performance of meaningless experiments. A summary of the lunar model used in our experiments is presented in Appendix A. Appendix A is written at a level intended for a reader who is relatively uninformed with regard to the lunar environment, but who, nevertheless, wishes to understand the context in which our experiments were carried out.

A probable model of the lunar environment, such as that presented in Appendix A, does not, however, provide the answers to all simulation research problems. A valid research program must also encompass all likely alternatives, or at least clearly recognize the specific aspects

in which the environment simulated may differ from those alternatives. This is particularly true with regard to the composition, grain size, and grain shape of the test material.

The probable composition of lunar surface materials is discussed in Appendix A. Because the composition is almost certainly variable, the simulation experiments were planned using representative samples of all the major igneous rock types, in addition to chondrites and tektites. Thus, the experiments should have encompassed the limits of likely alternatives, although lunar rocks will have been slightly modified by long-term radiation damage. For instance, Wehner (1961) points out that sputtering from solar wind bombardment would have slightly enriched the surface with heavy atoms by preferential ejection of the lighter elements into space over long periods of time.

The particle size of the material used in the chamber poses a more difficult problem than does composition. Because the moon lacks an atmosphere, it is subjected to continual bombardment by high-velocity micrometeoroids. This mechanism should cause erosion of surface features of the moon and comminution of exposed materials (Salisbury and Smalley, 1963). Most of the energy in meteoroid impact is expended in the form of shock waves, which pulverize the target material and eject a portion of the debris to form a crater. In the higher-velocity impacts, volatilization at the impact site also contributes significantly to the loss, and the entropy change is great enough so that the material does not condense on expansion.

At velocities attainable in the laboratory (4.27 to 6.1 km/sec), Moore and Gault (1962) found that the mass of ejecta was roughly 10^2

times the mass of the projectile. Bjork's (1961) calculations of the mass of the projectile that produced Meteor Crater, Arizona, indicate ejecta mass/projectile mass ratios of approximately 10^3 at a meteorite velocity of 11 km/sec and $10^{3.4}$ at a velocity of 72 km/sec. It would seem, therefore, that 10^3 is an appropriate ejecta mass/projectile mass ratio to assume for lunar meteoroid impacts on a solid surface at the median velocity of 15-20 km/sec suggested for lunar meteoroids by Whipple (1961), or at higher velocities associated with comets or cometary debris. At these velocities, Gault (private communication) estimates on the basis of laboratory experiments that a very small percentage of the ejecta, amounting to 3-5 times the projectile mass, will escape from the moon, and a similar percentage will be vaporized or melted.

The work carried out at McGill University (Johnston, et al, 1963) involving a one-dimensional treatment of impact on thin bumpers can be used to check the estimated amount of material vaporized. Using a one-dimensional treatment, and assuming that the polytropic constant, k, is the same for meteoroid and target (i.e., the equation of state for each satisfied $p \propto \rho^k$ in an adiabatic process; for an ideal gas, k becomes the ratio of specific heats), one would expect the mass of vaporized debris (assuming a sublimation energy of 5×10^{10} ergs/gm) to exceed the meteoroid mass by the factors tabulated below; these are, to a large degree, independent of the relative densities of meteoroid and target.

Ratio of Mass of Volatilized Debris to Meteoroid Mass

Meteoroid Velocity	k = 2	k = 3	k = 4
10 km/sec	6	8	9
15 km/sec	10	15	20
30 km/sec	29	48	65

When a meteorid impacts on the moon, the shock decay with depth is more rapid than in the one-dimensional case due to radial expansion; thus, the volatilization will not extend to as great a depth as in the one-dimensional problem. The increase in volume of volatilized debris resulting from the radial spreading compensates for the loss in volume due to the more rapid attenuation of the shock with depth. These estimates are in good agreement with Gault's experimental results.

The data available in the literature on distribution of particle size resulting from hypervelocity impact on semi-infinite targets is misleading in estimating the particle size of lunar dust, because they do not take into account the effects of impact on small target fragments. If the diameter of the impacting particle is greater than about 0.3 times the thickness of the target particle, then scabbing or spalling will be an important source of fragmentation, since in this case the shock wave will reach the rear surface of the target before the rarefaction overtakes the shock. A rarefaction wave will travel from the rear surface into the shocked material, and when this intersects the rarefaction wave proceeding from the front surface, fragmentation will occur. The result will be the creation of particles predominantly smaller than the impacting particle, and most of this debris will remain near the original site. This may be an important mechanism in the creation of lunar "dust" and could lead to a particle size distribution in which fines predominate to a greater extent than in the distributions resulting from shatter of semi-infinite targets. On the other hand, it has been hypothesized that the large amount of energy put into a porous, fine-grained target material during hypervelocity impact may be sufficient to cause welding or sinter-

ing of the powder rather than further disintegration. Thus, the lunar surface could be covered with a partially fused microbreccia, rather than a fine dust. We have chosen in this phase of the research program to accept the pulverization model of hypervelocity impact, and have used a fine powder in the experiments.

If one accepts Whipple's latest (1963) estimate of the meteor spectrum, it is easy to see why the powder should be fine. If one assumes a sharp cut-off in particles below 10^{-9} gm, then Whipple's distribution would have a median mass of about 8×10^{-9} gm, which implies a mass median diameter between 1 and 10 microns for particles striking the lunar surface. Thus, a lunar dust in the range of 1 to 10 microns mass median diameter is a probable lunar surface condition, and was simulated in the experiments described hereafter.

The shape of these dust particles is a third simulation problem. Three types of particle shapes may possibly be found on the lunar surface: (1) rounded droplets of fused material, (2) irregular shards or grains of shattered material, and (3) whisker-like crystals of condensed material.

In accord with the results of the hypervelocity impact experiments performed by Gault et al, (1963), it was assumed that the second type of particle was by far the most numerous. (Shards might also result from the fractured vesicles postulated in the genesis of lunar lavas.) A dust layer of this sort, if highly porous and complex, would account for the very distinct backscattering of light from the lunar surface as demonstrated by Hapke (1963). It must be noted, however, that other models of the surface layer would also

account for the lunar backscattering characteristics and that the dust model was chosen only as a first approximation. Sytinskaya (1959) suggests a rock slag model formed by the fusion of silicates under micrometeoroid impact and subsequent cooling and foaming in vacuum, while Cudaback (1963) suggests a structure like "cotton candy".

Hibbs (1963) states that the fraction of the lunar material which has been subject to vaporization and redeposition as a result of micrometeoroid impact would be deposited on the surface in the form of whisker crystals or needles by condensation of material from a vapor to a solid phase in a region of pressure and temperature that precludes a liquid phase. Similarly, Donn and Sears (1963) have hypothesized that the growth of whisker-like crystals played a role in the surface formation.

Despite the possibility of other grain shapes suggested by Sytinskaya, Hibbs, Cudaback, and others, finely crushed rock and mineral samples were used in the experiments reported here. Other materials will be used when warranted by increased knowledge of the lunar surface layer.

SECTION II

SUMMARY

A. PURPOSE AND SCOPE

The purpose of this study was to carry out research to obtain an increased understanding of the effects of the lunar environment on the physical properties of probable lunar surface materials through use of a lunar environment simulation chamber. The detailed objectives and scope of the portion of the study reported here were the following:

1. Installation of an ultra-high-vacuum system capable of reaching 10^{-10} torr at the Air Force Cambridge Research Laboratories.

2. Theoretical and experimental studies of the effect of ultra-high vacuum on the adhesive properties of silicate powder particles to obtain a qualitative concept of the trafficability of the lunar surface.

3. Combined theoretical analysis and experimental measurement of the thermal conductivity of powders in vacuum to determine, if possible, the nature of materials on the lunar surface and the most likely physical form that they would take.

4. Experimental measurements of the spectra of common rocks and minerals.

B. APPROACH

To achieve the stated objectives, the following work was carried out during the period from March 1962 to November 1963:

1. Simulation of the Lunar Environment

A high-vacuum chamber was obtained and modified so as to accomodate a number of planned experiments for operation at pressures in the range

of 10^{-10} torr for extended periods of time. A residual gas analyzer was installed on the chamber to determine the masses of the constituents of the residual atmosphere and thereby to characterize the performance of the chamber. Procedures were worked out to minimize the contamination of test samples during experiments within the chamber. A proton beam source was built for use with the chamber.

2. Materials Preparation

A range of materials was selected that included representative samples of the igneous rock types as well as chondrites and tektites, so as to simulate all probable lunar surface materials. The selected materials were carefully characterized, and powdered test samples with a desired range of particle sizes were prepared in controlled atmospheres.

3. Measurement of Adhesive Properties

Experimental apparatus was constructed and data were obtained to provide an indication of the adhesion existing between powder particles and a substrate. Analyses of the experimental results were carried out to provide an indication of the possible strength characteristics of materials in a high vacuum.

4. Theoretical Surface Studies

The behavior of clean surfaces in a high vacuum was studied to explain the observed adhesive phenomena of particles in a simulated lunar environment. The magnitude of forces which could be responsible for these phenomena was established on the basis of surface conditions postulated to exist in the high-vacuum environment.

5. Measurement of Electrostatic Phenomena

Studies were made to establish the contribution of electrostatic forces to the observed behavior of particles in the high-vacuum chamber. Apparatus was constructed to measure the charges on the particles and to determine the nature of these charges.

6. Measurement of Thermal Properties

Apparatus was constructed to measure the thermal conductivity of powders in the high-vacuum chamber. The effects of different variables on thermal conductivity were established by measurements carried out over a range of pressures. The contributions of the different heat transfer mechanisms were analyzed, and the experimental data were correlated with data obtained by other investigators.

7. Spectroscopic Studies

Spectroscopic studies were made on different test samples to obtain an indication of the spectral detail produced by mid-infrared emission spectra. Theoretical proton radiation damage studies were carried out to examine the possible effects of solar radiation on exposed materials on the lunar surface.

Section I established the basis for choosing the model of the lunar surface dust layer and discussed simulation of environmental parameters. The following sections describe the theoretical and experimental investigations.

BLANK PAGE

SECTION III

MATERIAL SELECTION AND PREPARATION

The test materials that were chosen consisted of natural igneous rocks representing most of the major geologic rock-type classifications ranging from siliceous to basic rocks. In addition, a chondritic meteorite (a piece of the Callihan, Texas meteorite) and tektites were obtained as examples of extra-terrestrial infall. An impactite which had been studied by the Astro-Geological Laboratory of the USGS was also obtained as an example of material physically affected by impact. The other samples were obtained from Ward's Natural Science Establishment, General Electric Company, and American Meteoroid Company. Samples selected by our supplier were chosen for their visibly low degree of alteration products; however, some degree of alteration is present in all materials.

Thin sections of each of the sample materials were examined under polarized light, using an American Optical petrographic microscope. Whenever possible, volume percentages of the minerals contained in the rocks were determined by the Rosenbusch integrating micrometer stage technique. A standard linear scale was used to determine the linear percentages of the minerals present in a single traverse across the rock specimen. After many evenly spaced traverses the mineral percentages were averaged. This average was then equivalent to the volume percent. It can be seen that the accuracy depended on the homogeneity of the sample, the size of the mineral grains present, and the fineness of the scaling device, as well as the interpolation of the viewer. While no precise values can be assigned to the accuracy, we estimate that the percentages given are within a few percent

of the true value represented by the slide. Results of the petrographic examination are given in Table III-1.

Selected materials were ground in a Spex Industries Model 8000 shaker and tungsten carbide ball mill. To insure minimum contamination of the powders (by H_2O, O_2, CO_2, etc.) the grinding operation was carried out in an inert atmosphere. Each sample was first reduced to pieces approximately 1/4" x 1/4" x 1/2". Together with sieves, jars, and a ball mill, the sample was placed in a transparent polyethylene bag. Argon was introduced to fill the bag. After three purges with argon, the rock sample was placed in the ball mill, and the mill was hermetically sealed (neoprene rings were used to insure good sealing). Access to the inside of the bag was by means of a rubber glove attached to the bag (see Figure III-1). A positive pressure was maintained in the bag during removal of the ball mill to minimize contamination with the atmosphere. The samples were crushed and returned to the protective argon atmosphere in the closed bag. After each run, the mill was emptied onto the desired size sieve and reloaded. Depending on the toughness of the sample, up to 10 ml of material could be ground per run.

TABLE III-1

RESULTS OF PETROGRAPHIC EXAMINATION

MINERAL	FORMULA	VOL. PERCENT
Granodiorite		
Albite	$NaAlSi_3O_8$	17.5
Anorthite	$CaAl_2Si_2O_8$	7.5
Orthoclase	$KAlSi_3O_8$	30.0
Quartz	SiO_2	20.0
Biotite	$K(MgFe)_3(AlSi_3O_{10})(OH)_2$	24.0
Hematite	Fe_2O_3	0.7
Dunite		
Olivine	$(Mg,Fe)_2SiO_4$	96.5
Serpentine	$Mg_6(Si_4O_{10})(OH)_8$	2.0
Chromite Magnetite	Fe_3O_4 - $FeCr_2O_4$	1.5
Pyroxene		
Quartz	SiO_2	12.0
Augite	$Ca(MgFeAl)((SiAl)_2O_6)$	88.0
Gabbro		
Bytownite		
Albite	$NaAlSi_3O_8$	29.2
Anorthite	$CaAl_2Si_2O_8$	68.8
Biotite	$K(MgFe)_3(Si_4O_{10})(OH)_2$	1.0
Ilmenite	$FeTiO_3$	1.0

TABLE III-1 (Cont'd.)

RESULTS OF PETROGRAPHIC EXAMINATION

MINERAL	FORMULA	VOL. PERCENT
Andesite Labradorite[1]		
Albite	$NaAlSi_3O_8$	30.0
Anorthite	$CaAl_2Si_2O_8$	30.0
Hematite	Fe_2O_3	20.0
Biotite	$K(MgFe)_3(Si_4O_{10})(OH)_2$	20.0
Nepheline Syenite		
Hornblende	$Ca_4Na_2(MgFe)_8(AlFe)_2(Al_4Si_{12}O_{44})(OHF)_4$	4.0
Biotite	$K(MgFe)_3(Si_4O_{10})(OH)_2$	8.0
Orthoclase	$KAlSi_3O_8$	43.0
Albite	$NaAlSi_3O_8$	20.5
Anorthite	$CaAl_2Si_2O_8$	15.0
Nepheline	$(Na,K)AlSiO_4$	8.5
Hematite	Fe_2O_3	2.0
Serpentine		
Magnetite	Fe_3O_4	6.0
Calcite	$CaCO_3$	4.0
Antigorite	$Mg_6(Si_4O_{10})(OH)_8$	90.0
Chondrite		
Bronzite	$(MgFe)_2Si_2O_6$	80.0
Magnetite	Fe_3O_4	15.0
Hematite	Fe_2O_3	5.0
Impactite[1]		
Calcite	$CaCO_3$	-
Quartz	SiO_2	-

TABLE III-1 (Cont'd.)

RESULTS OF PETROGRAPHIC EXAMINATION

PURE MINERAL SAMPLES	FORMULA	VOL. PERCENT
Orthoclase	$KAlSi_3O_8$	100%
Chert	SiO_2H_2O	100%
Magnetite	Fe_3O_4	100%
Bauxite	$AlO(OH) + Al(OH)_3$	100%
Hematite	Fe_2O_3	100%
Sphene	$CaTiSiO_5$	100%
Ilmenite	$FeTiO_3$	100%
Sandstone[2]		
Calcite	$CaCO_3$	100%
Orthoclase	$KAlSi_3O_8$	100%
Bauxite	$Al(OH)_3 + AlO(OH)$	100%
Quartz	SiO_2	100%
Hematite	Fe_2O_3	100%
Tektite[3]		
Glass	-	100%
Obsidian[3]		
Glass	-	100%
Pumice[3]		
Glass	-	100%
Basalt[4] - dense	-	-

NOTES

1. Percentages of albite and anorthite were determined by the extinction angle of the feldspars. The percentage of Ab and An were then estimated using the Michel Lévy method (Kerr, 1959).

TABLE III-1 (Cont'd.)

RESULTS OF PETROGRAPHIC EXAMINATION

NOTES (Cont'd.)

2. Because of their alteration products, these samples could not be well classified. However, some minerals were identified and listed to give an over-all impression of the rock type.
3. In glasses no information about the composition can be gained petrographically. Therefore, compositions are not given.
4. The very dense basalt have such small grains that the percentage of constituents can only be estimated. Because of the fine grains, optic-figures are not possible, and extinction angles cannot be accurately measured. Therefore, composition was not obtained for this material.

FIGURE III-1 ARRANGEMENT FOR HANDLING SAMPLES IN INERT ATMOSPHERE

When a sufficient amount of the sample had been sieved, the powdered material was sealed in an Atlas Arc Lid jar. Since the jars were sealed in the argon-filled bag, the sample was within a protective atmosphere from the time it was crushed until the jar was opened. The powdered samples were analyzed for particle size distribution; the results are given in Table III-2 as the percentage of the total number of particles measured.

TABLE III-2

PARTICLE SIZE DISTRIBUTION

	Particle Size (microns)					
	0-3.48	3.48-17.4	17.4-34.8	34.8-69.6	69.6-104.4	104.4-1740
Granodiorite	94.6	3.4	1.5	<1	<1	<1
Dunite (olivene)	95.5	4.4	<1	<1	<1	<1
Pyroxene (augite)	90.0	6.2	2.6	<1	<1	<1
Andesite	89.8	7.2	2.7	1.0	<1	<1
Obsidian	93.0	3.0	2.1	1.1	<1	<1
Gabbro	87.0	6.3	4.5	0.9	<1	<1
Pumice	89.2	6.0	3.2	1.0	<1	<1
Syenite	95.9	2.8	0.6	0.7	<1	<1
Chondrite	90.2	7.0	2.1	1.6	<1	<1
Tektite	95.6	3.7	1.3	<1	<1	<1
Basalt (shoc ed)	90.3	8.9	0.6	<1	<1	<1
Basalt (unshocked)	81.9	10.0	6.0	1.0	<1	<1
Sandstone	96.8	2.7	<1	<1	<1	<1
Impactite	93.4	5.1	1.3	<1	<1	<1
Serpentine	93.0	4.9	1.3	<1	<1	<1

NOTE

The tabulated figures indicate the percentage of the total number of particles measured.

Figure III-2 shows microphotographs of twelve typical ground materials and indicates the form and approximate size distribution. Because of particle shape, especially in minerals with an acicular or fiberous habit, the maximum dimensions observed in the photos may be greater than the size range indicated, because particles elongated in one dimension will pass through the sieve screens designed to eliminate them.

Great care was taken in the handling of the test materials, both in the grinding operation and subsequent storage, and also when introduced into the test apparatus, so that atmospheric contact would not contaminate the surfaces formed by grinding.

The densities of the solid materials were measured with a pycnometer, using samples weighing about 5 grams. The densities of the solid-packed powders and the loose powders were measured by weighing a 1 cc volume in air. The data shown in Table III-3 indicate that rocks with significantly different densities, such as pumice and gabbro, do not exhibit any difference in density after the minerals are ground to a loose powder.

Where possible, the weight percentages of the minerals contained in the rocks studied were calculated by volumetric analysis of the petrographic thin sections. Table III-4 shows the composition (by oxide) of the minerals studied. The impactite and sandstone cannot be chemically analyzed by petrographic methods.

FIGURE III-2a GRANODIORITE - X24
Coarse-Grained Silicate
0-74 Microns

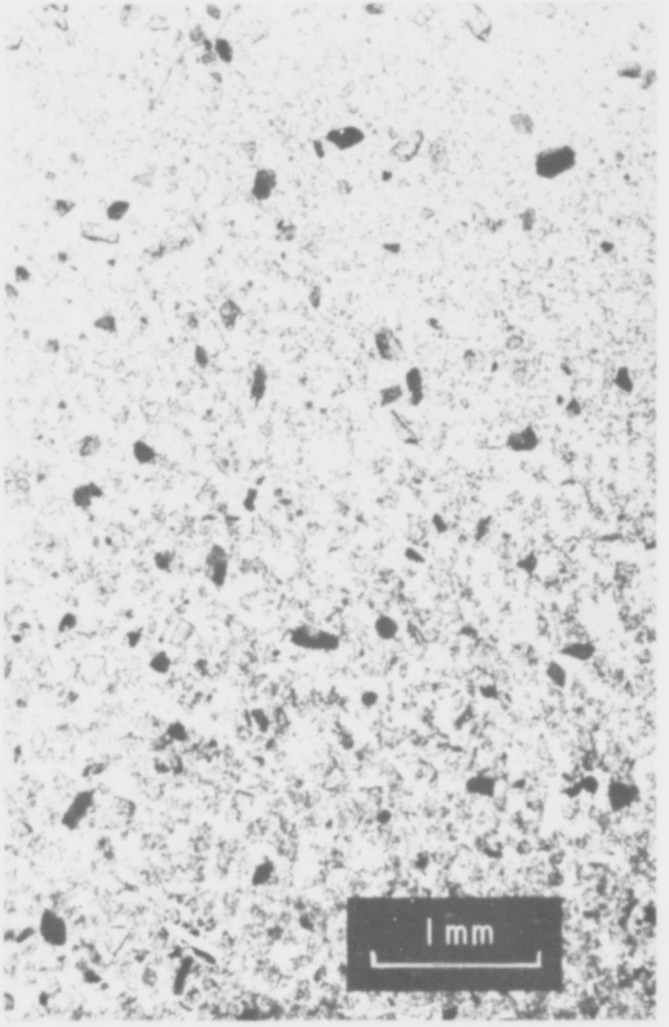

FIGURE III-2b GRANODIORITE - X24
Coarse-Grained Silicate
74-149 Microns

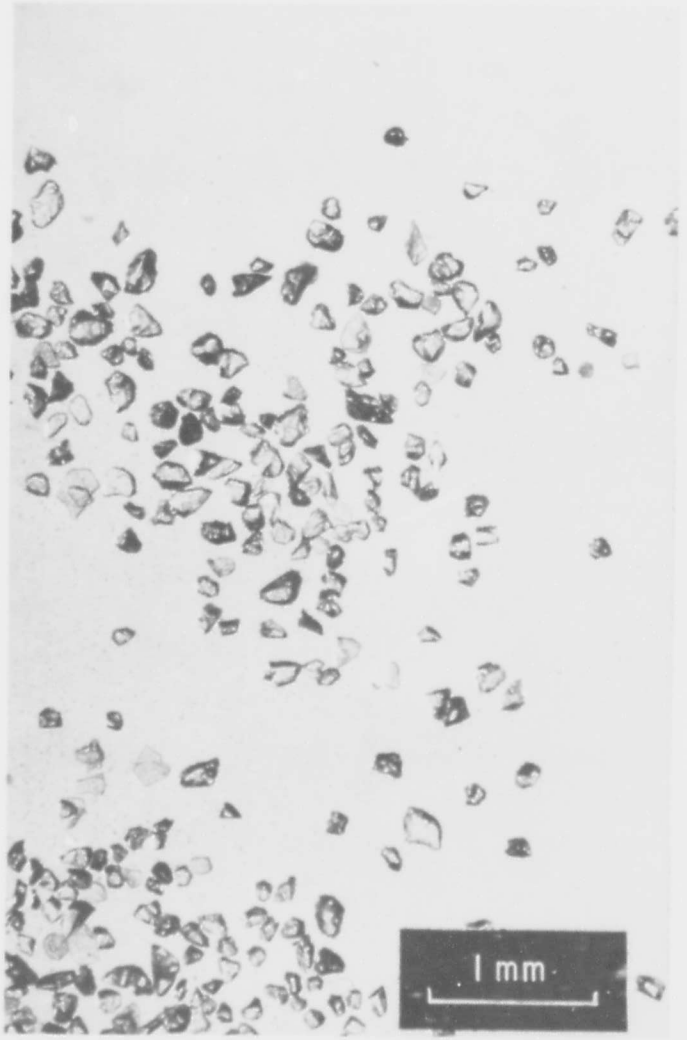

FIGURE III-2c DUNITE - X24
Magnesium Iron
Silicate 74-149 Microns

FIGURE III-2d DUNITE - X24
Magnesium Iron
Silicate 149+ Microns

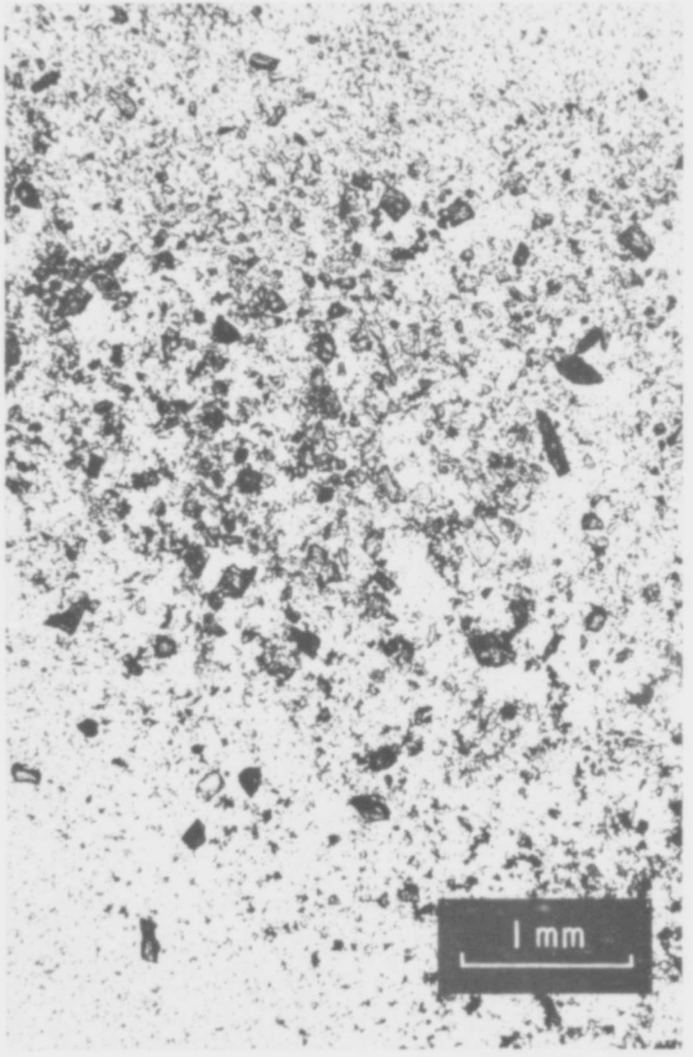

FIGURE III-2e PYROXENITE - X24
Iron Magnesium Silicate
0-149 Microns

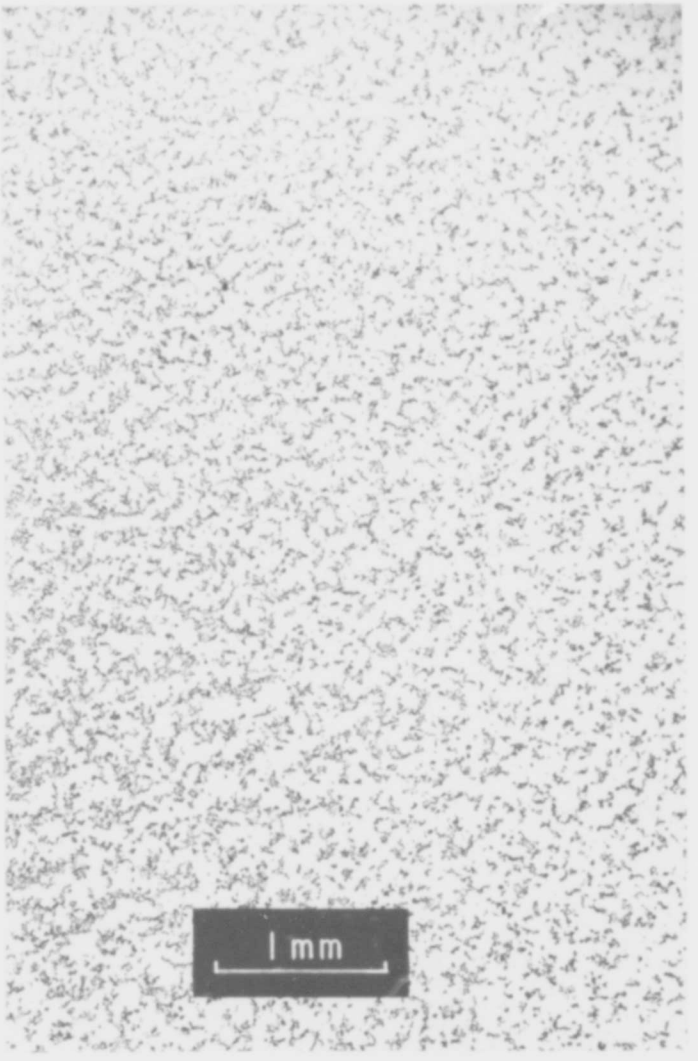

FIGURE III-2f ANDESITE - X24
Fine-Grained Silicate
with No Quartz
0-149 Microns

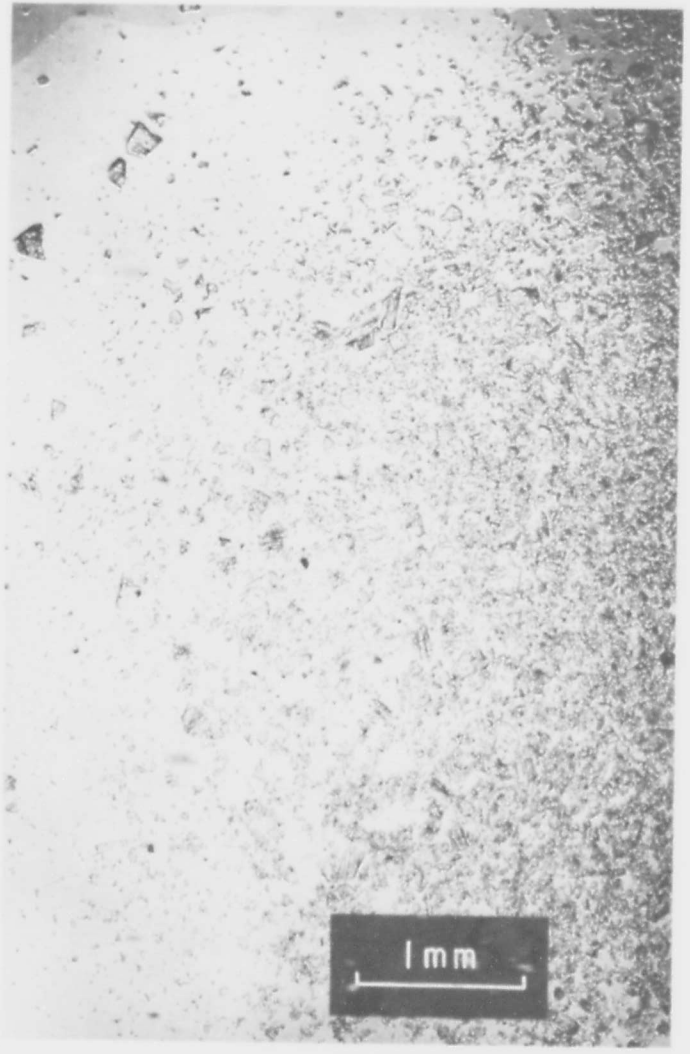

FIGURE III-2g OBSIDIAN - X24
Basalt Glass
0-149 Microns

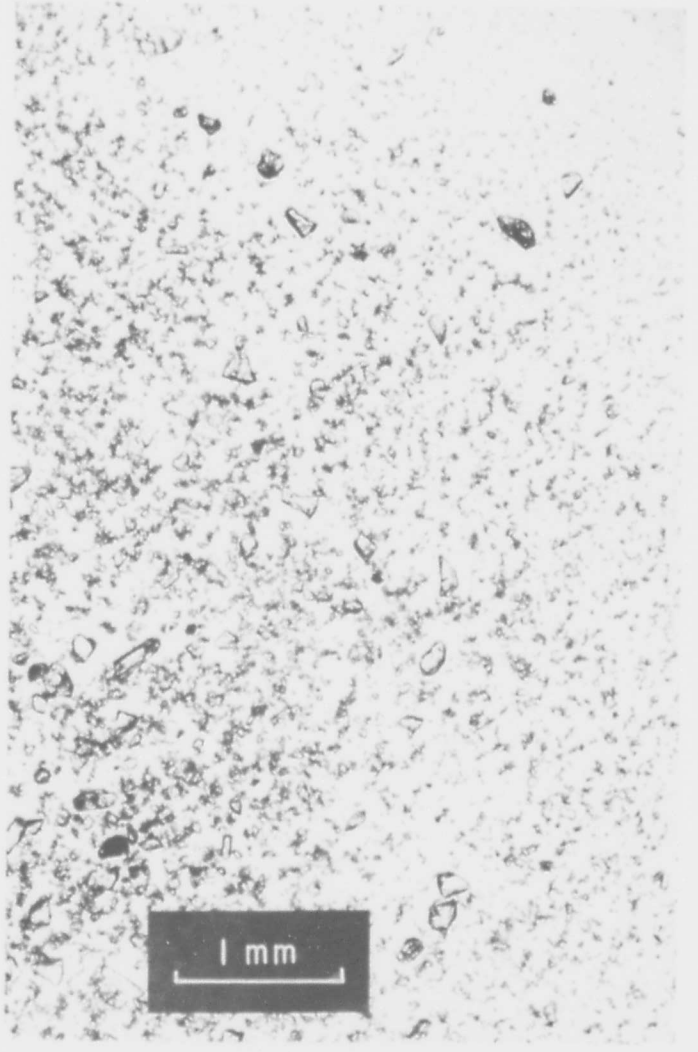

FIGURE III-2h GABBRO - X24
Coarse-Grained,
Silica-Poor Rock
0-149 Microns

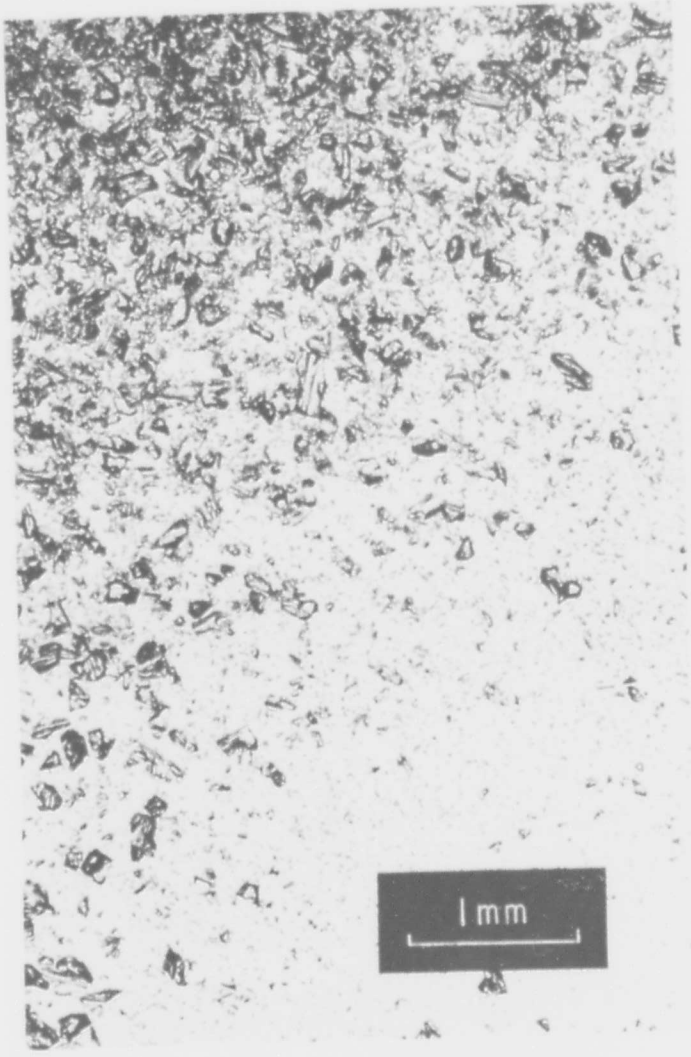

FIGURE III-2i PUMICE - X24
Silica Rich Glass
0-149 Microns

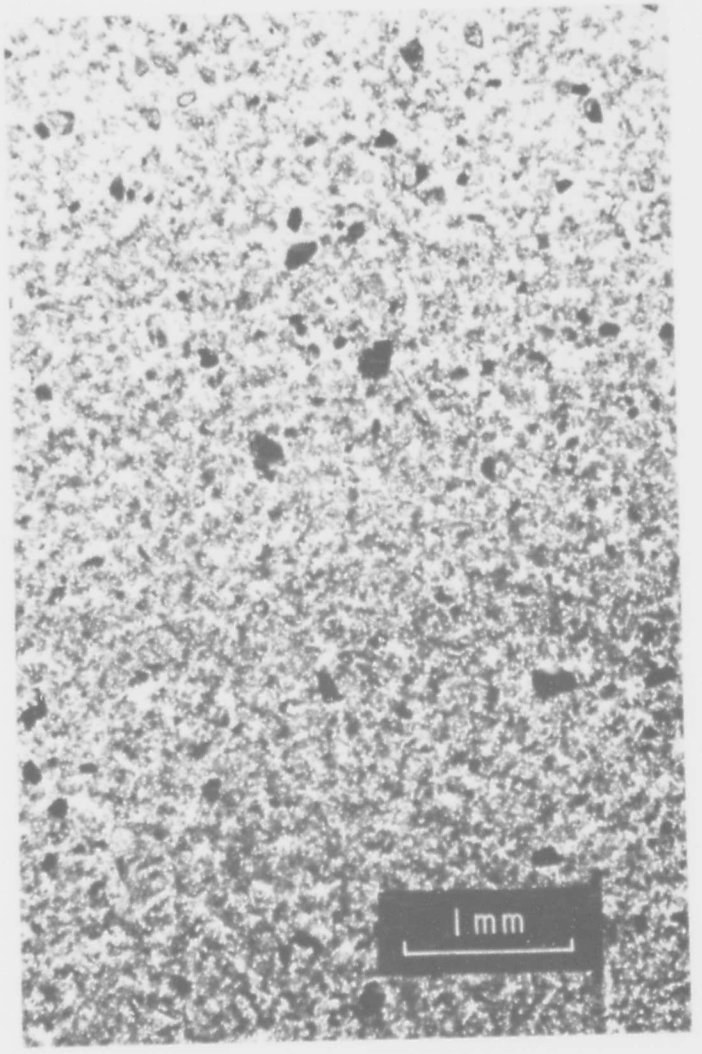

FIGURE III-2j SYENITE - X24
Coarse-Grained Silicate
with No Quartz
0-149 Microns

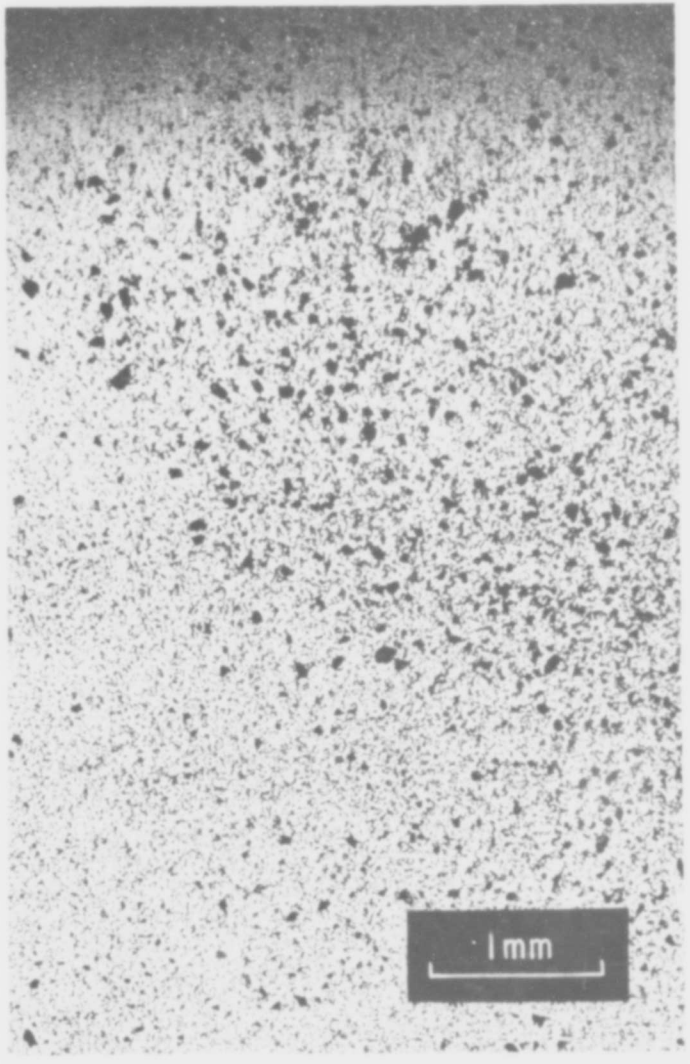

FIGURE III-2k CHONDRITE - X24
Meteorite 0-149 Microns

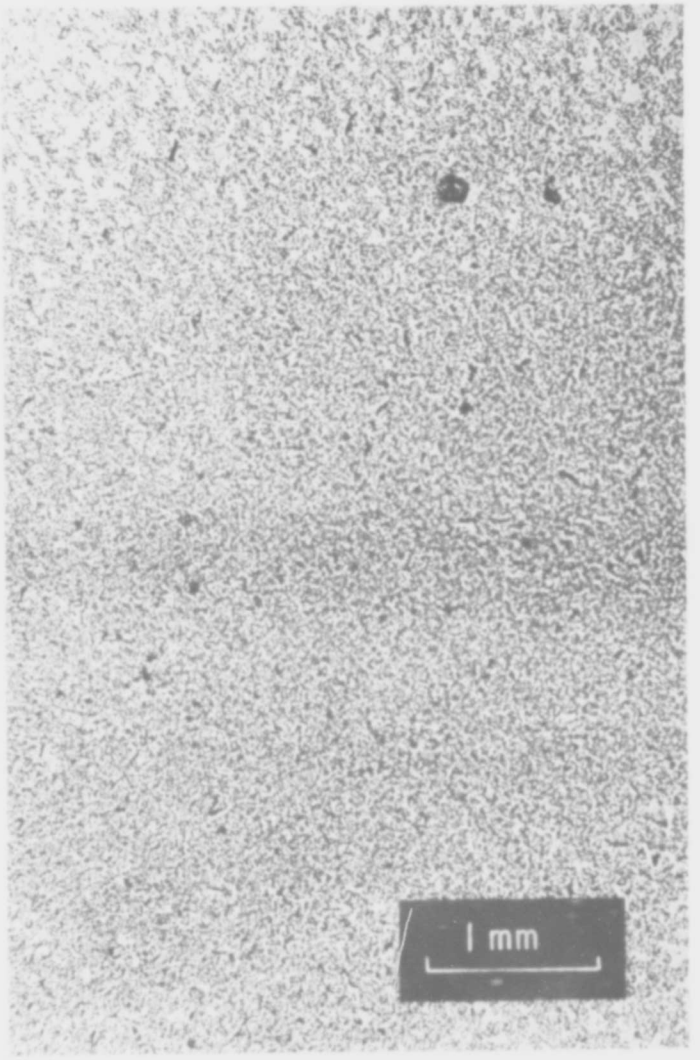

FIGURE III-2ℓ TEKTITE - X24
Silica-Rich Glass,
Probable Meteorite
0-149 Microns

TABLE III-3

DENSITIES OF TEST MATERIALS

(gm/cc)

	Solid	Packed Powder*	Loose Powder*
Granodiorite	2.76	1.84	0.86
Dunite (olivine)	3.30	1.54	1.06
Pyroxene (augite)	3.40	1.47	0.97
Andesite	2.72	1.33	0.74
Obsidian	2.35	1.37	0.85
Gabbro	3.02	1.57	0.84
Pumice	1.66	1.54	0.72
Syenite	2.73	1.06	0.60
Chondrite	3.31	1.21	0.83
Tektite	2.31	1.07	0.69
Basalt (shocked)	2.56	1.59	0.98
Basalt (unshocked)	2.57	1.61	0.96
Sandstone	1.80	0.95	0.48
Impactite	2.09	1.24	0.75
Serpentine	2.70	0.94	0.50

*Powder densities measured in air.

TABLE III-4

APPROXIMATE CHEMICAL COMPOSITION

	Andesite*	Basalt*	Pumice*	Tektite*	Granodiorite	Dunite
SiO_2	59.59	49.06	72.80	76.37	63.0	40.1
Al_2O_3	17.31	15.70	13.49	12.59	14.1	1.0
Fe_2O_3	3.33	5.38	1.45	0.26	1.3	4.2
FeO	3.31	6.68	0.96	0.62	4.5	6.1
MgO	2.75	6.17	0.38	0.17	2.4	46.1
CaO	5.80	8.95	1.20	0.79	1.3	-
Na_2O	3.58	3.11	3.38	3.36	1.7	-
K_2O	2.04	1.52	4.46	4.67	1.2	-
H_2O	1.26	1.62	1.47	0.97	1.1	2.4
TiO_2	0.77	1.36	0.33	0.11	-	-
P_2O_5	0.26	0.45	0.08	-	-	-

	Pyroxene*	Gabbro	Syenite	Serpentine	Obsidian*	Chondrite**	
SiO_2	52.33	50.6	55.0	36.5	49.06	39.49	Silicate Phase
Al_2O_3	3.54	19.5	21.1	-	15.70	2.61	
Fe_2O_3	2.61	1.1	2.7	9.7	5.38	-	
FeO	5.34	3.0	3.6	4.3	6.68	14.97	
MgO	23.92	3.0	2.1	31.5	6.17	24.55	
CaO	10.30	13.5	6.9	2.0	8.95	1.96	
Na_2O	0.43	2.0	7.1	-	3.11	1.04	
K_2O	0.35	7.1	1.8	-	1.52	0.18	
H_2O	1.03	1.0	1.0	11.0	1.62	-	
TiO_2	0.10	1.0	-	-	1.36	0.11	
P_2O_5	0.06	-	-	-	0.45	0.24	
CO_2	-	-	-	1.0	-	-	
Cr_2O_3	-	-	-	-	-	0.43	
MnO	-	-	-	-	-	0.27	

Metal Phase	Fe	7.04
	Ni	1.06
	Co	0.07
	FeSi	5.77
	P	0.04
	H_2O	0.24

*Average compositions as listed in Spock, (1953)

**Composition of chondrites is not highly variable; values listed represent average of low-iron-content chondrites compiled by Urey and Craig (1953). The low iron indicates that the major part of the iron is contained in the silicate rather than in the metallic phase.

BLANK PAGE

SECTION IV

LUNAR ENVIRONMENT SIMULATION

A. INTRODUCTION

The hypothesized lunar environment has been previously described with regard to temperature, gas composition and flux (micrometeoroid, electromagnetic, and particulate). Exact reproduction of this environment with laboratory apparatus is, of course, impossible; the approach taken in this work has been to simulate the important effects of such an environment to the degree that current technology will permit. In the different experiments, samples of postulated lunar materials are exposed to simulated radiation conditions in an ultra-high-vacuum chamber while properties of interest are measured. The various experiments are described in more detail in subsequent sections. This section deals with the methods of simulating different aspects of the lunar environment.

B. VACUUM SYSTEM

1. Design and Construction

A vacuum system was needed that would produce pressures down to 1×10^{-10} torr with substantial amounts of the sample materials present in the vacuum chamber. Hence, it was important that the system have not only a low ultimate pressure but also good pumping speed at very low pressures. Accordingly, a bakeable, metal, ultra-high-vacuum chamber with an oil diffusion pump system was selected as representative of the best system available at the time of procurement (January 1962).

The vacuum chamber and pumping system are shown schematically in Figure IV-1.* The chamber is fabricated of 1/4-inch thick 304 stainless steel. The work space, as shown in Figure IV-1, is 14 inches in diameter by 21 inches long. One end of the chamber has a full-opening door. Further access to the work space is provided by an instrument head atop the chamber and a sample holder port at the bottom. Both the instrument head and sample holder can be replaced with other covers to provide flexibility in setting up the experiments. The flanges on the door, instrument head, and sample holder port utilize the refrigerated single "O" ring principle. A refrigeration compressor circulates Freon 12 through a copper tube soft-soldered in a groove adjacent to the "O" ring. This provides cooling to keep the "O" ring at a moderate temperature during bakeout of the chamber, and to reduce outgassing from the "O" ring during pumpdown to ultimate pressure. Heaters are mounted on the exterior walls of the chamber, and a removable insulating blanket can be installed for bakeout up to about 500°F. Insulated aluminum ovens cover and heat the door and instrument dome during bakeout.

At one end of the chamber a right angle elbow leads to the diffusion pumping system. A pot containing liquid nitrogen forms a cold trap to reduce oil backstreaming. Below the pot, and immediately above the diffusion pump, a Freon-cooled baffle system further reduces backstreaming.

---

*The vacuum system was supplied with blanked-off ports by the Ilikon Corporation, Natick, Massachusetts.

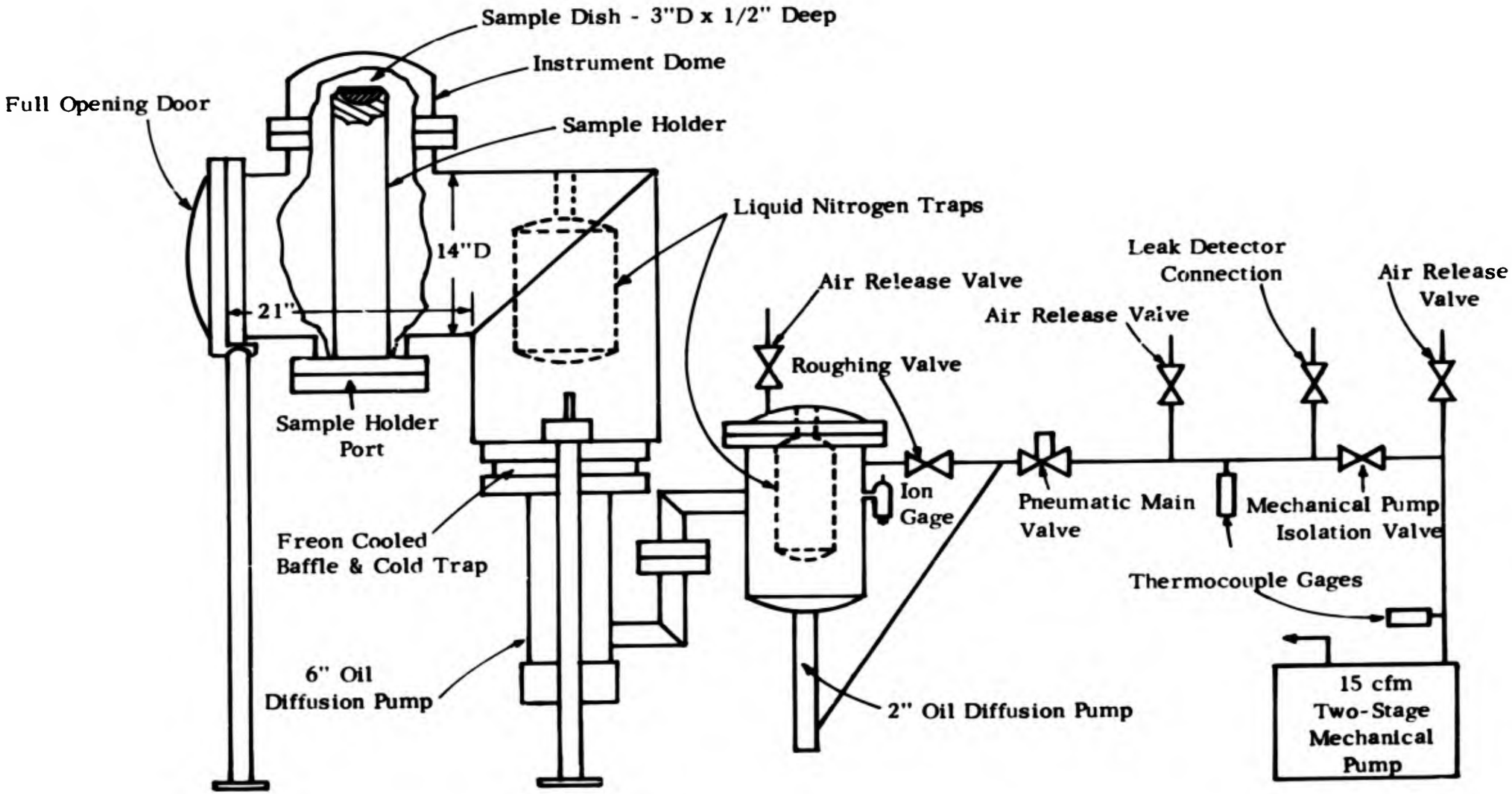

FIGURE IV-1 SCHEMATIC DIAGRAM OF VACUUM CHAMBER AND PUMPING SYSTEM

Modifications made to the original arrangement shown in Figure IV-1 are discussed in Section 2 below. The pumping system consists of a 6-inch NRC Model HS6-1500 oil fractionating diffusion pump discharging into a small stainless steel receiver. The two seals between the diffusion pump and Freon-cooled baffle and between the Freon-cooled baffle and the chamber flange are also refrigerated "O" rings. A 2-inch oil diffusion pump is connected in series to the 6-inch pump receiver and discharges into a 15-cfm, two-stage mechanical pump. The receiver contains a liquid nitrogen pot, which acts as a cold trap when the system is operated with only the 2-inch diffusion pump running. Both oil diffusion pumps used DC-704 silicone oil during the experiments described herein. The foreline arrangement is indicated by Figure IV-1.

Either a sample holder such as shown in Figure IV-2 or some other experimental device can be mounted in the work space through the sample holder port in the bottom of the chamber. The port may also be blanked off with a plain flange. The sample holder shown in Figure IV-2 has provisions for maintaining the sample dish at any temperature between 600°C and -150°C and for tilting the sample surface at angles from the horizontal (to facilitate certain observations through windows in the instrument dome).

The instrument head is shown in Figure IV-3. It contains two sapphire windows for visual observation and spectroscopic measurements of the sample, a beryllium window for admission of X-rays to irradiate the sample, a flanged port for mounting a proton source (further described in Section IV-D-2), and a sieve mechanism for sifting powder samples

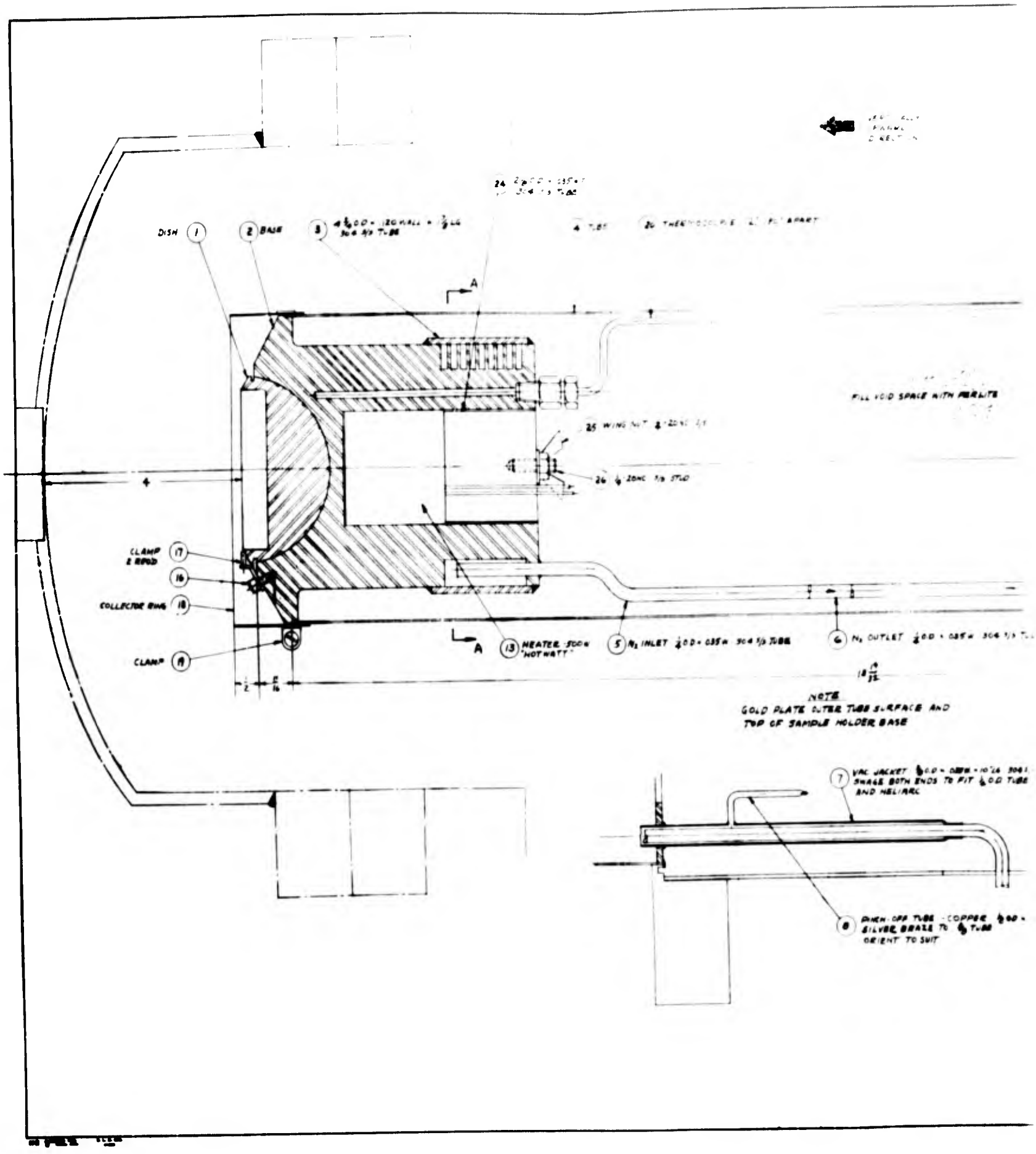
DISH (1)
(2) BASE
(3) 4 5/8 OD x .120 WALL x 3/8 LG 304 S/S TUBE
24 2 PCS .035 x 304 S/S TUBE
4 TUBE
26 THERMOCOUPLE 2" APART
A
FILL VOID SPACE WITH PERLITE
25 WING NUT & 1/4-20 NC S/S
26 1/4-20NC S/S STUD
4
CLAMP & ROD (17)
(16)
COLLECTOR RING (18)
CLAMP (19)
(13) HEATER 500W "HOTWATT"
(5) N2 INLET 1/4 OD x .035 W 304 S/S TUBE
(6) N2 OUTLET 1/4 OD x .035 W 304 S/S TU
1/2
5/16
18 21/32
NOTE
GOLD PLATE OUTER TUBE SURFACE AND TOP OF SAMPLE HOLDER BASE
(7) VAC JACKET 1/4 O.D. x .028 W x 10"LG 304 S/S
SWAGE BOTH ENDS TO FIT 1/4 O.D. TUBE AND HELIARC
(8) PINCH-OFF TUBE - COPPER 1/4 OD x SILVER BRAZE TO 1/4 TUBE ORIENT TO SUIT

FIGU

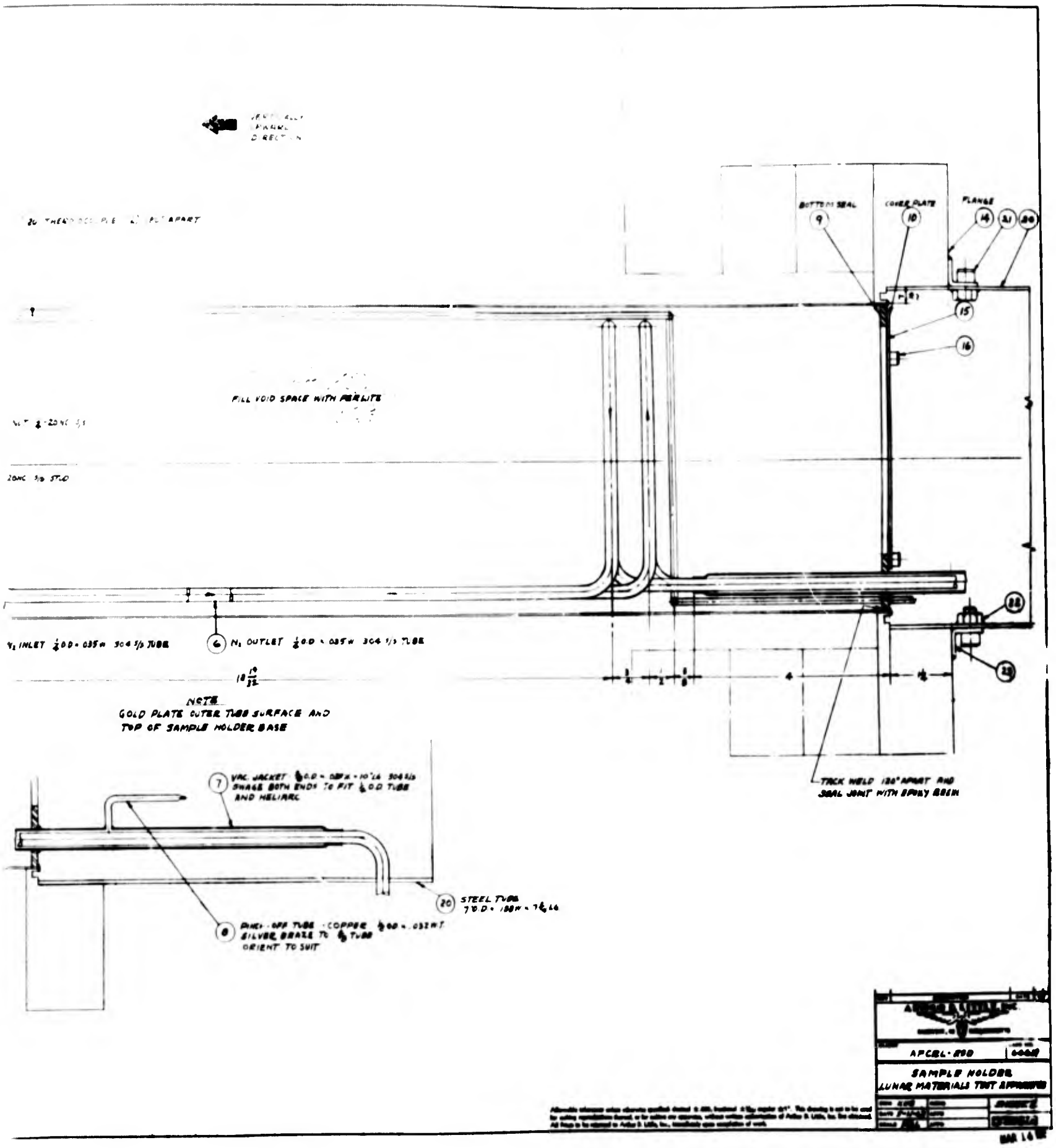

FIGURE IV-2 SAMPLE HOLDER - ADL Drawing D3441-1

B

into the sample dish or other receiver.

The full-opening end door contains the following instrumentation and feedthroughs:

a. A Bayard-Alpert type hot-cathode ionization gauge

b. A Vactek, Kreisman-type cold cathode gauge, Model 1410

c. A G.E. partial-pressure analyzer tube, Model 22 PT110

d. Two 1½-inch diameter ports with Conflat flanges, for instrumentation and thermocouple leadthroughs.

Pressures down to about 2×10^{-10} torr, the X-ray limit, can be measured with the Bayard-Alpert type ion gauge. Lower pressures are measured with the cold cathode gauge, which indicates down to the order of 10^{-14} torr. The partial-pressure analyzer, used for analysis of the residual gases in the chamber during an experiment, indicates partial pressures down to about 10^{-14} torr.

2. Operating Experience and Modifications

With the vacuum chamber clean and empty, low pressures near 10^{-10} torr have been reached in 12 hours after a pre-conditioning bakeout. With powder samples in the work space (in the sieve or sample dish), pumpdown takes substantially longer, due to outgassing from the powder. Nevertheless, pressures as low as 2×10^{-10} torr have been achieved after three to five days' pumping with substantial quantities (up to 200 gm) of powder in the chamber.

Analyses of the residual gases in the chamber at pressures down to 3×10^{-10} torr have been made. The G.E. partial-pressure analyzer is adequately sensitive to normal gases at these low pressures.

A typical spectrum shows mass peaks, in order of decreasing amplitude, for H_2O, CO, CO_2, O_2, H_2, mass 60, and N_2. The H_2O peak is dominant, with an amplitude of about three times the next largest peak, even though the system is baked out. The sources of water vapor are thought to be the refrigerated flange areas of the instrument dome, door, and sample holder port. At present, the sensitivity of the analyzer to hydrocarbon and particularly to silicone oil vapor is low. The 2.8-kilogauss deflection magnet now in use covers the mass range 0 - 50 quite well, but the range from 50 - 80 lacks resolution. Silicone oil vapor has significant peaks at masses 78 and 55 - 58. Hydrocarbon groups can be seen in the region of masses 22 - 30, 40 - 44, and, to some extent, 50 - 56, as families of peaks associated with the CO_2^+ peak.

Minor leaks have developed from time to time, primarily in instrument feedthroughs and the main liquid nitrogen trap. Typically the leaks have been of such magnitude as to prevent the chamber pressure from going below the high pressure of 10^{-9} torr (i.e., a leak of the order of 10^{-6} std cc/sec). In all cases, leak detection with helium gas and a helium mass spectrometer leak detector, or with acetone and observation of the ion gauge reading, has permitted location of the leaks and subsequent repair, so that the system was able to reach the desired low pressures.

As part of the procedure for monitoring conditions in the chamber, techniques have been developed for detecting minute quantities of diffusion pump oil that may have backstreamed into the powder samples. Originally an infrared technique was used; this has now been supplemented

with a more sensitive gas chromatographic technique. In a typical analysis, a portion of a powder sample that has been exposed in the chamber, usually about 10 grams, is extracted with 20 milliliters of Freon precision cleaning agent (a pure grade of Freon TF) by agitation in an ultrasonic tank for about ten minutes at room temperature. The slurry is centrifuged to permit sampling of the extracting solvent. An F & M Gas Chromatograph, fitted with a 6-foot high column packed with 6% SE-31 Silicone Gum Rubber on Gas-Chrom Z support and maintained at 250°C, is used to analyze the extract. A 6-microliter sample is injected into the gas chromatograph. When necessary, the extract is concentrated tenfold by evaporation. The presence of DC-704 diffusion pump oil is indicated by a peak with a retention time of 13.5 minutes, which has been found by calibration with known samples. Comparison of the area of an observed peak with that for known concentrations of DC-704 and Freon give a semi-quantitative measure of the amount of oil present in the extract and, hence, initially on the powder. Control samples of powder which have not been exposed to the vacuum show no detectable oil. With this technique, as little as 5 micrograms of oil in a 10-gram powder sample can be readily detected.

Early in the program, contamination of powder samples with diffusion pump oil was detected using the infrared technique. Table IV-1 shows pertinent data for five different samples that were examined for DC-704 oil content.

TABLE IV-1

CONTAMINATION OF POWDER SAMPLES WITH

DC-704 DIFFUSION PUMP OIL

Powder Sample	Sample Weight grams	Approximate Elapsed Time Sample Was In Chamber days	Estimated Weight Of Oil Present On Sample micrograms	Estimated Oil Weight Per Unit Exposed Area (1) micrograms/cm^2
Augite	16.9	7	300	6
Augite	9.58	4	200	4
Basalt	14.19	26	2000	40
Chondrite	12.34	37 (2)	100 or less	2 or less
Obsidian	17.69	7	300	6

(1) Based on an exposed area (projected) of 50 cm^2. Although the area varied somewhat, depending on the experiment, this figure is typical.

(2) Two successive runs of 30 and 7 days.

In the experiments with these samples, chamber pressures in the low range between 10^{-9} and 10^{-10} torr were achieved. The start up, operating, and shut down procedures varied considerably, so the amount of oil per unit of exposed area should be viewed as only a very rough measure of the oil backstreaming rate. For DC-704, a weight per unit area of about 0.08 micrograms/cm^2 corresponds to a unimolecular layer over the exposed area. As shown in Table IV-1, the amount of oil contamination in early tests was several orders of magnitude higher and was considered excessive.

To reduce backstreaming, the original cold baffle arrangement, which is shown in Figure IV-4, was modified to the one shown in Figure IV-5. In addition to a Freon-cooled interior baffle, the wall of the pumping duct is now also Freon-cooled. The proportions of the liquid nitrogen pot have been changed, and a copper skirt has been added. The Freon-cooled baffle is removable through the bottom flange for cleaning. The geometry of the baffle and walls is such that all molecules emitted from the diffusion pump will first be condensed at -25°C on one of the Freon-cooled surfaces. The subsequent re-evaporation rate will be proportional to the vapor pressure at -25°C. Hence, the effective source pressure for backstreaming is reduced below that for the original geometry by a factor of about 10^3 (the ratio of the vapor pressure of DC-704 at room temperature to that at -25°C). Furthermore, molecules streaming upward from the Freon-cooled surfaces after re-evaporation have a high probability of striking the liquid-nitrogen-cooled surfaces, where most of them would be retained.

Even with the baffle geometry shown in Figure IV-5, some backstreaming may occur. The probability that a molecule striking a liquid-nitrogen-cooled surface will condense and be retained is less than unity. Its value is not accurately known, and for this reason nitrogen-cooled baffles are frequently arranged so that molecules must make numerous bounces to pass through. Space limitations in the present chamber and the desirability of maintaining a high pumping speed ruled out complicated baffle geometries and led to the fairly simple arrangement of Figure IV-5. Condensate on the Freon-cooled baffle may migrate up the inner surface of the vertical cylinder portion, over the lip, and down

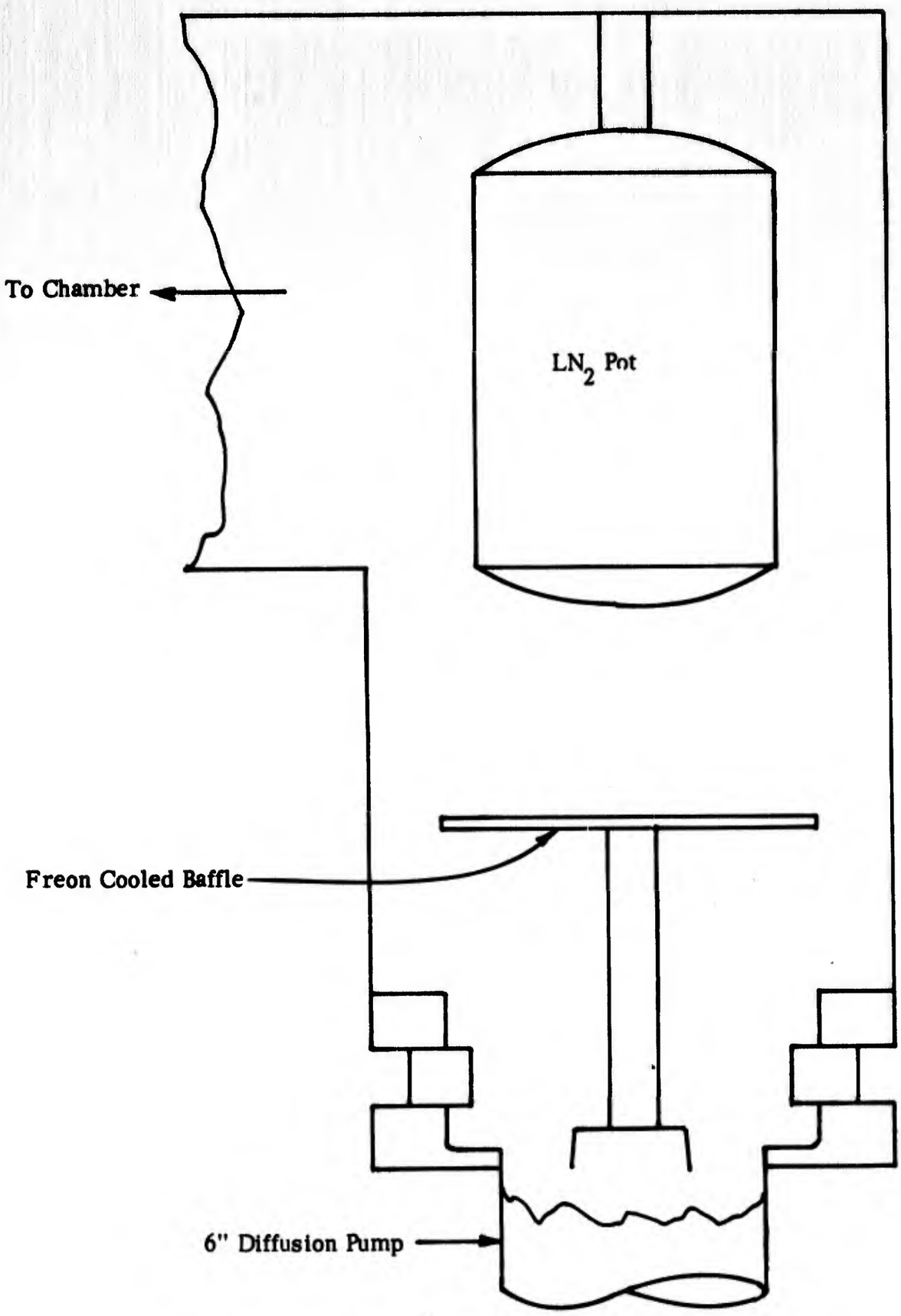

FIGURE IV-4 ORIGINAL COLD BAFFLE ARRANGEMENT

BLANK PAGE

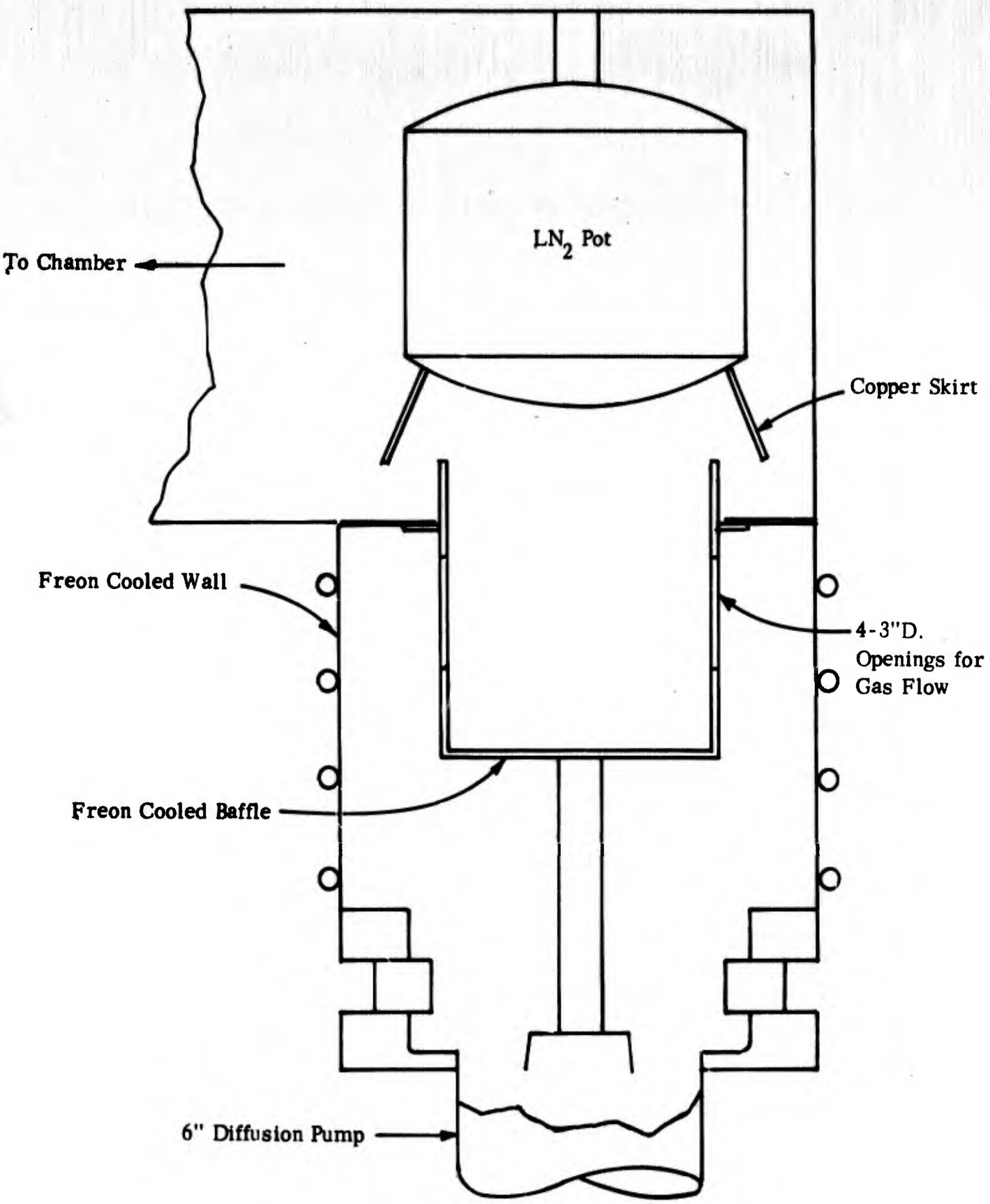

FIGURE IV-5 MODIFIED COLD BAFFLE ARRANGEMENT

the outside of the cylinder, where re-evaporation could carry the oil molecules into the chamber without striking a liquid-nitrogen-cooled surface. Hence, the arrangement is not truly an "anti-migration" baffle. To prevent migration, the baffle surfaces that are now Freon-cooled would have to be liquid-nitrogen-cooled, because surface migration at $77^{\circ}K$ is considered negligible.

After modification of the baffles, powder samples used in four tests were analyzed, using the more sensitive gas chromatographic technique, to determine their DC-704 content.

Table IV-2 lists the pertinent data.

The first test with Brazilian Quartz shows a substantial reduction in oil content per unit of exposed area in relation to tests before the modifications with comparable exposure times. The second test with Brazilian Quartz was of very short duration (4 hours), so that oil would have reached the sample primarily during start up or shut down. The amount of oil is high, considering the short exposure. In the two succeeding tests with pumice and olivine, the main liquid nitrogen trap and the Freon-cooled baffles were cooled down before the main pump was turned on, and at the end of the test the pump was cooled down with the trap still cold. Then, with the trap cold, the chamber was gas-released with argon. This procedure resulted in the low level of contamination indicated.

A partial pressure of DC-704 on the order of 1×10^{-11} torr would have been sufficient to form the degree of coverage shown in the seven-day period. As noted below, because of the slow diffusion of strongly sorbed molecules into a layer, the oil contamination would be confined

TABLE IV-2

CONTAMINATION OF POWDER SAMPLES WITH DC-704 DIFFUSION PUMP OIL AFTER BAFFLE MODIFICATIONS

Powder Sample	Sample Weight grams	Approximate Elapsed Time Sample Was In Chamber days	Estimated Weight of Oil Present On Sample micrograms	Approximate Exposed Area cm^2	Estimated Oil Weight Per Unit Exposed Area micrograms/cm^2
Brazilian Quartz	90	7	360	500	0.72
Brazilian Quartz	14	0.17	50	500	0.10
Pumice	16.3	7	18	50	0.36
Olivine	24.3	7	5	50	0.10

to particles at, or just below, the exposed surface (see Appendix B for an illustrative case on the contamination of a clean powder); the bulk of the samples would not be contaminated.

C. SAMPLE OUTGASSING AND CONTAMINATION

To gain insight into the outgassing and contamination of powder materials in vacuo, an analysis has been made of the transient flow of gas at low pressures out of and into a porous medium that is exposed to a pressure change at a bounding surface. The gas may be sorbable on the surface of the particles that comprise the medium; hence, desorption (during evacuation) and sorption (during pressurization) may occur. The analysis is presented in Appendix B, which also includes cases of a general nature that illustrate application of the results. Figures B2 and B4 of the Appendix summarize the results. Figure B2 is a plot of gas pressures that can exist in equilibrium with a sorbed phase covering 10% of the surface vs. the heat of sorption. Figure B4 is a plot of the characteristic time versus the heat of sorption. The characteristic time is defined mathematically in Appendix B; in essence, it is the time required for the bounding surface of a layer of powder to respond to a pressure change.

Figure B2 in Appendix B shows that for a gas pressure of 10^{-10} torr, only species sorbed with heats of sorption greater than about 21 kcal/gm-mole can remain on the surface with a coverage of 10%. Figure B4 in Appendix B shows that the characteristic time for a heat of sorption of 21 kcal/gm-mole is about 10^3 years. Hence, even if a fine powder on the lunar surface were initially highly contaminated, gases sorbed with energies less than about 21 kcal/gm-mole would by now be largely outgassed.

Only gases with heats of sorption greater than about 25 kcal/gm-mole, i.e., chemisorbed gases, would remain as a substantial sorbed layer on the particle.

The method of preparing samples for tests in the vacuum chamber was described in Section III. The particle surfaces generated by the grinding process are likely to be amorphous and highly disordered. The grinding is done in an argon atmosphere, but water vapor is released from the rocks as they are ground, and small quantities of impurities are present in the argon. (The amount of water vapor contained in the rocks is generally far greater than the amount of impurities that might be introduced with the argon.) Water vapor may be chemisorbed, if an activation energy is supplied. At room temperature, the rate of chemisorption is normally so low as to be negligible; however, the grinding action may supply activation energies (by causing elevated temperatures near contact points) so that some chemisorption of water vapor could occur. Other gases present can be physically adsorbed by the particles.

After removal from the grinding apparatus, the sample is maintained in an argon atmosphere until its placement in the vacuum chamber. As it is placed in the chamber, the sample is exposed to the atmosphere for a short period of time, usually about five minutes. During this exposure at room temperature, atmospheric constituents such as nitrogen, oxygen, water vapor, and some hydrocarbons may be physically adsorbed. Little or no chemisorption would be expected to take place during the exposure, because the temperature is not high enough for the rates of chemisorption to be appreciable.

The chamber is quickly evacuated, and, within a few hours, pressures of 10^{-8} torr and below are reached. Pressures below 10^{-9} torr are usually achieved within about 24 hours. The sample may be exposed to pressures in the range of 10^{-10} to 10^{-9} torr for three to five days. For most physically adsorbed gases, the heat of adsorption will be less than about 10 kcal/gm-mole. The equilibrium pressure to maintain a 10% surface coverage for that heat of adsorption is about 10^{-2} torr, i.e., a pressure much higher than that achieved in the chamber. Conversely, at a pressure of 10^{-9} torr, the surface coverage that remains after equilibrium is achieved between adsorbed and gas phases would be extremely small, and essentially negligible. The characteristic time for a heat of adsorption of 10 kcal/gm-mole is about 200 seconds (less for lower heats of adsorption) so that physically adsorbed gases of the common types, with heats of adsorption less than 10 kcal/gm-mole, will be largely outgassed from the powder in about one hour. After 100 hours of exposure, gases with heats of adsorption greater than about 13 - 14 kcal/gm-mole may still remain on the surface with appreciable coverages. Thus, surface coverages different from those which could be retained by a powder on the lunar surface may exist on the samples being tested in the vacuum chamber. While in the vacuum chamber, a sample is exposed to residual gases produced by outgassing from the chamber walls and other materials exposed to the vacuum, and from oil backstreaming from the diffusion pumping system. The ambient pressure level in the chamber is generally less than 10^{-9} torr. As may be seen from Figure B2 (Appendix B), gas species that would be sorbed with heats of sorption of 20 kcal/gm-mole or greater could form surface coverages

of 10% or more. At 10^{-9} torr, enough gas molecules strike the exposed surfaces in about 180 seconds to form a 10% sorbed unimolecular layer, if each molecule were sorbed. Hence, the particles on the exposed surface of a layer and those just beneath the surface may acquire significant sorbed layers during the test. However, the characteristic time for a gas with heat of sorption of 20 kcal/gm-mole is about 10^2 years; since most tests last on the order of only 100 hours, powder particles more than a few layers beneath the exposed surface would not be expected to acquire significant sorbed layers from the residual gases in the chamber.

As noted above, only gases with heats of sorption greater than about 20 kcal/gm-mole will be retained. Because the powder is at or near room temperature during its exposure, the rates of chemisorption should be very low. However, certain hydrocarbons, particularly the silicone diffusion pump oil, can be physically sorbed with relatively high heats of sorption and are capable of forming appreciable surface coverages even when the ambient pressure is as low as 10^{-9} torr. The heat of condensation of the DC-704 diffusion pump oil is about 25.5 kcal/gm-mole. Its heat of physical adsorption would be over 20 kcal/gm-mole.

D. LOW-ENERGY PROTON SOURCE

1. Introduction

For the purpose of studying the simulated effects of solar proton flux upon the lunar materials, a low-energy proton source was constructed as an accessory to the existing ultra-high-vacuum chamber. The design of the proton source was based on that developed by Bruce W. Hapke at Cornell University.

The proton source output was planned to be greater than that corresponding to the proton flux density of the quiescent sun, i.e., about 10^8 protons/sec cm^2. A proton current of 1-microampere intensity is equivalent to a flux of 6.3×10^{12} protons per second; when distributed over a typical sample area 3.5 inches in diameter, this current gives a proton flux density of approximately 10^{11} protons/sec cm^2, or 1000 times greater than the solar flux. The source can deliver at least ten times as much, and possibly more, under optimum adjustments of operating parameters. The proton current could be increased further by enlarging the accelerator orifice, but this would permit a greater flow of hydrogen into the vacuum chamber.

The increase of proton current is also limited by the heating caused by impingement of the proton beam upon the sample. A beam of 1-microampere/cm^2 current density and 10-kilovolt energy delivers a power density of 0.01 watt/cm^2. A ten-fold increase in power density might cause an undesirable rise of surface temperature in samples of low thermal conductivity.

The energy distribution of protons in the beam has not yet been determined, as these experiments have just begun, and further adjustments will be made to the proton gun. However, judging from the results presented by Hapke, the energy spectrum is probably broad. Also, based on the experience with proton sources of the Penning type, one may expect that, in addition to protons, the beam contains a considerable percentage of H_2^+ ions (Barnett et al, 1953).

2. Description of Apparatus

The apparatus consists of two principal components: the proton tube and the power supply. Connected to the proton tube are the ion gauge (separately controlled) and the solenoid electromagnet. A photograph of the apparatus is shown in Figure IV-6. Figure IV-7 is a diagram of the electrical connections between the tube and the power supply unit.

The proton tube is schematically shown in the upper left part of Figure IV-7. The base of the tube is a standard Varian Conflat flange, 4-1/2 in. OD, which mates with the Conflat flange on the top of the dome on the ultra-high-vacuum-chamber. The glass envelope of the assembly contains the cylindrical anode and the two disc cathodes of the Penning discharge ion source. Below the lower cathode is the accelerator electrode, which is mounted on a hollow pedestal attached by four screws to the flange. The diameters of the cathode and accelerator orifices are 0.120 and 0.100 inch respectively and their separation is approximately 0.120 inch. The entire electrode assembly can be withdrawn and replaced from below. The high-voltage terminals are connected by flat spring contacts to two tungsten wire lead-throughs sealed in the upper part of the glass envelope.

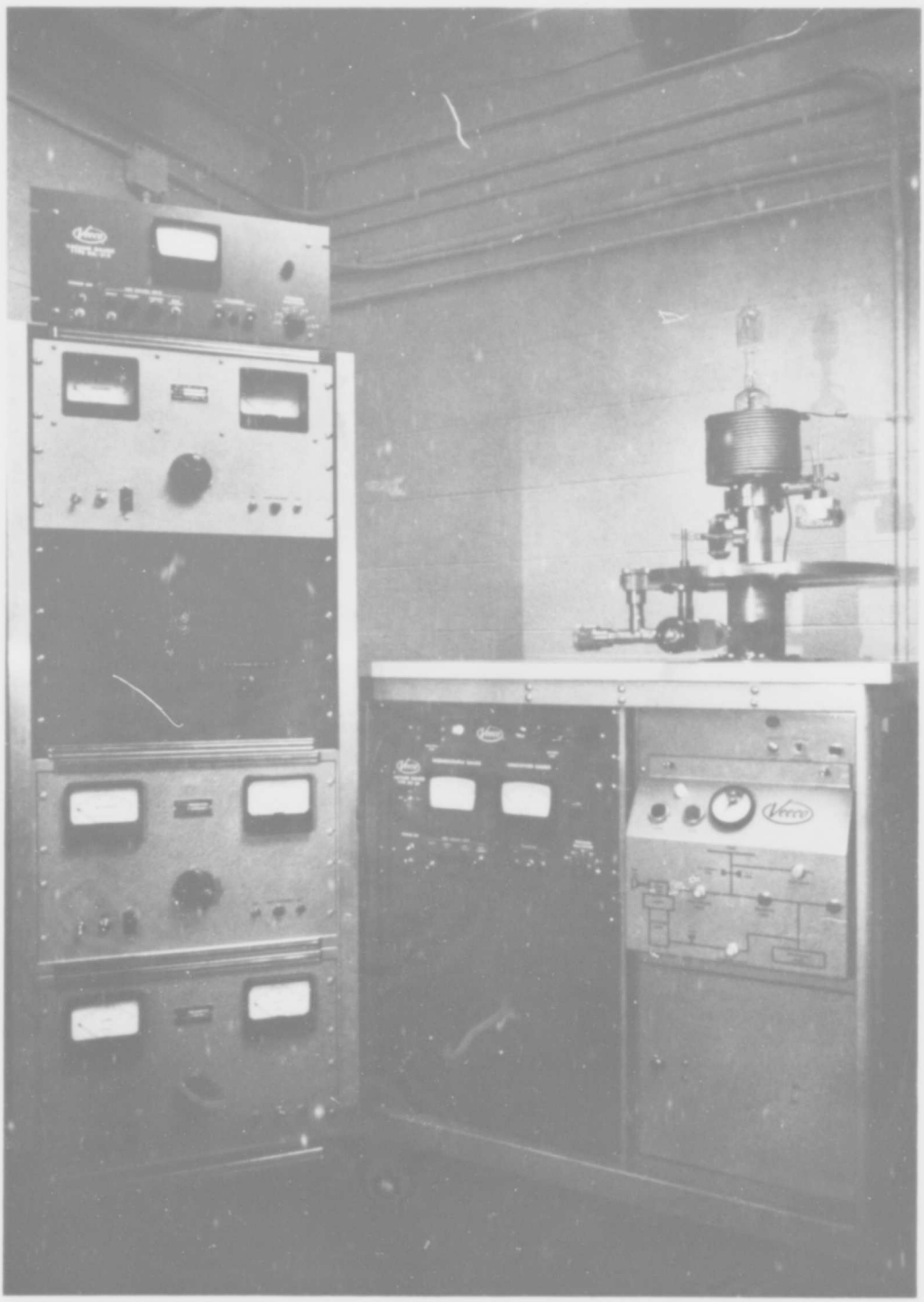

FIGURE IV-6 PROTON SOURCE APPARATUS

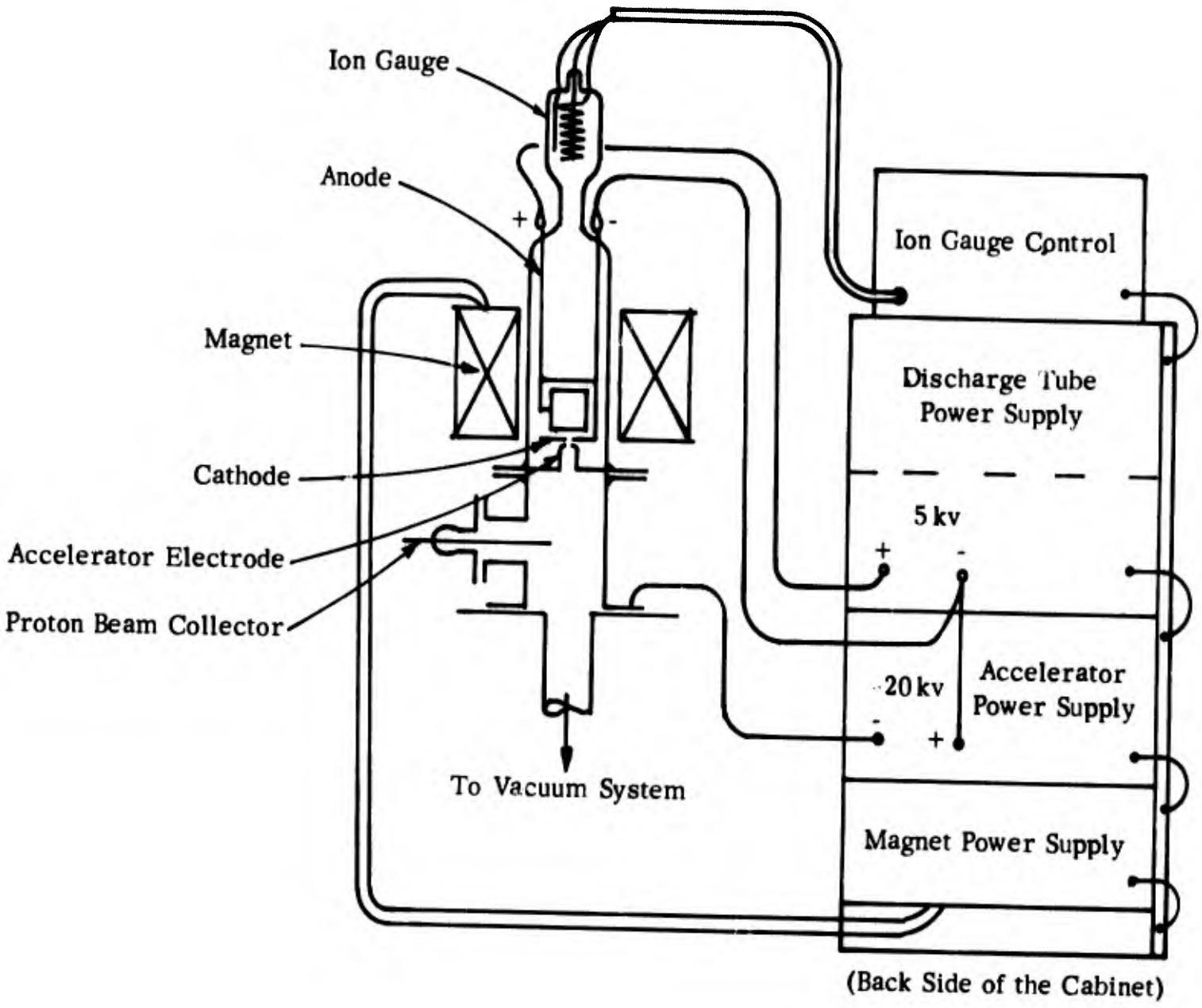

FIGURE IV-7 SCHEMATIC DIAGRAM OF PROTON SOURCE APPARATUS

All electrodes are made of aluminum. This metal is much less susceptible to sputtering than the nonmagnetic stainless steel used in earlier experiments, and its use has greatly reduced the frequency of spark-overs on the insulators.

The upper part of the glass envelope carries an ion gauge of the Bayard-Alpert type (Westinghouse WL-22643) which is operated with its own control unit (Veeco, Type RG 21X). When used with hydrogen, the response of the ion gauge is no more than half as great as with dry air. See, for example, Dushman-Lafferty (1962). When the Penning discharge is operated, the volume of the proton tube above the pedestal and the accelerator orifice is filled with hydrogen at a pressure typically between 10^{-3} and 10^{-4} torr. The gas is continually withdrawn through the accelerator orifice by the pumps of the ultra-high-vacuum chamber and must be replenished by leaking hydrogen into the tube from a supply tank. The rate of leakage is controlled by a precision variable leak valve (Granville-Phillips, Model 9100) permanently attached to the proton source through a glass tube. The rate of flow of hydrogen is determined by the equation:

$$dq/dt = S_1 p_1 = S_o p_o,$$

where S_1 denotes the effective "speed" of the orifice and p_1 the pressure in the discharge space. S_o denotes the speed of the leak and p_o the supply pressure of hydrogen. The value of S_1 calculated from the dimensions of the orifice is approximately 2.5 liter/sec. If $p_1 = 10^{-3}$ torr and $p_o = 1000$ torr, $dq/dt = 2.5 \times 10^{-3}$ liter-torr/sec, or approximately 0.01 liter per hour at 1000 torr. In the tests, hydrogen was discharged by the vacuum pump system into an exhaust system.

Commercially pure hydrogen (reduced to 15 psi pressure) from a tank was used. To keep the proton flux free of the ions of impurities, spectrally pure hydrogen, which is available in 1-liter glass flasks, may be preferable.

The proton tube can be baked out to outgas the glass walls and metal parts. The variable leak valve is also bakeable, if the worm-gear drive and counter are removed.

The power supply is shown in Figure IV-7. It contains two high-voltage d-c power supplies and one low-voltage d-c power supply for the electromagnet. The 5-kilovolt power supply for the Penning discharge tube is housed in the upper two compartments of the rack, and the high-voltage cables connecting it with the proton tube are attached to the properly marked terminals in the back of the unit.

The negative terminal of the discharge tube power supply is connected to the 20-kv accelerator power supply, whose positive terminal is grounded. Thus the discharge tube power supply operates at a potential up to 20 kv above ground. Therefore, it was modified to give proper protection to the operators.

All power supplies have individual current-limiting circuit breakers which turn off the power when the maximum rated current is exceeded. The circuit breaker can be manually reset and the high voltage re-applied after the control Variac is manually returned to zero.

The solenoid electromagnet increases the collision frequency in the glow discharge at low pressures. This is the principle of operation of the Penning ionization gauge. Without a magnetic field, no d-c discharge is obtained in the proton tube. The solenoid generates the axial field of approximately 300 gauss/amp at the location of the discharge electrodes. Up to about 1 amp, cooling by natural air convection is sufficient. At higher current levels, a flow rate of about 2 gal/hr is needed in the water cooling coil.

To permit the beam output of the proton tube to be tested on a laboratory vacuum system, a T-flange is provided with removable terminals on the side arm. Since the lower flange and the side arm are gasketed with O-rings, it is not suited for high-temperature bakeout.

A diagram of the proton beam test setup is shown in Figure IV-8. The stainless "T" provides a side port for insertion of the collector electrodes or a container for experimental irradiation of small samples.

To measure the proton beam current, the circuit is connected as shown. A small negative potential (about 100 volts) on the cup electrode is sufficient to collect the proton current. As it impinges upon the collector electrode, the proton beam causes secondary electrons to be ejected from it; the electron current flowing to the ground then adds to the current measured by the microammeter in the collector circuit.

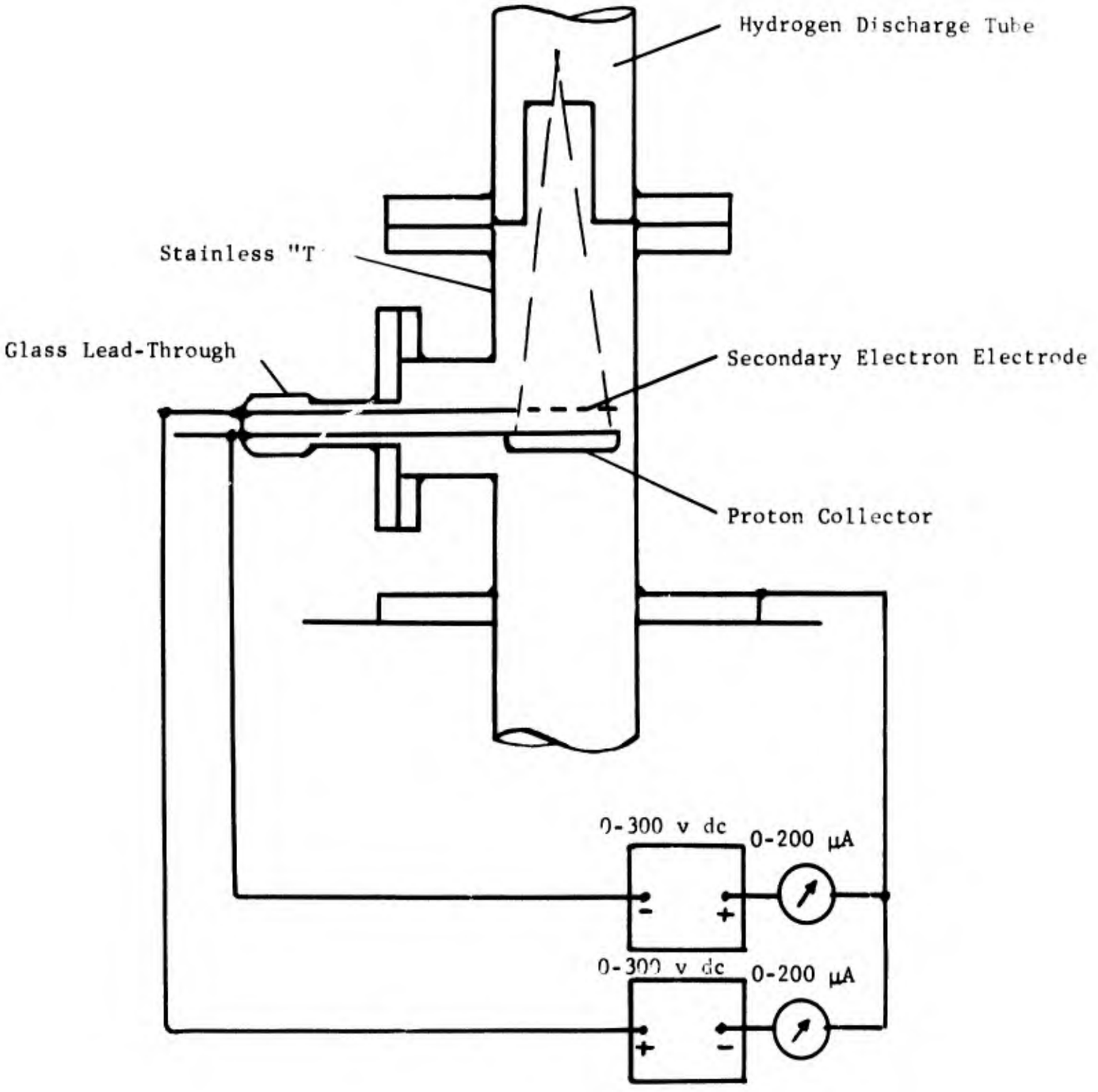

FIGURE IV-8 DIAGRAM FOR PROTON BEAM CURRENT MEASUREMENT

To separate the secondary electron current from the proton beam current, a ring-shaped electrode is placed above the collector cup and brought to a positive potential of a few hundred volts with respect to ground. (The exact voltage varies from one experiment to the next.) All electrons are then attracted to the ring electrode, and the microammeter reads only the proton beam current.

During the use of the proton source for bombardment of probable lunar materials, secondary electrons are produced. These are eliminated by arranging a similar positively charged electrode in the vicinity of the sample.

In case the irradiated material is substantially nonconducting, proton bombardment will cause it to become positively charged and eventually to acquire a sufficient potential to prevent proton flux from reaching the sample. We plan to install an auxiliary electron source (an incandescent tungsten filament) in the vicinity of the sample to neutralize this proton charge.

The T-flange attachment was also used to determine the divergence of the proton beam as it leaves the aperture of the accelerator electrode. For this purpose a glass plate covered with a fluorescent material (section of a screen of a cathode-ray oscilloscope) was supported at a 45-degree angle in the "T" so that it could be viewed through the side arm. The side arm was closed by a round plate-glass window ¼ inch thick in place of the lead-through flange. From the length of the minor axis of the brightly fluorescing elliptical area on the screen and the distance from the accelerator electrode, the cone angle of the proton beam was found to be approximately 14 degrees.

The T-flange attachment was used for experimental irradiation of small quantities of various materials while the proton source was set up on a vacuum table.

BLANK PAGE

SECTION V

EXPERIMENTAL INVESTIGATION OF PARTICLE ADHESION

A. INTRODUCTION

Various laboratories have conducted experiments to obtain an indication of the magnitude of the strength of particles. Although similar standard soil-mechanics techniques have been used, different results have been obtained. There appear to be two major reasons for this; one being the extreme difficulty, if not impossibility, of outgassing - the basic technique - a bulk mass of relatively fine powder. The other and more important reason is that the usual soil-mechanics techniques are designed to measure the soil shear strength, which is a function of (1) particulate bonding or adhesion, (2) the frictional forces between particles, (3) the angle of internal friction (which can be related to the coefficient of friction for dry soils), and (4) the internal pore pressure, which is probably negligible in lunar surface soils. Although the difficulty of separating these parameters is obvious, one of the purposes of the present work has been to devise experimental ways to measure them separately.

B. PRELIMINARY EXPERIMENTS

We performed preliminary experiments to measure the adhesive strength under high-vacuum conditions of probable lunar materials; the high-vacuum conditions were intended to simulate the atmospheric pressure of the lunar environment.

1. Angle of Repose

We compared the angle of repose of dust samples (see Section III) sifted in air and samples sifted at 10^{-9} and 10^{-10} mm of mercury.

Powdered samples were placed in a sieve above the sample holder. The sieve mechanism was then tapped so that less than a monolayer of particles was deposited per tap on the sample holder three inches below the sieve. The circular sample holder contained a rectangular aluminum foil boat three inches long, which was part of the thermal conductivity experiment (see Section VIII). The thin wires, visible in the illustration, were associated with the heat source and thermocouple used to measure thermal conductivity.

Figure V-1 illustrates the angle of repose of powdered basalt sifted in air. Although the angle of repose is generally low, steep angles are apparent at the rear of the sample holder.

Figure V-2 shows the remarkable difference in the behavior of basalt powder sifted at a pressure ranging from 4.8-to-9 x 10^{-10} mm of mercury. Powder deposited on the edges of the aluminum boat and on the rim of the circular sample holder has a 90-degree angle of repose, and powder clinging to the underside of the wires of the thermal conductivity experiment can no longer be considered to have an angle of repose. The geometry of these powder deposits clearly demonstrates high-vacuum adhesion. The range in pressure during sieving was caused by a temporary pressure rise when sieving was started, indicating that the powder was not completely outgassed. The smallness of the gas load and its temporary nature, however, suggest that powder contamination was minor.

2. Gross Adhesion

An effort was made to obtain semi-quantitative information on the strengths of the adhesive bonds between grains, and between the grains and the surfaces upon which they rested. In the case of the basalt

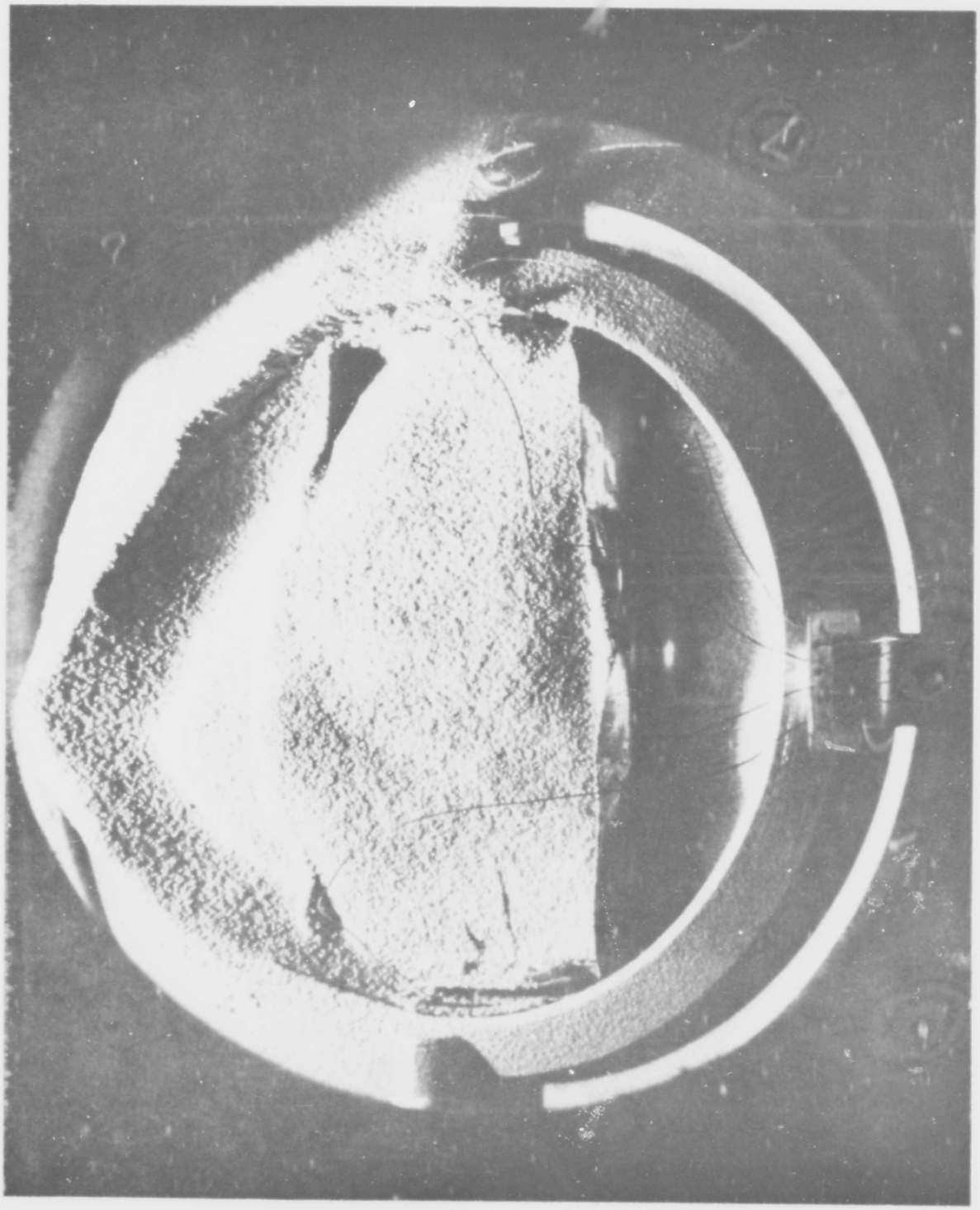

FIGURE V-1 BASALT POWDER SIEVED IN AIR

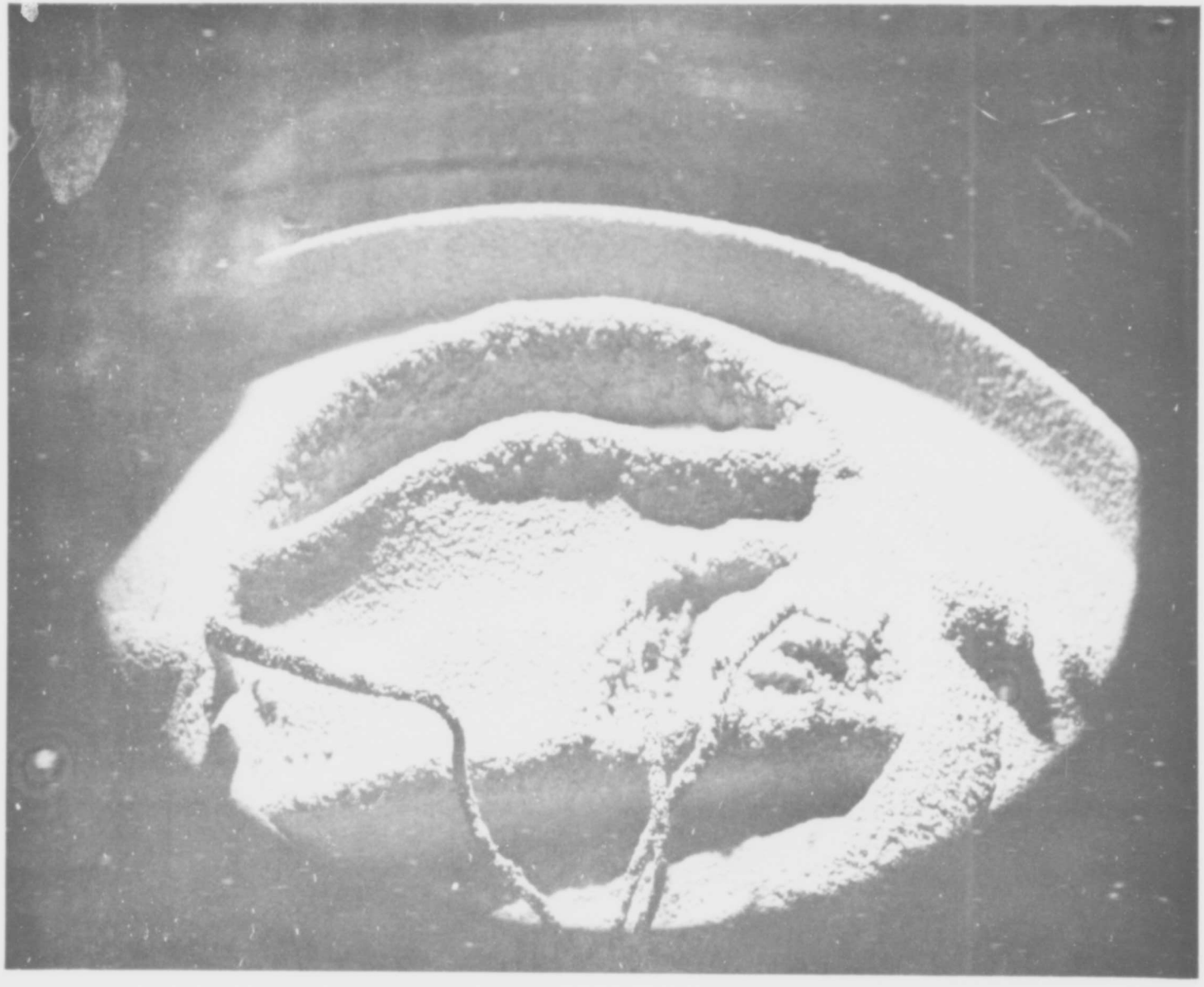

FIGURE V-2 BASALT POWDER SIEVED AT 10^{-10} MM MERCURY

powder deposit shown in Figure V-2, vibration was applied to the sample holder with results shown in Figure V-3. It is apparent that the dust behaved as a solid, breaking up into large fragments, and that the adhesion of the particles to the metal surfaces was slightly less strong than their adhesion to one another, as indicated by the manner in which fragmentation took place.

To determine the adhesive force acting under these conditions of vibration, duplicate experiments were run with an accelerometer mounted at the top of the sample holder column. Since the column is quite rigid and the vibration is applied to it externally, the impact is transmitted as a rather high-frequency wave (about 3000 cps). At the damage threshold, the peak acceleration along the axis of impact was about 100 g, and between 50 and 75 g along other axes. The force (shear) transmitted between a substrate excited to 100 g peak acceleration and particles sitting on the substrate is readily calculated. If we assume the average mass of a particle to be 1.4×10^{-9} g, $F = ma = (1.4 \times 10^{-9})(100)(980) = 1.4 \times 10^{-4}$ dynes.

It is, unfortunately, much more difficult to compute the stresses acting, since the interparticle or particle-substrate contact area is unknown and extremely difficult to estimate with any certainty; but we can at least discuss the limits. If we assume that the bonding is atomic, contact is required to produce adhesion. To estimate this case, we may assume the only situation which can readily be calculated, that is, that the particles are 10μ spheres under elastic stress. The solution to this problem has long been available and is tedious, although not difficult. Assuming, as before, a particle mass of 1.4×10^{-9} g and diameter of 10μ,

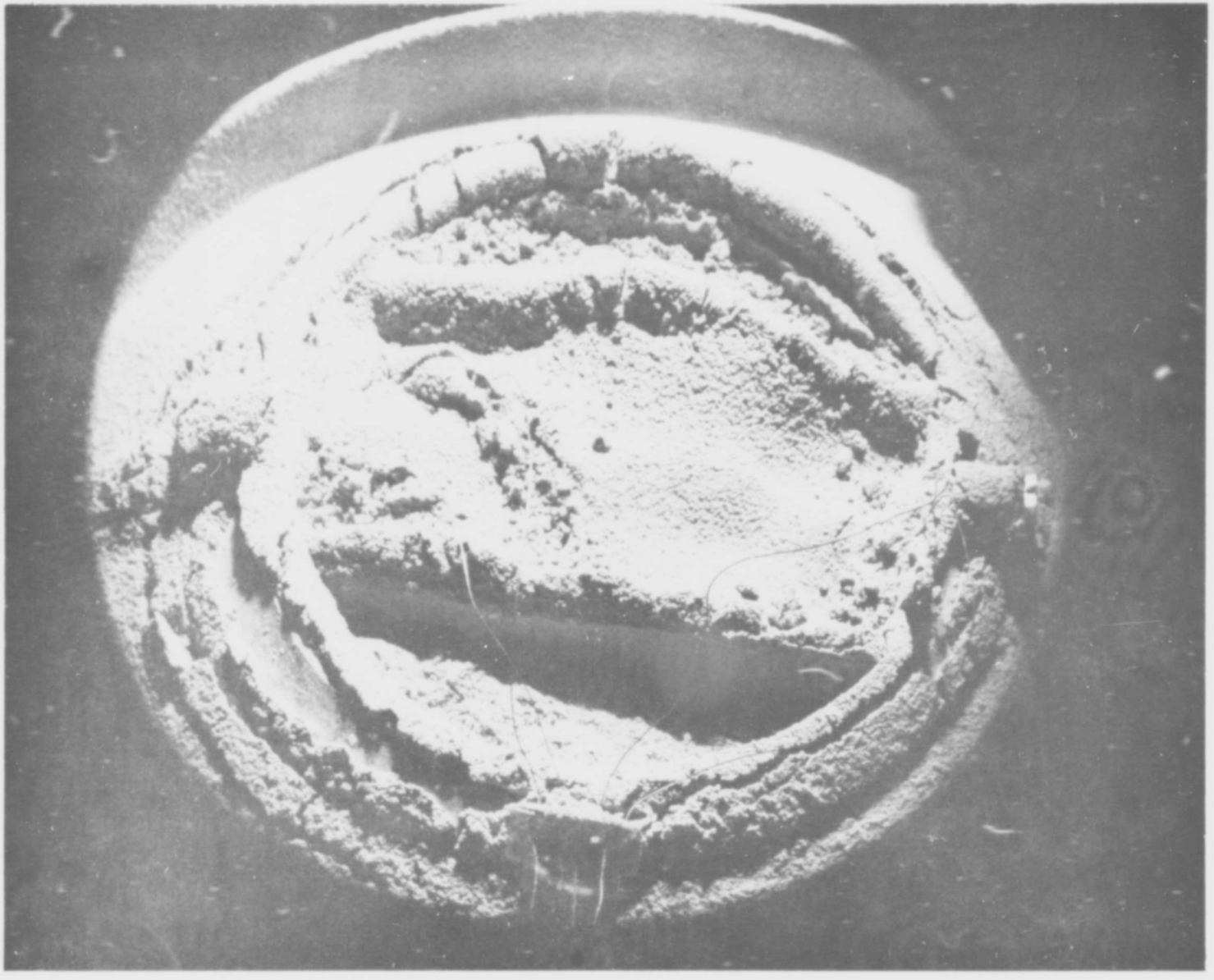

FIGURE V-3 BASALT POWDER SIEVED IN VACUUM AFTER DISRUPTION BY VIBRATION

and a typical substrate, the calculated contact area is approximately 3×10^{-14} cm^2. The calculated area is proportional to the 2/3 power of the normal load, so if we assume a surface loading of 1 mm of powder (100 particles), the area will become about 6.5×10^{-13} cm^2. The calculated shear stress is then

$$\frac{(1.4 \times 10^{-9})\ (100)\ (980)}{6.5 \times 10^{-13}} = 2 \times 10^{8} \text{ dynes/cm}^2 \qquad (1)$$

or 3000 psi. This is of the order of the shear yield stress for homogeneous bulk material. However, the nature of the calculation and assumptions is such as to maximize the results; non-spherical particles, such as normally exist, will have a larger contact area.

If, on the other hand, we assume that the bonding in question is electrostatic, direct contact is not required to produce adhesion, and the majority of particles will behave, with respect to the substrate, very nearly as if they were in contact over the entire interface. If we assume that particles act independently under these circumstances, and if we have a mass of 1.4×10^{-9} g (and a radius of .005 mm) acting on an effective area of (let us say) 50% of the projected cross section, the shear stress would be

$$\frac{(1.4 \times 10^{-9})\ (100)\ (980)}{(.5)\ (5 \times 10^{-4})^2\ (\pi)} = 350 \text{ dynes/cm}^2 \qquad (2)$$

or less than 10^{-4} psi. It may be that, from an engineering viewpoint, only this effective stress is important. As we shall see in Section VI, the long range van der Waals forces can also account for the observed adhesion. Since an interacting volume rather than a contact area is involved, however, a meaningful stress cannot be calculated.

The strength of adhesive bonds was also studies by trying to determine how deep a layer of powder would cling to a metal or glass slide, or to a solid piece of similar rock, when the slide or rock was turned upside down. Powder layers up to 2 mm in depth proved firmly enough bonded to be repeatedly inverted and could be left inverted indefinitely in air outside the chamber.

As above, the force, F, is readily computed. For a 2-mm layer (200 particles), $F = (200)\ (1.4 \times 10^{-9})\ (980) = 3 \times 10^{-4}$ dynes. If we assume electrostatic forces and an effective area of 1/2 the projected area, the stress (normal) between the particles and the substrate equals

$$\frac{3 \times 10^{-4}}{(.5)\ (10^{-6})\ (\pi/4)} = 750 \text{ dynes/cm}^2 \qquad (3)$$

If, as before, we assume contact forces only and elastic loading, the stress equals

$$\frac{3 \times 10^{-4}}{10^{-12}} = 3 \times 10^{8} \text{ dynes/cm}^2 \qquad (4)$$

or 4000 psi. These stresses are of the same magnitude as those computed earlier for the vibration experiments. Although a stress cannot be calculated, the observed force is entirely consistent with the effect of van der Waals attraction.

Because the true density of the powder sifted onto the substrate was not known, it was not possible to obtain an accurate figure for the force and adhesion existing between the powder column and the substrate. The subsequent experiments were designed to provide more accurate data for this situation.

C. SUBSEQUENT EXPERIMENTS

The vacuum chamber used in this work has been described in Section IV. In these experiments powders between 100 and 140 microns in diameter were prepared in the manner described in Section III. The larger particles were used so that the behavior of individual particles could be more easily observed.

1. Description of Experimental Apparatus

The techniques used to measure adhesion involved an impacting cantilever beam calibrated in terms of acceleration. A schematic drawing of the impact experiment is shown in Figure V-4. The steel beam is a built-up box (for rigidity) and is approximately six inches long. It carries on its upper surface the rock substrate, which is 1/4 inch thick, 4-1/2 inches long, and 1-1/2 inches wide. The beam, in turn, is held down by a steel collar screwed onto its upper surface. A thermocouple, which passes through holes in the upper and lower surfaces of the beam, is used to monitor the temperature of the base of the rock during surface bake-out with a heat lamp. When the end of the beam is driven against the impact stop, the stop delivers the actual impact to the specimen to dislodge powder particles lying on the rock substrate.

A photograph of the apparatus is shown in Figure V-5. The long column simply serves to elevate the apparatus to a point in the vacuum chamber near the upper dome and its sapphire windows, so that adequate observations can be made during a test. The bellows fastening the yoke drive rod to the flange is used not only to seal the vacuum chamber, but also to provide the driving spring for the yoke, and through it, for the beam. With this particular bellows, a maximum velocity at the

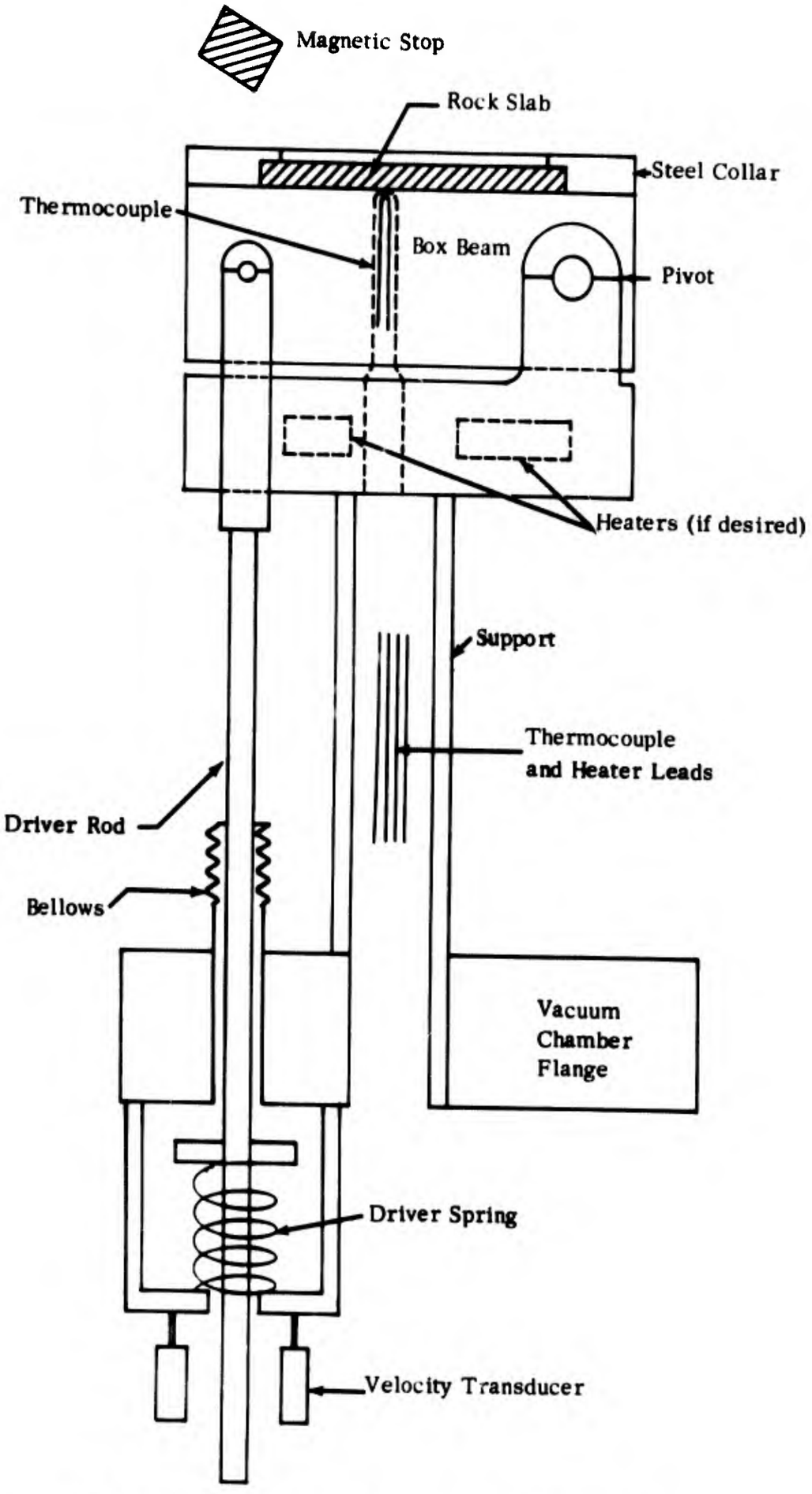

FIGURE V-4 IMPACT APPARATUS - SCHEMATIC DIAGRAM

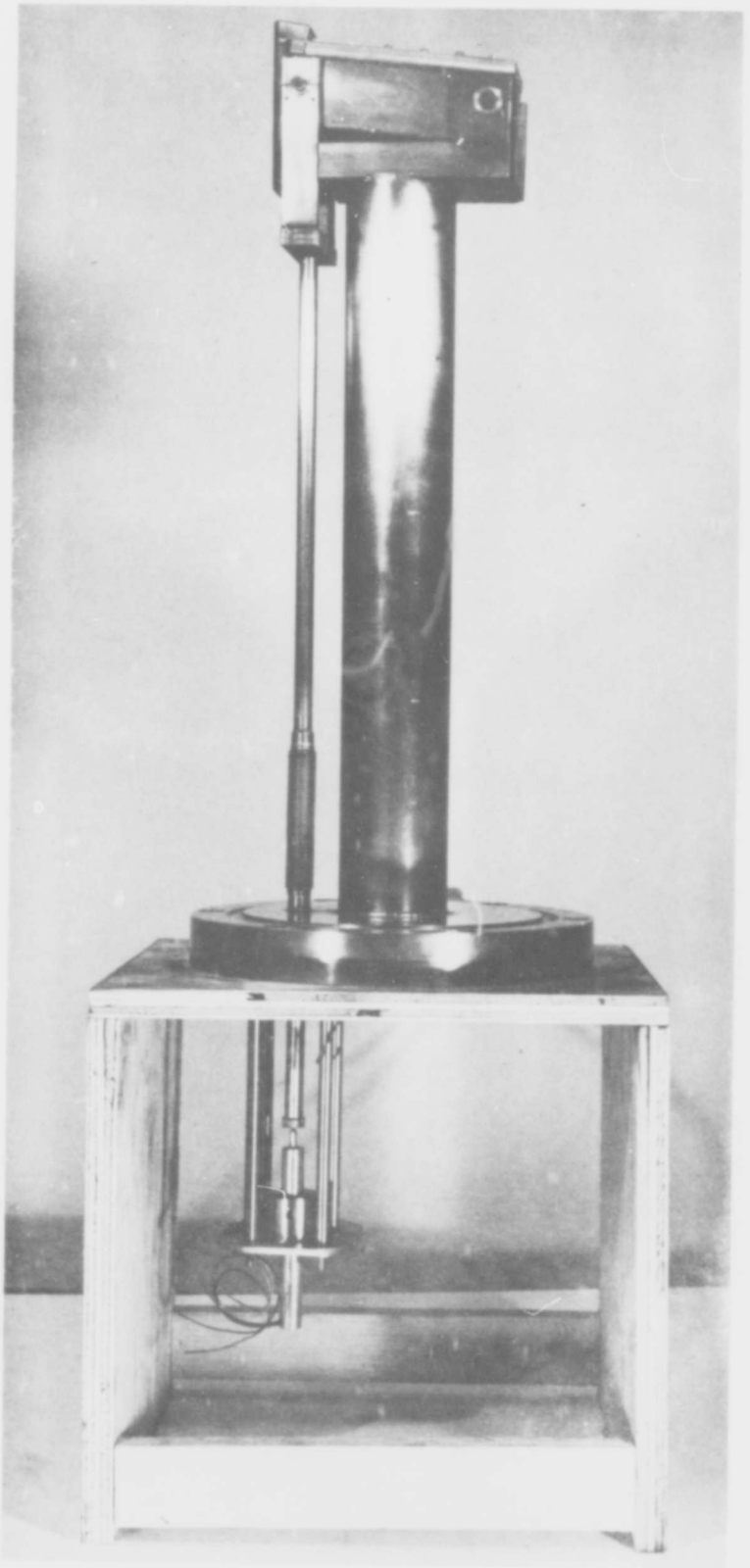

FIGURE V-5 IMPACT APPARATUS

impacted end of approximately 1 ft/sec was achieved. Stiffer springs can be arranged externally if more force is desired. The device shown under the flange is a velocity transducer used to measure the impact velocity of the beam. A typical trace from this transducer is shown in Figure V-6, at an impact velocity of 2 in/sec. The output of this transducer is of the order of 600 millivolts for a velocity of 1 in/sec, so that reliable measurements can be made even in the low-velocity range.

2. Operation of Experimental Apparatus

The impact beam device was positioned in the vacuum chamber and the upper dome was removed. The rock substrate, approximately prepared, was then fastened to the beam with the steel shoulder. (All substrates used were ground and honed but not polished.) Following this, powder of the same material, prepared as described previously, was sifted onto the substrate through a mask to provide an arrangement of parallel lines. Reasonable precautions were taken to minimize powder pile-ups and to assure a wide distribution of individual particles on the substrate. Following this procedure, the upper dome was replaced and the chamber evacuated. An infrared heat lamp was then positioned over one of the sapphire windows to heat the surface of the substrate and the attached powder particles. The thermocouple was used to monitor the temperature of the base of the rock.

When the desired pressure level was reached and the substrate surface heating was accomplished, the drive rod was pulled down to the desired position (calibrated in advance) and released. The velocity of the impact beam was measured with an oscilloscope, and the presence or absence of motion of the powder was determined visually.

FIGURE V-6 TRACE FROM VELOCITY TRANSDUCER

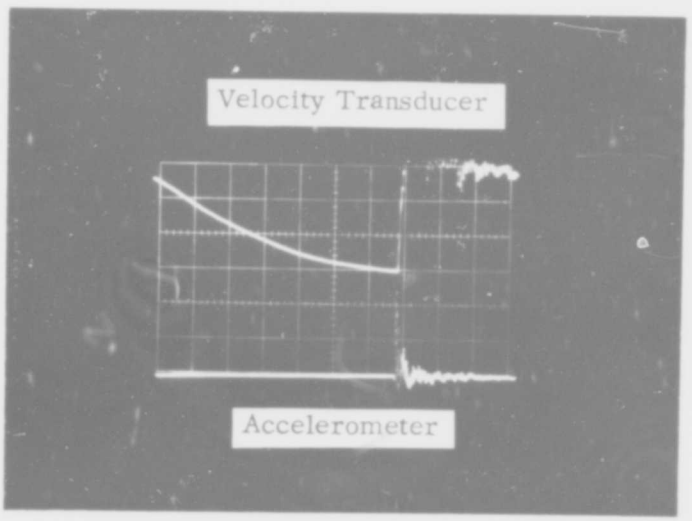

FIGURE V-7 ACCELEROMETER VELOCITY TRANSDUCER TRACES

Experiments to data indicate that it is quite easy to observe changes in the position of the powder, since in the impact position the beam is slightly tilted from the normal, and the particles, once freed from the substrate, tend to roll toward the pivot point. The impact velocity can be increased by small increments until all of the powder particles have come loose from the substrate. Adhesion forces can then be determined by referring to the calibration data to obtain the critical acceleration and then calculating the forces using Newton's law.

3. Calibration of Experimental Apparatus

To calibrate the acceleration forces at various points along the upper surface of the impact beam, the rock substrate was replaced by a hardened and ground aluminum plate of the same dimensions. Aluminum was chosen because its elastic modulus is approximately that of olivine and obsidian. Five holes, spaced along the length, were drilled and tapped into the surface of this plate so that it could accept a piezoelectric accelerometer unit (manufactured by the Bruel and Kjaer Company, Denmark), consisting of an accelerometer, an internal calibration standard, and an amplifier. The accelerometer unit was mounted in each of the five holes, in turn, and a sequence of impacts were generated to calibrate the impact acceleration of the beam at each such point.

The output from the accelerometer was displayed on one trace of a dual-trace oscilloscope, while the output of the velocity transducer was displayed on the other. A typical photograph from such a trace is shown in Figure V-7. The calibration curves are shown in Figure V-8 as a function of the accelerometer position along the beam. The acceleration is shown to be substantially constant for about 80% of the length

of the beam, changing significantly only near the pivot end. Although these calibration figures are not exact, they are sufficiently accurate for the purpose of the present apparatus. In particular, a linear relationship between acceleration and velocity of impact at a given point along the beam is quite adequate. Deviations from this linearity are not more than $\pm$ 1/2 g.

D. EXPERIMENTAL DATA

Four experiments were performed--three on olivine and one on obsidian--at pressures ranging from 6.1×10^{-10} to 1.3×10^{-9} mm of mercury. Evidence for motion or lack of motion of the particles were strictly visual. In all of these experiments, a heat lamp was used to heat the surface material for at least 24 hours. The thermocouple at the base ordinarily reached a steady-state temperature of about $100^{\circ}C$.

Table V-1 includes all of the data from these experiments; note that the evidence of motion is presented as a function of position. Successive impacts at the same velocity frequently caused motion at points increasingly near the pivot point, although in principle there should have been no difference in the acceleration for each of these tests. It is possible to rationalize this effect because of the difficulty of observing small motions of these particles. Thus, if the initial impact barely loosened a particle at a given point, a second impact at the same level would probably cause it to move a sufficient distance for visual observation. Although complete accuracy is not claimed for this procedure, reasonable values were obtained with reasonable consistency. The approximate calibrations corresponding to particular impacts are also listed in Table V-1 as taken from the calibration curves of Figure V-8.

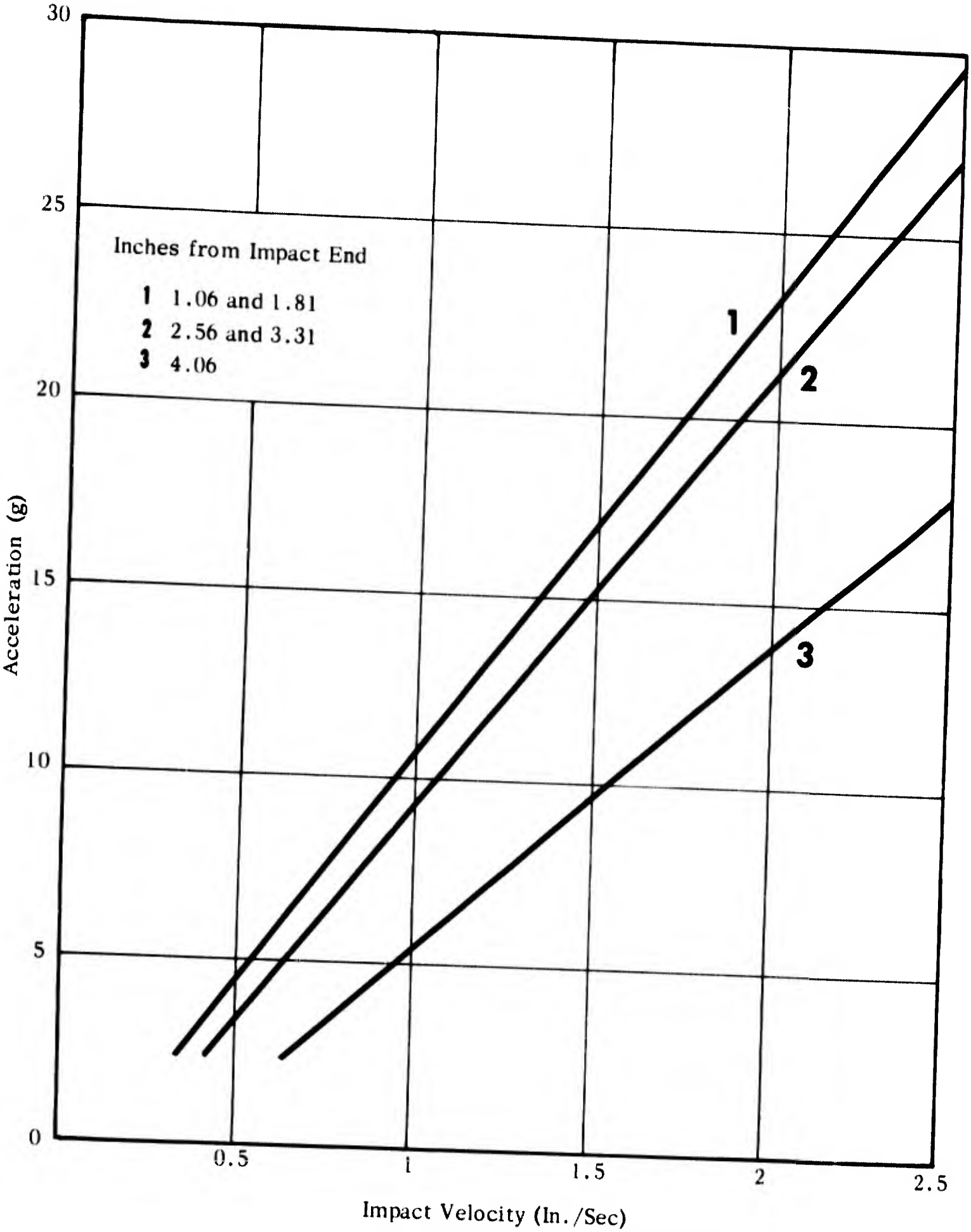

FIGURE V-8 ACCELERATION CALIBRATION AT FIVE POSITIONS ALONG BEAM

TABLE V-1

EXPERIMENTAL RESULTS

Material and Pressure	Transducer Voltage	Impact Velocity (in./sec.)	Farthest Position of Powder Motion (in. from impact end)	Acceleration (g)
OLIVINE	0.7	1.2	1.31	13
1.8×10^{-9} mm Hg	0.7	1.2	1.56	13
	0.7	1.2	2.06	13
	0.6	1.0	none	> 11
	0.7	1.2	2.31	12
	0.8 - 0.9	1.4 - 1.5	> 4.06	< 10
OLIVINE				
8.2×10^{-10} mm Hg	0.2	0.3	none	-
	0.4	0.7	1.81	7
	0.4	0.7	1.81	7
	0.4	0.7	1.81	7
	0.4	0.7	1.81	7
	0.4	0.7	2.06	6
	1.0	1.7	> 4.06	< 11
	1.2	2.1	> 4.06	< 15
OLIVINE				
1.3×10^{-9} mm Hg	1.0	1.7	1.31	19
	1.0	1.7	1.56	19
	0.6	1.0	3.56	6-9
	0.6	1.0	none	> 11
	1.6	2.7	3.56	20 - 28
	1.6	2.7	> 4.06	< 20
	1.6	2.7	> 4.06	< 20
	1.0	1.7	> 4.06	< 12

TABLE V-1 (Continued)

EXPERIMENTAL RESULTS

Material and Pressure	Transducer Voltage	Impact Velocity (in./sec.)	Farthest Position of Powder Motion (in. from impact end)	Acceleration (g)
OBSIDIAN				
6.1×10^{-10}	0.8	1.4	none	>16
mm Hg	0.8	1.4	1.06	16
	0.8	1.4	1.06	16
	0.8	1.4	1.81	16
	1.8	3.1	3.56	24 - 34

It is evident that the one run on obsidian does not differ enough from the three runs on olivine to justify separate statements or calculations. The average of all data points is approximately 12 g. That is, particles between 100 and 140 microns in diameter, loaded only by their weight on a substrate of identical material, require a force of 12 times their weight to separate them from the substrate under the conditions of these tests. This can readily be put in terms of force, but is somewhat more difficult to interpret in terms of stress unless some assumptions are made regarding contact area.

The most straightforward technique assumes that the particles can be represented as spheres and that the Hertzian analysis for the elastic deflection of spheres on surfaces can be applied to calculate the contact area. For an assumed average particle diameter of 125 microns, a contact area of approximately 3.5×10^{-11} cm^2 was calculated. Since, as noted above, the force to separate these particles from the substrate is 12 times their weight or 3.2×10^{-2} dynes, the calculated stress in this case is 9.1×10^{8} dynes/cm^2 or 13,000 psi. This is of the order of the bulk strength of the material.

If the above assumptions are sufficiently valid to justify these calculations, then it appears that contact stresses are very large and that adhesion occurs where these surfaces are in contact. Since the actual contact area is a very small fraction of the apparent cross sectional area, it is necessary to separate the actual contact stress

from the apparent stress, which would be measured on the total cross section. In this case, using the same force value but the total cross sectional area of a 125-micron particle, the apparent stress would be on the order of 10^{-3} psi.

E. DISCUSSION

It is instructive to compare these results with those derived in the preliminary experiments for powders clinging to a slide. These particles (99% of which were smaller than 70 microns; 90%, smaller than 17 microns; and 80%, smaller than 3 microns) were sifted in a vacuum onto a substrate to a depth of up to 2 millimeters. We have assumed in the calculations that the particles averaged 10 microns in diameter.

The Hertzian model for elastic loading of spherical particles was used to calculate a contact area of $A = 1.0 \times 10^{-12}$ cm^2 from the expression $A = 2.4 \times 10^{-8} (f \cdot d)^{2/3}$, where f is the normal force in dynes and d is the diameter in centimeters. The force that the lowest contact surface supports is equivalent to the weight of 200 particles or 2.8×10^{-4} dynes and we therefore were able to say that the stress equalled 2.8×10^{8} dynes or 4000 psi.

Considering the extremely rough nature of the calculations, it is surprising that agreement with the impact experiments is within an order of magnitude. However, since this agreement depends significantly on the diameter chosen for the particles as well as on the density of material loading the particles in the sifting experiments, we cannot really conclude that the results are equivalent. We can merely state that, at least by this model, they are consistent.

If, on the other hand, we apply the more usual multiple-asperity model used to explain observed behavior in general friction, wear and adhesion experiments, the contact area becomes a direct function of the load; this model assumes that contact is made at a large number of small points (asperities) which deform under load until their aggregate areas can support the applied load. Applying this kind of proportionality, we now conclude that the stress would be about 1100 psi. This differs by a factor of 2 from the previous calculation, and we cannot be certain that this model is less applicable than the previous one.

Although the multiple-asperity model is reasonably accurate for experiments involving relatively large particles, there are good reasons for assuming that it might not apply in the present case. If, for example, we consider the actual contact area calculated for the 5-micron sphere, that is 2.3×10^{-13} cm^2, this area is equivalent to about 50 atoms. In other words, the area involved is so small that one would predict very few contact points. The situation is not quite so clear for the 125-micron particles, although the consistent results obtained above for the Hertzian loading assumptions may indicate that we are still dealing only with the single-asperity model.

To resolve this question and to obtain better information about the actual contact stress, additional experiments are required. In particular, one should measure, with somewhat greater precision, the force of adhesion between particles of various sizes ranging from submicron to perhaps 500 microns. It is expected that over this range the variation of adhesion force with particle diameter would show a break, corresponding to the

point at which the multiple-asperity model breaks down and begins to be replaced by the Hertzian model. This information would also provide justification for applying one model or the other and give a physical insight into the nature of the contact surfaces.

The method by which particles are placed onto the substrate is another factor that has an important influence on the experimental results. All of the analyses discussed previously are based on the assumption that particles are placed one on top of the other. However, if they are actually sifted (i.e., dropped), as is the case in both experiments, the actual surface of contact initially generated would be somewhat larger than that calculated for the static condition, due to the momentum carried by the particles as they impact the plate. In fact, if these particles were dropped from a sufficient height relative to their size and in high vacuum where no limiting velocity would be reached, the increase in contact area due to the impact effect might be quite pronounced. Experiments along these lines could be done to demonstrate whether or not this occurs. These would also provide information on the nature of the contacting surfaces and the types of interactions which would be developed by a sequence of such layers falling one on top of the other in the lunar environment.

Particles of silicate materials in a high-vacuum environment do exhibit adhesion. In the present experiments, 125-micron particles require an average acceleration of 12 g's to remove them from the substrate. The stress corresponding to this force can only be calculated if a model for contact area is assumed, but it is apparently of the order of the bulk strength of the materials involved.

The contact stresses estimated from the preliminary observations of vibrational detachment and static loading are in substantial agreement with the present results. The measured adhesion is expected to be a function of particle size but there are not sufficient data to decide upon a model. The estimated stress values are large enough to suggest that primary bonds across the contact interface may be involved. On the other hand, the observed adhesion is entirely consistent with the effect of van der Waals forces as discussed in the following section.

BLANK PAGE

SECTION VI

THEORY OF PARTICLE ADHESION

The forces of attraction between particles--if electrostatic effects are neglected--must be accounted for either in terms of the relatively long-range London-van der Waals forces of attraction (the so-called molecular dispersion forces) or in terms of relatively short-range chemical bonding at a contact interface. The van der Waals forces between macroscopic bodies have, in general, been ignored by the scientific community; the adhesion of solids has been considered principally in terms of the real area of contact between solid surfaces (the asperities) and the detailed nature of the surfaces in this region. London-van der Waals attraction between macroscopic bodies has recently received considerable attention, however, particularly with respect to the stability of colloids. This work suggest that the long-range body forces of attraction can, under certain conditions, make significant contributions to the adhesion between solid particles.

A. THE CONTRIBUTION OF CHEMICAL BONDING TO ADHESION

Chemical bonding is significant only at distances of the order of atomic or molecular dimensions and practically disappears at distances of only a few angstroms. Most technically flat solids possess surface irregularities, so that if two such surfaces are pressed together statically at moderate loads they come into contact only over a very small fraction of their apparent area.

The adhesion theory of friction (Bowden and Tabor, 1950) requires that these regions of intimate contact represent junctions that have strengths of the same order of magnitude as those of the solids.

According to this theory, these junctions at the real contact areas (the asperities) are responsible for resistance to sliding, and the frictional force is equal to the force required to shear the junctions. Adhesion is generally not observed between surfaces that have simply been pressed together. This is explained as due to the release of elastic stresses which fracture the junctions as the load is being removed. In short, it is postulated that if one neglects very soft metals, sliding, and lubricating films, the area of contact--and, therefore, the junction area--is, to a first approximation, a function of the load. Consequently, under zero or tensile loads, both the area of real contact and the adhesion due to short-range chemical forces will be negligible.

Although the Bowden and Tabor theory has been successful in explaining the observations of friction, it has little to say about the nature of the chemical bond that is assumed to form under load. The model is most often applied to the friction forces between metal surfaces covered with an oxide skin and generally contaminated with a lubricant or, at least, absorbed gases. Any chemical bond that forms under these conditions must be due to the generation of new metal-to-metal contact.

The type of materials, whether they are metals or insulators, and the atomic nature of their surfaces will influence the amount of chemical bonding that can occur over the real area of contact. With clean metal surfaces, a chemical bond will readily form as soon as atomic separations are reduced to about one angstrom. This is due to the fact that valence forces are not saturated and that only minor rearrangement of surface

atoms is required for the formation of the metallic bond. Plastic deformation of metallic asperities may also occur with relative ease and increase the real area of contact. Chemisorption of active gases will also occur most readily on metal surfaces. The chemisorbed layer can act as an effective barrier against bond formation by shielding the unsaturated valence orbitals.

The possible contribution of chemical bonding to the adhesion between dielectric particles is not readily apparent. Ionic materials, like the alkali halides and oxides such as MgO, are believed to have only slight changes in atomic separation in the surface layer. On the other hand, Lander, et al. (1963) have shown that extensive atom rearrangements take place on freshly cleaved semiconductor surfaces of silicon, even at room temperature. Further rearrangements occur as the temperature is increased. These surface changes proceed in the direction of greater stability and tend to consume the bonding orbitals made available by the cleavage. At least part of the rearrangement is thermally activated. Two such surfaces, when brought together, could conceivably require thermal energy for full development of the bond.

The often quoted example that illustrates the chemical bonding possible between silicate surfaces is that of mica. Recent measurements by Bryant (1962) show a recovery of 87% of the original cohesive strength of mica (10,250 ergs/cm^2) after it is separated and rehealed in a vacuum of 10^{-13} torr. The same value was obtained for separation in an atmosphere of dry helium, argon, or nitrogen. Contamination of the surface by water vapor reduced the work of separation to 300 ergs/cm^2 or less.

Mica is unique, however, in that the silicate layers are bonded ionically with a plane of potassium and it is, therefore, possible to obtain perfect cleavage. Most silicate surfaces consist of numerous atomic steps and ledges. Silicates are also brittle materials. However, plastic deformation of asperities on the microscopic scale of importance for the adhesion between fine silicate particles cannot be ruled out.

B. THE CONTRIBUTION OF LONDON - VAN DER WAALS ATTRACTION TO ADHESION

In contrast to chemical bonding, which decreases exponentially and has a negligible effect beyond several atomic radii, the van der Waals forces between neutral species decrease according to a power law and may be significant at distances approaching a micron. The basic van der Waals attraction between molecules is due to the pair-wise interaction of dipole moments and to the polarizing action of a dipole in one molecule on another molecule. In addition, London (1930 - 1942) has shown that a quantum mechanical attraction--known as dispersion forces--exists, even for nonpolar atoms or molecules, due to the presence of rapidly fluctuating dipoles (10^{15} - 10^{16} cycles sec^{-1}) at the zero-point energy of the electron clouds. The interaction energy between individual atoms was shown to vary as $1/r^6$. Casimir and Polder (1948) have applied a retardation correction to the London - van der Waals effect for distances larger than a characteristic wavelength, λ_o, which derives from the fact that it takes a finite time for the electromagnetic radiation to traverse the distance between atoms.

1. Theoretical Background

Since the force is given by $F = - dU/dr$, where U is the potential energy of interaction, the force will decrease as $1/r^7$ between atoms

($1/r^8$ if retardation effects are accounted for). Reviews on molecular attraction were given by London(1937) and by Margenau (1939).

If the attractive force between macroscopic bodies decreased so rapidly, the van der Waals force would have a minor effect on the cohesion of solid particles. By assuming the additivity of dispersion forces, however, de Boer (1936) and Hamaker (1937) derived the following equations for the potential energy and attractive force between two spheres of radius ρ at a minimum distance, h, apart for $h \ll \rho$:

$$U = -A\rho/12h \qquad F = A\rho/12h^2 \qquad (1)$$

where A was given by the theory as $\pi^2 q^2 C$ with $C = 3/4\ E\ \alpha^2$; q is the number of atoms/cm^3 with polarizability α, and E is a characteristic energy (Margenau, 1939; and Overbeek and Sparnaay, 1954). The same quantities would be twice as large for the interaction between a sphere and a flat plate. For two parallel flat plates the interaction <u>per unit area</u> was considered to be

$$u = -A/12\pi h^2 \qquad f = A/6\pi h^3 \qquad (2)$$

At distances between flat plates ($h \gg \lambda_0$), the retardation correction (Derjaguin, et al, 1956) yields

$$u = A'/30\pi h^3 \qquad f = A'/10\pi h^4 \qquad (3)$$

where $A' = 251(\pi q\ e\ \alpha)^2$ and e is the electronic charge. Equation 3 has been found to give reasonable agreement with experiment (Derjaguin, 1958;

and Kitchener and Prosser, 1957). Doubts have been expressed by the Russian workers (Dzyaloshinskii, et al, 1961), however, on the suitability of summing dispersion forces based on individual atomic properties and the effect that close packing of atoms in the solid must have on the electronic envelope.

Lifshitz (1955), starting with the macroscopic viewpoint that the interaction between continuous media is due to the same fluctuating electromagnetic fields that give rise to thermal radiation, derives a general formula for the force of attraction per cm^2 between flat plates as a function of their separation, which depends only on the dielectric permeability of the material. For small separations ($h < \sim 300$ Å for quartz) the theory predicts that f is proportional to $1/h^3$, while for larger separations the dependence is $1/h^4$. This dependence is the same as given in Equations 2 and 3, although the proportionality constants differ slightly. In the Lifshitz theory (1955) for distances greater than the characteristic wavelength, the force of attraction per unit area is given by

$$f = \frac{\hbar c \pi^2}{240 h^4} \left(\frac{n^2 - 1}{n^2 + 1}\right)^2 \Psi(n) \qquad (4)$$

where the square of the optical index of refraction, n, is substituted for the dielectric permeability, $\hbar$ is Plank's constant divided by 2π, c is the velocity of light, and $\Psi(n)$ is a tabulated function that has the value 0.35 for $n \leq 2$.

The experimental verification of the Lifshitz theory was extremely difficult, due to the small but rapidly varying force that had to be measured (10^{-4} to 20 dynes), the small distances of separation (10^{-5} to 10^{-3} cm), the need for complete freedom from dust, and the difficulty of removing static charge from the surfaces. Using quartz, thallium halide, and chromium, Derjaguin, et al (1956, 1958) were apparently successful in overcoming these difficulties. They measured the force as a function of distance between a flat plate and a spherical surface. The radius of curvature was varied from 5 cm to 25 cm, and the equivalent energy and force per unit area for parallel plates could be calculated. For example, the measured force between a quartz plate and spherical surface with ρ = 11.1 cm fit the equation $F = 2 \times 10^{-18}/h^3$ dynes. The equivalent energy, including results with a 25-cm curvature lens, was given by $u(h) = F/2\pi\rho = 3 \times 10^{-20}/h^3$ ergs/cm^2. The equivalent parallel plate force was $f(h) = 9 \times 10^{-20}/h^4$ dynes/cm^2, compared with the theoretical value $f(h) = 7.5 \times 10^{-20}/h^4$ dynes/cm^2 calculated with 1.544 for the refractive index of quartz.*

Overbeek and Sparnaay (1954), on the other hand, measured the force per unit area between flat plates directly and obtained a value that was not only several thousand times greater than the expected value but varied only by $1/h^3$. In spite of the care which they took to eliminate static charge, they apparently did not succeed. The conflict was resolved when Kitchener and Prosser (1957) repeated the flat plate

---

*For purpose of comparison, the theoretical value for olivine with a refractive index of 1.67 is $f = 10.0 \times 10^{-20}/h^4$.

experiments using borosilicate glass and fitted the $1/h^4$ law with a coefficient of 11 x 10^{-20} erg cm, in good agreement with the theoretical Lifshitz value of 6.7 x 10^{-20} erg cm for a refractive index of 1.5. The Casimir and Polder theory (1948) appears to yield an even closer value of 9 x 10^{-20} erg cm, but this may be somewhat fortuitous since measured values are likely to be on the high side. Sparnaay (1957), in more recent work, has also been able to fit the $1/h^4$ law.

Figure VI-1 has been drawn with a coefficient of 10^{-19} erg cm for distances greater than 300 Å and with a $1/h^3$ section joined for shorter distances, as required by theory (unretarded attraction). This section, as drawn, has the form $f(h) = 3.16 \times 10^{-14}/h^3$ dynes/cm^2 and gives forces only 40% lower than those estimated with Equation 2 (see for example, Overbeek and Sparnaay (1954). The dotted portion of the curve reflects the steep drop in attraction due to the repulsive action of overlapping electron clouds in the absence of chemical bonding.

In the use of Figure VI-1 it should be kept in mind that the plates must be smooth and parallel, have dimensions that are large compared with the separation, h, and be thick enough for the entire force to be developed. Because of the strong dependence on separation, however, the last factor is not very critical. To treat real surfaces, a hypothetical plane surface can be defined and located which would be acted upon with the same force per unit area. Finally, the attractive force in dynes between two spheres with radius ρ or between a sphere and a plate can be obtained from Figure VI-1 and the relation

$$F = k \pi \rho h f(h) \qquad (5)$$

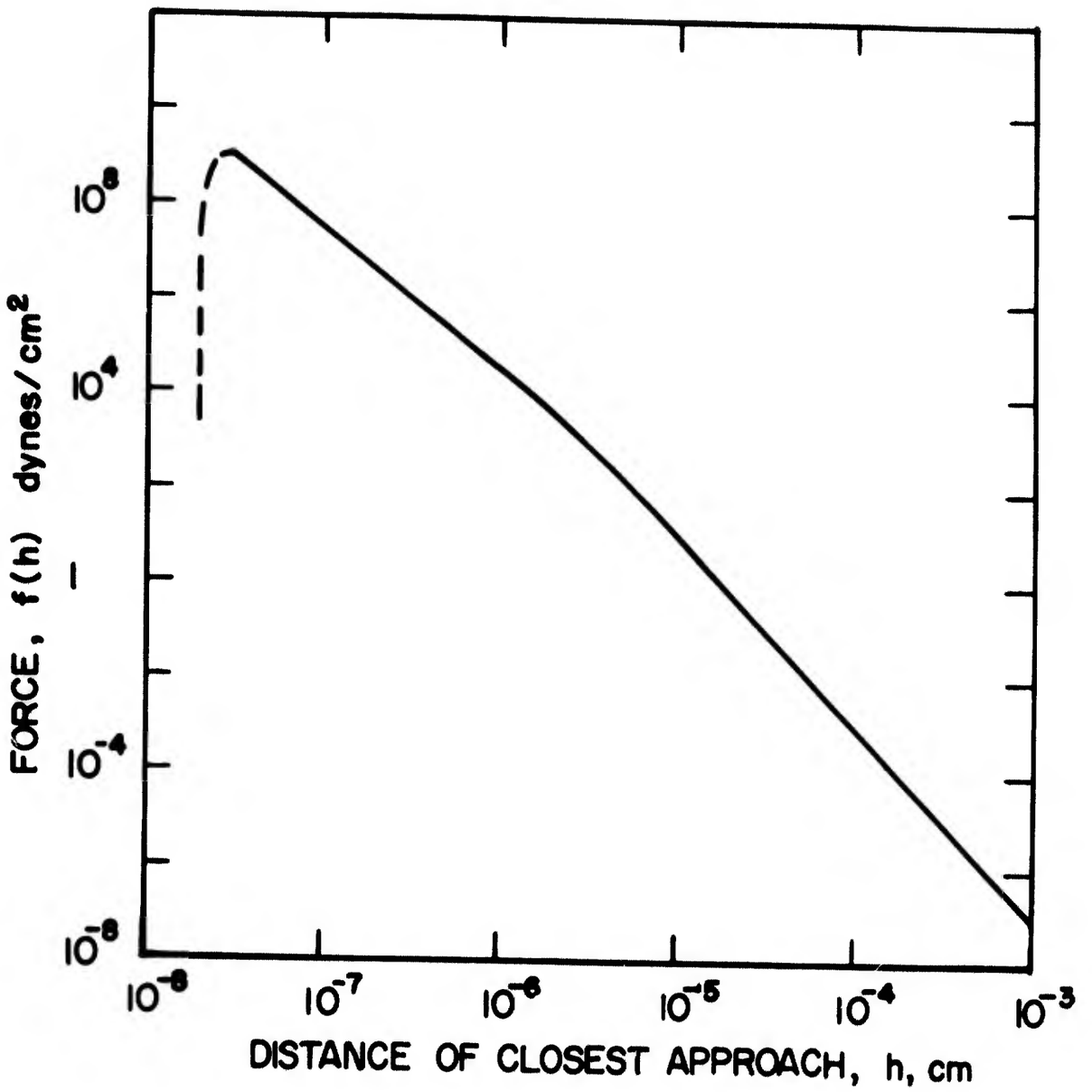

FIGURE VI-1 VAN DER WAALS ATTRACTIVE FORCE BETWEEN FLAT QUARTZ PLATES

where k has the value 1/3 or 1/2 for the two-sphere case, depending on whether or not the force is retarded ($1/h^4$ or $1/h^3$) and similarly has the value 2/3 or 1 for the sphere-and-plate case.

2. Discussion of Observations

The results so far developed can be used to explain many of the observations of cohesion. Some time ago, Bradley (1932) measured the cohesion between quartz spheres (~ 0.02 to 0.1 cm radii of curvature) that had been heated to incandescence, cooled, and then brought into contact, either in air or in a moderate vacuum. The results were the same and closely fit the equation, $F = 212\ \rho$ dynes. If we assume that h is the distance between the spheres just before the applied load pulls them apart, and calculate the equivalent potential energy for flat plates at that separation, we obtain $u(h) = F/\pi\ \rho = 67$ ergs/cm^2 or about 1 kcal/mole, assuming a surface concentration of 10^{15} atoms/cm^2. This is precisely the magnitude of the energy expected from a van der Waals interaction.

We may also estimate from Equation 5 and Figure VI-1 (or the equivalent analytic expression) that the distance between spheres at the point of separation corresponded to h = 1.5 Å and the force to $f(h) = 9 \times 10^9$ dynes/cm^2 or about 130,000 psi. It is not surprising, therefore, that Bradley observed a slight flattening of the spheres at the point of contact before load was applied, since at the equilibrium separation the force would even be greater.

Benjamin and Weaver (1963) measured the shear force required to remove a number of vacuum-evaporated metal films from various alkali halides and from glass. The measured force of 3.9×10^8 dynes/cm^2 is

only a few per cent of the van der Waals attraction that would be estimated if all of the metal atoms were removed simultaneously from their equilibrium position. It does correspond, however, to the attraction that would be observed at several angstroms's separation. The fact that the measured force correlated linearly with the estimated van der Waals attraction for the various material combinations is adequate proof that van der Waals attraction rather than chemical bonding occurred, at least initially. For the alkali halides this was true even after 600 hours. However, with a metal such as aluminum on glass, the measured force increased by a factor of 30 after about one week. In terms of energy the increase was from a few kcal/mole (van der Waals) to about 100 kcal/mole (obviously chemical bonding). The fact that the higher value was not obtained immediately is evidence of a potential barrier for the rearrangement of the silicate surface. Presumably, this results from the breaking of Si-O-Si bridges or the removal of hydrogen from surface siloxyl (Si-OH) groups in order that Si-O-Al bonds can subsequently form.

The dynamical measurement of olivine and obsidian cohesion to a rock slab in the ultra-high-vacuum chamber (see Section V) can also be explained on the basis of London-van der Waals attraction. In this work an average acceleration of 12 x 980 cm/sec^2 was required to dislodge particles in the 125-micron size range. From the density and volume of a sphere with this diameter, the cohesive force per particle was estimated to be 0.03 dyne. If the cohesion relation found by Bradley for quartz spheres is assumed to apply to olivine as well, the measured force would correspond to a single plate-to-sphere contact

where the radius of curvature was 1 micron. Figure VI-1 is an excellent fit for the theoretical f(h) curve for olivine (refractive index - 1.67) and also demonstrates that Bradley's results are due to London-van der Waals attraction. It is, therefore, reasonable to assume that the same van der Waals force applied for olivine as for quartz. The measured force is then readily accounted for by the 5×10^{-12} cm^2 effective area of contact corresponding to that for a 1-micron quartz sphere at its equivalent equilibrium separation of 1.5 Å.

The cohesive force of fine powder estimated from the preliminary experiments described in Section V can also be attributed to van der Waals attraction. The estimated forces of 1.4×10^{-4} and 3×10^{-4} dynes for the vibrational detachment and static load (powder or slide) experiments are less than 0.1% of the van der Waals attraction that could be obtained between spherical 10-micron particles. The lack of uniformity and the presence of submicron particles undoubtably contribute to the low values observed. The decrease in cohesive force with decreasing particle size is further evidence that the van der Waals effect is the principal source of the observed cohesion.

SECTION VII

ELECTROSTATIC EFFECTS

A. INTRODUCTION

The possible presence of charged particles on the lunar surface is an important consideration in many phases of the lunar exploration program, since it would affect the bearing strength of the surface, dust agglomeration on men and vehicles, and communications. Before discussing the experimental results obtained in this program, we shall review the existing areas of agreement and disagreement about the electrostatic properties of the lunar surface and their influence on lunar exploration.

It is almost universally agreed that lunar dust particles will exhibit some electrostatic charge, and several mechanisms of generating this charge have been suggested. Grannis (1961), Walker (1962), and Coffman (1963) derived theoretical expressions for the random charge fluctuations to be expected as a result of local statistical variations in the flux of solar electrons and protons, and of secondary photoelectrons resulting from ultraviolet radiation. These statistical fluctuations might be expected to result in large charges on individual particles and some locally high electric fields, but the net field of all the particles together should be small and die off within a few particle radii from the surface.

A second charging mechanism which has been suggested involves the removal of electrons from silicates by solar ultraviolet radiation. Not only will this radiation raise the lunar surface potential to several tens of volts relative to the surrounding space by the escape of high energy photoelectrons, but those electrons which do not have enough

energy to escape from the neighborhood of the moon will create a region of increased electron density just above the surface (Singer and Walker, 1962a, b).

If the general qualitative nature of these charging mechanisms is accepted, the average positive potential of the moon can be estimated to be on the order of 20 - 40 volts. With this assumption, we can estimate theoretical values for the charge distribution spectrum on the dust particles, the maximum charge on individual particles, and the electron space charge distribution, all of which rely critically on (1) the flux of solar electrons, (2) the flux of the solar wind, and (3) the work function and quantum efficiency as a function of wavelength of the lunar surface materials. As none of these parameters is well-known, the values derived from them can be expected to give only an order-of-magnitude estimate.

Grannis estimates an upper limit for the charge on a 5-micron particle as 2800e, using a statistical argument which neglects the effects of already existing charge on the additional accumulation. Walker (1962) includes these effects and arrives at values an order of magnitude lower. Coffman (1963) approaches the problem of maximum charge on a grain of sand from a different point of view. He considers the total energy in a system of an uncharged sand grain and an electron considered both together and separately; then, by making the assumption that the electron affinity of SiO_2 is the same as that for an oxygen molecule, he seeks to minimize the total potential energy of the system. While he obtains 7600e for the maximum value of the charge on a 5-micron particle, his analysis applies only to the creation of negatively charged grains. In addition, this highly simplified model neglects all interactions tending to remove electrons from the particle.

In spite of the controversy centered around the absolute magnitude of the charges to be expected, all investigators believe that local fluctuations of charge concentration are to be expected and that extreme values of the charges may be of the order of 10^3e on a 5-micron particle. These charges are greater, by several orders of magnitude, than the mean value of those charges due to the photoelectric effect; however, the latter effect will predominate at a distance of a few particle radii from the surface, as it is the result of a net positive charge increase for all particles.

B. EFFECTS OF ELECTROSTATIC CHARGES

Several important effects of electrostatic charges on the behavior of lunar dust have been suggested, some of these in direct conflict with one another.

It has been suggested that the presence of electrostatic attraction between particles of opposite charge will result in increased cohesion of the dust. This, of course, would have an important influence on the bearing strength of lunar surface layers. Two aspects of electrostatic attraction must be considered: (1) the effect of charge on the initial adhesion of silicate powders, and (2) the length of time that the initial effects can be expected to persist as the charge becomes neutralized due to the finite conductivity of the surface layer caused by intergranular contact. Only the first of these effects has been investigated up to now in this program.

Levitation of surface particles caused by the counteracting forces of gravitational attraction and electrostatic repulsion has been considered as a possible transport mechanism for materials between different areas on the lunar surface. For this to happen, several conditions must

be met. First, a particle with a positive charge must be torn loose from the surface and ejected into the exosphere, either by its own repulsion from particles or through meteorite impact. If there were no space charge above the lunar surface, this particle would then either fall back or be ejected completely from the moon's gravitational field, depending on the initial kinetic energy, its mass, and the charge with which it started or which it acquired in flight. The lack of a stable equilibrium position is a direct result of the theorem that a particle finds no position of minimum energy in a region of space where its potential can be written as a solution to Laplace's equation.

If, on the other hand, there is a space charge in the region just above the surface formed by photoelectrons that are ejected with insufficient energy to escape into space, a potential minimum will exist for a particle with the proper ratio of charge to mass. Thus, the particle may remain suspended somewhere in the cloud of photoelectrons. Estimates of the height of the cloud vary between a fraction of a centimeter (Grannis, 1961) and several centimeters (Singer and Walker, 1962a) and depend critically on the exact spectrum of the solar photon flux. The latter is not well determined.

To further compound the uncertainties in the estimates of possible effects of levitation, the work function for the removal of photoelectrons from the surface of silicate powders and the quantum efficiency of the electron removal may be incorrect.

For the levitation of particles to occur, a mechanism must be available for the erosion of the particles from the surface. Gold (1962) has suggested that the initial charge on the particles may be sufficient to tear them loose and make them hop gradually downhill. Grannis (1961)

suggests that this erosion mechanism may be feasible but that the action of micrometeorite impacts may also be significant. Walker (1962) casts considerable doubt on Grannis's estimates of the magnitudes of the charges, and then Singer and Walker (1962b) show that by considering in detail the charging of particles ejected by meteor impacts this erosion mechanism is likely to be the most important. Particles so ejected would acquire their charge while in flight and then would be reflected in the region of the electron space charge.

Whatever the cause of the charging and levitation, if a cloud of such particles exists, it may be expected to collect on any grounded metallic surface, a surface which is negatively charged, or a surface on which it may become imbedded or trapped. The success of any attempts to repel it once it has agglomerated will depend on the electrical conductivity of the particles and the intergranular adhesion.

An additional effect of electrostatic charges, encountered on earth in military operations in areas of sand deserts, is that of disruption of radio communication due to static caused by the charge generated by the movement of the vehicle over the sand. This effect, unlike the levitation effects, will be important during the lunar night as well as the day.

C. EXPERIMENTAL PROCEDURES

The importance of electrostatic effects in the process of adhesion was first suggested by the results of sifting powder in the high-vacuum chamber during the thermal conductivity experiment (Salisbury, et al 1964). The deposition of powder on the underside of the thermal conductivity experiment wires suggested that electrostatic forces were active in controlling the behavior of powder particles. For this reason, the role of electrostatic forces in the adhesion process was studied by means of three experiments.

Two of these experiments are shown in Figure VII-1. The first is concerned with the square brass plate (shown covered with powder), which was insulated from the sample holder and connected to ground through an electrometer. During sifting, when the particles made frictional contact with each other and the steel sieve screen, the electrometer measured the net charge produced. In each of the obsidian and andesite powder samples tested in this way, a net negative charge was indicated. Sieving at an intermediate vacuum (10^{-5}mm) and in air produced the same kind of electrostatic charge seen at an ultra-high vacuum, but no significant adhesion took place. Although the data are subject to considerable variability because the amount of powder deposited on the plate varied from stroke to stroke of the sifter and from pressure to pressure within the chamber, a rough estimate indicates that the powder had a net charge of approximately 10^{11} electrons/gram.

The second experiment was accomplished with the three rods shown crossing the sample holder on a glass tube frame. Two of the rods were made of copper, one grounded and one insulated. The third rod was made of quartz. As illustrated in Figure VII-1, the buildup of powder on the grounded copper rod (rear of photograph) was many times that on the two insulated rods. This phenomenon, which was demonstrated with obsidian, andesite, and pyroxenite powders, indicates that the net negative charge built up on the two insulated rods was able to repel many of the incoming powder particles sufficiently to cause them to alight on the plate instead of the rods. All powder deposits did, however, demonstrate adhesion. The rods could be inverted without loss of powder, and the plate lost only isolated areas of powder upon inversion.

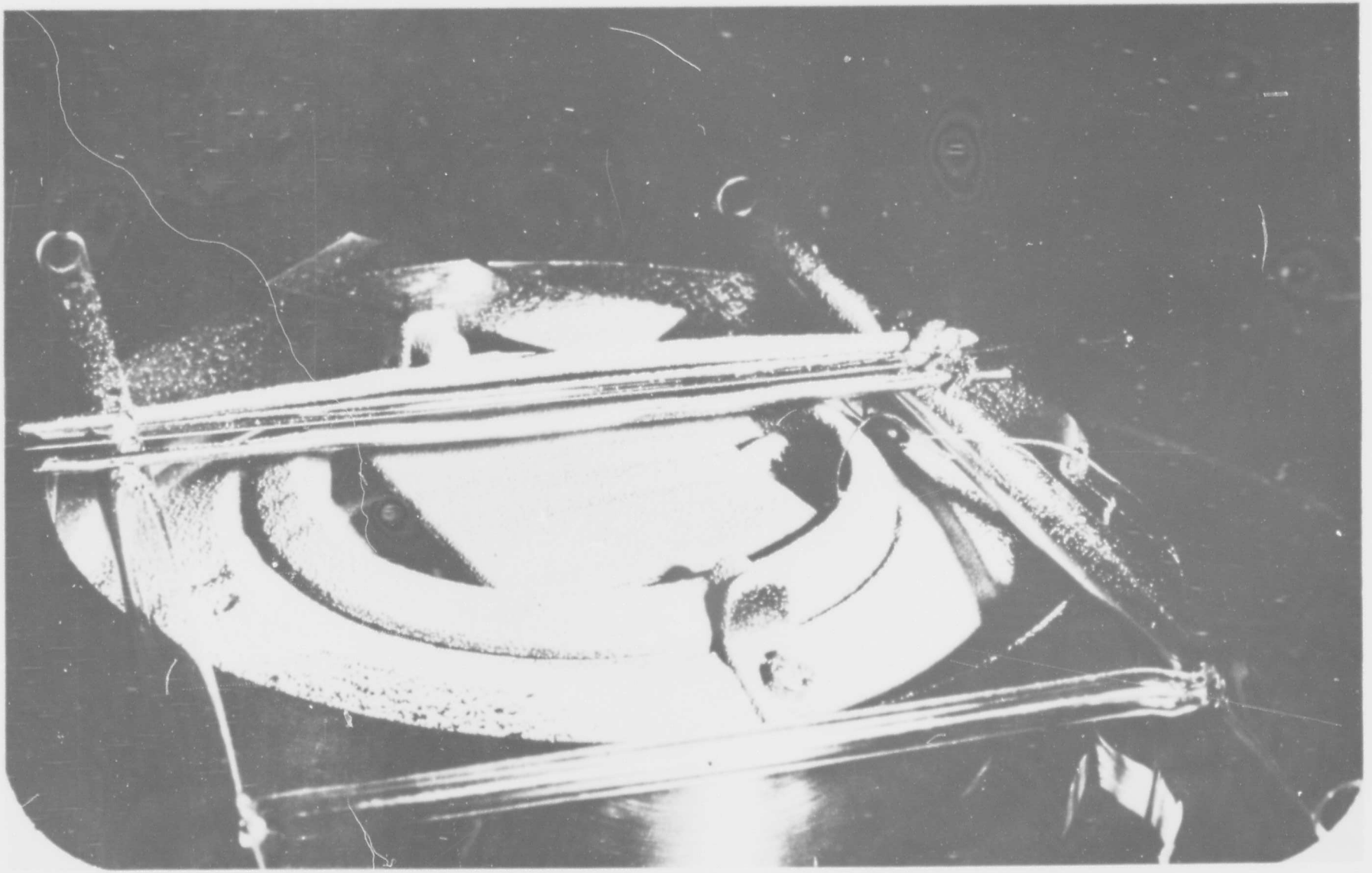

FIGURE VII-1 ELECTROSTATIC-FORCE EXPERIMENTS INVOLVING GROUNDED AND INSULATED RODS OVER ELECTROMETER PLATE

In the third electrostatic force experiment, illustrated in Figure VII-2, an electrostatic spectrometer was used to determine the magnitude and distribution of charge in the powdered samples. Tests run on andesite and pyroxenite showed that the powder particles had both positive and negative charges, as well as being neutral. The number of particles with a negative charge outweighed those with a positive charge by at least an order of magnitude, although small powder losses from the plates during disassembly of the spectrometer prevented an accurate determination of the ratio. Particle charge to mass ratios were computed from the position of the charged particles on the plates. Preliminary calculations show that the most highly charged particles of both signs, which deposited on the upper portion of the spectrometer plates, carried a charge of at least 10^{13} elementary charges/gram. If the average particle mass was 1.4×10^{-9} g, the individual highly charged particles carried at least 10^{4} elementary charges.

Although the charge generation mechanism in the sifting experiment is considerably different from that envisaged on the undisturbed lunar surface, the magnitudes of the greatest charges are within an order of magnitude of those predicted for the lunar surface by the various theoretical expressions. A direct comparison cannot be made, since the size of the particles carrying the largest charges was not determined.

The importance of gross electrostatic forces in high-vacuum adhesion was emphasized during an accident within the chamber. The accident occurred during the second electrostatic spectrometer experiment (with pyroxenite) when the sample became contaminated with back-streamed oil vapor from the diffusion pump. When sifted, the sample exhibited negligible adhesion,

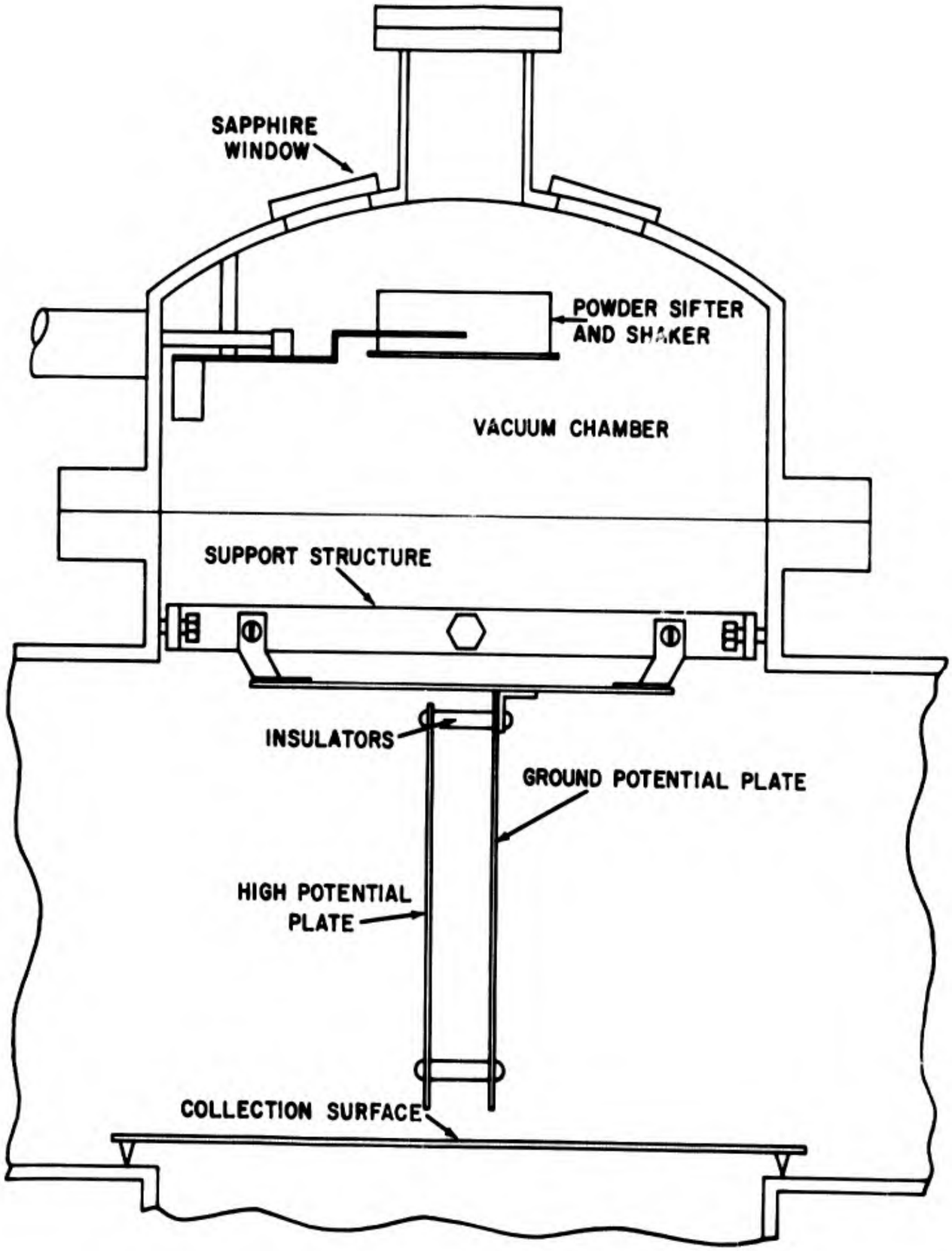

FIGURE VII-2 SCHEMATIC DIAGRAM OF HIGH-VACUUM CHAMBER SHOWING ELECTROSTATIC SPECTROMETER

although the electrostatic spectrometer measurements showed that the distribution and intensity of charge were unchanged. This suggests, as does the fact that adhesion did not take place in air, that an adsorbed monolayer of oil or water vapor will prevent adhesion of particles. Thus, it appears that atomic forces are probably the controlling factors in high-vacuum adhesion, while electrostatic effects may control the site of deposition.

D. FUTURE WORK

The results of these experiments indicate that, as might be expected, powders become electrified in a vacuum in much the same way as they do in the dry atmosphere. The experiments made thus far are of considerable value in indicating the course of future work. In the case of generation of charge on powders, it appears desirable to carry out experiments which correlate the development of charge to the details of interactions between surfaces. Accordingly, experiments will be carried out in which charge generation will be measured when two surfaces are operated under carefully controlled conditions.

In addition to the charge measurements, preliminary attempts were made to measure the electrical conductivity of mineral powders under high-vacuum conditions. In these experiments, samples of powders were dusted on a glass surface covered with two evaporated metal electrodes; the resistance of the powder was determined by observation of current that flowed when a potential was applied between the electrodes. Under high vacuum, the current which flowed indicated quite a high conductivity — so high, in fact, that one would expect any static charge to leak away rapidly. Probably these preliminary measurements are in serious error, for the electrical current may not have been flowing through the powder but instead through

the glass seal in the lead into the vacuum system or through the sample holder itself.

Based on these results, the technique for measuring the conductivity of mineral powders will be improved. The errors induced through feed-through leakage will be eliminated by placing a high-impedance electrometer in the vacuum itself and only bringing the low impedance output through the vacuum feed-through. A scheme for measuring electrical conductivity is being considered in which the electrical relaxation time will be measured by observing the behavior of a sample in which a dipole is induced by the application of an external electric field. This might be done by measuring the torque on the sample suspended on a torsion fiber. Such a scheme would have the advantage of eliminating any polarization effects that might occur at the interface between the powder and any conducting electrode.

SECTION VIII

THERMAL PROPERTIES OF POSTULATED LUNAR SURFACE MATERIALS

The thermal and optical properties of the lunar surface materials play an important role in establishing the lunar temperature environment. Conversely, a knowledge of the apparent thermal environment of the lunar surface and subsurface can lead to an understanding of the nature of the lunar surface. Accordingly, lunar surface and subsurface temperatures have been measured by infrared and microwave methods. These studies have yielded data on the temperature variations during normal lunations and eclispses.

The objectives of this portion of the program were to:

a) Establish a method suitable for measurement of thermal conductivity and diffusivity of postulated lunar materials in the lunar environmental chamber designed and constructed under this program;

b) Determine the thermal conductivity of powder materials in a simulated lunar environment, and measure the effects of temperature, hard vacuum, X-ray, ultraviolet, and particulate radiation on the thermal conductivity of powder materials; and

c) Use the thermal property data thus obtained to gain a better understanding of the nature of the lunar surface.

Several types of steady-state and transient methods have been used for measurement of thermal properties of powders in vacuum (Kannuluik and Martin, 1933; Masamune and Smith, 1963; Everest, et al, 1963). The line heat source method was chosen for the present study for the following reasons:

a) The high-vacuum chamber was of limited size; minimum electrical feed-throughs and modifications were to be made to accommodate the conductivity measurements.

b) Only small amounts of several postulated lunar surface materials were available. The materials were to be prepared within the high-vacuum chamber and placed in the thermal conductivity apparatus to eliminate handling and contamination and to promote outgassing.

c) The transient method is more rapid compared to more conventional steady-state methods, and it is not necessary to maintain controlled environmental conditions for long periods.

d) The line heat source apparatus can be arranged so that variations in thermal conductivity with pressure, temperature, and time of exposure to infrared, ultraviolet, and proton beam radiation can be studied.

A. THERMAL CONDUCTIVITY OF POWDERS IN VACUUM

1. Heat Transfer Mechanisms

The flow of heat through powdered materials involves the simultaneous operation of several different heat transfer mechanisms:

a) Solid conduction through the particles and conduction between particles across areas of contact.

b) Gas conduction within the void spaces of the material.

c) Radiation across the void spaces and through the particles.

As will be explained below, solid conduction and radiation are the most important mechanisms of heat transfer through powdered material on the lunar surface. The relative importance of these mechanisms depends upon the physical properties of the particles, their size,

shape, and packing arrangement, the physical properties of the gas filling the voids, the adsorption of gases by the particles, and the temperature and pressure of the environment. Of these variables, the effects of adsorbed gases are the least known.

A practical method of examining the importance of each mechanism and the influence of the above-mentioned variables on the heat transfer rate is to consider the contribution of each mechanism to the over-all thermal conductivity of a material. The sum of the individual contributions of thermal conductivity is taken as the effective conductivity of the medium, and its value can be used in Fourier's general conduction equation. The following paragraphs contain a brief review of the mechanisms of heat transfer in powdered materials and a description of several theoretical and experimental investigations of the thermal conductivity of these materials.

a. Solid Conduction

In most two-phase solid-gas systems, the thermal conductivity of the solid is many times greater than that of the gas. One might expect a fairly high effective conductivity for systems with a moderate or high proportion of solids. However, experimental evidence has shown that the effective conductivities of powders is quite low. This accounts for the widespread use of powders in insulating materials. Consideration of the conduction mechanism within powders confirms these observations. Heat can be transferred from particle to particle by two different conduction paths: first, the transfer across areas of direct solid contact and, second, from a particle through the gas adjacent to it to the next particle. This heat transfer through solid and gas may occur through many

paths, both in series and in parallel. Since the gas conductivity is generally low, conduction in series through the gas is limited; also, the contact area for most particulate media is small. Therefore, powders show relatively low conductivities.

Models of particulate systems have been proposed by many investigators, and formulas have been derived for determination of the effective conductivity due to the conduction mechanism. To simplify calculations most authors have considered beds of spherical particles (Deissler and Eian, 1952), others have considered cylindrical pellets (Schumann and Voss, 1934), cubes (Russell, 1935), and particles of arbitrary shape (Gorring and Churchill, 1961; and Tsao, 1961). The results of the analyses yield fairly complicated expressions relating the effective conductivity to the conductivities of the solids and gas, the porosity, the shape factor, and occasionally to the particle size and density. Most investigators are interested in the regions where a gas fills the voids between the particles, and under these conditions solid conduction at contact points is small compared to conduction through the solid-gas-solid path. Deissler and Boegli (1958) point out, however, that when the ratio of solid conductivity to gas conductivity (k_s/k_g) is high, the effective conductivity of a particulate medium is very sensitive to the way in which particle make contact and to any surface irregularities that may exist near the contact points. This is one reason why the conductivities of powders are not easily correlated by the same relationships that hold for larger, more uniformly shaped particles; sensitivity to particle contact is particularly applicable to evacuated powders.

For specific materials, it is possible to construct models that indicate approximate areas of contact and contact pressure, and, therefore, the dimensions of the heat flow paths (Timoshenko, 1945). This method has been successfully applied to arrays of glass fibers (Strong, Bundy, and Bovenkirk, 1960). Riemann (1919) considered arrays of truncated spheres for models of a porous media, and Gorring and Churchill (1961) have tried to evaluate the effects of finite contact area. We have proposed several models to account for solid contact between spherical particles, both with and without adsorption of gases on the particle surface (Goldstein, 1961; and Glaser, 1961). Wilhelm, et al (1948) have devised an empirical correction to account for conduction by solid contact. Despite the many investigations, exact methods of predicting the contribution of solid conduction in powdered or fine particulate media are not available.

Another variable of practical interest is the dependence of thermal conductivity on density (Glaser, 1961). Both the contributions of radiation and solid conduction to over-all conductivity are affected by density changes. Usually, a particulate material exhibits a density at which the effective conductivity is a minimum; a decrease in density increases the solid conduction contribution. Significant variations in the effective conductivity of perlite of different densities have been observed (Glaser, 1961). This work covered temperatures between $77^{o}K$ and $390^{o}K$, a range similar to that anticipated in the lunar environment.

Other factors that may have a bearing on the contribution of solid conduction are the influence of particle cohesion due to electrostatic charges, welding at point contacts, and the effects of the gravitational

field. The contact areas between particles can be changed by variation of these factors.

b. Gaseous Conduction

The effects of gas conduction on the thermal conductivity of powders has been indicated above. The gas provides a conduction path between the particles of the media. The effects of pressure on the contribution to thermal conductivity by gaseous conduction have been observed by several investigators (Deissler and Eian, 1952; Glaser, 1961; Schotte, 1960; Verschoor and Greebler, 1952; Wechsler and Glaser, 1961). Two separate regions are observed: (1) a pressure-independent region ranging from atmospheric pressure to a few millimeters of mercury and (2) a pressure-dependent region at pressures below a few millimeters of mercury. The transition between the two regions depends upon the mean diameter of the particles, the arrangement of the particles, and the type and temperature of the gas filling the voids. At higher pressures, the mean free path of the gas molecules is smaller than the particle spacing, and the gas conductivity is independent of pressure. When the pressure of the gas is sufficiently reduced, the mean free path becomes greater than the particle spacing, and the gas conductivity within the media becomes directly proportional to the pressure. The larger the particle spacing and the lower the temperature of the system, the lower the pressure required for reduction in gas conductivity.

Gas conduction should be negligible for the range of pressures expected on the lunar surface, except where gases may be trapped within the rock or where gases percolate through the surface layers. Solid

conduction (due to point contacts) and radiation heat transfer will be the most important mechanisms to consider in the lunar environment.

c. Radiation Heat Transfer

When radiant energy impinges on particulate media, it may be reflected, transmitted through the particles or void space, absorbed by the particles and later re-radiated, or scattered by the particles. In the case of small particles where the wavelength of the radiation is larger than the particle dimensions, scattering is likely to occur. The phenomenon of absorption is intimately tied to the physical properties of the material and is influenced by the emissivity of the particle and the "absorption cross section." Similarly, the transmission of energy depends on the characteristics of the material.

Many investigators have analyzed radiation through porous and particulate media and obtained effective radiation conductivities without considering the phenomena of absorption and scattering in detail (Strong, Bundy and Bovenkirk, 1960). The general result is that the "radiation conductivity" is proportional to the cube of the mean temperature, various functions of the emissivity of the materials, and some geometrical factors. Therefore, the radiation contribution becomes more important at higher temperatures. This has been demonstrated experimentally by Hill and Wilhelm (1959) and Chen and Churchill (1963). However, in low-density materials that are fairly transparent, radiation energy transfer can also be significant compared with other mechanisms, especially where gas conduction has been reduced. Larkin and Churchill (1957) and Strong, Bundy and Bovenkirk (1960) have demonstrated this experimentally.

Other investigators (Chen and Churchill, 1961; Glaser, 1961; Hamaker, 1947; Larkin and Churchill, 1959) have considered absorption and scattering in more detail and have shown that the radiation conductivity is a function of absorption and scattering cross sections, which are, in turn, functions of the temperatures of the material and the nature of the radiant energy. Experiments have been devised for measuring these quantities, but sufficient experimental confirmations of the theoretical work have not been reported.

2. Previous Investigations

Little definitive information is available in the literature on the thermal properties of postulated lunar materials. There is, however, a considerable amount of data on the thermal conductivity and diffusivity of silica powders, glass beads, beds of sand particles, and other powdered materials whose properties should be similar to those of lunar surface materials.

As early as 1910, Smoluchowski studied the thermal conductivity of powders in vacuum. His data is often referred to in papers which relate observed lunar temperatures to analytical models. Smoluchowski studied the thermal conductivity of quartz powder, emery, diatomite, and other powders at pressures from 5×10^{-2} torr to atmospheric. It has been recently pointed out (Liu and Dobar, 1964) that Smoluchowski's data is often misinterpreted. The lowest value of thermal conductivity measured by Smoluchowski was 5.6×10^{-5} cal/cm-sec-^{o}C for quartz sand of 92-micron average grain size. Following Smoluchowski's pioneering work, many other investigators studied the effect of gas pressure and composition

on the thermal conductivity of powders (Aberdeen and Laby, 1926; Kannuluik and Martin, 1933; Deissler and Eian, 1952).

Table VIII-1 is a compilation of data on the thermal conductivity of powdered materials in vacuum. It can be seen that although a large range of materials with many different particle diameters were studied, little work has been done in the gas pressure range below 10^{-5} torr. Table VIII-1 also shows the value of the thermal parameter $(k \rho C)^{-1/2}$. There is a considerable range of the thermal parameters for the various materials, compared to the value of 1000 (in cgs units) normally accepted for powdered materials in vacuum. Figure VIII-1 shows the effect of gas pressure on the thermal conductivity of powders in vacuum.

With specific reference to simulated lunar surface materials, Bernett, et al (1963) investigated the thermal conductivity of powdered basalt and quartz. Liu and Dobar (1964) investigated and presented data on the thermal conductivity of solid pumice and scoria and crushed pumice of 2-cm particle diameter at pressures from 10^{-2} torr to atmospheric. The thermal conductivity of solid pumice and basalt have also been reported (Wechsler, Glaser and Allen, 1963). Continuing studies in this program will determine the effective thermal conductivity of powdered granite, basalt, and pumice at pressures from 10^{-6} torr to atmospheric. Particle sizes from 10 to 200 microns are being investigated. Data are not yet available on the thermal properties of powdered materials in the pressure range between 10^{-6} to 10^{-11} torr, the range in which physical and chemical adsorption of gases on particulate surfaces could strongly affect the thermal conductivity of powders.

TABLE VIII-1

THERMAL PROPERTIES OF EVACUATED POWDERS

Material	Density (gm/cm^3)	Temperature (^oK)	Gas Pressure (torr)	Thermal Conductivity ($cal/sec\text{-}cm^oK$)	$(k\rho c)^{-\frac{1}{2}}$ (cgs units)	Remarks
Perlite, 200μ particles	0.080	77-370	$<10^{-4}$	5.5×10^{-6}	3300	Everest, Glaser, Wechsler (1963)
Colloidal Silica, 200Å	0.08	77-370	$<10^{-4}$	9.0×10^{-6}	2900	Everest, Glaser, Wechsler (1963)
Tektite, <20μ	1.5	77-370	$<10^{-4}$	8.5×10^{-6}	630	This work
Crushed Pumice	1.1	290	2×10^{-2}	1×10^{-5}	650	Liu and Dobar (1964)
Quartz sand, 90μ	1.3	290	6.4×10^{-2}	5.6×10^{-6}	830	Smoluchowski (1910)
Quartz sand, 90μ	1.6	290	3×10^{-2}	1.5×10^{-5}	460	Woodside and Messmer (1961)
Olivine, < 70μ	2.0	77-370	$<10^{-4}$	3.2×10^{-6}	910	This work
Silica Sand, 200-400μ	1.6	200	$<10^{-4}$	8.0×10^{-6}	680	Bernett, et al (1963)
Olivine Basalt, 10-200μ	1.5	200	$<10^{-4}$	4.0×10^{-6}	870	Bernett, et al (1963)
40% Carbon-60% Perlite	0.085	77-290	3×10^{-6}	1.0×10^{-6}	7800	Glaser (1961)
25% Carbon-75% Silica	0.055	77-290	2×10^{-6}	1.7×10^{-6}	7300	Glaser (1961)

B. THE LINE HEAT SOURCE METHOD

1. Historical Review

The line heat source method was suggested by Schleiermacher (1888) and independently by Stalhane and Pyk (1931). The first practical use of the method was by Van der Held and Van Drunen (1949), who measured thermal conductivity of liquids. The thermal conductivity probe, a modification of the line heat source method, was first described by Hooper and Lepper (1950) and has been used by over twenty investigators in the past 13 years, primarily for measurements of the thermal conductivity of soils and building insulating materials. Woodside and Messmer (1961) have used the probe method for measuring the thermal conductivity of solid and granular rocks in both the dry form and saturated with fluids. The probe or line heat source method is presently being used to measure the properties of alumina particulate beds as a function of temperature and pressure (De Nee, 1963).

2. Theory of the Line Heat Source Method

The line heat source method is based upon measurement of the temperature field produced by a line source of heat surrounded by an infinite medium of a homogeneous material. If heat is liberated by a line source at the rate q per unit time per unit length, beginning at time zero ($t = 0$), and if the surrounding material is at zero temperature throughout, the temperature at time t and at a distance r from the heat source can be given as (Carslaw and Jaeger, 1959):

$$T = \frac{q}{4\pi k} \int_{r^2/4\alpha t}^{\infty} \frac{e^{-u}\, du}{u} \qquad (1)$$

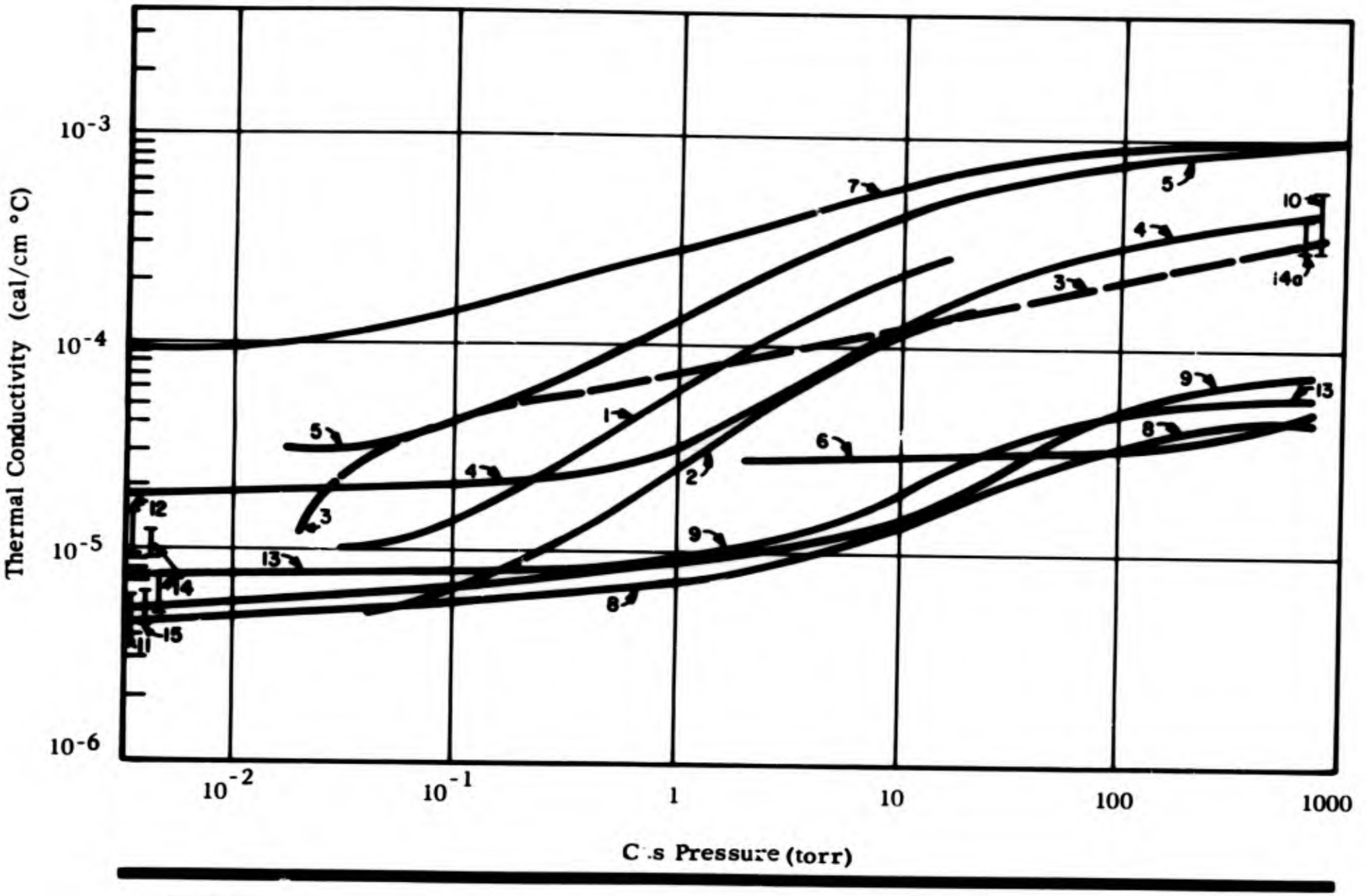

FIGURE VIII-1 EFFECT OF GAS PRESSURE ON THERMAL CONDUCTIVITY OF POWDER MATERIALS

LEGEND FOR FIGURE VIII-1

Number	Material	Particle Size	Remarks[a]	Reference
1	Quartz Powder	264 μ	Data extrapolated below 10^{-1} torr and above 50 torr	
2	Quartz Powder	94 μ	Data extrapolated below 10^{-1} torr and above 50 torr	Smoluchowski (1910)
3	Crushed Pumice	2 cm	Some fine powder mixed with 2 cm particles	Liu and Dobar (1964)
4	Quartz Sand	74 to 105 μ	Porosity of 0.59	Woodside and Messmer (1961)
5	Quartz Sand	590 to 840 μ	Porosity of 0.33	Kistler (1935)
6	Silica Aerogel	--	--	Schuman and Voss (1934)
7	Steel Shot	0.126 cm		
8	Colloidal Silica	0.02 μ	Density: 0.08 gm/cm^3 Temperature Range: 77 to 370°K	Everest, Glaser, Wechsler (1963)
9	Expanded Perlite	300 to 350 μ	Density: 0.08 gm/cm^3 Temperature Range: 77 to 370°K	Everest, Glaser, Wechsler (1963)
10	Olivine Basalt	200 to 400 μ	Density: 1.4 to 1.6 gm/cm^3 Temperature Range: 170 to 370°K	Bernett, et al (1963)
11	Olivine Basalt	5 to 100 μ	Density: 1.6 gm/cm^3 Temperature Range: 270 to 370°K Pressure: 5×10^{-6} torr	Bernett, et al (1963)
12	Olivine Basalt	200 to 400 μ	Density: 1.56 gm/cm^3 Temperature Range: 220 to 370°K Pressure: 5×10^{-6} torr	Bernett, et al (1963)
13	Aerosil	--	--	Leidenfrost (1955)
14	Olivine	40 μ	Density: 1.5 gm/cm^3 Pressure: 1×10^{-5} torr	Wechsler, et al (1963)
15	Tektite	40 μ	Density: 1.1 gm/cm^3 Pressure: 1×10^{-5} torr	Wechsler, et al (1963)

[a] Room temperature data unless otherwise noted.

or

$$T = \frac{-q}{4\pi k} Ei\left(-\frac{r^2}{4\alpha t}\right) \qquad (2)$$

where Ei(x) = exponential integral of x

r = radial distance from the line heat source

k = thermal conductivity of the media

α = thermal diffusivity ($k/\rho c$) of the media

Several assumptions are inherent in the derivation of the above equation, as discussed in Sub-Section B-3 below. If an experimental apparatus can be arranged to correspond to a line heat source and appropriate temperature measurements can be made, the potential applicability of the line heat source method can be examined.

For small values of $r^2/4\alpha t$ the exponential integral function can be approximated as (Carslaw and Jaeger, 1959):

$$Ei(-x) = \gamma_E + \ln x - x + 1/4\, x^2 \qquad (3)$$

where γ_E = Euler's constant = 0.5772 . . .

For values of $x \leq 0.03$, Ei(-x) can be approximated as $\gamma + \ln x$ to an accuracy of better than 1%. The usual line heat source experiments rely on the latter approximation. Therefore, for $x \leq 0.03$, Equation 2 can be rearranged to give:

$$T = \frac{-q}{4\pi k}\left[\gamma_E + \ln \frac{r^2}{4\alpha t}\right] \qquad (4)$$

or, if r and α are constant,

$$T = \frac{q}{4\pi k}\left[A + \ln t\right] \qquad (5)$$

(where $A = -\gamma_E - \ln \frac{r^2}{4\alpha}$)

The thermal conductivity can then be evaluated from the heating rate and a plot of logarithm of time versus temperature.

For most of the powdered rock samples, conditions are such that small values of $r^2/4\alpha t$ are not attained in reasonable time. For example, for an evacuated olivine powder with $k = 0.9 \times 10^{-5}$ cal/cm sec ^{o}C, $\rho = 2.0$ gm/cm^3, and $c = 0.2$ cal/gm ^{o}C for a value of $r = 0.25$ cm, about six hours must elapse before the approximations discussed above can be used. It is not desirable to use much smaller values of r because of possible powder-bridging across the wires and resultant inhomogeneities. It is also impractical to wait for such long times because changes in sample temperature and pressure and boundary effects may contribute to errors.

Another method was therefore used to obtain thermal conductivity values from the line heat source equation. By differentiation and rearrangement of Equations 1 and 2, the following equation holds for an ideal line heat source at all times:

$$k = \frac{q}{4\pi} \quad \frac{\left[t_1 \left(\frac{dT}{dt} \right)_1 \right]^{b_1}}{\left[t_2 \left(\frac{dT}{dt} \right)_2 \right]^{b_2}} \qquad (6)$$

where $b_1 = \frac{t_1}{t_2 - t_1}$, $b_2 = \frac{t_2}{t_2 - t_1}$, t_1 and t_2 being any two different times.

By plotting the temperature rise as a function of time, and finding slopes at various times, the thermal conductivity can be determined. If slopes are taken at times of 10, 20, 30, 40, and 50 minutes, for example, 10 values of the ratio

$$\frac{\left[t_1 \left(\frac{dT}{dt} \right)_1 \right]^{b_1}}{\left[t_2 \left(\frac{dT}{dt} \right)_2 \right]^{b_2}}$$

can be obtained, and the average value can be used to determine the thermal conductivity. In this method errors due to graphical evaluation of the slopes cause a considerable lack of precision in computation of thermal conductivity.

Consideration of Equation 1 will show that if the experimental apparatus corresponds to the ideal line heat source, plots of the experimental data in the form of logarithm of $\frac{4\pi T}{q}$ versus logarithm of time should all have the same shape, independent of the thermal properties of the media under study. Moreover, this shape should correspond to a standard "type" curve of the logarithm -Ei(-1/x) versus logarithm x. By matching the experimental curves with the standard "type" curve and determining the required shifts in the axes to make the curves coincide, one can obtain values of the thermal conductivity. Figure VIII-2 shows a standard "type" curve and two typical experimental curves. Since the curve-matching technique utilizes a greater portion of the data and does not require graphical differentiation, more precise values of thermal conductivity can be obtained. The fit between the experimental curves and standard "type" curve is generally good; there are some deviations at very short and long times. These are expected from theoretical analysis of the errors encountered in the practical application of the line heat source method.

3. Applicability of the Theory

The experimental data obtained in this investigation have been analyzed by the curve-matching technique in terms of the theory for an ideal line source embedded in a homogeneous material at uniform temperature. Because it is not possible to construct an experimental apparatus

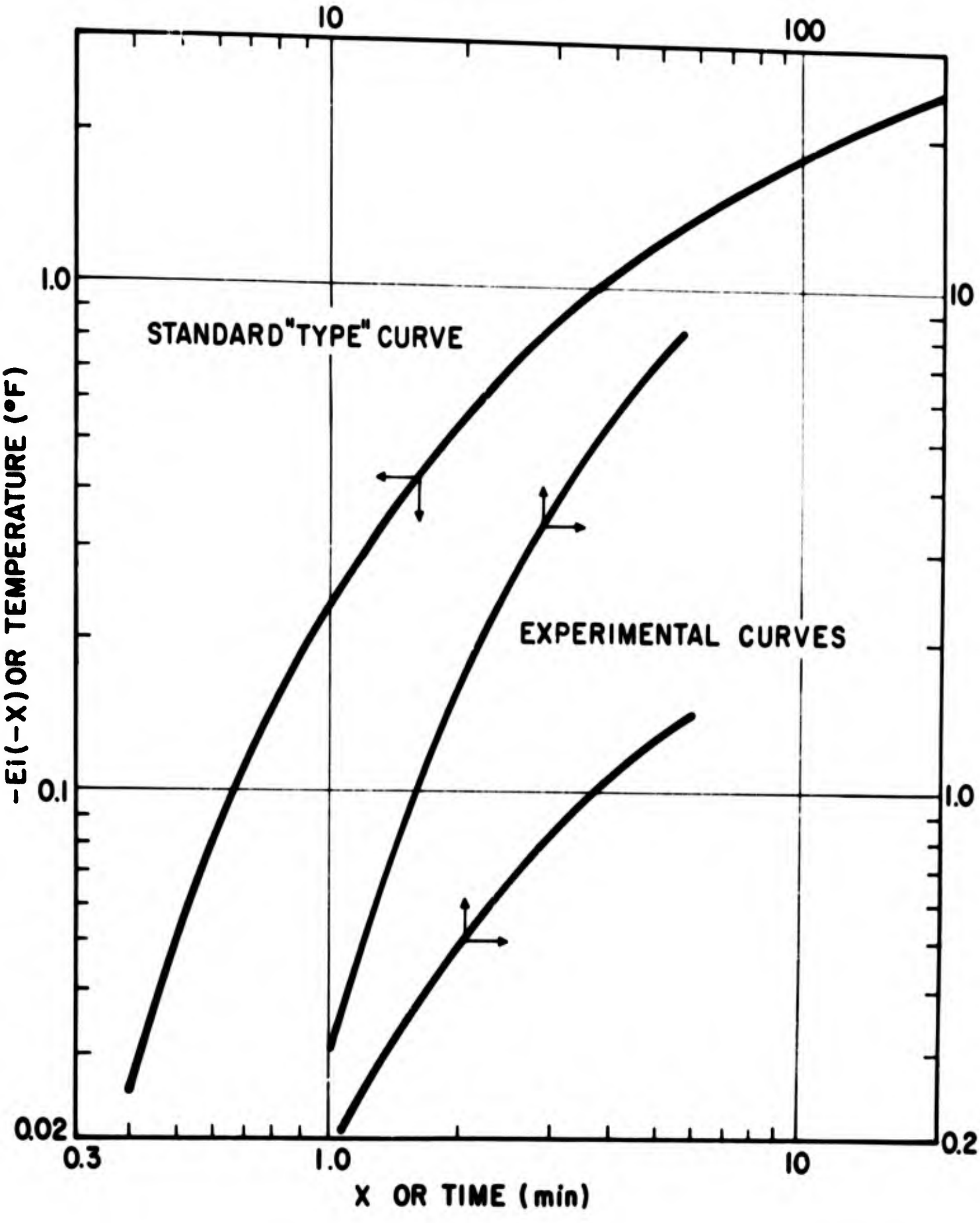

FIGURE VIII-2 STANDARD AND EXPERIMENTAL CURVES FOR LINE HEAT SOURCE METHOD

which corresponds exactly to the theoretical model, it is necessary that the finite properties of the actual apparatus -- such as the conductivity, radius, and specific heat of the heater wire -- do not introduce sufficient departures from the ideal case to cause significant error in the test results.

If assumptions 1 through 8, listed below, are satisfied, the temperature field produced in a sample by an actual line heat source will be the same as that for an ideal source (Equation 1).

(1) The medium surrounding the line heat source is both continuous and homogeneous.

(2) The thermal properties of the medium are independent of temperature, temperature gradients, and time. This assumption also implies that thermal conduction is the only heat transfer mechanism of any significance, and that there are no changes in the environmental conditions during a single experiment.

(3) The radial boundaries of the medium being studied are sufficiently far from the line source and temperature measuring device so that they will have no effect on the temperature distribution during the measurement period.

(4) The radius of the heat source is sufficiently small that it can be regarded as infinitesimal in establishing the temperature distribution during the test.

(5) The line heat source has a sufficiently low heat capacity that a negligible fraction of the input power is used to raise its temperature.

(6) The line heat source is sufficiently long, compared to the radius and other dimensions, that the effects of lack of sources beyond the ends can be neglected.

(7) Heat-leaks out of the ends of the sample or heater wire do not affect the temperature distribution.

(8) There is no contact resistance between the line heat source and the surrounding medium.

Assuming that the ideal temperature field has been created, it must then be measured accurately. To make the temperature measurement, a fine thermocouple suspended parallel to the heater wire is used. Direct utilization of this temperature data in the ideal line source equations implies two additional assumptions:

(9) The temperature distribution in the medium is not altered by the temperature measuring device.

(10) There is no "contact resistance" between the temperature measuring device and the surrounding medium.

Assumptions 4, 5, 6, 7 and 9 are most susceptible to quantitative mathematical analysis. Although formal solutions to the errors introduced by the relaxation of these assumptions can be obtained relatively easily, the exact numerical evaluation of these errors requires the use of an electronic computer. Fortunately it is possible to obtain, without elaborate computing facilities, approximate solutions which suggest the order of magnitude of the errors. These approximate solutions are particularly useful for determining within what ranges each assumption can be expected to hold and where more detailed analysis may be necessary.

Several possible mathematical models will be used to approximate the actual experimental conditions. Although these models represent slight departures from the experimental conditions, the departures are sufficiently small that their influence will not affect the main conclusions.

In addition to the variables already defined, we shall represent the radius of the heater wire by a and the length of the wire by ℓ. The subscripts "1" and "2" applied to the thermal constants will refer to the materials comprising the heat source and the sample, respectively.

For simplicity in representation we shall also find it convenient to utilize the following dimensionless variables:

$$\left.\begin{aligned} \bar{T} &= \frac{4\pi k T}{q} & \bar{t} &= \frac{4\alpha t}{r^2} \\ \lambda &= \frac{\ell}{r} & \zeta &= \frac{z}{r} \end{aligned}\right\} \qquad (7)$$

z is the axial coordinate indicated in Figure VIII-3.

Thus, Equation 2 will take on the dimensionless form

$$\bar{T} = -\mathrm{Ei}(-1/\bar{t}) \qquad (8)$$

It is possible to examine each of the assumptions separately and estimate the extent to which each will affect the measured conductivity.

a. Sample Homogeneity

The effects of sample homogeneity are difficult to assess analytically. It will suffice to say that the results of a line source test depend to a greater extent on the properties of the material immediately surrounding the line heat source and temperature measuring device than on the properties of the material situated at greater distances from the heat source. In tests carried out under conditions where the powder material is placed in a container surrounding the heat source and then

brought to desired environmental conditions, the sample should be uniform and homogeneous. The normal vibration and movement during the filling of the sample holder with a powder in air helps to establish homogeneity. It cannot be assumed, however, that the powder sample prepared in this manner will be identical in packing arrangement and density to a second sample prepared similarly. Asymmetric particle shape and variation in particle size contribute to differences in sample density and arrangement. Thus, for experiments in which the same type of powder is used, it is not possible to control the density or homogeneity accurately. Experience with beds of spherical particles has shown that for single-size particles the porosities of samples which have been settled by vibration invariably are close to that of an orthorhombic-packed system, i.e., porosity or void fraction equals 0.37. Therefore, in tests where more spherical uniform size particles are used, one can expect greater homogeneity both within a single sample and between "duplicate" samples.

In samples prepared in the high-vacuum chamber and deposited on the line heat source apparatus by sifting, it is difficult to assure homogeneity. "Shadowing" due to the wires, adhesion of the powder on the wires, and nonuniform sieving can result in a nonuniform sample. Little can be done to improve the method and to insure uniformity. Visual observation of the samples during preparation and deposition has not indicated any gross discontinuities. A distance of about 0.20 cm must be maintained between the heater wire and thermocouple wire in an experimental apparatus to insure that bridging of powder and subsequent inhomogeneities do not occur.

b. Constant Thermal Properties

The thermal conductivity and diffusivity of a powder material are generally dependent upon temperature. The more important the contribution of radiation to heat transfer, the more the effective thermal conductivity depends upon temperature. In the normal line heat source experiments, the total temperature rise of the material between the line source and thermocouple is less than 20°C. The effect of temperature on thermal conductivity over this narrow range should be small. The thermal conductivity value obtained during any test can be considered representative of the material at the average temperature of the test.

The influence of radiation heat transfer is difficult to assess. With the dense, relatively opaque lunar materials that have been postulated and at the low temperatures considered, the contribution of radiation to total heat transfer should be limited. For more transparent materials, particularly if higher temperature studies are made, radiation heat transfer may introduce errors in measurements by the line heat source method. In the present tests no definite evidence of the effects of radiation heat transfer was found under the experimental conditions most likely to produce these effects.

At gas pressures below 10^{-3} torr, where gas conduction gives a negligible contribution to heat transfer in powder materials, changes in gas pressure should have little influence on the test results. In studies at higher gas pressures, it is essential to maintain constant gas pressure during an experiment to insure constancy of the thermal conductivity. When comparing the results of tests carried out in different samples at various times, it must be remembered that the actual gas pressure within

the sample bed is never measured. The difference between the actual gas pressure in the powder and the pressure measured in the sample chamber will depend on the condition of the powder--i.e., its cleanliness, degree of bakeout, time of pumpdown, etc. In some experiments where great care was not taken to insure sample cleanliness and thorough outgassing, variation in gas pressure within the powder (especially in tests conducted at pressures above 10^{-4} torr) contributed to the lack of reproducibility between tests.

c. Effects of Sample Boundaries

In most line heat source experiments, it is customary to use samples large enough so that the sample boundaries have a negligible effect on the test results. In the high vacuum chamber, it is not possible to prepare large volumes of samples and deposit them upon the line heat source. Typical sample widths used in the experiments were 2 to 2.5 cm; sample heights ranged from 0.5 to 0.7 cm. The sample height can be considered the critical dimension for the evaluation of the effects of the radial boundaries.

Consider the line heat source to be imbedded in the center of a sample of height 2s. The effects of boundaries can be estimated by placing appropriate image sources at distances $\pm$ 2s, $\pm$ 4s, etc., from the real source. The effects of image sources at $\pm$ 4s will be much less than those at $\pm$ 2s, so that we can restrict our analysis to the first two image sources. The contribution of the image source can be estimated from Equation 2 is q is replaced by the strength of the image source and r is replaced by the distance from the image source to the point in question. If the boundaries are kept isothermal (the base plate of the apparatus, for example, is of sufficient mass to be isothermal during

the test), the strength of the image source (i.e., a heat sink) will be in the order of -q. If the boundaries are adiabatic, the image source will have a strength of approximately +q. At a point in the plane formed by the heater and thermocouple wires, the contribution of the real heat source at a distance r and one image source at a distance s from the heater can be written as:

$$\bar{T} \approx -Ei(-1/\bar{t}) + Ei\left[\frac{-(4s^2 + r^2)}{r^2 \bar{t}}\right] \qquad (9)$$

If the second term on the right side of the equation is much smaller than the first, the effect of sample boundaries can be neglected. For typical values of r and s (r = 0.25 cm, s = 0.65 cm) the apparent error is less than 2% for dimensionless times up to 20, and less than 5% for dimensionless times up to 100 (experimental times of about 1 and 5 hours, respectively). Since most experiments are completed within 2 hours, and the line heat source is covered by at least 0.65 cm of powder, the effects of radial boundaries can be neglected.

d. Effect of the Finite Radius of Heater Wire

Several effects might be expected to alter the temperature distribution when the radius of the heater is not infinitesimal. One is strictly geometrical; with a finite radius wire we might expect that since the near edge of the wire is closer than the point where the temperature is being measured, a somewhat higher temperature would result. To estimate an upper limit for this effect, we can assume that the entire source is evenly distributed at the outer boundary of a cylinder of radius a.

The exact solution for the temperature is given by:

$$\bar{T} = \frac{4}{\pi a} \int_0^{\infty} \frac{1 - \exp(-\alpha u^2 t)}{u^2} \left\{ \frac{J_o(ur)Y_1(ua) - Y_o(ur)J_1(ua)}{J_1^2(ua) + Y_1^2(ua)} \right\} du \quad (10)$$

For small values of a/r and for dimensionless times greater than 1, Equation 10 can be shown to reduce to

$$\bar{T} \approx -E_i(-1/\bar{t}) \left[1 + 1.76 \frac{a^2}{r^2 \bar{t}} \frac{Y_o(2.24/\sqrt{\bar{t}})}{J_o(2.24/\sqrt{\bar{t}})} \right] \quad (11)$$

(The derivation of pertinent equations is given in Appendix C.)

Since the largest values of a/r normally used in line source measurements are about 0.03, the errors introduced by this assumption will be less than 0.001 in units of dimensionless temperature. This is completely negligible in the temperature range used for conductivity determinations.

Because the thermal conductivity of the wire is considerably greater than that of the powder, the only geometrical errors would be in the direction of increasing the temperature prematurely, and these must be less than the effects of locating the entire source at the outer edge of the conductor. Therefore, the above calculation should put an upper limit on all geometrical effects of wire radius.

e. Effect of the Heat Capacity of the Heater Wire

Another effect of finite radius of the heater wire is due to its finite heat capacity. To study this effect, we will introduce a somewhat more sophisticated model which involves the thermal properties of the apparatus as well as the material under study. One suitable model is shown in Figure VIII-3.

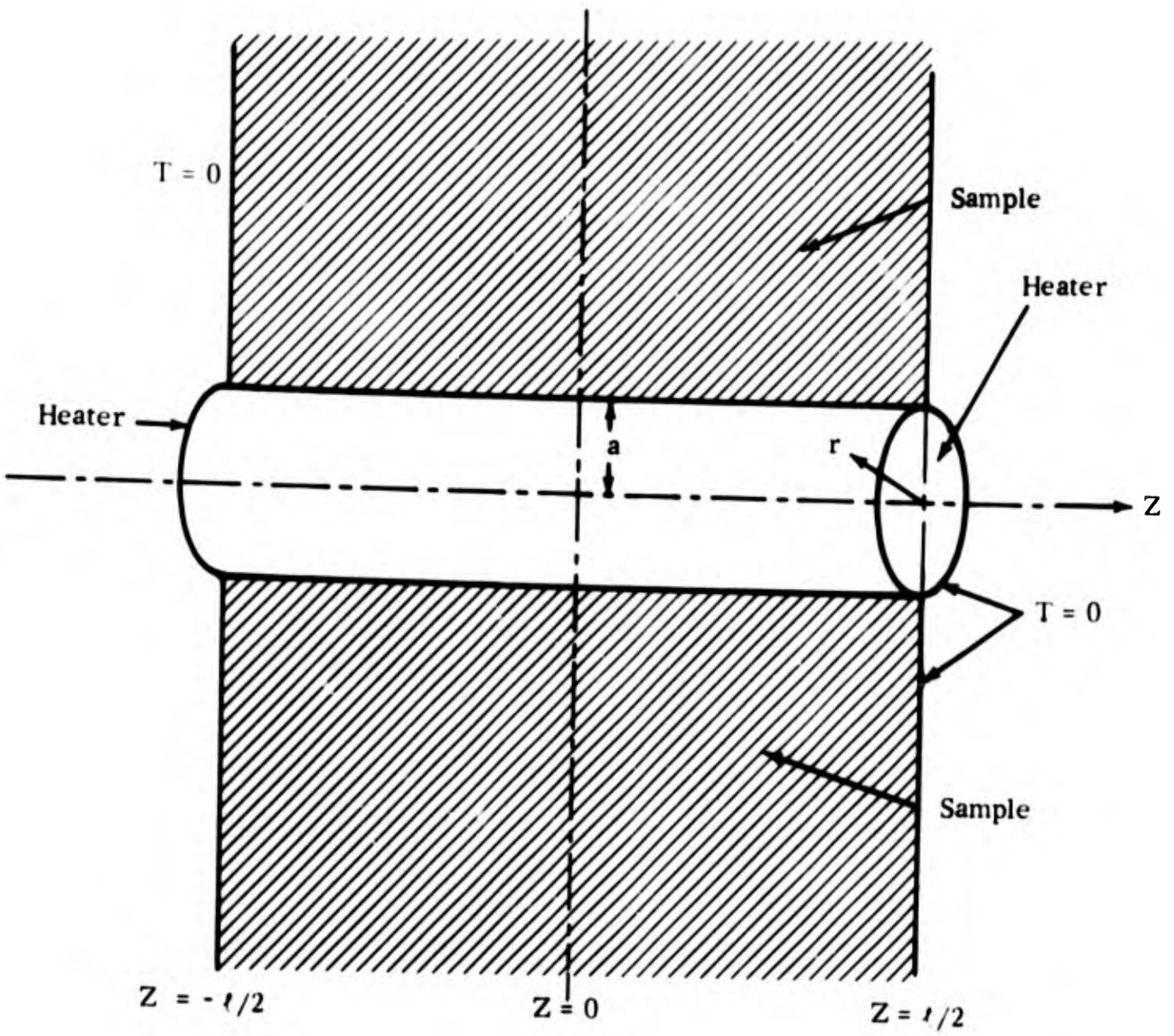

FIGURE VIII-3 MODEL FOR ANALYSIS OF ERRORS IN LINE HEAT SOURCE METHOD

A heater wire of length ℓ and radius a contains heat sources of strength q per unit length distributed evenly throughout the volume. The wire lies along the z axis with its center at the point z=0. The temperature at $z = \pm \ell/2$ is held constant, both at the ends of the heater wire and at the ends of the sample. Contact resistance between the wire and the sample is assumed to be negligible. The Laplace transform of the temperature distribution can be shown to be (Appendix C, Equations 48 and 63).

$$L\{\bar{T}\} = \frac{16\alpha_1}{\pi p^2 a^2} \sum_{m=0}^{\infty} \frac{(-1)^m}{(2m+1)} \left(\frac{\gamma^2}{\gamma^2 + \mu_m^2} \right)$$

$$\left(\frac{\beta_m^1 I_1(\beta_m^1 a) K_o(\beta_m^2 r) \cos\left[(2m+1)\frac{\pi z}{\ell}\right]}{\beta_m^2 I_o(\beta_m^1 a) K_1(\beta_m^2 a) + \frac{k_1}{k_2} \beta_m^1 I_1(\beta_m^1 a) K_o(\beta_m^2 a)} \right) \qquad (12)$$

$I_o(x)$ and $K_o(x)$ are the modified Bessel functions of the first and second kinds, respectively, of order zero. The following parameters have been introduced to simplify the expression:

$$\left.\begin{aligned} \gamma &= \sqrt{p/\alpha_1} \\ \beta_m^n &= \left[(2m+1)^2 \frac{\pi^2}{\ell^2} + \frac{p}{\alpha_n}\right]^{\frac{1}{2}} \\ \mu_m &= (2m+1)\pi/\ell \end{aligned}\right\} \qquad (13)$$

The relationship between the temperature and its Laplace transform is given by

$$\overline{T} = \frac{1}{2\pi i} \int_{\delta - i\infty}^{\delta + i\infty} e^{pt} L\left\{\overline{T}\right\} dp \tag{14}$$

where δ is a constant large enough so that all singularities of the integrand lie to the left of the path of integration in the complex plane.

Not only is the evaluation of the transform of the temperature in (12) extremely difficult, but the temperature itself usually cannot be calculated without an electronic computer. By considering the significance of the individual terms of Equation (12) and applying the principles of dimensional analysis, however, it is possible to decide which assumptions are sufficiently important to deserve more careful analysis.

To apply these techniques to the specific problem of the effect of a finite heat capacity of the heater wire, the behavior of Equation (12) can be investigated for the case of an infinitely long wire in which the radius a is small but finite compared with the distance r. Here the transformed temperature can be shown to reduce to (Appendix C, Equation 69)

$$L\{\bar{T}\} = \frac{\frac{2}{p} K_o (r\sqrt{p/\alpha_2})}{1 + \frac{k_1}{2k_2} \frac{pa^2}{\alpha_1} K_o (a\sqrt{p/\alpha_2})} \tag{15}$$

Recognizing that the greatest contributions to the integral defining the inverse transform (14) will occur in the neighborhood of the point $p = 1/t$, the behavior of the denominator of (15) with this value of p can be examined. That is, if

$$\frac{k_1}{2k_2} \frac{a^2}{\alpha_1 t} K_o (a/\sqrt{\alpha_2 t}) \ll 1 \tag{16}$$

it is unlikely that significant error will be introduced by the assumption of infinitesimal radius. The relationships involved are brought out more clearly if (16) is written as

$$\frac{-\rho_1 C_1 a^2}{\rho_2 C_2 r^2 t} \ln \left(\frac{4a^2}{r^2 t}\right) \ll 1 \tag{17}$$

where C_1 and C_2 are the heat capacities of the materials in zones 1 and 2, respectively.

For the worst cases normally encountered in our conductivity measurements, the term on the left is approximately 10^{-3}, even for dimensionless times as short as 1.0. It is, therefore, safe to conclude that the effects of heater wire size and heat capacity are not significant.

f. Effect of Finite Heater Length

The effect of finite heater length can be evaluated in several ways. Consider a source of length ℓ embedded in a large sample which surrounds it on all sides. The temperature distribution may be calculated by integrating the effects of point sources over the entire length and duration of the pulse. This yields

$$T(r,t) = \frac{q}{2\pi k} \int_0^t \int_{-\ell/2}^{\ell/2} \frac{e^{-(r^2 + z^2)/4\alpha\tau}}{4(\alpha\pi)^{\frac{1}{2}} \tau^{3/2}} \, dz \, d\tau \tag{18}$$

which, upon substitution of the dimensionless variables (7), reduces to

$$\bar{T} = \frac{2}{\sqrt{\pi}} \int_0^{\bar{t}} \int_0^{\lambda/2} \frac{e^{-(1 + \zeta^2)/\bar{\tau}}}{\bar{\tau}^{3/2}} \, d\zeta \, d\bar{\tau} \tag{19}$$

The exact evaluation of this integral is difficult, but if we rewrite it as

$$\bar{T} = \frac{2}{\sqrt{\pi}} \int_0^{\bar{t}} \int_0^{\infty} \frac{e^{-(1 + \zeta^2)/\bar{\tau}}}{\bar{\tau}^{3/2}} \, d\zeta d\bar{\tau} - \frac{2}{\sqrt{\pi}} \int_0^{\bar{t}} \int_{\lambda/2}^{\infty} \frac{e^{-(1 + \zeta^2)/\bar{\tau}}}{\bar{\tau}^{3/2}} \, d\zeta \, d\bar{\tau} \tag{20}$$

the first integral is the temperature distribution due to the infinite line source. Through several simplifying assumptions, it can be shown that the second term, which reflects the departure of the temperature

from the ideal case, is less than

$$\frac{-2\,(\bar{t})^{3/2}}{\pi^{1/2}} \quad \frac{\exp\left[-(1+\lambda^2/4)/\bar{t}\right]}{\lambda(1+\lambda^2/4)} \tag{21}$$

(For details see Appendix C, Equations 14 to 25).

If the dimensionless time interval during which the temperature rise is observed is kept less than 100 and the ratio of length to radius at which the temperature is measured is greater than about 30, the strictly geometrical effects of finite length should remain under 0.5%. As these conditions are normally maintained in all conductivity measurements by the line source method, it can be concluded that the strictly geometrical effects of finite length can be neglected.

g. Effect of Heat Leaks at End of Sample and Wire

The effect of finite-length heater wire in an infinite sample has already been investigated. By introducing boundaries at the ends of the sample where the temperature is held constant, additional errors may be introduced into the conductivity measurements.

If the radius of the heater is allowed to become infinitesimally small, Equation 12 reduces to

$$L\left\{\bar{T}\right\} = \frac{8}{\pi p} \sum_{m=0}^{\infty} \frac{(-1)^m}{(2m+1)} K_o(\theta_m^2 r) \tag{22}$$

at the point z=0. This may be compared with the value for the infinite

wire by noting that as ℓ becomes very long,(22) may be further simplified to

$$L\{\overline{T}\} = \frac{8}{\pi p} \sum_{m=0}^{\infty} \frac{(-1)^m}{(2m+1)} K_o(r\sqrt{p/\alpha_2}) \tag{23}$$

which is the Laplace transform of

$$\overline{T} = \frac{4}{\pi} \sum_{m=0}^{\infty} \frac{(-1)^m}{(2m+1)} \int_{1/\sqrt{t}}^{\infty} \frac{e^{-u}}{u} \, du \tag{24}$$

$$= -Ei(-1/t) \tag{24a}$$

This is, of course, the normal expression for the temperature due to the infinitely long source.

To investigate the temperature due to the finite wire and sample length, the Laplace transform must be left in the form of Equation 22. By making the substitution

$$p \equiv \eta - (2m+1)^2 \frac{\pi^2}{\ell^2} \alpha_2 \tag{25}$$

$$= \eta - C_m$$

in (22) it can be shown to result in the transform of the temperature distribution (for details see Appendix C).

$$\overline{T} = \frac{4}{\pi} \sum_{m=0}^{\infty} \frac{(-1)^m}{(2m+1)} \int_{1/\sqrt{t}}^{\infty} \frac{e^{-(\frac{C_m r^2}{4\alpha u} + u)}}{u} \, du \tag{26}$$

While (25) reduces to the expression for the infinite line source for small values of the time, as soon as the first term in the exponent becomes important, that is, when

$$(2m + 1)^2 \frac{\pi^2 \alpha t}{\ell^2} \rightarrow 1 \tag{27}$$

the temperature may depart significantly from that of the infinite line source. The magnitude of the error is difficult to estimate, but it will certainly be less than the absolute magnitude of the first term in which the error appears. By substituting for the dimensionless time and length in (27) and rearranging, we can see that the first term to be significantly affected will be of the order

$$m \approx \left(\frac{\lambda}{\pi \sqrt{\bar{t}}} - \frac{1}{2} \right) \tag{28}$$

That is, in a case where ℓ / r is 30 we can expect even the first term of the expansion to be affected by the time $\bar{t} = 100$. Since all the following terms in the alternating series will also be reduced, the exact extent of the error is difficult to estimate without more extensive analysis.

Having shown that heat leaks out the end of the sample may be expected to slightly influence the conductivity measurements, it is possible to compare this with the extent to which leaks out of the heater wire

influence the results. Assume a model in which the length of the wire is finite but where the conductivity and diffusivity of the wire are large compared to the corresponding properties of the sample. In this case it can be shown (Appendix C) that (12) is approximately:

$$L\{\bar{T}\} = \frac{\frac{8}{\pi p} K_o(r\sqrt{p/\alpha_2}) \sum_{m=0}^{\infty} \frac{(-1)^m}{(2m+1)}}{1 + \frac{k_1}{2k_2}\left[(2m+1)\frac{\pi a}{\ell}\right]^2 K_o\left[(2m+1)\frac{\pi a}{\ell}\right]} \tag{29}$$

Here most of the effects are time-independent, and the fractional error in the first term of the series will be of the order of

$$\frac{k_1}{2k_2}\left(\frac{\pi a}{\ell}\right)^2 \ln\left(\frac{\pi a}{\ell}\right) \tag{30}$$

When typical values are substituted in Equation 30, the error introduced will be of the order of 5%. In view of the approximate nature of the analysis, this will be considered in more detail.

h. Effects of Heat Leaks Out of the Thermocouple Wire

The effects of heat losses out of the thermocouple wire are considerably more difficult to evaluate than those from the heater wire, but it is to be expected that they will have the same general form. If the magnitude of the ratio given by (30), with the constants appropriate to the thermocouple wire, is not very much less than unity, the error whould not be negligible. Typical values of this parameter are of the order of 0.7 for some early experiments. This seems to indicate, then, that in many cases the effects may not have been insignificant. The most recent conductivity measurements have utilized thermocouple leads with the term (30) in the order of 0.06. These tests should be expected to yield more accurate conductivity measurements.

i. Effects of Contact Resistance

In the analysis presented above, it has been assumed that there was no resistance to heat flow at the interface between the heater wire and the powder or between the thermocouple wires and the powder. In most apparatus for thermal conductivity measurements, the contact resistance between the heat sources or isothermal surfaces and the samples is unknown. It is especially important when studying high-conductivity materials to minimize this resistance; accordingly, contacting agents are sometimes used, or static pressure may be applied to bring the sample into good contact with other surfaces. These methods are not applicable to the line heat source method.

In the present experiments, the diameter of the heater or thermocouple wires was at least as large as the average particle diameter, and in most experiments the wires were many times larger than the particles. Thus, the particles could contact the wire freely as well as contact each other. If

the particle size were much larger than the wire size, one could envisage packing arrangements in which the particles contacted each other, but not the heater or thermocouple. It is therefore assumed that the thermal resistance between the wires and the powder is of the same magnitude as the resistance of the powder itself, i.e., the resistance of the individual powder grains. For this case, specific corrections for contact resistance are not required.

j. Summary of Error Analysis

The above analysis has shown that for the types of experimental apparatus and sample materials used in this study, the three most probable sources of error in thermal conductivity measurements are: 1) the effects of sample boundaries, 2) heat losses in the thermocouple wires, and 3) heat losses in the heater wire. The first is normally not important unless sample size is very limited. The second and third types of errors can be reduced by making the heater and thermocouple wires of smallest possible diameter, of materials with lowest thermal conductivity, and making the leads as long as possible before contact with heat sinks.

In some of the experiments described in the following sections, the errors discussed above may have been significant. As a result, several series of tests were specifically designed to point out these errors and confirm the theoretical analysis. At the conclusion of these tests, a new line heat source thermal conductivity apparatus was designed, on the basis of experimental and analytical results, so that errors in measurement should be held to a minimum. By using these design concepts, it is estimated that measurement error can be reduced to about 10%, even for the small samples considered in this investigation.

C. EXPERIMENTAL PROGRAM

1. Experiments in High-Vacuum Chamber

During the initial part of the program (November 1962 to February 1963), preliminary experiments were conducted in the high-vacuum chamber at AFCRL. These tests were designed to give preliminary information on the effects of high vacuum on the thermal conductivity of powders and to indicate the potential use of the line heat source method. Because these experiments were exploratory in nature, and because the operating conditions and variables of the high-vacuum chamber had not been thoroughly studied at that time, a high degree of precision and accuracy of the test results was not expected. The tests did show interesting results, from the viewpoint of thermal conductivity of powders and adhesion of powders in vacuum, confirmed the usefulness of the line heat source apparatus, and indicated what specific problems must be solved in order to obtain more accurate and reliable data.

a. Apparatus

The line heat source apparatus used in the experiments at AFCRL is shown in Figure VIII-4. It consisted of a stainless steel base plate--2-3/4 inches long, 1-1/8 inches wide and 1/16-inch thick--and two mica end sheets to support the heater and thermocouple wires. The heater wire was 0.003-inch constantan, 2.60 inches long. A copper-constantan thermocouple, also 0.003-inch diameter, was placed parallel to and approximately 0.125 inch from the heater. Thermocouple wires were insulated with mica spacers and connected to a copper-constantan feedthrough in the chamber door. Copper

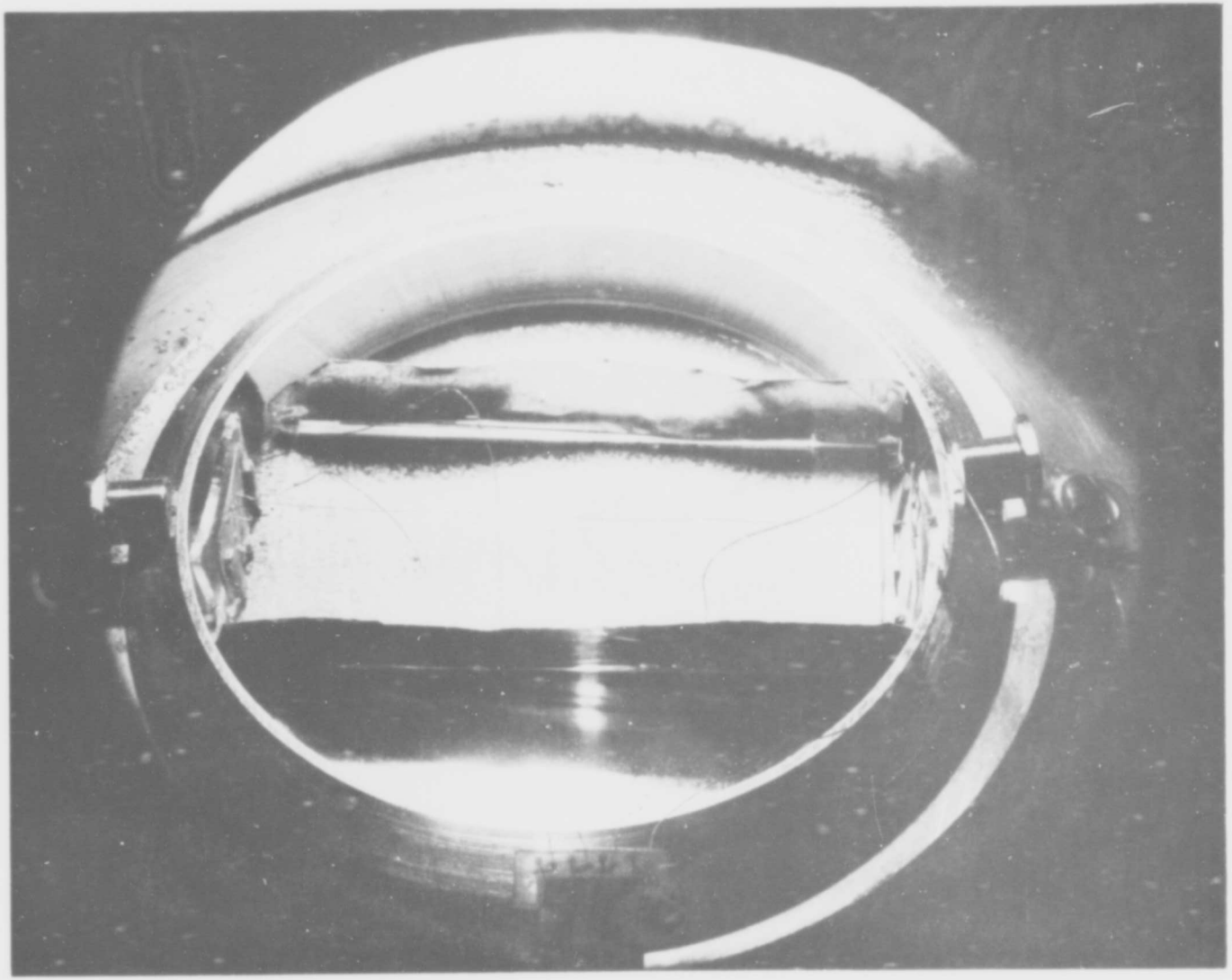

FIGURE VIII-4 EMPTY SAMPLE HOLDER INSIDE CHAMBER (Holder, which is about three inches in diameter, contains aluminum boat for thermal conductivity experiment; wires are to line heat source and thermocouple wire for this experiment)

lead wires were used with the heater. Figure VIII-5 shows a schematic diagram of the apparatus in the sample holder.

A thin aluminum foil holder was used to contain the powder. Powder was sifted onto the line heat source apparatus until the wires were covered by at least 1/4 inch of powder. When the desired sample temperature and chamber pressure were reached, line heat source tests were made. (Operation of the chamber, the sieve for depositing powder, and other aspects of these experiments relating to particle adhesion have been described earlier in this report.)

b. Instrumentation

Two 1-1/2 volt dry cells were used as the power supply for the line heat source apparatus. The voltage across the heater wire and the current flowing in the wire were measured with a precision voltmeter and ammeter, respectively. The output of the thermocouple was referred to a thermocouple junction in an ice bath, amplified with a Brown recorder amplifier, and displayed on an indicating potentiometer. Calibration of the system was made with a Rubicon precision potentiometer. The gain of the system was adjusted so that full scale on the recorder corresponded to approximately 100 microvolts or 2.5^{o}C. Chart speeds of 0.2 and 2.0 inches/minute were used. Test durations were between 50 and 120 minutes.

c. Materials

Tests were made using olivine, chondrite, tektite, and shocked basalt. The method of preparation of these materials has been described in Section III. Table VIII-2 shows the density and particle size distribution of the materials used in these tests. Density measurements were made in air.

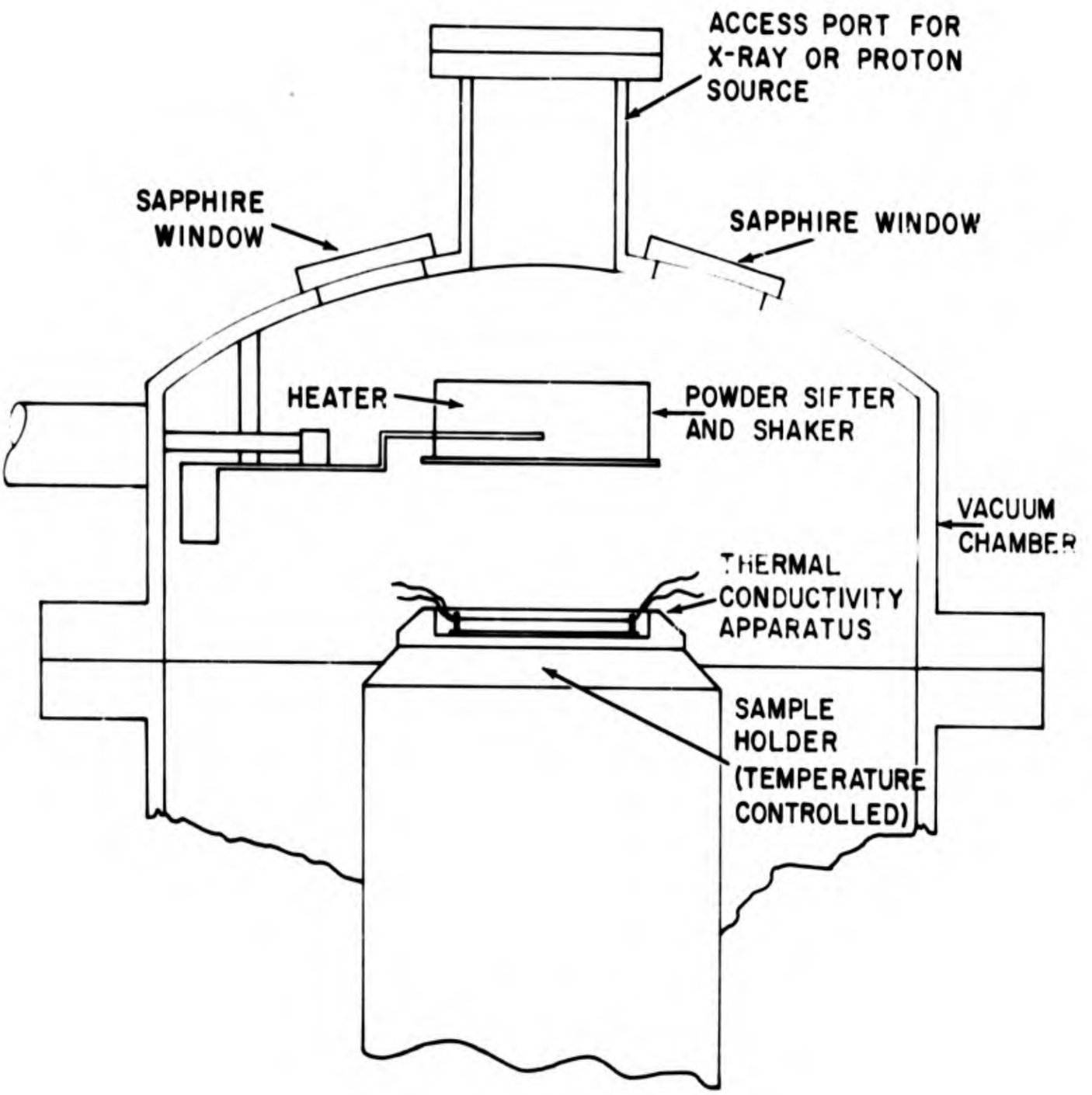

FIGURE VIII-5 SCHEMATIC DIAGRAM OF SAMPLE HOLDER AND THERMAL CONDUCTIVITY APPARATUS

TABLE VIII-2

DENSITY, PARTICLE SIZE, AND CHEMICAL COMPOSITION OF POSTULATED LUNAR SURFACE MATERIALS

Material	Density Solid (gm/cm^3)	Density[a] Packed Pwdr. (gm/cm^3)	Density[b] Loose Pwdr. (gm/cm^3)	Percentage Particle Size Distribution - size in microns[c]					
				0-3.5	3.5-17.4	17.4-35	35-700	700-1000	>1000
Olivine	3.30	1.54	1.06	95.5	4.4	< .1	< .1	< .1	< .1
Chondrite	3.31	1.21	0.83	90.2	7.0	2.1	< .1	< .1	< .1
Basalt (Shocked)	2.36	1.54	0.98	90.3	8.9	0.6	< .1	< .1	< .1
Tektite	2.31	1.07	0.69	95.6	3.7	< 1.0	< .1	< .1	< .1
Granodiorite	2.76	1.84	0.86	94.6	3.4	1.5	< .1	< .1	< .1

APPROXIMATE CHEMICAL ANALYSIS

	SiO_2	Al_2O_3	FeO	MgO	CaO	Na_2O	K_2O	H_2O
Olivine	40.1	1.0	10.3	46.1	--	--	--	2.4
Basalt[d]	49.0	15.7	12.3	7.2	9.0	3.1	1.5	1.6
Tektite[d]	76.4	12.6	--	--	--	3.4	4.7	1.0
Granodiorite	66.0	15.0	3.7	2.9	4.4	3.7	2.7	2.0

(a) Vibration-settled to obtain a packed powder
(b) Loose filling with no packing
(c) Measured by counting of approximately 3000 particles using 430 X magnification
(d) Average composition for this rock type

The table also shows the approximate chemical composition of the materials used.

d. Test Results and Discussion

Table VIII-3 shows the results of the preliminary thermal conductivity tests. The data were calculated by the curve-matching technique described in the preceding sub-section (B) on the theory of the line heat source method. (The results differ slightly from the values reported in previous progress reports due to different methods of calculation. The method used and the results reported here are considered more accurate than those used previously.) Examination of the data shows considerable self-consistency. No sizable effect on the thermal conductivity was found when the gas pressure was reduced from 10^{-5} to 10^{-10} torr for the materials studied under the experimental conditions of these tests. There was a slight apparent change of thermal conductivity with temperature, the thermal conductivity increasing with increasing temperature. Subsequent analysis of the operation of the high-vacuum chamber has shown that the powders were contaminated by vacuum pump oil. These initial results may, therefore, not indicate the true effects of hard vacuum on the thermal conductivity of powders.

During the experiments using chondrite, overheating of the sample probably occurred. This was evidenced by darkening of the powder in the vicinity of the heater wire. For this reason, the results of test 10 (Table VIII-3) are questionable. Following test 10, five other tests were made using chondrite; the results are not considered sufficiently valid for inclusion in this report. In test 13, the basalt powder formed on the thermal conductivity apparatus was light and fluffy. Tapping the sample

TABLE VIII-3

RESULTS OF THERMAL CONDUCTIVITY MEASUREMENTS IN HIGH-VACUUM CHAMBER

Test	Material	Initial Temperature (^{o}K)	Temperature after 40 min. of Test[a] (^{o}K)	Gas Pressure (torr)	Thermal Conductivity (cal/sec cm ^{o}K) x 10^{5}	Thermal parameter[b] $(k\rho C)^{-\frac{1}{2}}$ (cgs units)
1	Olivine	295	297	1×10^{-4}	1.7	460
2	"	296	299	4×10^{-5}	1.5	500
3	"	267	270	2×10^{-10}	1.4	510
4	"	290	293	5×10^{-10}	1.4	510
5	"	294	297	1×10^{-5}	1.4	510
6	Chondrite	292	295	5×10^{-5}	0.95	720
7	"	291	294	3×10^{-10}	1.0	700
8	"	413	436	2×10^{-8}	1.1	670
9	"	196	224	1×10^{-9}	0.81	780
10	"	413	416	8×10^{-9}	0.86	760
11	Tektite	273	281	1×10^{-9}	0.55	940
12	"	270	278	4×10^{-10}	0.53	960
13	Basalt	279	289	5×10^{-10}	0.43	950
14	"	307	314	5×10^{-10}	0.98	620

(a) Temperature measured by thermocouple 1/8 inch from line heat source

(b) Calculated using density of loose powders in air (see Table VIII-2) and specific heat of 0.21 cal/gm^{o}C.

holder compacted the powder and increased its thermal conductivity, as indicated by the results of test 14.

In Table VIII-3 we have also indicated values of the thermal inertia parameters $(k \rho C)^{-\frac{1}{2}}$; these data are based on density measured in air. Experiments are in progress to determine the density of powders which have been sieved in the high-vacuum chamber. The values of the thermal parameter are close to the value of 1000 normally chosen for lunar powders. The results of these tests are compared to those obtained by other methods later in this section.

The experiments showed that reproducible data could be obtained by the line heat source method. Several discrepancies between the experiments and simple line heat source theory indicated the need for more specific tests to determine the accuracy and precision of the test method. It was also apparent that the physical form and dimensions of the line heat source apparatus should be modified in subsequent tests. Amplifier stability, temperature stability, preparation of materials with reproducible densities, and reduction of heat leaks in the apparatus were other problem areas which were pointed out by the initial experiments.

2. Experiments Using Guarded Cold Plate Thermal Conductivity Apparatus

The thermal conductivities of several materials were measured in a guarded cold plate apparatus to check the results of the line heat source measurements. The apparatus and method for guarded cold plate measurements has been described by Black et al. (1959). In principle, the method relies on measurement of the steady-state, one-dimensional flow of heat through a sample contained between plates with known, but different, temperatures. In our experiments, an average or effective thermal conductivity

is measured, since the cold and hot plate temperatures differ by up to 275°C and corresponding temperature gradients exist in the samples. Table VIII-4 shows the test conditions and results for olivine, granodiorite, tektite, perlite, and colloidal silica.

Comparison of the results of the guarded cold plate method with those of the line heat source (see Table VIII-3) shows reasonable agreement for tektite samples. The guarded cold plate results are higher due to the larger thermal gradients and the higher sample density. There is an unexplainable difference in the thermal conductivity of olivine as measured by the two methods. Data presented later show that the preliminary data obtained in the high-vacuum chamber at AFCRL using the first line heat source may be in error. Comparison of granodiorite and perlite data by cold plate and line heat source methods will also be made later. The guarded cold plate method is estimated to be accurate to $\pm$15%.

TABLE VIII-4

RESULTS OF GUARDED COLD PLATE MEASUREMENTS

Material	Density (gm/cm^3)	Temperature Range (^oK)	Gas Pressure (torr)	Thermal Conductivity (cal/sec cm ^oK) x 10^5	Remarks
Olivine(1)	1.97	77-372	$2x10^{-4}$	0.28	Sample baked at 420°K, N_2 residual gas.
Olivine(2)	2.00	77-376	$2x10^{-4}$	0.38	Sample baked at 420°K, exposed to argon only.
Olivine(1)	2.02	77-372	$2x10^{-4}$	0.32	Sample not baked, exposed to argon only.
Tektite(1)	1.50	77-375	$5x10^{-5}$	0.90	Sample baked at 370°K, N_2 residual gas.
Tektite(1)	1.50	77-334	$5x10^{-5}$	0.81	Sample baked at 370°K, N_2 residual gas.
Tektite(1)	1.50	77-289	$5x10^{-5}$	0.94	Sample baked at 370°K, N_2 residual gas.
Granodiorite(1)	1.03	77-370	$5x10^{-5}$	0.72	Sample baked at 370°K, N_2 residual gas.
Perlite(3)	0.08	77-377	$5x10^{-6}$	0.55	Sample baked at 370°K, air residual gas.
Perlite(3)	0.08	232-383	$2x10^{-6}$	0.62	Sample baked at 370°K, air residual gas.
Colloidal Silica(4)	0.08	77-279	$4x10^{-4}$	0.48	Sample baked at 370°K, air residual gas.
Colloidal Silica(4)	0.08	77-376	$1.5x10^{-4}$	0.97	Sample baked at 370°K, air residual gas.

Note: (1) Particle size given in Table VIII-2.
(2) Contained slightly larger particles than other tests with olivine.
(3) Average particle size 300 to 350 microns.
(4) Average particle size 200 Å, but material tends to agglomerate.

3. Experiments Using the Line Heat Source Apparatus in the Pressure Range from 10^{-5} Torr to Atmospheric

Several series of tests using several line heat source apparatus were conducted to calibrate the line source apparatus, to establish operating characterics, and to investigate the thermal properties of postulated lunar surface materials.

a. First Line Heat Source Apparatus

Several tests were made with the first line heat source apparatus before it was placed in the high-vacuum chamber. The same instrumentation was also used, except during two tests in which a Sargent recorder was substituted. The vacuum system consisted of a "laboratory vacuum table" with a 5-cfm mechanical pump and a liquid nitrogen cold trap. The results of tests using olivine, granodiorite, and perlite are shown in Table VIII-5. The olivine and granodiorite sample had particle size distributions as shown in Table VIII-2. The expanded perlite was a commercially available material which had been sieved to a particle diameter range from about 300 to 350 microns. The thermal conductivity of olivine measured in these preliminary tests was apparently less than that indicated in the subsequent tests; since the density of the material could not be controlled, a considerable difference in the test results could be expected. Although perlite has a thermal conductivity apparently twice as large as that of olivine or granodiorite, its thermal inertia parameter is much greater because its density is so low.

TABLE VIII-5

PRELIMINARY RESULTS WITH LINE HEAT SOURCE

APPARATUS NO. 1

MATERIAL	INITIAL TEMPERATURE (^{o}K)	TEMPERATURE AFTER 40 MINUTES OF TEST (^{o}K)[a]	GAS PRESSURE (Torr)	THERMAL CONDUCTIVITY (cal/cm sec ^{o}K) x 10^{5}	THERMAL PARAMETER[b] $(k \rho c)^{-\frac{1}{2}}$ (cgs units)
Olivine	293	294	6×10^{-3}	0.76	700
Olivine	294	296	6×10^{-3}	0.67	740
Granodiorite	294	295	7×10^{-3}	0.60	880
Granodiorite	294	295	7×10^{-3}	0.72	800
Perlite[c]	293	294	1×10^{-2}	1.2	2080
Perlite	294	295	8×10^{-3}	1.2	2080

(a) Temperature measured by thermocouple 1/8" from line heat source

(b) Calculated using density given in Table VII-2 for loose powders in air and specific heat of 0.21 cal/gm ^{o}C

(c) Perlite density, measured in air, was 0.092 gm/cm^{3}.

Comparison of the data from the first line heat source apparatus with the guarded cold plate data shows good agreement for granodiorite; however, the thermal conductivity values for perlite and olivine were higher (by a factor of two) than the results reported in Table VIII-4. This could be caused by the higher gas pressure. In the initial line heat source tests a diffusion pump was not used, and the gas pressure within the powder may have been considerably higher than that indicated by the thermocouple gauge. Also, longer pumpdown times were used in the guarded cold plate apparatus than in the line heat source apparatus. As in previous tests, precise density control was not possible.

b. Second Line Heat Source Apparatus

A second line heat source apparatus, suitable for use in the high-vacuum chamber, was constructed. The apparatus is shown in Figure VIII-6. The stainless steel base plate, approximately 1/16 inch thick and 5 inches in diameter, was attached to a 3-inch diameter copper block; the latter could be inserted in the sample holder of the high vacuum chamber.

In the initial tests with this apparatus, a 0.002-inch diameter constantan thermocouple was used. The wires were spaced approximately 0.150 inch from the base plate and 0.120 inch from each other. The fine wires were approximately 2.75 inches long, and their ends were soldered to heavier wires approximately 0.010 inch in diameter. The latter were fastened to metal-glass feed-throughs which were fixed to the steel base plate. A plastic sample container was used to contain the powder. Tests were made with olivine powder, of particle size shown in Table VIII-2. Gas pressure was varied from about 10^{-4} torr to atmospheric, and several power levels were used.

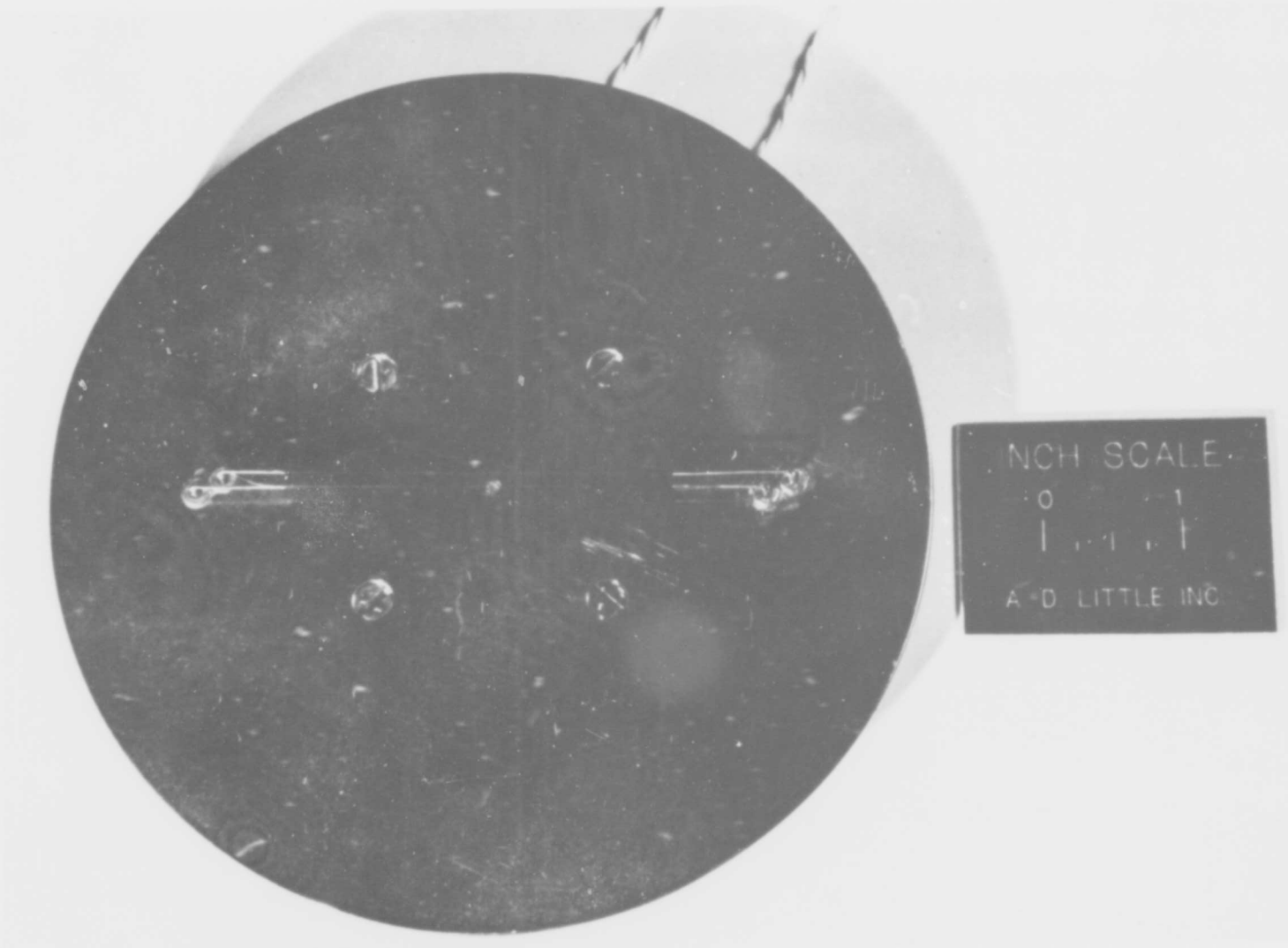

FIGURE VIII-6 SECOND LINE HEAT SOURCE APPARATUS

The instrumentation for these (and all subsequent tests described in this report) consisted of a Leeds and Northrup Type K-3 precision potentiometer, a L&N Type 9834 null meter, L&N Type 9835 amplifier, and a L&N Speedomax Type H recorder. In the R-series experiments described later, a Brown recorder was used. A thermoelectric reference junction, made by Joseph Kaye,Inc., was used with copper-constantan thermocouples; an ice bath reference junction was used with iron-constantan and chromel-alumel thermocouples, and in all tests in the R-series.

The test results are shown in Table VIII-6 and in Figure VIII-7. Reasonable agreement was obtained when two different samples were used with the same apparatus (tests 4 through 9 and 10 through 14). The effect of gas pressure on thermal conductivity can be observed in Figure VIII-7; this type of behavior is expected and is in agreement with theoretical analysis (Schotte, 1960; Wechsler, Glaser and Allen, 1963).

After test 14, the line heat source apparatus was changed to a constantan heater wire, 0.002-inch diameter, and an iron-constantan thermocouple (0.0007-inch iron and 0.0015-inch constantan). Wire lengths and system configuration were unchanged. Since the thermal conductivity of the iron is much less than that of copper, the heat leaks along the thermocouple wire were reduced. As a result, the measured values of thermal conductivity of the powder (tests 15 through 21) were lower, as indicated in the analysis of the errors of the line heat source method. Thus, the thermal conductivity of olivine at low gas pressures is probably close to one-half the value measured in the experiments using the copper-constantan thermocouple.

In the next test series (22 through 29) the thermal conductivity of 20-30 mesh perlite was measured as a function of pressure. The

TABLE VIII-6

RESULTS OF LINE HEAT SOURCE MEASUREMENTS OF THERMAL CONDUCTIVITY OF OLIVINE AND PERLITE

TEST*	INITIAL TEMPERATURE (^{o}K)	GAS PRESSURE (torr)	POWER/LENGTH (watt/cm) x 10^{3}	THERMAL CONDUCTIVITY (cal/cm sec ^{o}K) x 10^{5}
Olivine				
4	295	757	6.6	31
5	297	757	18.8	34
6	295	104	6.4	22
7	295	12	6.3	7.3
8	296	4×10^{-2}	6.4	0.88
9	296	5×10^{-3}	0.8	0.88
10	298	1×10^{-4}	2.7	0.91
12	294	3×10^{-4}	1.8	0.72
13	297	12	6.4	6.7
14	297	760	6.4	35
15	296	760	6.1	40
17	295	136	6.2	23
18	295	13	6.3	9.8
19	295	5×10^{-3}	6.3	0.45
20	298	5×10^{-3}	6.2	0.45
21	297	2×10^{-4}	6.3	0.41
Perlite				
22	297	760	6.3	12.4
23	297	120	6.3	12.2
24	297	13	6.3	7.9
25	297	1×10^{-2}	6.3	1.7
26	298	5×10^{-3}	0.8	1.4
27	298	5×10^{-3}	0.6	1.6
28	297	5×10^{-3}	2.4	1.2
29	297	4×10^{-5}	6.1	1.5

TABLE VIII-6 (Continued)

RESULTS OF LINE HEAT SOURCE MEASUREMENTS OF THERMAL CONDUCTIVITY OF OLIVINE AND PERLITE

TEST*	INITIAL TEMPERATURE (^{o}K)	GAS PRESSURE (torr)	POWER/LENGTH (watt/cm) x 10^{3}	THERMAL CONDUCTIVITY (cal/cm sec ^{o}K) x 10^{5}
Olivine				
30	289	6×10^{-2}	4.4	0.48
31	294	2×10^{-4}	4.5	0.38
32	299	120	4.5	6.9
33	296	760	4.5	35
Perlite				
34	295	2×10^{-5}	4.5	1.45
35	295	5×10^{-3}	4.5	1.45
36	297	9	4.5	11.0
37	296	116	4.5	11.2
38	295	766	4.5	11.2
Olivine				
39	297	1×10^{-3}	6.1	0.38
41	296	1×10^{-3}	9.7	0.48
42	301	1×10^{-3}	6.1	0.53
43	301	1×10^{-3}	4.5	0.74
44	295	1×10^{-3}	6.5	0.62
45	295	2×10^{-4}	6.5	0.62
46	295	5×10^{-5}	4.6	0.55
47	301	1×10^{-4}	4.6	0.48
48	302	1×10^{-4}	6.4	0.72
49	297	1×10^{-3}	4.5	0.55
50	301	1×10^{-3}	6.4	0.64

*Tests 11, 16, and 40 were not considered sufficiently valid for calculation of data.

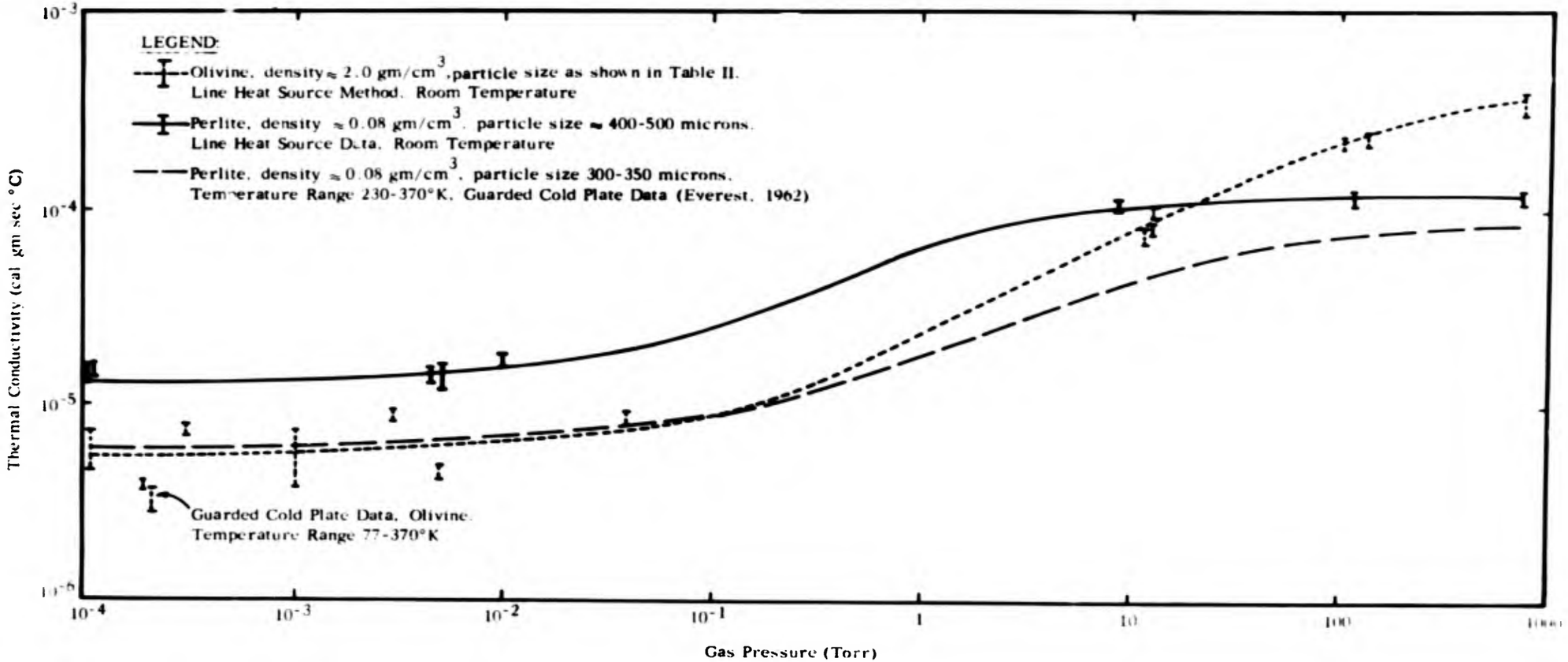

FIGURE VIII-7 EFFECT OF GAS PRESSURE ON THE THERMAL CONDUCTIVITY OF OLIVINE AND PERLITE

results, at low pressures, are about twice those obtained in the cold plate apparatus. This can be explained on the basis of the temperature level of the line heat source measurements and the fact that heat transfer in evacuated perlite occurs partly by thermal radiation. The results of these tests are also shown in Figure VIII-7.

To determine if further reduction in thermal conductivity values could be obtained by lengthening the thermocouple wires and correspondingly reducing the longitudinal heat flow, the line heat source was further modified to have an iron-constantan thermocouple and constantan heater 3.75 inches long, with no change in diameter. Also, the thermocouple was raised to approximately 0.75 inch from the stainless steel base to reduce any possible effects of sample boundaries. The sample size was also increased in volume so that the wires were immersed in powder at least 0.50 inch in any direction. The results of these tests (30 through 38) were essentially the same as those of tests 15 through 29, and indicated that the heat leaks in the existing apparatus were small.

Another series of measurements were made to determine the reproducibility of the test procedures. The line heat source apparatus for these tests (39 through 50) consisted of a copper-constantan thermocouple (0.0007-inch diameter constantan and 0.0016-inch diameter copper) and constantan heater, 0.002-inch diameter. The wires were 2.78 inches long and were mounted 0.190 inch from the base. The sample used in tests 39 through 41 was removed and replaced with another sample of the same material, and tests 42 o 45 were carried out. This second sample was removed, the material used in tests 39 to 41 was replaced

TABLE VIII-7

ADDITIONAL RESULTS OF LINE HEAT SOURCE MEASUREMENTS OF THERMAL CONDUCTIVITY OF EVACUATED POWDERS

TEST	INITIAL TEMPERATURE (^{o}K)	GAS PRESSURE (torr)	POWER/LENGTH (watts/cm x 10^{3})	THERMAL CONDUCTIVITY (cal/cm-sec-^{o}K) x 10^{5}	REMARKS
Quartz					
51	298	1.6×10^{-4}	1.4	1.77	Bright heater wire, fresh sample
52	300	1.8×10^{-5}	6.0	1.90	
53	299	4.4×10^{-4}	12.0	*	
54	295	760	12.0	*	
55	300	6.5×10^{-5}	13.0	0.93	Oxidized heater wire, fresh sample
56	296	1.8×10^{-4}	4.1	1.02	
57	300	3×10^{-3}	4.1	0.97	
58	297	6.0×10^{-4}	1.1	1.06	
Quartz					
59	296	5.5×10^{-4}	1.3	0.60	Bright heater wire, fresh sample
60	299	2×10^{-4}	0.15	0.74	
61	299	4×10^{-4}	17.1	0.94	
62	299	3×10^{-5}	1.0	0.91	Sample water-saturated, then evacuated
63	301	2×10^{-5}	4.4	1.11	
64	301	1.8×10^{-5}	1.2	1.07	
No. 660 Glass Beads, 50μ					
65	298	3.8×10^{-4}	0.14	0.82	Oxidized heater wire
66	299	1×10^{-5}	1.5	0.95	Bright heater wire
67	299	3.5×10^{-4}	3.6	*	Oxidized heater wire
68	297	3.2×10^{-4}	3.6	0.84	Bright heater wire
69	298	1.0×10^{-4}	10.4	0.94	Bright heater wire
70	297	1.0×10^{-4}	10.3	0.93	Oxidized heater wire

TABLE VIII-7 (Continued)

ADDITIONAL RESULTS OF LINE HEAT SOURCE MEASUREMENTS OF THERMAL CONDUCTIVITY OF EVACUATED POWDERS

TEST	INITIAL TEMPERATURE (^{o}K)	GAS PRESSURE (torr)	POWER/LENGTH (watts/cm x 10^{3})	THERMAL CONDUCTIVITY (cal/cm-sec-^{o}K) x 10^{5}	REMARKS
No. 660 Glass Beads, 50 u---continued					
71A	296	1×10^{-4}	0.85	1.14	Copper-Constantan
71B	296	1×10^{-4}	0.85	0.62	Iron-Constantan
72A	297	3×10^{-4}	3.6	1.09	Copper-Constantan
72B	297	3×10^{-4}	3.6	0.59	Iron-Constantan
73A	297	2×10^{-4}	9.7	1.06	Copper-Constantan
73B	297	2×10^{-4}	9.7	0.60	Iron-Constantan
74	298	5×10^{-4}	1.1	0.42	Small container
75	297	4×10^{-4}	4.5	0.50	Small container
76	299	6×10^{-4}	4.5	0.55	Medium container
77	296	3×10^{-4}	4.5	0.65	Large container
78	298	3×10^{-4}	1.7	0.57	Large container
79	298	2×10^{-4}	6.5	0.66	Large container

TABLE VIII-7 (Continued)

ADDITIONAL RESULTS OF LINE HEAT SOURCE MEASUREMENTS OF THERMAL CONDUCTIVITY OF EVACUATED POWDERS

TEST	INITIAL TEMPERATURE (^{o}K)	GAS PRESSURE (torr)	POWER/LENGTH (watts/cm x 10^{3})	THERMAL CONDUCTIVITY (cal/cm-sec-^{o}K) x 10^{5}	THERMOCOUPLE	HEATER LENGTH (cm)
No. 660 Glass Beads, 29μ						
80A	295	2×10^{-4}	9.5	0.84	Copper-Constantan	7.0
80B	295	2×10^{-4}	9.5	0.69	Iron-Constantan	7.0
81A	295	2×10^{-4}	9.4	0.69	Copper-Constantan	7.0
81B	295	2×10^{-4}	9.4	.56	Iron-Constantan	7.0
82A	295	9×10^{-5}	9.4	0.66	Copper-Constantan	7.0
82B	295	9×10^{-5}	9.4	0.60	Chromel-Alumel	7.0
83	295	3×10^{-4}	2.8	0.58	Iron-Constantan	17.8
84	295	1×10^{-4}	2.8	0.60	Iron-Constantan	17.8
No. 660 Glass Beads, 50μ						
84A	295	2×10^{-4}	2.8	0.41	Iron-Constantan	17.8
No. 660 Glass Beads, 200μ						
85	295	3×10^{-4}	2.8	0.64	Iron-Constantan	17.8
86	295	4×10^{-4}	2.8	0.63	Iron-Constantan	17.8
87	295	2×10^{-4}	4.6	0.61	Iron-Constantan	17.8
No. 660 Glass Beads, 50μ						
R-1	298	1×10^{-4}	0.18	0.57		6.9
R-2	298	1×10^{-4}	0.18	0.46		12.6
R-3	298	1×10^{-4}	0.17	0.37		22.7
R-4	299	1×10^{-4}	2.0	0.58		6.9

TABLE VIII-7 (Continued)

ADDITIONAL RESULTS OF LINE HEAT SOURCE MEASUREMENTS OF THERMAL CONDUCTIVITY OF EVACUATED POWDERS

TEST	INITIAL TEMPERATURE (^{o}K)	GAS PRESSURE (torr)	POWER/LENGTH (watts/cm x 10^{3})	THERMAL CONDUCTIVITY (cal/cm-sec-^{o}K) x 10^{5}	HEATER LENGTH (cm)
R-5	298	9×10^{-5}	1.9	0.49	12.6
R-6	298	1×10^{-4}	1.7	0.39	22.7
R-8	297	5×10^{-5}	5.2	0.47	6.9
R-9	297	5×10^{-5}	4.1	0.46	12.6
R-10	295	8×10^{-5}	4.5	0.39	22.7
R-11	295	8×10^{-5}	8.3	0.49	6.9
R-12	295	8×10^{-5}	7.8	0.50	12.6
R-7	297	5×10^{-5}	7.0	0.42	22.7
R-13	295	6×10^{-5}	1.9	0.58	6.9
R-14	296	6×10^{-5}	1.8	0.57	12.6
R-15	296	6×10^{-5}	1.7	0.49	22.7
R-16	296	8×10^{-5}	4.5	0.50	12.6
R-17	295	---	5.1	0.63	6.9
R-18	295	8×10^{-5}	4.4	0.50	22.7
R-19	296	8×10^{-5}	8.2	0.58	6.9
R-20	295	8×10^{-5}	7.6	0.47	12.6
R-21	295	8×10^{-5}	7.2	0.56	22.7

*Fit against standard curve judged too poor for reliable results.

(with a small addition of unused material to make up losses), and tests 46 through 49 were carried out.

Examination of the results shows considerable scatter. Most can be attributed to the variation in gas pressure (there is probably variation of pressure within the sample in addition to that measured by the pressure gauges) and to the changes in powder packing or density on removal and replacement on the line heat source.

Runs 51 to 54 and 55 to 58 were intended to provide information on the effects of variation of heater wire emissivity and thereby indicate the importance of radiation heat transfer. These tests, however, seem to be more indicative of the effects of vacuum-pump oil backstreaming and resultant sample contamination or of the difficulty in duplicating test samples. The tests were made on the same apparatus used previously with a quartz powder of particle size less than 44 microns. Runs 51 to 54 were made with bright wire of low emissivity and three days of pumping down (without a cold trap); the resulting conductivity was nearly double that measured in runs 55 to 58, which used an oxidized wire, a fresh sample, and a shorter pumpdown time. (See Table VIII-7 for test results and conditions.)

The next two test series, runs 59 to 61 and 62 to 64, were designed to provide further information on the effects of sample history. The same line heat source apparatus was used with the same type of quartz powder; the powder was carefully dried and then evacuated in the first series, and saturated with water vapor and then evacuated in the second. The powder which had been saturated with water vapor and then evacuated showed a slightly higher conductivity, 1.0×10^{-5} cal/cm sec ^{o}K, compared

with 0.75×10^{-5} cal/cm sec ^{o}K for the initially dry material. This indicates the effect of sample history on test results and demonstrates the slow outgassing rates for moisture absorbed or entrapped in powder materials.

c. Tests with Other Line Heat Source Apparatus

Runs 51 to 64 clearly demonstrate the effects of random "secondary parameter" variation on test results and the difficulty of duplicating exactly the experimental conditions from test to test. To overcome this problem, a new three-wire apparatus, shown in Figure VIII-8, was constructed. The use of three parallel, coplanar wires (spaced 0.10 inch apart) permitted 1) simultaneous monitoring of a test with two different, but similarly placed, thermocouples or 2) the running of successive tests with different heaters without disturbing the test cell and sample. (The latter would be done by placing a thermocouple between two heater wires.)

Several series of tests were carried out using glass beads to improve test reproducibility and to achieve more quantitative relationships between the major variables. Because the glass beads were more uniform in size and shape, they could be packed to uniform densities and had less inherent outgassing than samples of comminuted rock.

In runs 65 to 70 a copper-constantan thermocouple was mounted between heater wires of high and low emissivity. Alternate tests were made with the two heaters. The sample chamber was filled with dry nitrogen between runs to reduce the time required to establish equilibrium conditions. The results of the six runs show no discernible variation that could be attributed to differences in the emissivity of the two wires.

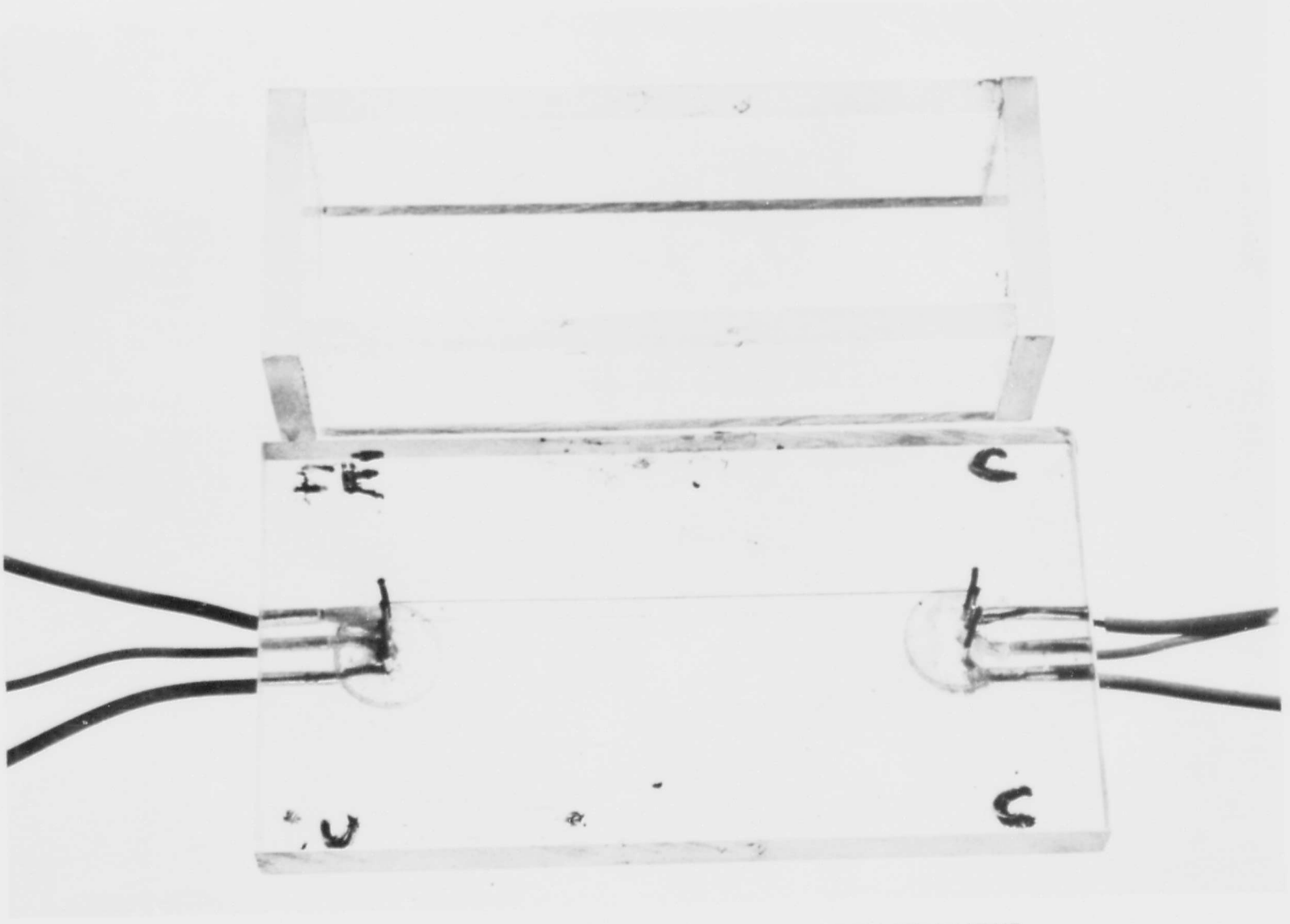

FIGURE VIII-8 THREE-WIRE LINE HEAT SOURCE APPARATUS

In runs 71 to 73 a central constantan heater wire (0.003 inch-diameter) was bounded bya 0.0007 -inch diameter iron-constantan thermocouple and a 0.0017-inch copper-0.0007 -inch constantan thermocouple. Power was applied to the heater wire, and the outputs of the two thermocouples were simultaneously recorded. The iron-constantan thermocouple indicated a sample conductivity about 50% lower than the copper-constantan thermocouple. This can be explained by the greater conductance, and consequently greater heat leak, of the copper wire in the thermocouple, and is the type of result anticipated from the analytical study.

The effect of container size was studied in runs 74 to 79 to confirm the analytical result that edge effects were unimportant for most sample sizes and experimental times. Three similar Plexiglas test cells of various sizes were constructed. From the test results we conclude that the slow outgassing rates of the larger containers led to abnormally high conductivities and masked any boundary effects. (The unimportance of boundary effects was later demonstrated in run 82.) An interesting result of this test series was the low conductivity values obtained from the smallest container. This container was of similar cross-sectional area but double the length of those previously used. The reduction in heat leak due to the longer wires probably led to the low conductivity value.

To further explore the effect of wire length on test results, runs R 1-12 and R 13-21 were performed. Three similar test cells with wire length of 6.9, 12.6, and 22.7 cm were constructed and tests run at various power/length ratios. Figure VIII-9 shows the test apparatus and instrumentation. Heater wires were 0.003-inch constantan. A 0.0017-inch

FIGURE VIII-9 APPARATUS AND INSTRUMENTATION FOR DETERMINATION OF THE EFFECTS OF HEATER WIRE AND THERMOCOUPLE LENGTH

copper-0.0007-inch constantan thermocouple was used in each apparatus. Results showed no appreciable variation with power level. A good correlation between wire length and measured conductivity could be observed. As was expected, the increase in lengths from 12.6 to 22.7 cm had a smaller effect on results than the increase from 6.9 to 12.6 cm. If a test had been run with a 45cm wire, it is doubtful that any significant further drop in observed conductivity would have occurred. The data also show that samples with larger particle size have a slightly larger thermal conductivity when measured in comparable apparatus.

Increasing wire length is one of several approaches to the problem of excessive heat leaks; other possibilities previously mentioned are the use of finer wires, wires of a lower thermal conductivity (as iron-constantan or chrome-constantan), or redesign of the wire supporting posts to increase their thermal resistance. In subsequent tests, all of these approaches have been employed.

Runs 80 to 82 were made with glass beads (29μ average diameter) and with the same apparatus and test procedure as used in runs 71 to 73. Results of run 80 are unusually high and may be attributed to incomplete outgassing of the sample. Consider the results of runs 81, 82, and 73 as tabulated below:

RUN	HEATER	THERMOCOUPLE	SAMPLE CONDUCTIVITY
81	0.0031" constantan	0.001" copper-constantan	0.69×10^{-5} cal/cm-sec-^{o}K
		0.0007" iron-constantan	0.56×10^{-5} "
82	0.0031" constantan	0.001" copper-constantan	0.66×10^{-5} "
		0.001" chrome-alumel	0.60×10^{-5} "
73	0.0031" constantan	0.0017"copper-0.0007" constantan	1.06×10^{-5} "
		0.0007" iron-constantan	0.60×10^{-5} "

The reduction in conductivity, as measured with the copper-constantan thermocouple, between run 73 and run 81 or 82 is attributed to the two-thirds reduction in area of the copper leg of the thermocouple. When the 0.0007-inch iron-constantan thermocouple was replaced with a 0.001-inch chromel-alumel thermocouple, a slight increase in measured conductivity was observed. In run 82 a third thermocouple (0.0007-inch iron-constantan) was placed 1/16 inch from the Plexiglas wall of the test cell, in the plane of the heater wire and indicating thermocouple. The output of the third thermocouple was monitored during the test but showed no detectable temperature change during the run (75 minutes). This indicated that the temperature field created by the heater wire was very small near the sample boundaries and suggests the absence of container wall effects on the measurements.

A new test apparatus was constructed for the remaining tests of this phase of the program, runs 83 to 87. Wire length was increased to 17.8 cm, heater wire diameter was reduced from 0.003 to 0.001 inch, and a low-conductivity support post was employed. In addition, precautions were taken to reduce heat leaks out of the external lead wires. Tests results showed low conductivities and were very reproducible. The experimental data conform with great accuracy to the theoretical line heat source "type curves", thereby indicating a close approach to minimum error and optimum design.

4. Future Experiments in High-Vacuum Chamber

Based upon the results of tests made in the pressure range between 10^{-5} torr and atmospheric, we have designed and constructed another line heat source apparatus for use in the high-vacuum chamber

at AFCRL. The apparatus is shown in Figure VIII-10 and consists of a stainless steel base plate, a constantan heater wire of 0.001-inch diameter, and a copper-constantan thermocouple of 0.001-inch diameter with a spacing of approximately 0.080 inch. The length of the wires is substantially greater than in the apparatus previously used in the high-vacuum chamber and is supported by glass rods which are designed to have low heat losses. Ideally, the thermocouple should be iron-constantan to further reduce heat leaks and to obtain greater accuracy; however, since the available feed-throughs in the high-vacuum chamber were copper-constantan, we will reserve the iron-constantan system for subsequent experiments after the chamber feed-throughs have been modified. When iron-constantan thermocouples are used, this apparatus should give results which are accurate to within 10%. Future tests in the high-vacuum chamber should be combined with density measurements so that densities can be measured simultaneously with thermal conductivity.

D. SUMMARY

In this sub-section, literature survey, analytical study, and experimental measurements are summarized to indicate the results obtained and the direction of future efforts in studying the thermal properties of postulated lunar surface materials.

1. Literature Review

There is considerable data on the thermal properties of powder materials in the pressure range from 10^{-5} torr to atmospheric. These data indicate that solid conduction and thermal radiation are the

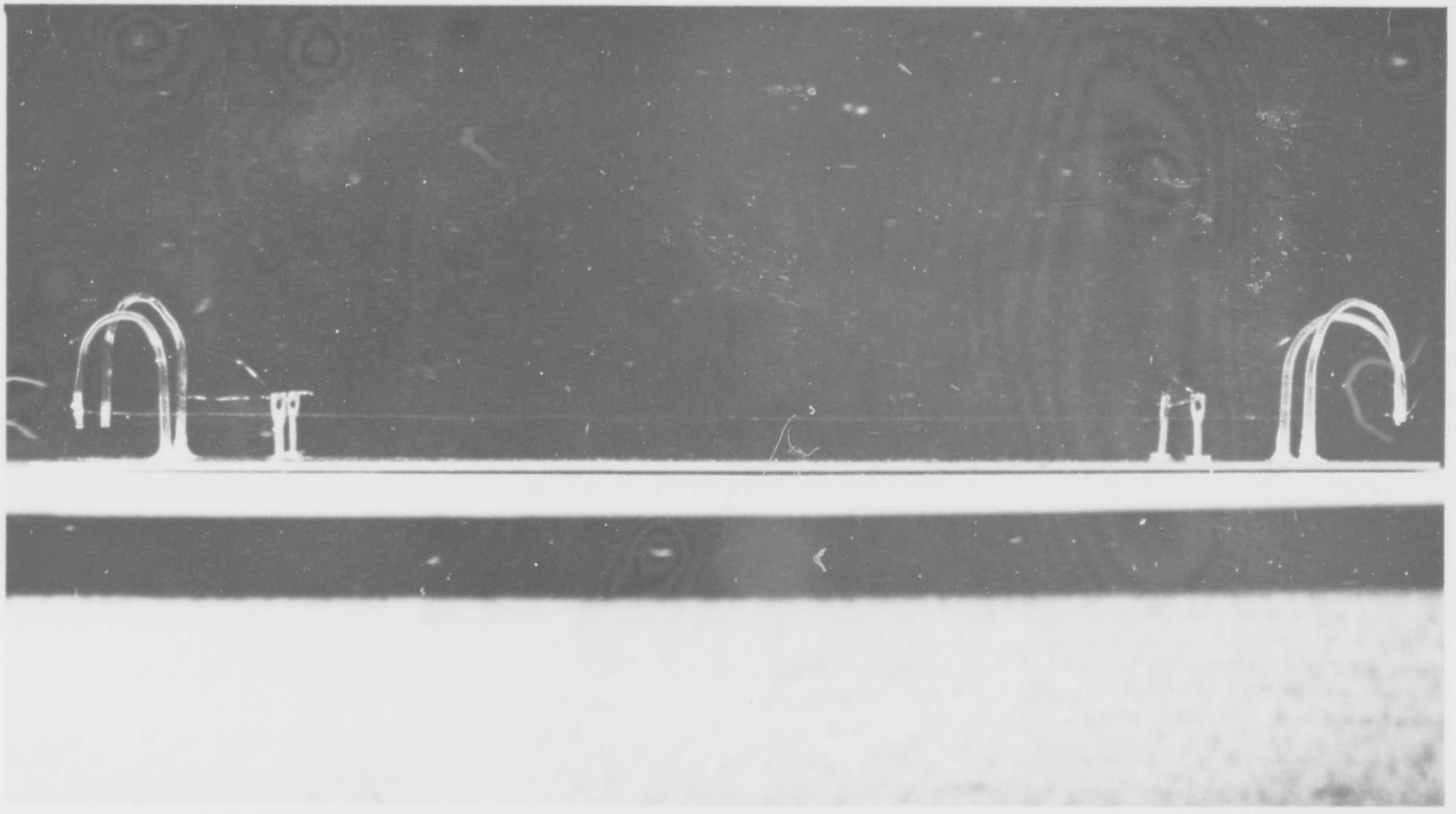

FIGURE VIII-10 LINE HEAT SOURCE APPARATUS WITH GLASS SUPPORTS AND LOW HEAT LEAKS

BLANK PAGE

principal mechanisms of heat transfer in evacuated powders. Few measurements of postulated lunar surface materials have been made.

Limited available data indicate that very low thermal conductivities and high values of thermal inertia are consistent with the properties of evacuated powders with particle sizes between 0.1 and 200 microns. No data have been reported on the effects of ultra high vacuum (less than 10^{-9} torr), solar radiation, or reduced gravity on the thermal properties of evacuated powders.

2. The Line Heat Source Method

A detailed analytical investigation of the line heat source method for measurement of thermal conductivity of powder materials has shown that this technique is very desirable for measuring the thermal conductivity of postulated lunar materials in a simulated lunar environment. When small samples of low thermal conductivity materials are studied the principal errors in the method are heat leaks in the heater and thermocouple wires and the effects of sample boundaries. The analysis has shown that these errors can be reduced by careful design of the line heat source apparatus and that the line heat source method should give results which are accurate to approximately $\pm$ 10%. A simple method of reducing the experimental data to yield thermal conductivity values has been established.

3. Experimental Measurements

a. Initial experiments using the line heat source apparatus in the high-vacuum chamber at pressures in the order of 10^{-9} torr with powdered basalt, olivine, tektite, and chondrite resulted in thermal conductivity values ranging from about 0.5-to-1.7 x 10^{-5} cal/cm-sec-^{o}K

and thermal inertia parameters ranging from about 450 to 1000 (cgs units). Due to the relatively large diameter of the heater and thermocouple wires and their short length, these thermal conductivity values are probably high by a factor of two, and the corresponding values of thermal inertia must be low by about 1.4. Analysis of the vacuum system parameters has shown that the samples used in these tests were contaminated with vacuum pump oil and that the thermal conductivity values may not be representative for powders at very low gas pressures.

b. Measurements of the effective thermal conductivity of olivine, tektite, granodiorite, expanded perlite, and colloidal silica in a guarded cold plate apparatus in the order of 10^{-5} torr gave thermal conductivity values ranging from 0.3-to-1.0 x 10^{-5} cal/cm sec ^{o}K. These values are probably accurate to about $\pm$ 10% for the materials under the conditions actually studied. Thermal inertias of these materials range from about 600 to 900, except for perlite and colloidal silica, which have inertias in the order of 3000 because of their very low density.

c. A systematic study of the "apparatus variables" associated with the line heat source technique has confirmed the type and magnitude of errors anticipated from the analytical study. Improved line heat source apparatus have been designed, constructed, and tested, and should give results which are accurate to approximately $\pm$10%.

d. Experimental measurements have shown that "environmental variables" such as sample history, pumpdown time, interstitial gas pressure, and sample packing have very important effects on the measured values of thermal conductivity. Better control and/or know-

ledge of these parameters must be established before the effects of high vacuum on the thermal conductivity of powders can be accurately assessed.

e. Material type and particle size seem to have little effect on thermal conductivity of powders measured in pressures near 10^{-5} torr. The true effects of these variables may have been masked by the gas contamination of surfaces.

4. Future Work

Experiments are now in progress using improved line heat source apparatus in the high-vacuum chamber. These measurements will be combined with density measurements so that accurate values of thermal inertia can also be obtained. Sample cleanliness and environmental conditions must be considered in evaluation of the experimental results. If powwible, thermal conductivity measurements should also be combined with spectroscopic studies to obtain maximum benefit from the tests.

In addition to continued line heat source measurements, other methods of assessing the effects of hard vacuum on thermal properties should be examined. Thermal comparator measurements, for example, may be able to define more clearly the effects of high vacuum on absorbed gases and contact areas between particles.

BLANK PAGE

SECTION IX

INFRARED SPECTRAL EMISSION CHARACTERISTICS OF PROBABLE LUNAR MATERIALS

The infrared spectral emission of probable lunar materials was measured to determine the amount of spectral information which can be expected from particles of rocks and minerals whose size range approximates the best estimates of the size of the particles composing the uppermost layers of the lunar surface. Representative samples of the entire series of igneous rocks as well as a tektite and chondritic meteorite were investigated in the wavelength range of 7-14 microns; a region in which a number of absorption and reflection bands are known to occur in silicates. The materials were pulverized and separated as described in Section III; the finest fraction was retained for use.

The spectra were obtained with a Perkin Elmer Model 221 spectrophotometer equipped with a sodium chloride prism. Auxiliary foreoptics were made to direct the energy from the sample and blackbody reference ovens to the spectrophotometer slits (Fig. IX-1). The sample was heated by means of an oven (Fig. IX-2). In addition to the oven as shown, a copper plate with a 3-mm wide slit was attached to facilitate heat conduction to the radiating part of the powder. The emitting surfaces of the sample powders were always slightly higher than this slit so that the "cavity effect" would not minimize any spectral information present.

The blackbody reference oven was made by lining the bottom and sides of the oven with graphite; a cover with a 3-mm slit was also attached to this oven.

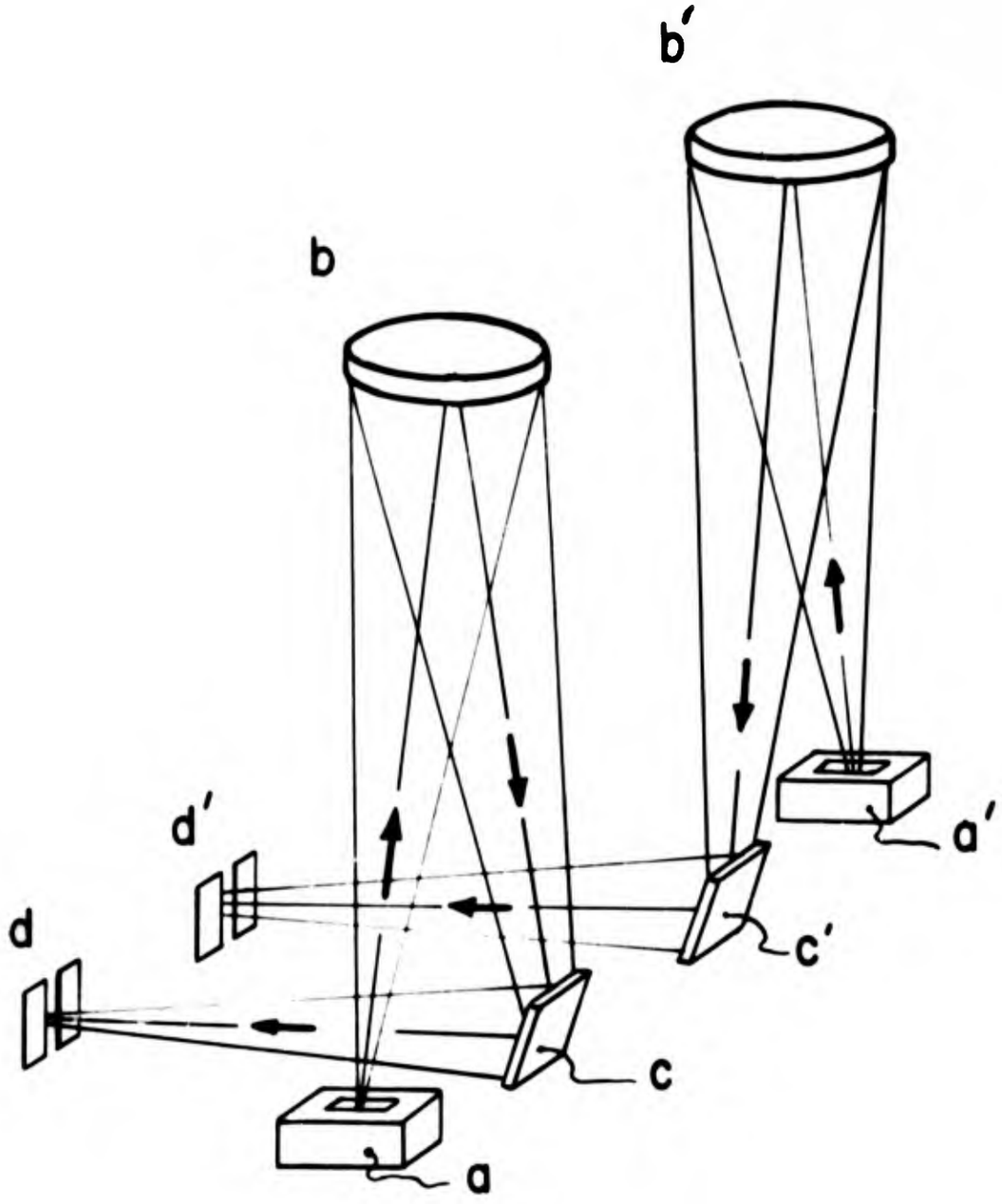

a - Sample Oven
a' - Reference Black Body Oven
b, b' - Spherical Mirrors
c, c' - 45° Flat Mirrors
d, d' - Entrance Slits of Double-Beam Spectrometer

FIGURE IX-1 SCHEMATIC DIAGRAM OF OPTICAL PATH FOR EMISSIVITY MEASUREMENTS

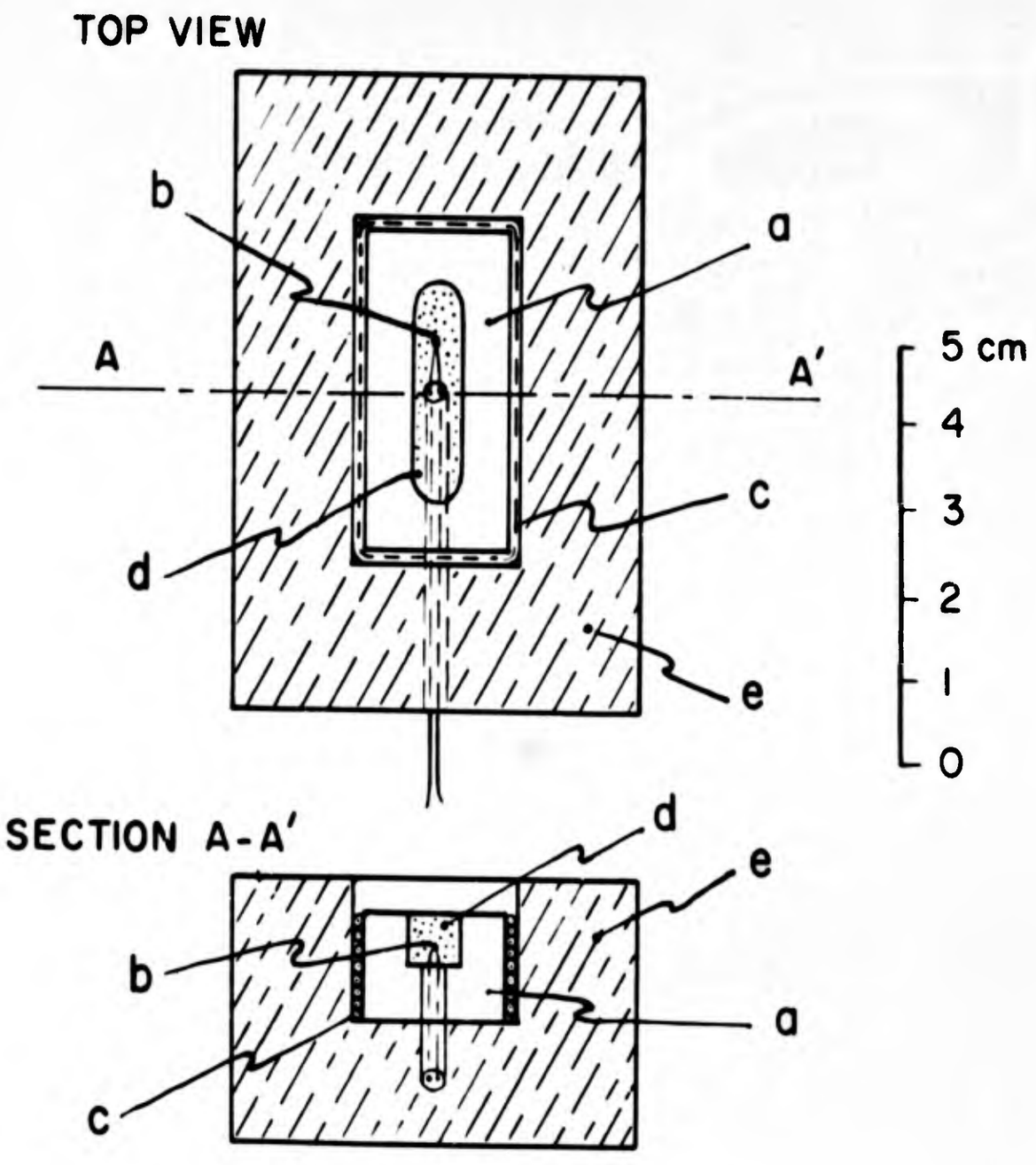

a - Copper Cavity Block
b - Thermocouple Junction
c - Heater Wire
d - Powder Material
e - Insulating Fire Brick

FIGURE IX-2 INFRARED EMISSION OVEN

The temperature of the ovens was maintained at 250°C by connecting a variable transformer to the heating wire within the oven. The temperature of the reference was measured by an iron-constantan thermocouple located within the copper block. The temperature of the sample was measured by a thermocouple placed in the center of the powder. The temperature, as measured by the thermocouples, was always 250 ± 1°C, however, the temperature of the radiating surfaces certainly was not maintained that critically because of drafts, etc. Figure IX-3 shows the Perkin Elmer 221 spectrophotometer, sample oven, variable transformers, and potentiometers, as used.

The effect of temperature on the response of the spectrometer was determined by putting an oven identical to the reference oven in the sample position and varying its temperature. Figure IX-4 shows the apparent emissivity as a function of wavelength for three different temperatures: 228°C, 250°C, amd 280°C. For small departures from 250°C an uncertainty of 1°C in the temperature gives an uncertainty of 0.01 in the apparent emissivity. Because of noise and drift in the spectrometer and drafts which cooled the surface powder, the apparent emissivity was reproducible only to within about 0.03.

Since the emissivity of the oxidized copper reference was not known and possibly deviated from a blackbody spectral distribution, and because the temperature of the surface was difficult to define and determine, the emissivities obtained are reported as apparent emissivities. Originally the loose sample powders were used, so as to reproduce the conditions presumed to exist on the lunar surface. In this condition the temperature of the surface layer was very poorly defined and extremely difficult

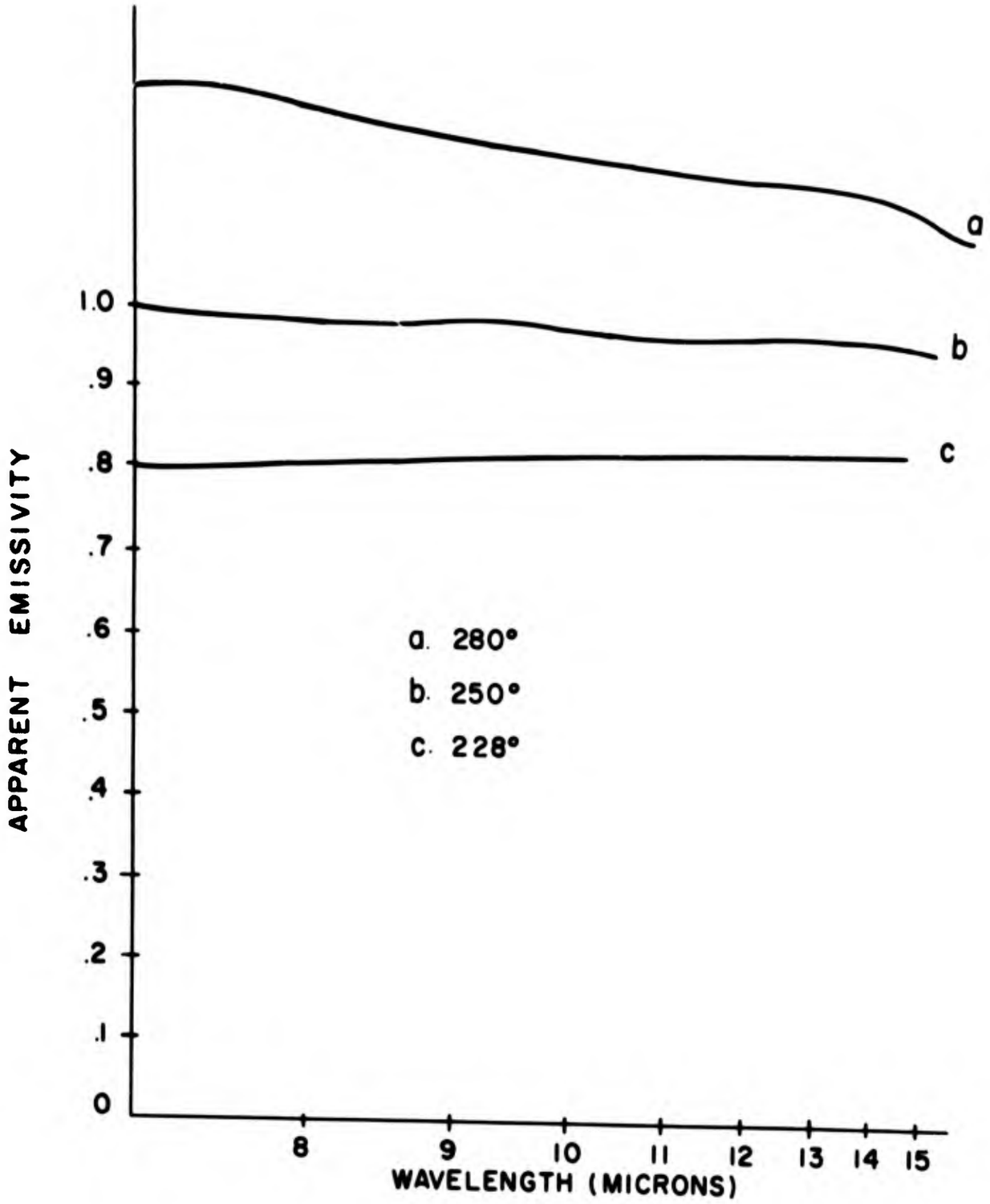

FIGURE IX-4 APPARENT EMISSIVITY OF BLACK BODY AT DIFFERENT TEMPERATURES

to control, resulting in spectra which were not acceptably reproducible. Therefore, the powders were tamped down by hand to increase the effective thermal conductivity. Data obtained in this manner with powdered andesite, augite, basalt, chondrite, granodiorite, and obsidian are shown in Figure IX-5. These results show that the infrared spectra of mineral powders of very small particle size contain very little spectral information over the region investigated.

Even for materials with strong absorption bands, the amount of observable spectral information available in emission is dependent on the particle size. This is illustrated by the data obtained with quartz powders as shown in Figure IX-6. The curve obtained with "sand" of 75-micron average particle size shows clearly the 8.6, 9.4 and 12.5 micron vibration bands of quartz. In the other curve, obtained with quartz "flour" of 1.2-micron average particle size, the bands are barely discernable. Similar effects were observed with olivine powders.

X-ray diffraction studies of the quartz showed that the material was all in the crystalline state; no amorphous material was present.

The results of this experimental investigation are significant, inasmuch as they show that the band structure, which is apparent in both the emission spectrum of a polished plate or even solid rock (Burns and Lyon, 1964) is effectively obliterated in the emission spectra of fine powders. The results are especially obliterated in the emission spectra of fine powders. The results are especially applicable to the lunar surface, because the samples used include a wide range of probable lunar materials, and because they were ground to a particle size comparable

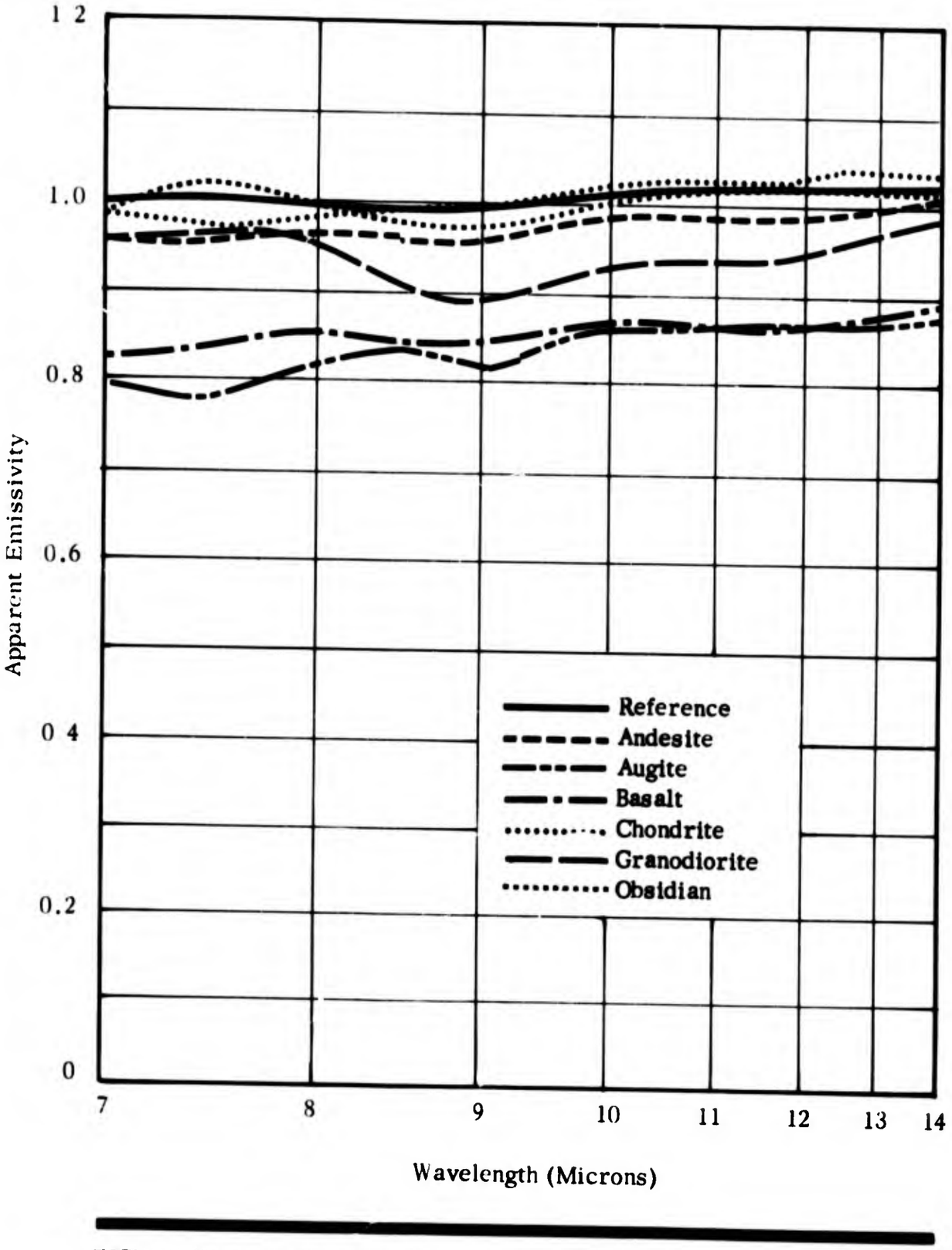

FIGURE IX-5 APPARENT SPECTRAL EMISSIVITY OF SIX POWDERED MINERALS AT 250°C

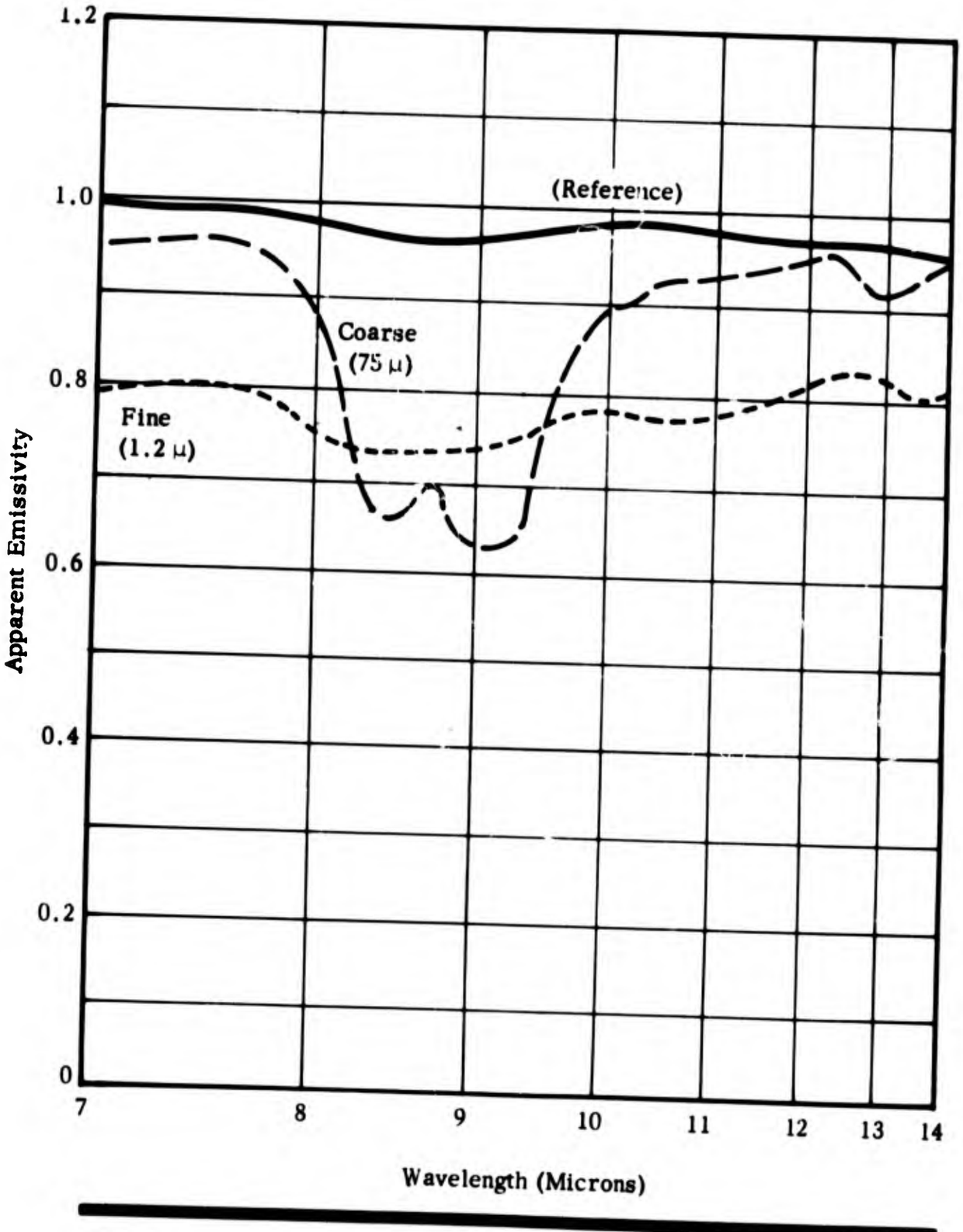

FIGURE IX-6 APPARENT SPECTRAL EMISSIVITY OF COARSE AND FINE QUARTZ POWDERS

with our best estimates of the size distribution of the lunar surface material. If this particle size range is correct, compositional mapping of the lunar surface by spectral analysis of the thermal emission is not feasible. However, if the average particle size is larger, this study shows that this method of analysis, first proposed by Burns and Lyon, would certainly be feasible, provided the lunar surface contains materials that, in bulk form, would have distinctly recognizable spectral band patterns.*

*After the work reported here was done (Van Tassel and Simon, 1963), Drs. Hunt and Salisbury of AFCRL obtained spectral information from the moon in the spectral region investigated here, as well as in the 16- to 24-micron region. This evidence indicates that at least some areas on the moon contain large enough particles to yield thermally-emitted spectral information.

APPENDIX A

THE LUNAR ENVIRONMENT

I. INTRODUCTION

Although our knowledge of the lunar environment is clearly speculative in many respects, it is possible to arrive at a reasonable model of this environment through assembly of all available evidence and judicious use of theory. Such a model, which is described below, has been used in our simulation experiments. This model is a working hypothesis, and should be treated as such.

II. ATMOSPHERE

The lunar atmosphere has long been known to be extremely tenuous because surface shadows on the moon are very black and sharply delineated, and because there are neither clouds nor sunset effects as on Earth. Just how tenuous the atmosphere is has, however, been debatable. Recently, Dollfus (1952) found from polarimetric observations at Pic du Midi that the surface density of the lunar atmosphere is less than 10^{-9} terrestrial atmospheres. From occultations of radio stars by the moon, Ellsmore and Whitfield (1955) and Costain, et al (1955) have estimated that the lunar atmosphere must be less than 10^{-13} terrestrial atmospheres. Opik and Singer (196) have postulated that the lunar atmosphere may have a pressure of essentially zero because of the repulsion of ionized gas molecules by the positively-charged lunar surface. It is generally conceded, however, that the minimum density of the lunar atmosphere must be at least the density of the interplanetary medium (Brandt, 1960). In the absence of experimental verification of a lower pressure, the pressure of the lunar atmosphere is here assumed to be 10^{-13} terrestrial atmospheres. It is of interest to note that, as this pressure would correspond to a terrestrial altitude of greater than 1,000,000 ft at the lunar surface, and as terrestrial meteors begin to vaporize at a maximum altitude of about 500,000 ft (Mitra, 1952, p. 82), the lunar atmosphere cannot be expected to shield the surface from the impact of meteorites. It also will not appreciably attenuate cosmic and solar radiation.

The composition of the lunar atmosphere is an unsolved problem. Some radiogenic krypton, xenon, argon, radon, and helium should be continually released from the interior, while trace amounts of xenon, helium, neon, and argon will be produced by cosmic-ray bombardment of the surface (Kopal, 1959). In addition, occluded gases will be liberated upon the impact and vaporization of meteorites, and some water vapor will be released, either from the interior or during the slow vaporization of possible relict solid phases present in perpetually shadowed zones (Green, 1960, p. 165; Watson, et al, 1961, p. 1600). The rapid escape of all these gases from the moon is assured by the low lunar escape velocity and by the repulsion of the ionized gases from the positively charged moon. The composition of this transient lunar atmosphere will depend largely upon the production rate of the various gases by the different processes outlined above ( ). No doubt the composition is complex, and may even be changing. The major constituents are probably water, carbon dioxide and hydrogen; the electron density of the lunar ionosphere is probably between 200 and 350 cm^{-3} (Opik and Singer, 1960; Weil and Barasch, 1963).

BLANK PAGE

III. THERMAL ENVIRONMENT

Because the moon has essentially no atmosphere, which would shield its surface and prevent rapid radiation of its heat, the differences between the temperatures on the dark and the illuminated hemispheres are very great.

The maximum surface temperature recorded is about 130°C and the minimum is known to be less than -168°C (Murray and Wildey, 1963). Figures A-1 through A-9 illustrate the distribution of temperatures over the lunar surface at different phases (Geoffrion, et al, 1960). The small circles in the upper right-hand corner of each figure indicate the maximum error in positioning the isothermal contours. The subsolar point is marked with a small cross, and cooler regions within an isotherm are marked by shading. Warmer regions are not shaded. More detailed thermal contour maps of the rayed craters, which show anomalous cooling behavior, have been obtained by Saari and Shorthill (1963).

Radio waves penetrate the surface of the moon, so that radio measurements of lunar temperature reveal the temperature some distance below the surface. Measurements of the steady-state subsurface temperature by Mezger and Strassl (1959) show an effective black body temperature of -23°C, while Medd and Broten (1961) find an equilibrium temperature of -53°C. Shorter wavelength measurements of temperatures at presumably shallower depths reveal generally higher temperatures which change with the phase of the moon.

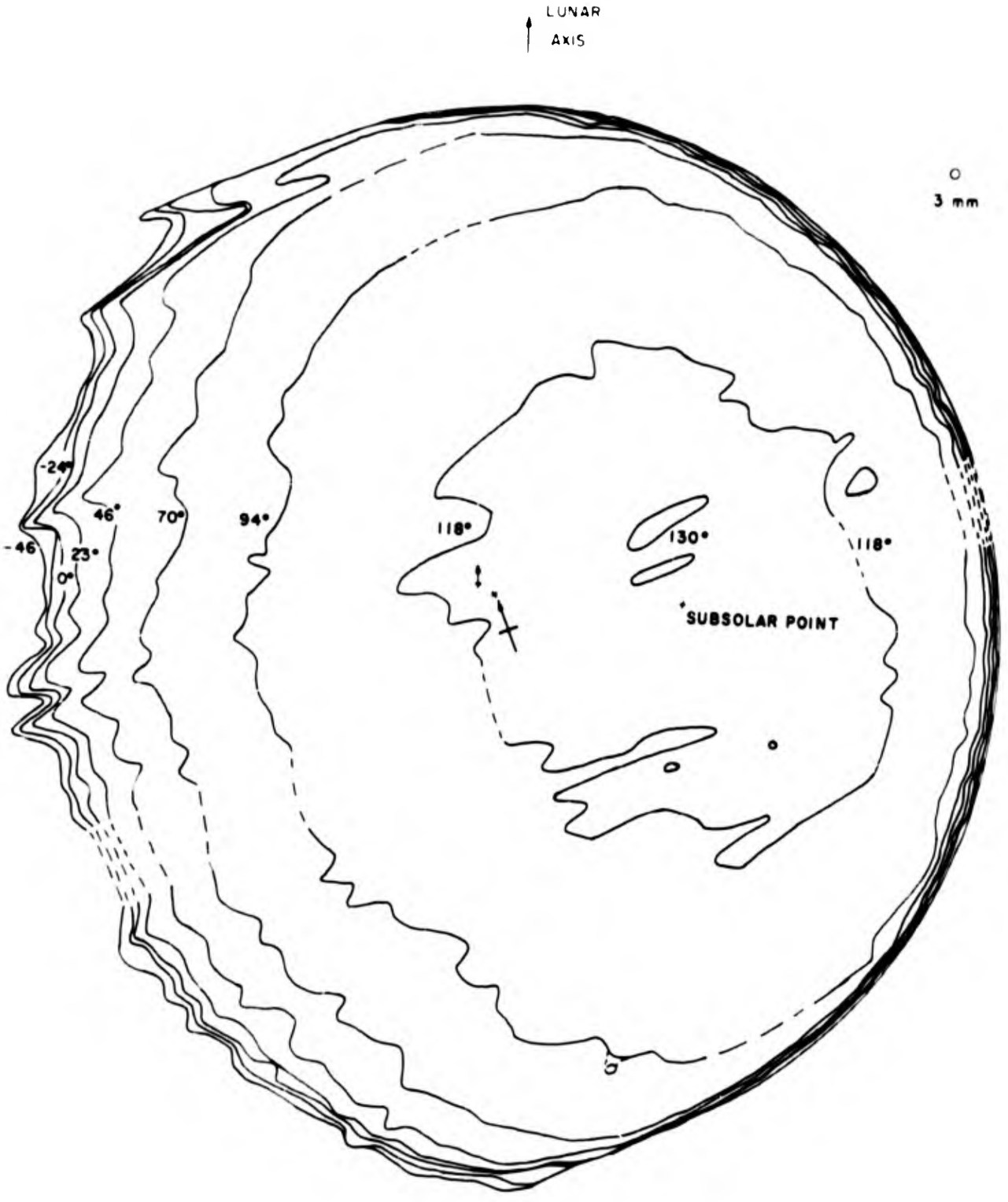

FIGURE A-1 DISTRIBUTION OF LUNAR TEMPERATURES IN ^{o}C. MOON OF SEPTEMBER 26, 1958, BEGUN 3:55, ENDED 7:01 UT, 63 SCANS, 0.98 ILLUMINATED.

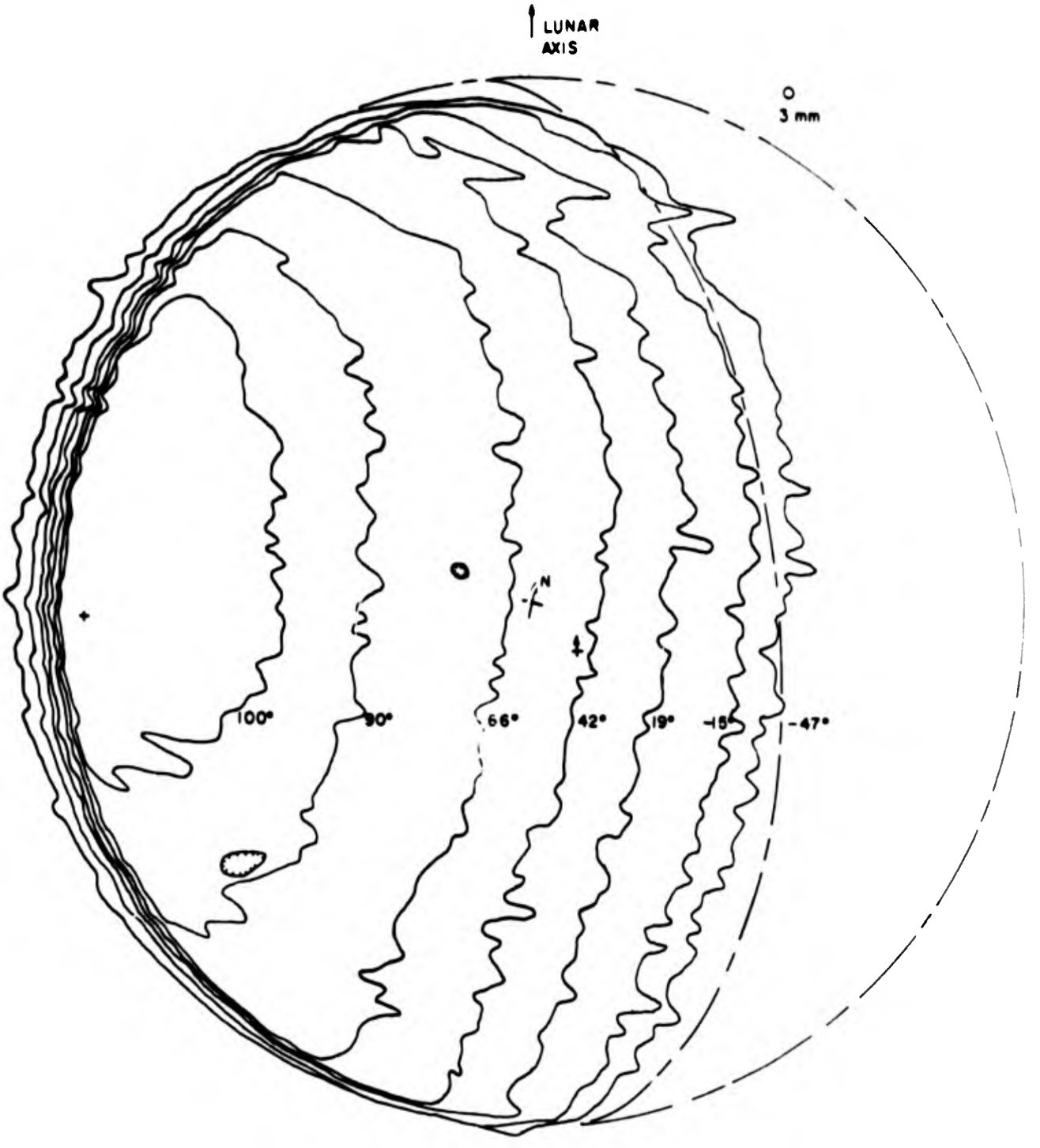

FIGURE A-2 DISTRIBUTION OF LUNAR TEMPERATURES IN ^{o}C. MOON OF DECEMBER 1, 1958, BEGUN 8:42, ENDED 13:00 UT, 86 SCANS, 0.77 ILLUMINATED.

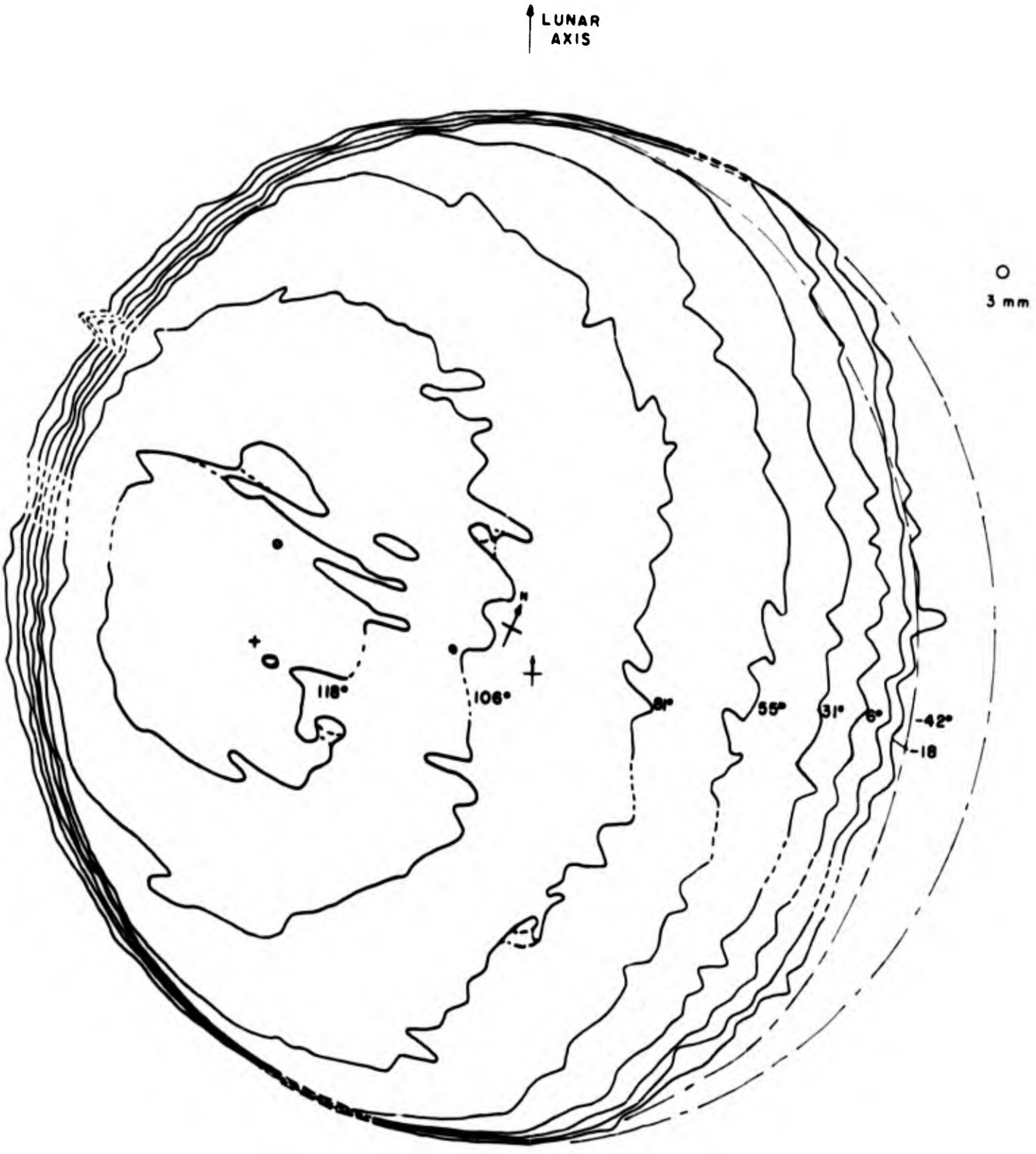

FIGURE A-3 DISTRIBUTION OF LUNAR TEMPERATURE IN ^{o}C. MOON OF JANUARY 27, 1959, BEGUN 7:42, ENDED 10:39 UT, 60 SCANS, 0.92 ILLUMINATED.

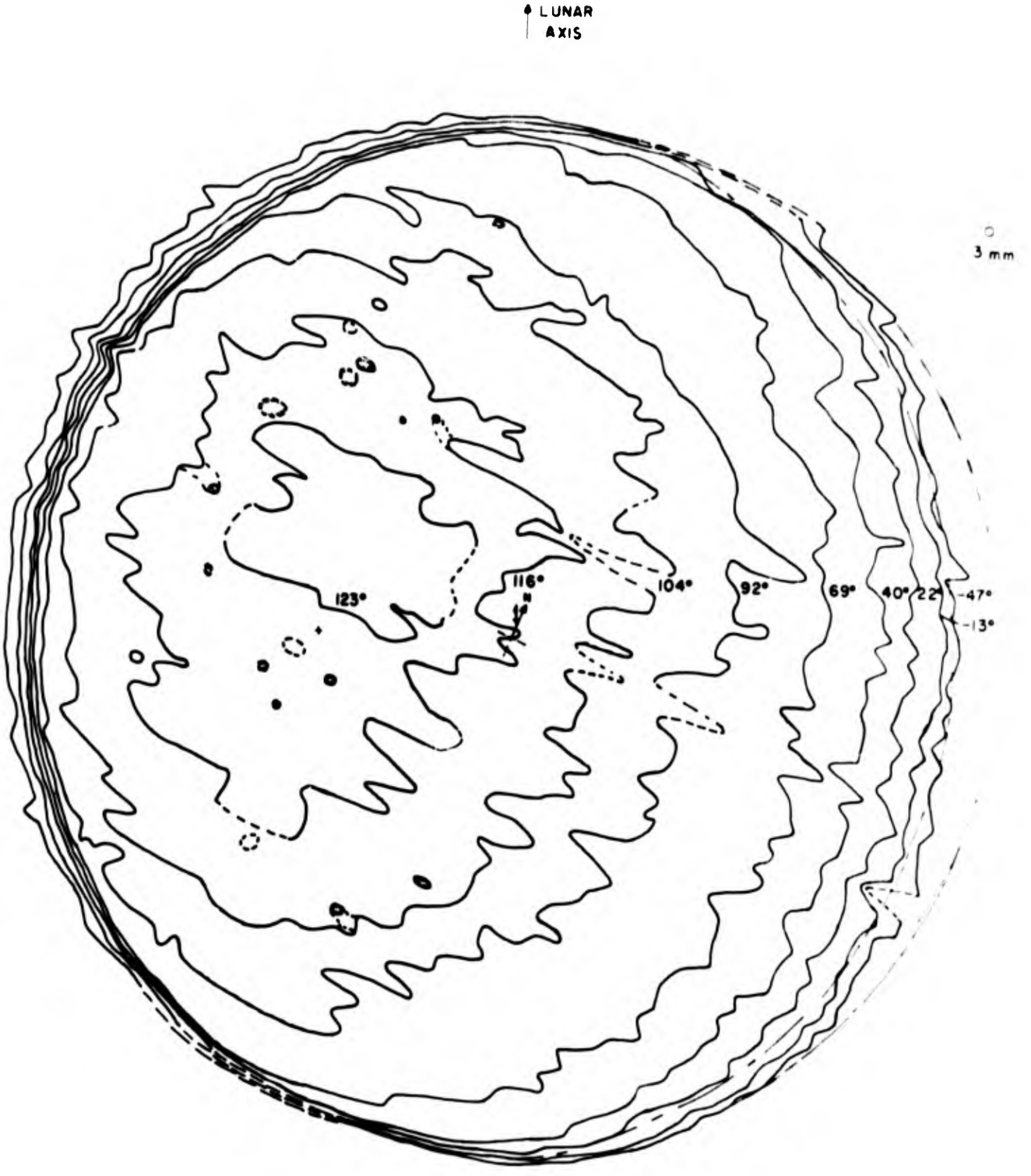

FIGURE A-4 DISTRIBUTION OF LUNAR TEMPERATURES IN ^{o}C. MOON OF MARCH 26, 1959, BEGUN 7:40, ENDED 10:58 UT, 66 SCANS, 0.96 ILLUMINATED.

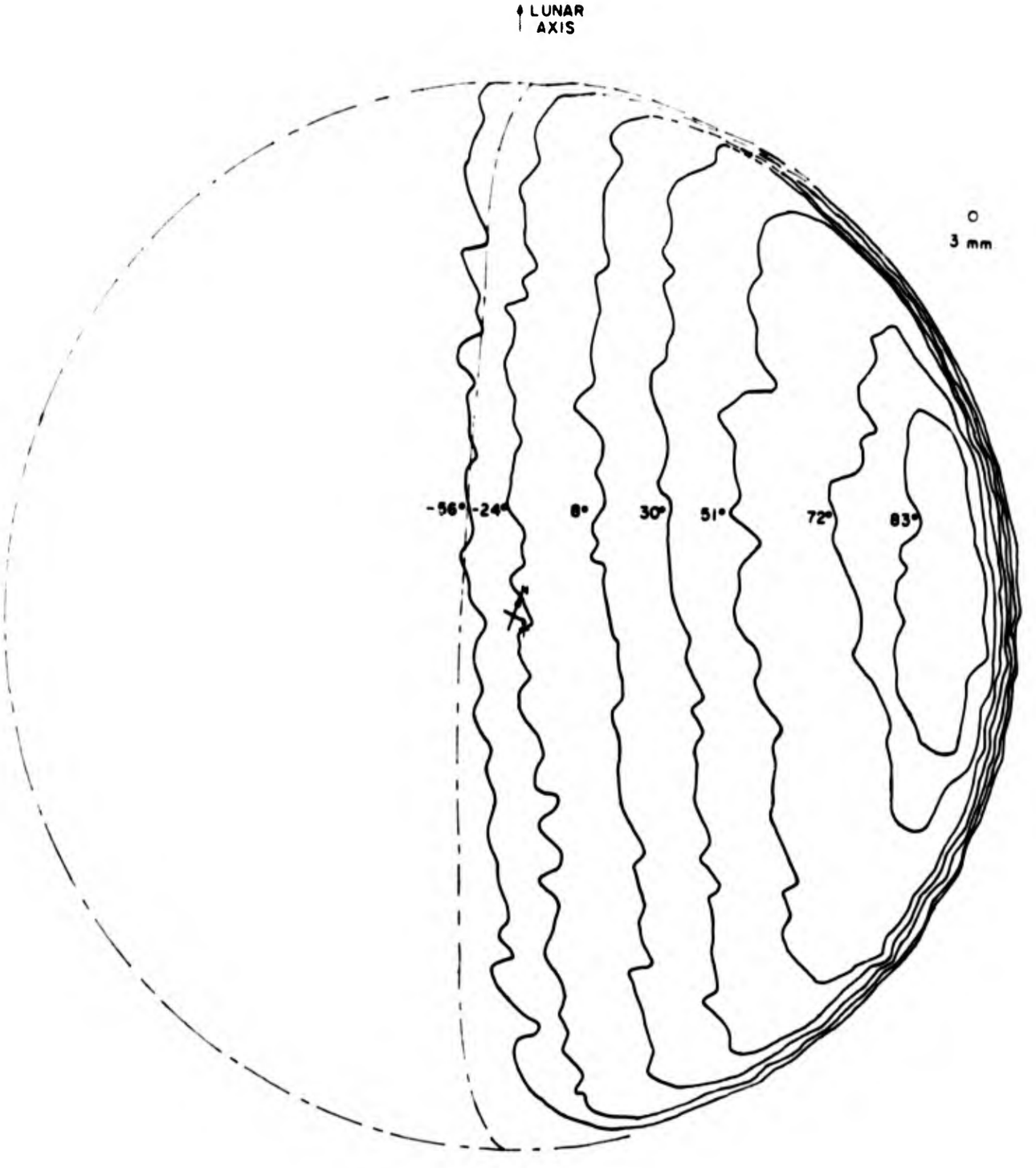

FIGURE A-5 DISTRIBUTION OF LUNAR TEMPERATURES IN ^{o}C. MOON OF MAY 16, 1959, BEGUN 1:49, ENDED 4:43 UT, 58 SCANS, 0.53 ILLUMINATED.

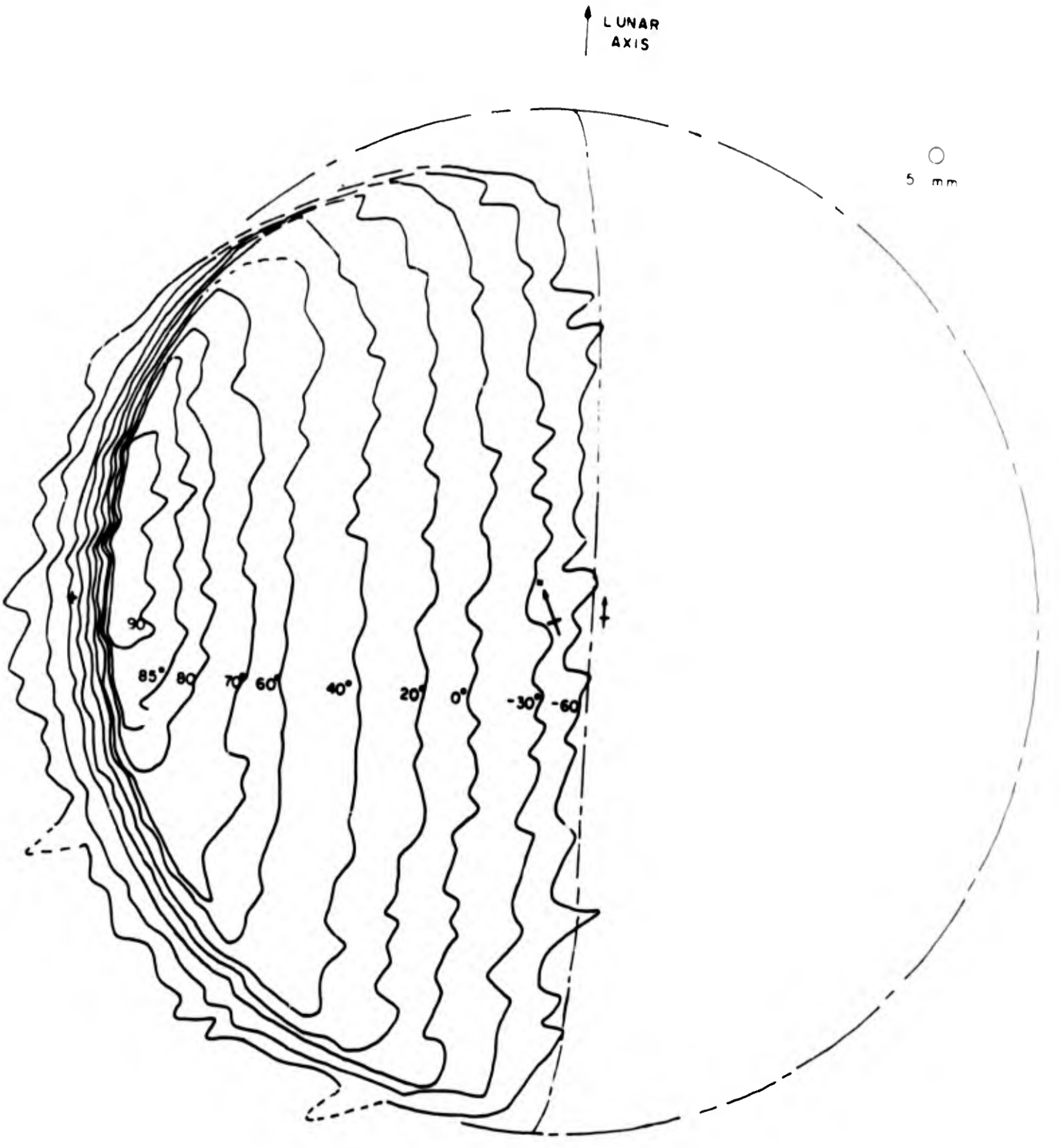

FIGURE A-6 DISTRIBUTION OF LUNAR TEMPERATURES IN ^{o}C. MOON OF JUNE 27, 1959, BEGUN 11:15, ENDED 14:12 UT, 60 SCANS, 0.54 ILLUMINATED.

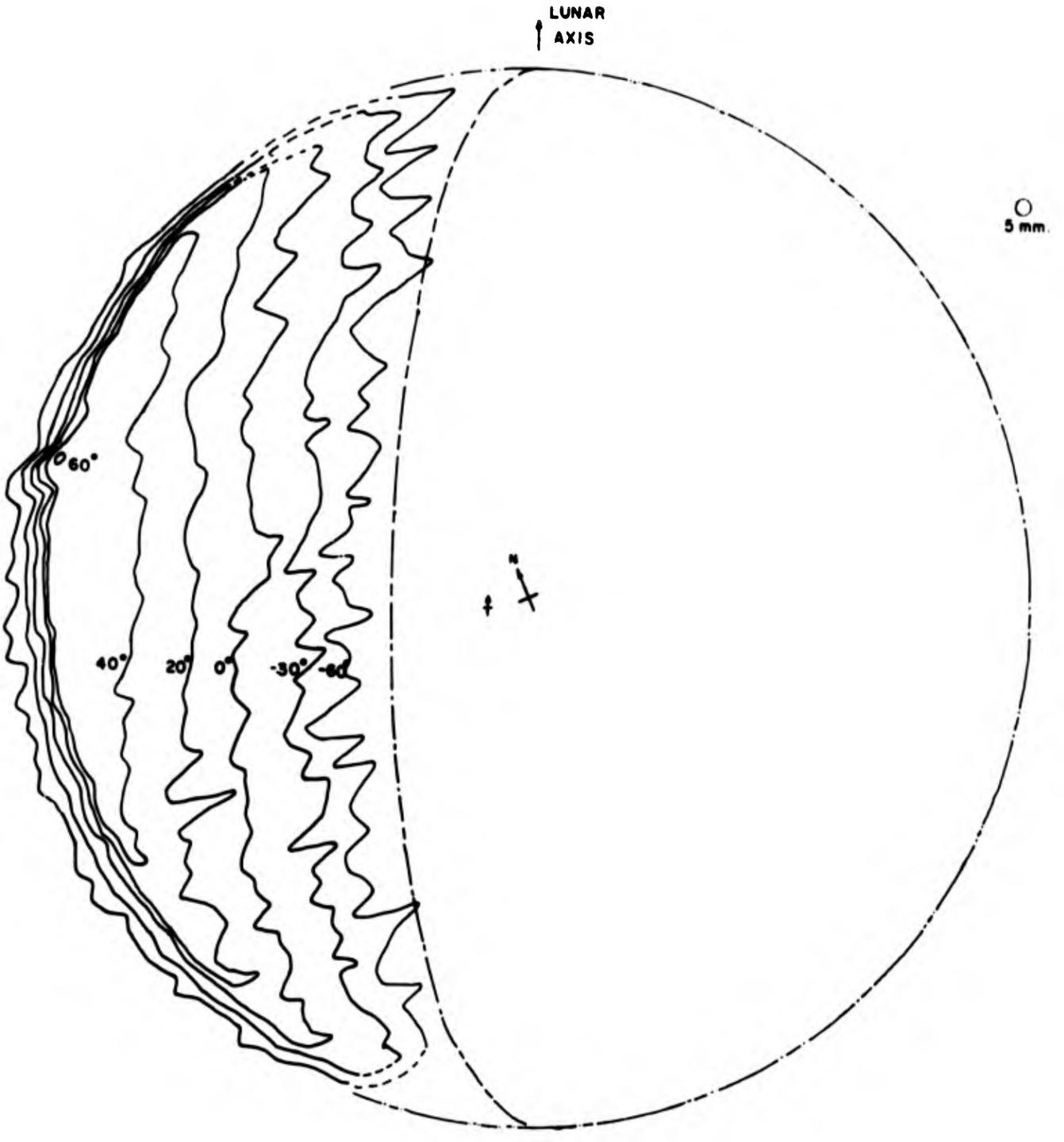

FIGURE A-7 DISTRIBUTION OF LUNAR TEMPERATURES IN ^{o}C. MOON OF JUNE 29, 1959, BEGUN 13:12, ENDED 16:09 UT, 60 SCANS, 0.36 ILLUMINATED.

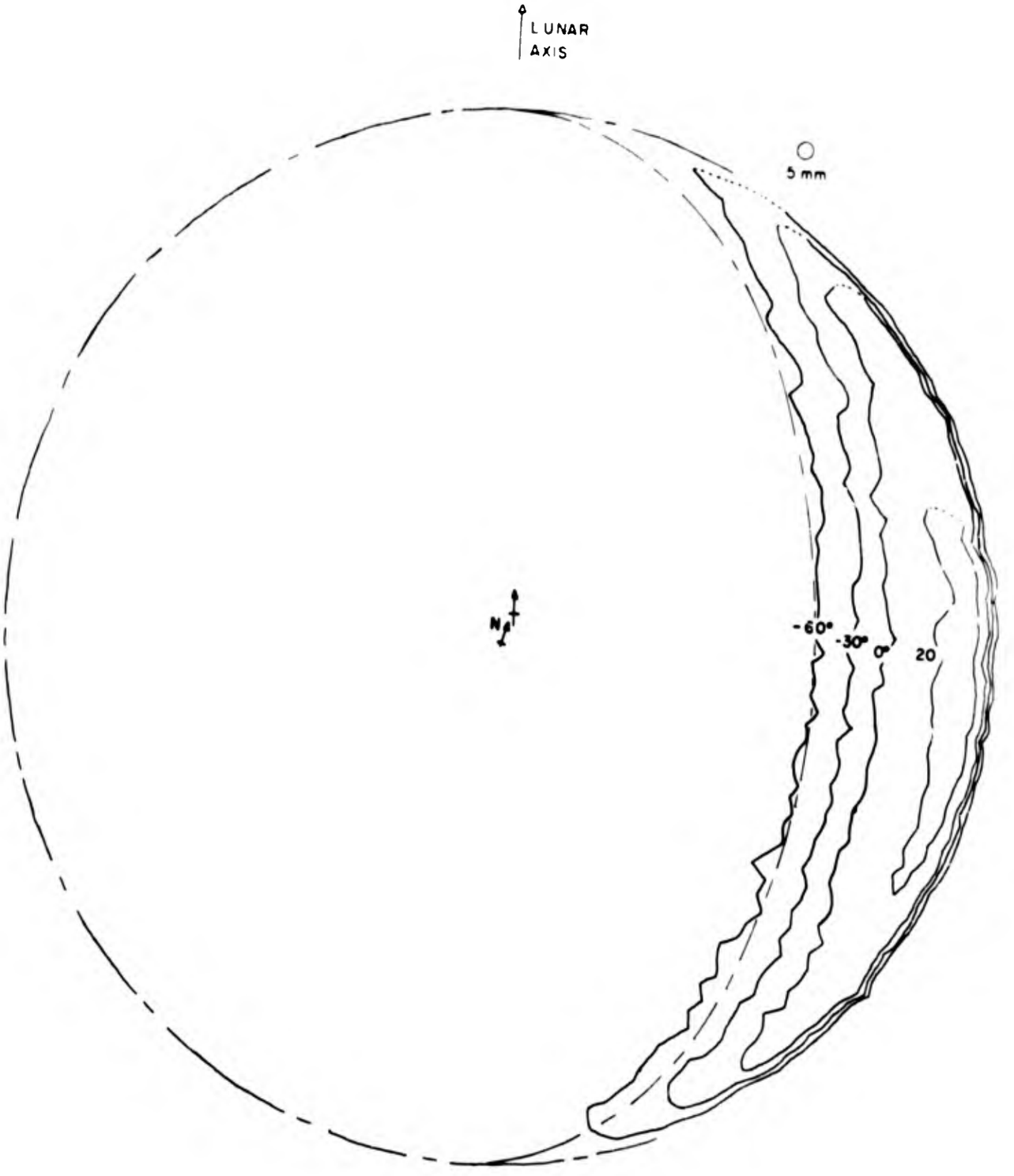

FIGURE A-8 DISTRIBUTION OF LUNAR TEMPERATURES IN ^{o}C. MOON OF SEPTEMBER 6-7, 1959, BEGUN 21:38, ENDED 0.44 UT, 63 SCANS, 0.19 ILLUMINATED.

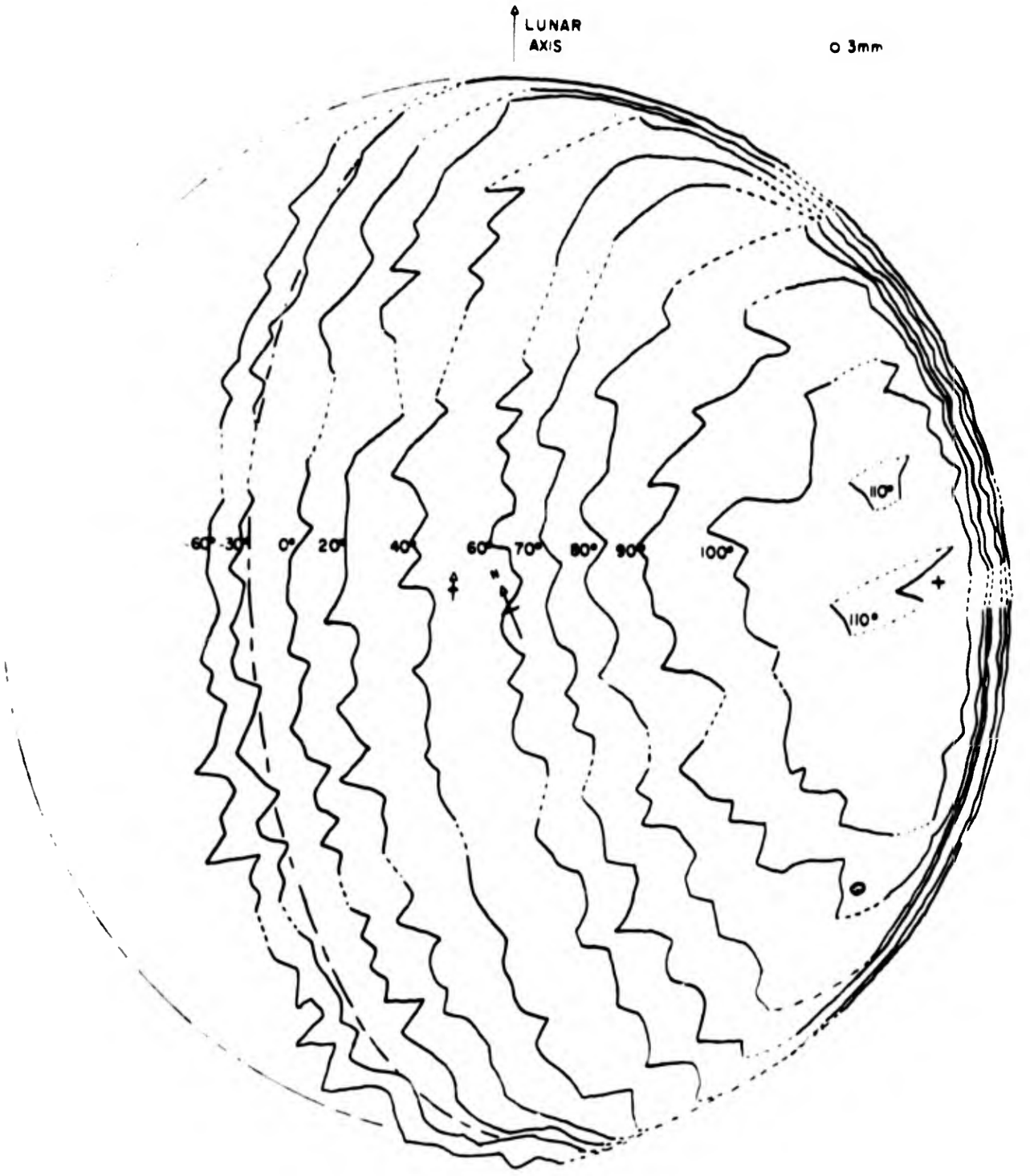

FIGURE A-9 DISTRIBUTION OF LUNAR TEMPERATURES IN ^{o}C. MOON OF NOVEMBER 10, 1959, BEGUN 2:17, ENDED 5:23 UT, 63 SCANS, 0.77 ILLUMINATED.

IV. MAGNETIC FIELD

Reports of the findings of the Russian Lunik II state that this lunar probe did not detect a magnetic field, indicating a field strength of less than 30 gammas.* Kopal (1959) has presented other evidence which corroborates this conclusion. He points out that the lunar luminescence studies of Kozyrev and Dubois revealed that the luminescence around Aristarchus ceases at the instant the sun drops below the lunar horizon. This indicates that the corpuscular radiation which causes the luminescence is not deflected by a magnetic field, so that the lunar magnetic field must have only a small fraction of the intensity of the terrestrial field.

If it is true (as seems likely from theoretical considerations) that the moon has no magnetic field of its own, it will still be affected by interplanetary fields. The intensity of the steady-state general interplanetary field is about 2.5 gammas, while transitory fields frozen into solar plasmas ejected from the sun reach a maximum intensity of about 40 gammas in the vicinity of the moon. In the absence of more complete data, it is assumed here that this is the range of intensity of the magnetic field at the lunar surface. It should be noted that fluctuations of the interplanetary field occur more frequently during a solar maximum than during a minimum.

*One gamma equals 10^{-5} gauss.

V. COMPOSITION

The composition of the moon is largely speculative. Kozyrev and Dubois (Kopal, 1959) have both obtained luminescent spectra from the vicinity of the crater Aristarchus. Kozyrev identifies his spectrum with quartz, while Dubois identifies his with the mineral willemite. Even if these spectra were more reliable, they deal only with local minerals, and information is needed on the gross composition of the surface.

Tektites have appeared to some investigators to provide just this sort of information. Chapman and Larson (1963) have presented convincing evidence to show that tektites are portions of the lunar crust blasted into space by meteorite impact and captured by the earth. Other investigators, such as Cohen (1960) and Hawkins (1960), have presented arguments to show that tektites are of terrestrial origin but, if they are not, the composition of tektites must reflect the gross composition of the portions of the lunar surface from which they were derived. Tektite composition is such that the rock from which they were formed must have been silicic in nature. It may be that maria are silicic differentiates of the more basic highlands materials (Lowman, 1963), but this is in the realm of speculation.

Many authors have postulated that the moon as a whole has the same composition as chondritic meteorites. Because of the low lunar density, however, it must always be assumed that the moon has gained a larger share of lighter elements. Urey (1952, p. 220) has suggested that this could be accounted for by a higher concentration of silicate phase relative to iron phase becuase of accumulation of the moon at a sufficiently low temperature that its silicates could not volatilize. He has also suggested (p. 205) that the addition of water of crystallization in oxidized chondrites to the extent of about 1 percent by weight would give them a density equal to that of the moon.

It appears best to assume a chondritic composition for the moon as a whole minus about 5 percent iron, and to assume that the crust has undergone differentiation to produce silicic as well as basic rocks. The location of these differentiates and their precise composition is as yet unknown.

VI. SURFACE AND SUBSURFACE STRUCTURE*

Lunar surface and subsurface structures are an important factor in the design of a lunar rocket and lunar roving vehicles or bases. Unfortunately, the nature of both the surface and subsurface structures is dependent upon the origins of the major surface features, which are open to debate. It is considered necessary in this section, therefore, to briefly review the current diversity of opinion before arriving at the lunar model to be adopted here, which is considered probable, although clearly speculative. It is particularly important to review the diversity of opinion in view of the complexity of the lunar environment, which does not admit of easy generalizations.

The origin of lunar craters has been a subject for controversy for many years. At this time there are two main theories, one supporting an internal igneous origin and the other an external meteoroid impact origin.

Volcanic craters on earth are typically small, cup-shaped depressions on top of a volcano, and the majority of lunar craters are clearly not of this type. On the contrary, they are broad shallow depressions surrounded by low rims of debris. Although not common, similar features, called calderas, occur in some volcanic regions on earth. Calderas are produced when molten material is blown from beneath the surface, emptying a lava reservoir and fracturing the overlying rock. The overlying rock collapses into the empty chamber to produce a depression surrounded by a ring of expelled debris. Subsequent volcanism may produce new volcanic cones on the caldera floor (see Figure A-10). It is apparent from a comparison of the features of the crater Ptolemaeus, shown in Figure A-11, that such features probably do exist on the moon. Ptolemaeus lacks a marked rim of debris, has a definite polygonal outline, and a flat floor. It appears from this morphology that the crater walls foundered along crustal fracture zones to produce the polygonal outline, while an outpouring of lava or ash flows filled the bottom of the crater to produce the flat floor. Most adherents of the volcanic school of thought (Green, 1960) would agree to this sequence of events, but this is by no means to say that all lunar craters are volcanic in origin. On the contrary, the morphology of a more typical lunar crater, such as Copernicus, is consistent with an impact origin for this feature (Baldwin, 1949). The feature most suggestive of an impact origin is the near-circular outline, which is characteristic of hypervelocity impact craters even at low angles of impact. Although often slightly polygonal in response to rock structure, they never assume the extreme polygonal outline characteristic of a collapse feature. The nature of the ejecta blanket and rays surrounding a crater like Copernicus are also indicative of an impact origin (Shoemaker, 1962b).

---

*A more detailed substantiation and reasoning behind the generalizations presented in this discussion can be found in Salisbury and Smalley (1964).

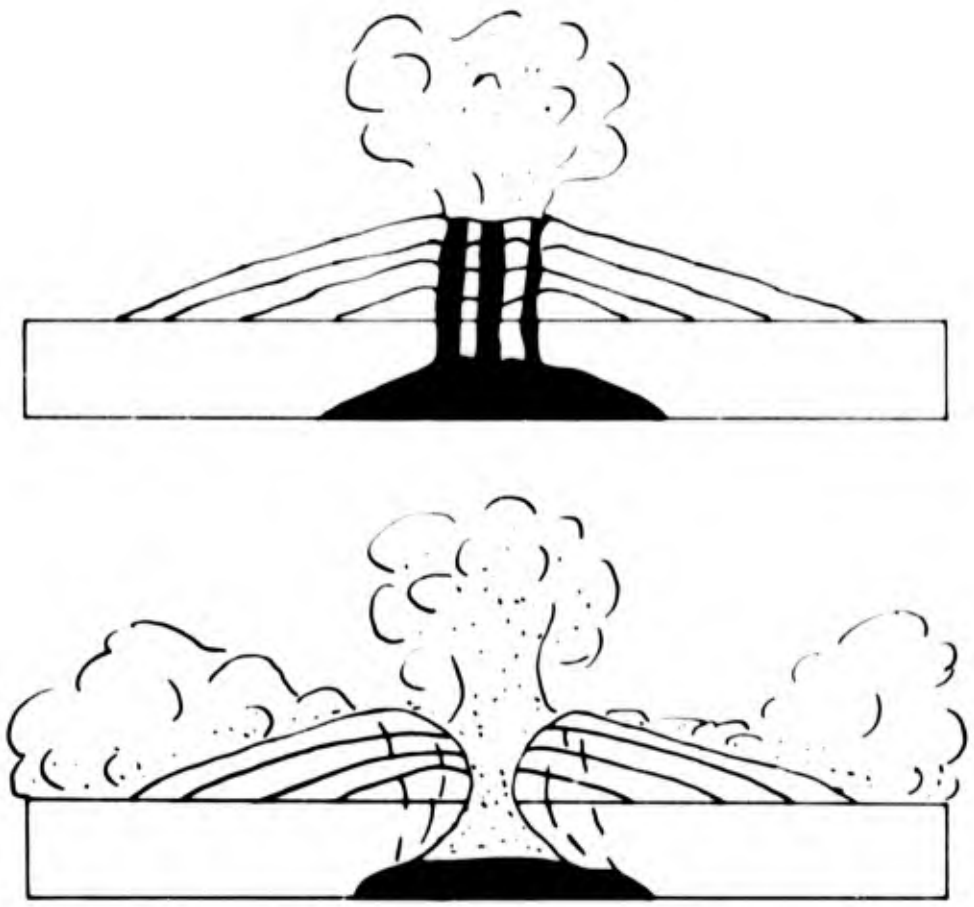

FIGURE A-10 STEPS IN THE FORMATION OF A CALDERA
(after J. Green, 1960)

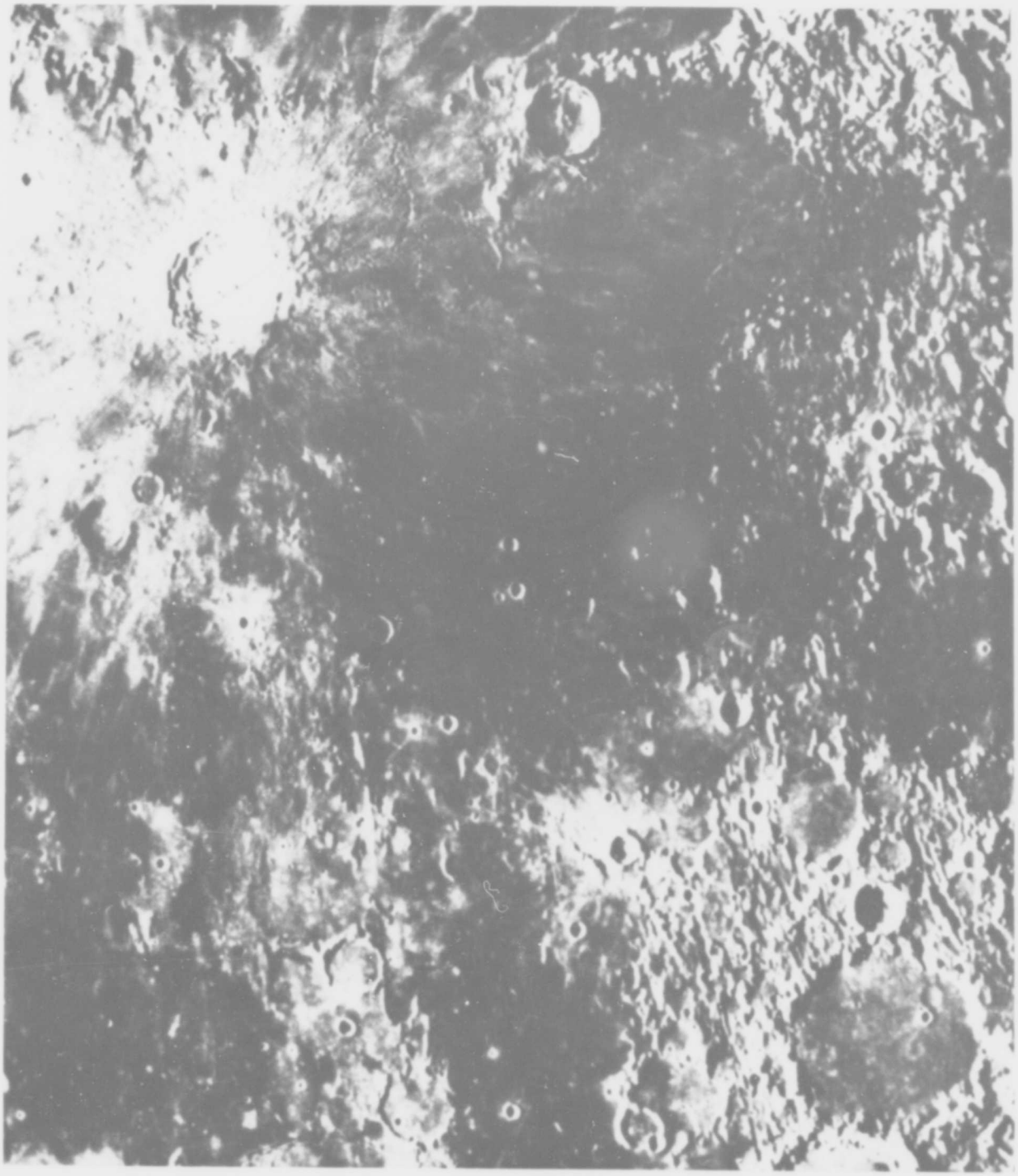

FIGURE A-11 MT. WILSON OBSERVATORY PHOTOGRAPH SHOWING THE CRATERS COPERNICUS (UPPER LEFT) AND PTOLEMAEUS (LOWER RIGHT). THE CRATERS ARE 56 AND 90 MILES IN DIAMETER, RESPECTIVELY.

It is possible for a single crater to be the product of both caldera formation and meteoroid impact. In such a case, the impact would create a zone of weakness in the lunar crust which would later localize the igneous activity. In fact, there probably is a complete spectrum of crater types ranging from pure impact to pure igneous. Thus, it is the height of folly to stoutly defend a single origin for all lunar craters as scientists on both sides of the crater controversy have done. Nevertheless, it does appear that the majority of lunar craters were produced by impact.

The origin of the maria and highlands is less controversial than that of the craters, since most scientists believe that the dark smooth maria are volcanic, while the highlands are not. A dissenting opinion held by some researchers (Gold, 1959) is that the maria are seas of dust eroded from the highlands by micrometeoroid impact and radiation damage. This dust hypothesis has found little support within the scientific community, but it has received such wide circulation by popular news media that it appears necessary to mention some of the evidence against it here.

The chief difficulty with the dust hypothesis is the inadequacy of the postulated means by which the dust could have been transported from the highlands to the maria basins. It has been said that electrostatic charging of dust grains by solar radiation will cause this levitation by mutual repulsion, thus permitting them to migrate downhill. It has been demonstrated that this charging is not sufficiently strong to accomplish the mass levitation of particles, although a small particle put in motion by micrometeorite impact will tend to have its duration of flight extended by an electrostatic cushion (Singer and Walker, 1962b). As soon as a dust particle touches the surface, however, it will stick fast, as we have recently demonstrated in our simulation experiments (Salisbury, et al, 1963).

An examination of the physical features of the moon also bears upon the validity of the dust hypothesis. It is obvious that local depressions in the highlands as well as the ocean basins will accumulate dust if downhill transport takes place on a large scale, but this does not occur. The presence of a dark flat floor in a crater such as Ptolemaeus would indicate a dust filling with only the walls of the crater acting as a "drainage area". If this were possible, then all craters of similar size and age should have similar flat floors, which they do not. Thus, on the basis of theoretical, laboratory, and physical evidence, one can discount the theory of maria composed of dust, which also eliminates the concept of dust hundreds of feet deep. As shall be pointed out later, however, local concentrations of dust up to three or four feet deep should commonly occur.

As was mentioned above, the maria are currently thought to be volcanic in nature. Many researchers believe that this volcanism has taken the form of lava flows, others that it has taken the form

of ash flows. Because an ash flow is no more than a lava flow literally blown to bits by gas pressure, there is little difference in origin between the two. There is, however, a difference in form and character of the resulting deposits. A lava flow may be vesicular or bubble-filled near its top, but generally forms a hard, dense rock. An ash flow is usually composed of loose material near its top, but is sintered into a hard mass below a depth of a few feet. It is generally of rather low density, and may even be highly porous.

There are good reasons for suspecting that the maria may be covered with ash flows, rather than lava flows, although they are not completely convincing. First, the maria do not appear to have any flow fronts or steep terminations as would be typical of lava flows. Second, where pre-existing craters are covered, they are reflected in the topography of the flow surface, indicating a significant volume decrease after deposition. With a constant percentage volume decrease the thicker portions of the flow suffer a greater change in elevation than the thinner portions, because the thicker the layer the greater the total change. Such a marked volume change does not take place in lavas, indicating the presence of ash flows over the ghost craters. This is not to say that there are no lava flows at all, nor that a single ash flow covered a particular mare. It is more likely that the maria were covered by a series of ash flows, possibly mixed with lava flows and significantly separated in time. The surface of the maria have subsequently been lightly cratered by impacts to produce local rubble layers, which may be several thousand feet thick in the vicinity of a major crater such as Copernicus, but which must thin rapidly to discontinuous patches in intercrater areas. Figure A-12 shows what is envisioned as a cross-section of a typical mare.

In contrast to the maria, the highlands have evidently had a much simpler history. The lunar crust appears to have been subjected to a long history of bombardment by meteorites and comets, leading to the formation of a complex rubble layer composed of overlapping, discontinuous lenses of debris (see Figure A-13).

The thickness of this rubbl. layer is highly variable, most of it being concentrated in and near crater rims. Considering the volume of rubble produced by highlands craters, however, an average depth of at least 90 feet is a reasonable value for rubble in inter-crater areas. Depths of 275 feet associated with rims of 1-mile diameter craters should be common, and many thousands of feet of rubble should be present around major impacts.

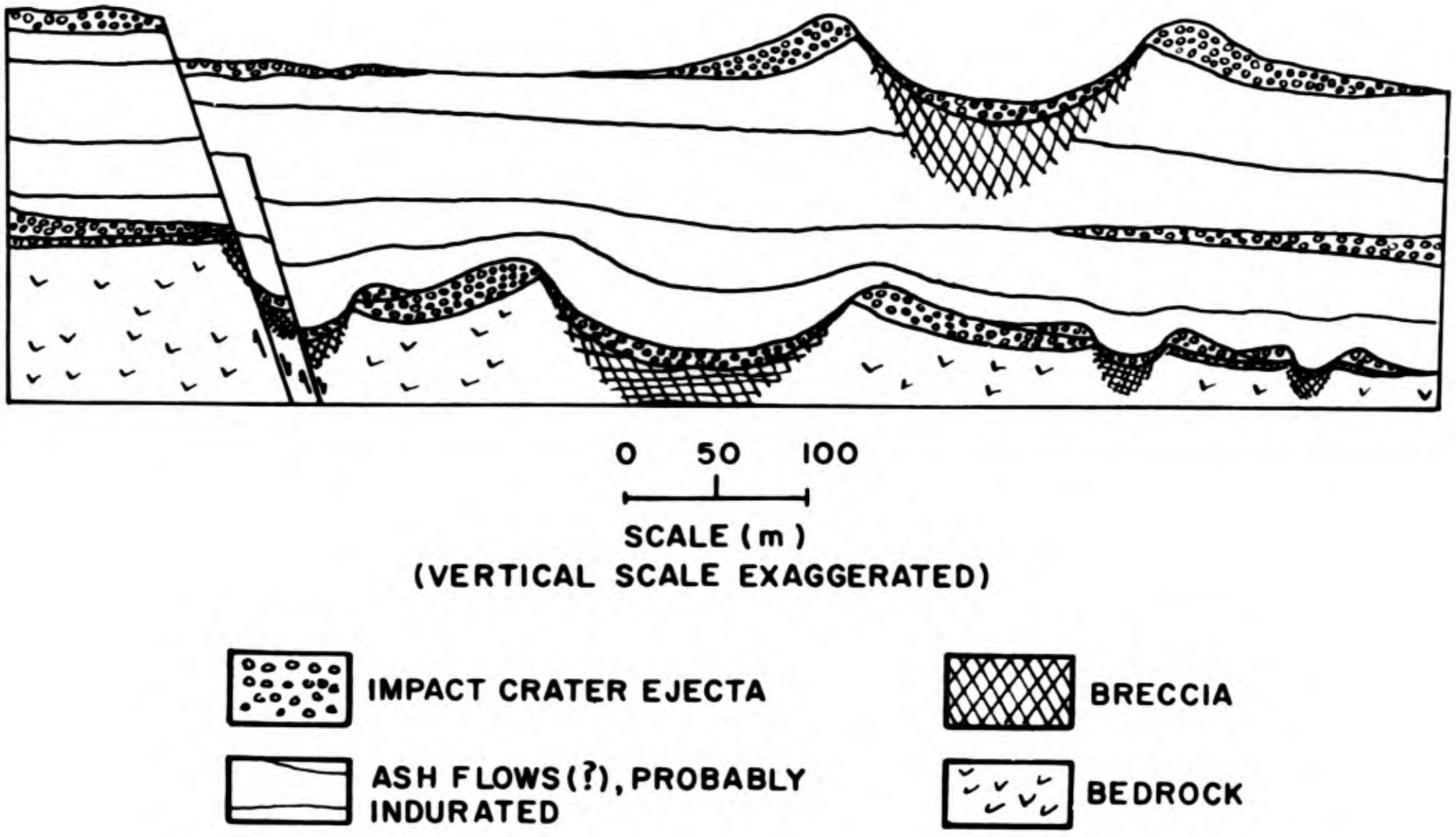

FIGURE A-12 CROSS-SECTION OF A TYPICAL MARE

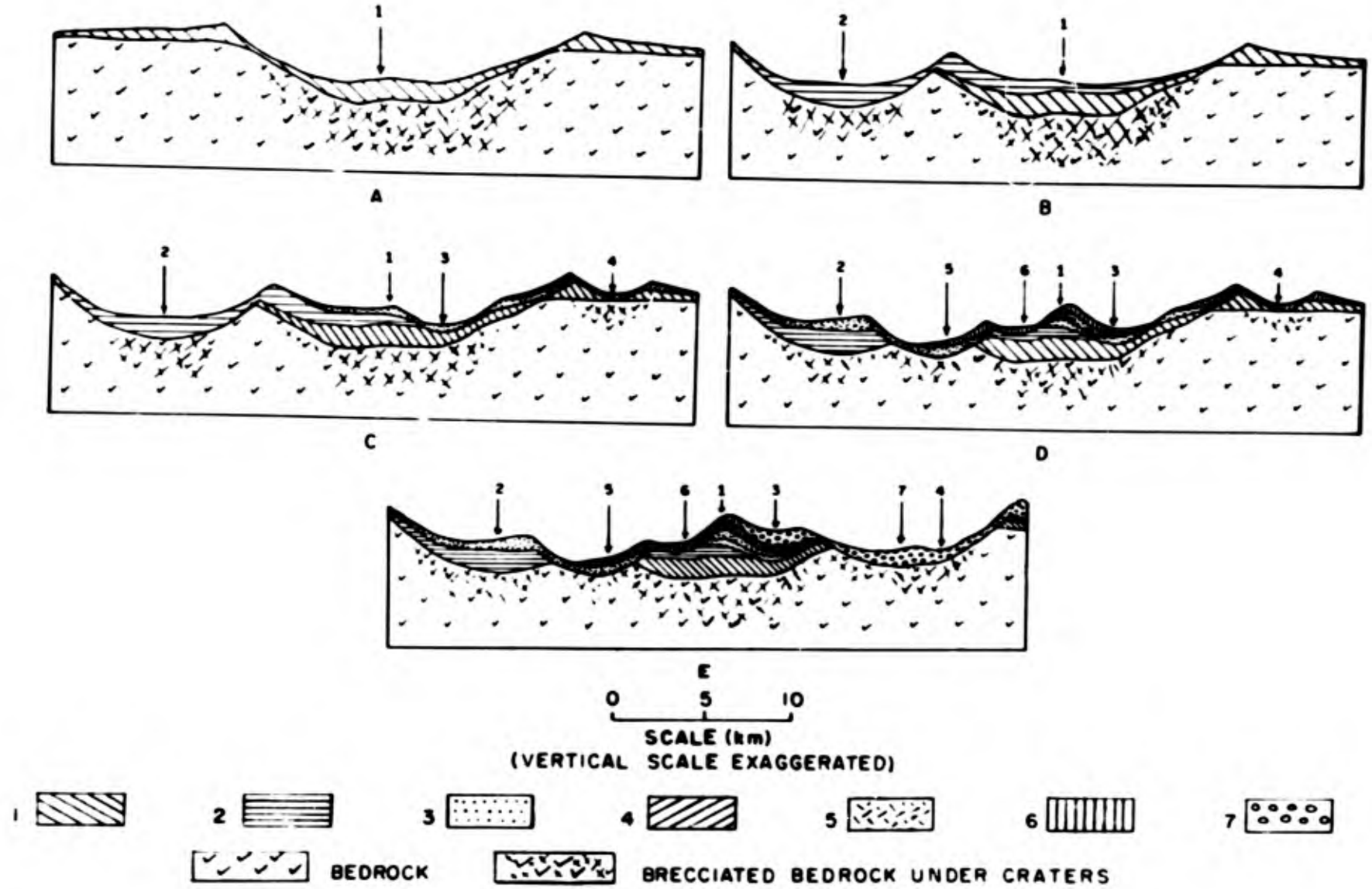

Creation of simplified lunar subsurface structure by meteoritic impact. A single crater with its associated debris is shown in A, and a second crater is created beside it in B. In C, two smaller craters (3 and 4) have penetrated the debris of the older craters, and in D two overlapping craters (5 and 6) have added to the complexity of the structure. A final large crater (7) has destroyed most of the crater 4 in E. Actual lunar structure will be even more complex. Negative accretion would change the thicknesses of the layers, but not the essential structure. (Key: 1-7, Debris symbols for each of seven consecutive meteorite craters.)

FIGURE A-13 CROSS-SECTION OF A TYPICAL HIGHLANDS TERRAIN

BLANK PAGE

VII. LUNAR SURFACE ROUGHNESS

When it is realized that the surface of the highlands is entirely covered with rubble ejected from meteorite craters, and that the surface of the maria is partially so, it is usually assumed that the surface must be very rough. Unless studied carefully, however, lunar surface roughness becomes a subject upon which it is easy to make erroneous judgments.

One of the first mistakes generally made is not to specify the scale at which roughness is being described. Clearly, yard-scale roughness is different from mile-scale roughness, and important for different reasons. Fortunately, mile-scale topography can be observed directly, leaving little room for argument, but plenty of room for misconceptions. The most common misconception is that the highly cratered highlands are rugged terrain on a mile scale, and that lunar craters in general are steep-sided features. This is far from true for the large craters, as is illustrated in Figures A-14, A-15 and A-16. The craters Aristillus and Autolycus, for example, appear in Figure A-14 to be deep and cup-shaped. Actually, as is shown in Figure A-15, they are shallow, bowl-shaped features with relatively flat slopes. Figure A-16 shows that Piton, which appears to be a needle-sharp peak in Figure A-14, is actually a low ridge.

The source of the illusion of steepness for these features is shadow exaggeration. The photograph was taken at a very low sun angle near lunar sunset, and the long shadows thrown by gentle features make them appear rugged.

It must be noted, however, that the small crater Archimedes C does have a steep slope on its western side. As a matter of fact, the average inner slope angle of small craters (less than 15 to 20 miles in diameter) is better than 30°. Since smaller craters comprise the vast majority of all craters, such steep slopes are common. On the other hand, the percentage of the surface area covered by these steep slopes is very small. Thus, we have, as is usually the case when a subject is studied closely, a complex statement of lunar surface roughness on a mile scale: the surface is not as rugged as it appears, since the major features do not have steep slopes; but steep slopes associated with smaller craters are common, although they cover only a small percentage of the surface area. As a result, the generalization is usually made that the moon is relatively smooth on a mile scale.

Surface roughness on a yard scale is of greatest interest to designers of space suits and exploration vehicles. The assumed presence of large amounts of coarse rubble on the lunar surface, particularly in the highlands, has generally led to the conclusion that the surface should be extremely rough. It must be remembered,

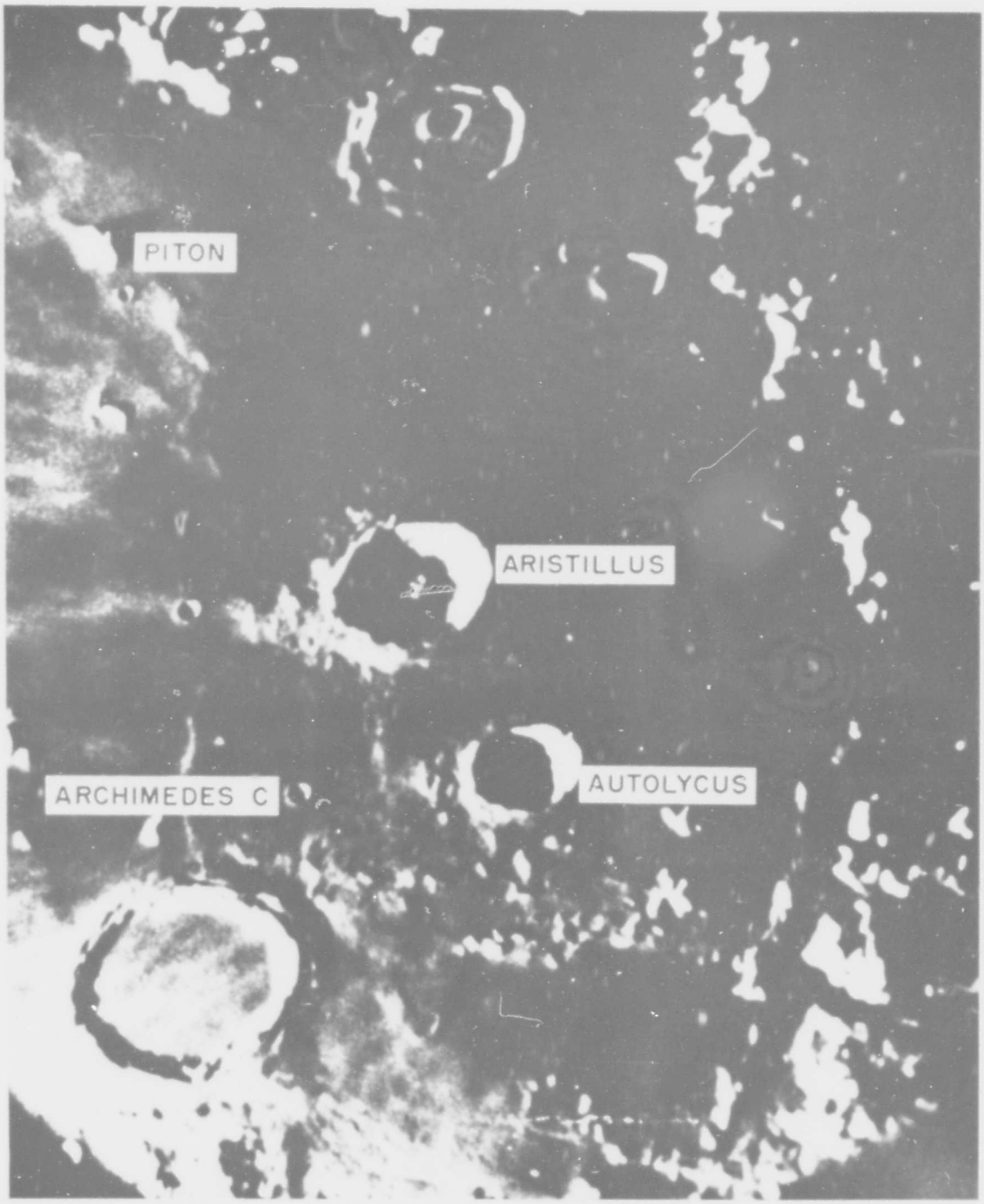

FIGURE A-14 EASTERN PORTION OF MARE IMBRIUM (PIC-DU-MIDI OBSERVATORY PHOTOGRAPH).

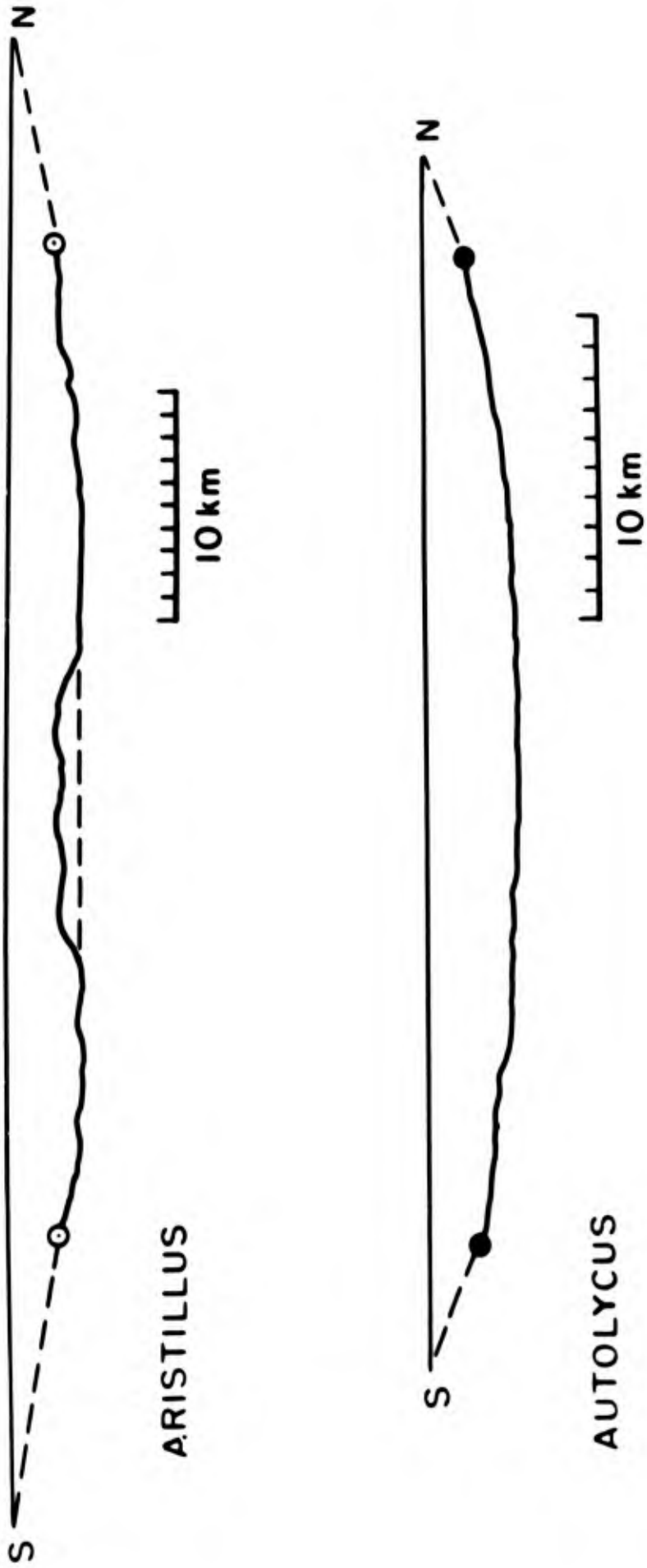

FIGURE A-15 CROSS-SECTIONS OF THE CRATERS ARISTILLUS AND AUTOLYCUS (KOPAL et al, 1961).

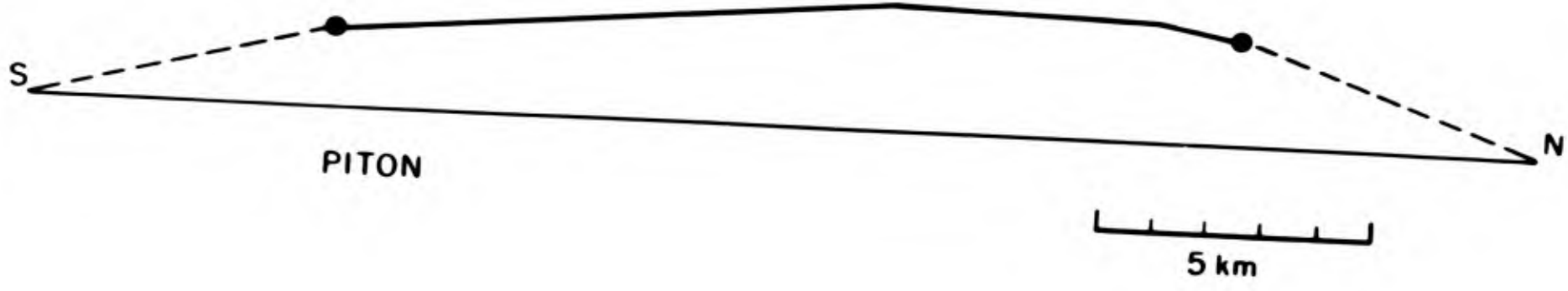

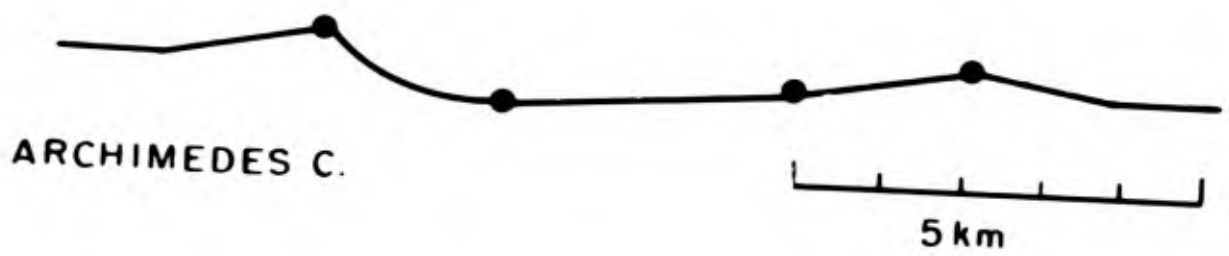

FIGURE A-16 CROSS-SECTIONS OF THE SMALL CRATER ARCHIMEDES C AND THE MOUNTAIN PITON (KOPAL et al, 1961).

however, that the rubble layers have been laid down during the course of a long lunar history. The large craters which produce the greatest amount of rubble are the result of rare events. Thus, the typical rubble layer has been exposed to the lunar environment for millions of years. Over this great span of time, the impacts of countless micrometeorites have acted as a potent erosion mechanism. The fine debris produced by these impacts has tended to collect in local depressions, armoring them against further erosion, while high points are gradually worn down (see Figure A-17). The collection of debris in local depressions, which makes possible this reduction of surface roughness, is a function of two processes. One, which is completely non-speculative, is the entrapment of debris from an impact within a depression by its walls, thus making the depth of dust increase faster in a depression than it would on flat ground. The second, which is partly speculative, depends upon the electrostatic repulsion between a charged particle and a surface of like charge to extend the time of flight of a particle. The effect of gravity will always tend to make such a particle migrate downhill, thus preferentially filling local depressions.

Evidence for the resulting smoothness of the lunar surface is obtained from the manner in which radar waves are reflected by the moon. Because the reflections of a radar pulse come almost entirely from the center of the disk, and not from its edges, the surface must be smooth at a scale equivalent to the length of the radar wave. If the surface of the moon were rough, it would act as a diffuse reflector, and approximately as much energy would be reflected from the edges of the disk as from the center. Diffuse reflection does occur at the wavelengths of visible light, which is why the full moon is equally bright over the whole disk. Thus, there is a change from smoothness to roughness somewhere between the scale of the shorter radar wavelengths (about an inch) and optical wavelengths (less than a micron).

It should be pointed out here that, as in the case of the mile-scale measurements, the yard-scale measurements do not indicate complete smoothness. They are usually taken to mean an average surface gradient of 1 in 10. In places where a recent rubble layer has been laid down, however, such as around the crater Copernicus, the surface is a great deal rougher than that. Recent craters as large as Copernicus are rare, but smaller craters a few hundred feet in diameter should be relatively common, even on the lightly cratered maria. "Common" in this context would be within a radius of 2 or 3 miles of random landing site. The maximum block size ejected from such a crater is about 15 feet in diameter. Thus, the rubble layer surrounding the crater should have significant relief on a yard scale. Yet, as in the case of the mile-scale steep slopes, the percentage of the total lunar surface area covered by rough rubble layers is small, so that the moon is generally referred to as smooth on a yard scale.

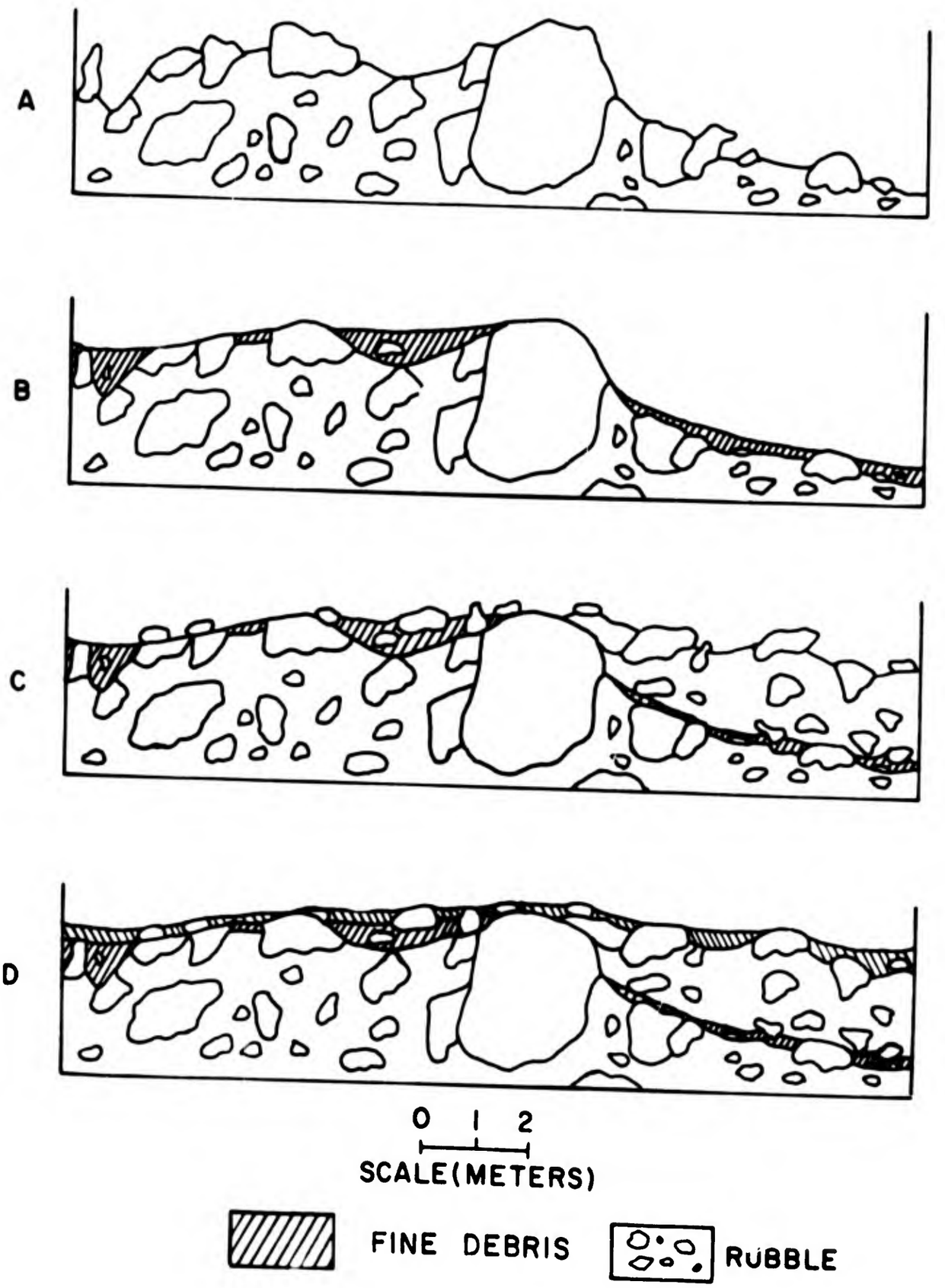

FIGURE A-17 EROSION OF RUBBLE LAYERS TO REDUCE RELIEF.

Since the smoothness of most of the highlands surface is made possible by the collection of fine debris in depressions on ancient rubble layers, the character of this material is of interest. As explained more fully in the Introduction of this report, we have assumed that the fine debris is composed primarily of crushed rock fragments, rather than fused or melted material. It must be remembered, however, that both fused material and larger rock fragments will have been mixed with the finer debris on the lunar surface. Thus, Figure A-17 is a simplified picture presented to illustrate the process of lunar erosion, not a realistic lunar cross-section. Our simulation experiments have also necessarily been simplified in the same way - i.e., only fine powders have been used. We do not believe, however, that deep pockets of pure "dust" exist on the lunar surface.

BLANK PAGE

VIII. TABULAR DATA
(Smithsonian Physical Tables, 1954)

Mass

In terms of Earth's = 0.0123
In tons = 8×10^{19}
In grams = 7.32×10^{25}

Mean Diameter

In terms of Earth's = 0.273
In miles = 2160
In kilometers = 3476

Mean Density

In terms of Earth's = 0.60
In terms of water = 3.33

Surface Gravity

In terms of Earth's = 0.16
In fps acceleration = 5.31
In cm/sec acceleration = 162

Velocity of Escape

In terms of Earth's = 0.21
In miles/sec = 1.49
In km/sec = 2.4

Rotation Period

Days = 27.3

Orbit (Brown, 1959)

a. Distance, maximum (miles) = 252,710
   minimum (miles) = 221,463
   mean (miles) = 238,860
   (kilometers) = 384,409
b. Parallax, mean = 57' 02" .54
c. Inclination of orbit plane:

   to ecliptic, mean = 5° 08' 43"
   to Earth's equator, maximum = 28° 35'
   minimum = 18° 19'

d. Inclination of moon's equator to ecliptic = 1^{o} 35'
e. Eccentricity, mean = 0.549
f. Velocity in orbit, mean:

Linear miles/sec = 0.6353
Angular/hour = 33'

Visual Magnitude = -12.7

Albedo, Spherical = 0.07

APPENDIX B

LOW PRESSURE GAS FLOW AND SORPTION IN POROUS MEDIA

I. THE PROBLEM

We are concerned with the transient flow of gases at low pressures out of (evacuation) and into (pressurization) a porous medium exposed to a pressure change at a bounding surface. The gas may be sorbable on the surface of the particles comprising the medium, hence, desorption (during evacuation) and sorption (during pressurization) may occur. In fact, as will be shown, the desorption and sorption processes are the crux of the problem.

II. APPROACH

A number of simplifications will be made to render the problem more tractable. We consider a one-dimensional gas flow, i.e., a slab of finite thickness with infinite length and width as shown in Figure B-1. Our aim will be to determine the interstitial gas density (n) and the concentration of sorbed gas on the surface of the particles (σ) as functions of position in the medium (x) and time (t) after some pressure change has occurred at the exposed boundary (X=L). Our primary interest is in the nature of the process at low pressures. We will assume that the pressure is low enough that the mean free path is large compared to the pore size and free-molecule flow obtains.

Only a single gas specie will be considered. In free-molecule flow, collisions between gas molecules are negligible. When more than one gas is present, but interactions between molecules in the sorbed phase are not significant, each gas will behave independent of the others, and the results of this analysis may be applied to each gas.

The properties of the medium, i.e., porosity, specific surface area, etc., and its temperature will be considered uniform throughout.

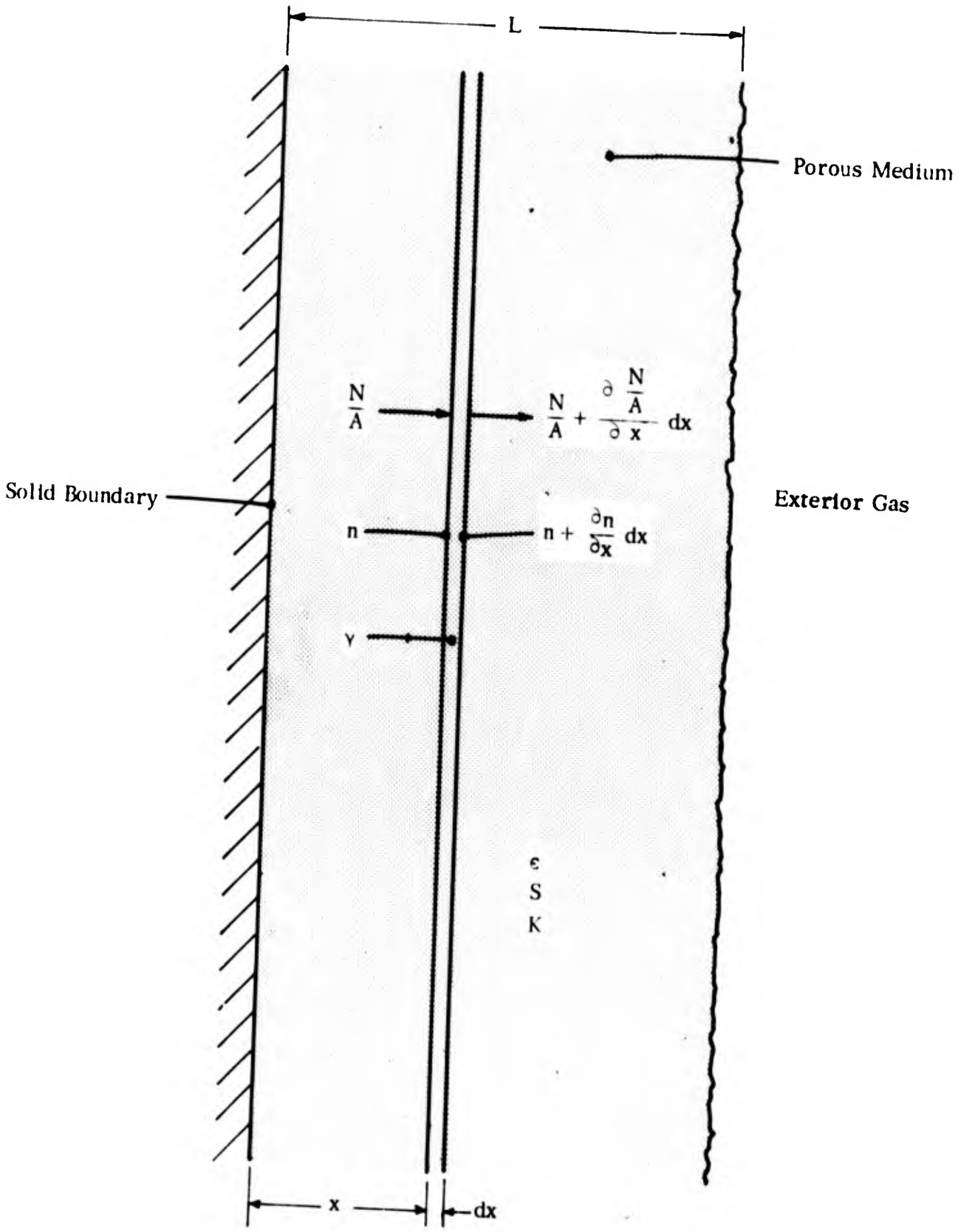

FIGURE B-1 ONE-DIMENSIONAL POROUS MEDIUM FOR ANALYSIS

III. GAS DIFFUSION PROCESS

The diffusional flow of gas through a porous medium is described by Darcy's Law (Carman, 1956),

$$\frac{N}{A} = -K \frac{\partial n}{\partial x} \tag{1}$$

which relates the flow per unit area to the density gradient. In the free molecule flow region, the diffusion coefficient, K, is independent of the gas pressure (or density) and is given by (Carman, 1956)

$$K = \frac{4}{3} \frac{\delta_o}{k'} \frac{\epsilon^2 \bar{v}}{S}$$

where

$$\frac{\delta_o}{k'} \simeq 0.45$$

thus

$$K \simeq 0.6 \frac{\epsilon^2 \bar{v}}{S} \tag{2}$$

We will assume that, at X, there is a net gas flow per unit area γ from the particle surface. Conservation of mass for the interstitial gas in the elemental volume Adx, yields

$$\frac{N}{A} + \gamma S dx - \left[\frac{N}{A} + \frac{\partial \left(\frac{N}{A} \right)}{\partial x} dx \right] = \epsilon dx \cdot \frac{\partial n}{\partial t}$$

which reduces to

$$\frac{1}{A} \frac{\partial N}{\partial x} = \gamma S - \epsilon \frac{\partial n}{\partial t} \tag{3}$$

Differentiating equation (1) with respect to X yields

$$\frac{1}{A} \frac{\partial N}{\partial x} = -K \frac{\partial^2 n}{\partial x^2}$$

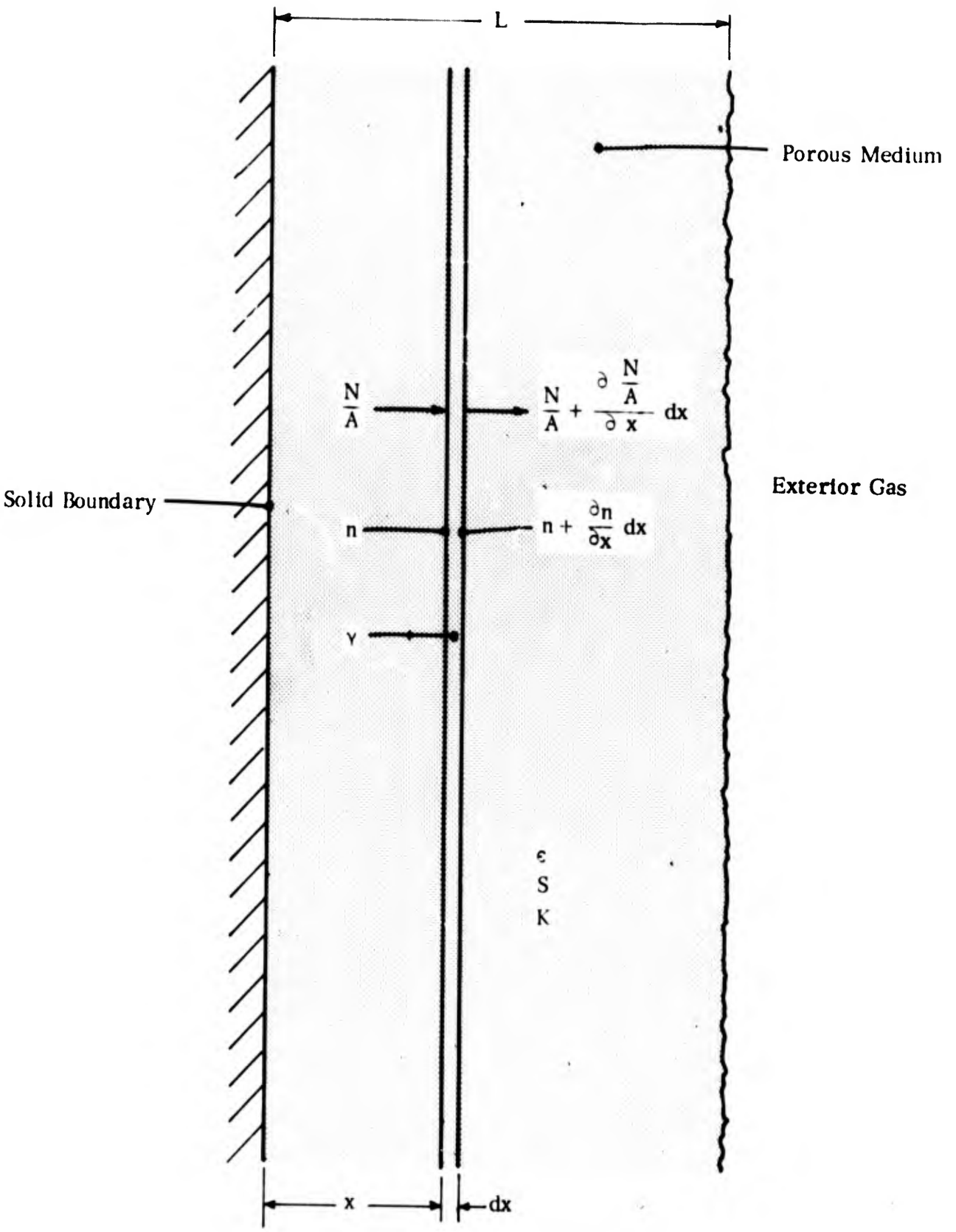

FIGURE B-1 ONE-DIMENSIONAL POROUS MEDIUM FOR ANALYSIS

III. GAS DIFFUSION PROCESS

The diffusional flow of gas through a porous medium is described by Darcy's Law (Carman, 1956),

$$\frac{N}{A} = -K \frac{\partial n}{\partial x} \tag{1}$$

which relates the flow per unit area to the density gradient. In the free molecule flow region, the diffusion coefficient, K, is independent of the gas pressure (or density) and is given by (Carman, 1956)

$$K = \frac{4}{3} \frac{\delta_o}{k'} \frac{\epsilon^2 \bar{v}}{S}$$

where

$$\frac{\delta_o}{k'} \simeq 0.45$$

thus

$$K \simeq 0.6 \frac{\epsilon^2 \bar{v}}{S} \tag{2}$$

We will assume that, at X, there is a net gas flow per unit area γ from the particle surface. Conservation of mass for the interstitial gas in the elemental volume Adx, yields

$$\frac{N}{A} + \gamma S dx - \left[\frac{N}{A} + \frac{\partial \left(\frac{N}{A} \right)}{\partial x} dx \right] = \epsilon dx \cdot \frac{\partial n}{\partial t}$$

which reduces to

$$\frac{1}{A} \frac{\partial N}{\partial x} = \gamma S - \epsilon \frac{\partial n}{\partial t} \tag{3}$$

Differentiating equation (1) with respect to X yields

$$\frac{1}{A} \frac{\partial N}{\partial x} = -K \frac{\partial^2 n}{\partial x^2}$$

which, combined with (3) gives

$$K \frac{\partial^2 n}{\partial x^2} = \varepsilon \frac{\partial n}{\partial t} - \gamma S \qquad (4)$$

the basic equation for transient, one-dimensional gas flow through a porous medium with gas sources; where γ is dependent on x and t; a second relationship between γ, x, and t comes from consideration of the gas-surface interaction.

IV. THE GAS-SURFACE INTERACTION

We will confine our interest to surfaces as they approach being "clean." Then the analysis can be limited to surface coverages of a fraction of a monolayer. Following deBoer's (1953) description of the dynamics of a unimolecular sorbed layer, the sorption rate is given by

$$\frac{\alpha n \bar{v}}{4} \left(1 - \frac{\sigma}{\sigma_m}\right) \tag{5}$$

and the desorption rate by

$$\xi \sigma \tag{6}$$

Hence, conservation of mass applied to the sorbed phase yields

$$\frac{\partial \sigma}{\partial t} = \frac{\alpha n \bar{v}}{4} \left(1 - \frac{\sigma}{\sigma_m}\right) - \xi \sigma \tag{7}$$

The desorption rate coefficient, ξ, is related to the heat of sorption by

$$\xi = \frac{1}{\tau_o} e^{-Qa/RT} \tag{8}$$

If the only interaction between the gas phase and the solid is that of surface sorption, then

$$\gamma = -\frac{\partial \sigma}{\partial t} \tag{9}$$

It is convenient here to consider equilibrium conditions that can exist between the gaseous and sorbed phases. These occur when $\frac{\partial \sigma}{\partial t} = 0$ and

$$\frac{\alpha n \bar{v}}{4} \left(1 - \frac{\sigma}{\sigma_m}\right) = \xi \sigma = \frac{\sigma}{\tau_o} e^{-Qa/RT}$$

This can be written with more common variables by noting that

$$n = \frac{P}{KT} = \frac{PN_A}{RT} \quad ; \quad \bar{v} = \sqrt{\frac{8RT}{\pi M}}$$

and introducing the fractional surface coverage ϕ as

$$\phi \equiv \frac{\sigma}{\sigma_m}$$

Then, the equilibrium equation solved for the pressure is

$$P = \frac{\sigma_m \sqrt{2\pi MRT}}{N_A \tau_o e^{Q_a/RT}} \quad \frac{\phi}{1-\phi} \qquad (10)$$

Equation (10), with T = constant and Q_a = constant is a form of the relation for the Langmuir adsorption isotherm. For our purposes, it is more useful to show (10) as in Figure B-2, a plot of P vs. Q_a for a constant surface coverage, ϕ = 10% and for

$\sigma_m = 10^{15}$ mols/cm

M = 30 (a representative value)

T = 300° K

$\tau_o = 10^{-12}$ to 10^{-14} secs. (range of magnitudes)

The figure shows, in a semi-quantitative way, that appreciable surface coverages can be retained in equilibrium with very low gas pressures if the heat of sorption is high, i.e., if the molecule is strongly held to the surface. Physically sorbed layers do not exhibit Q_a's greater than about 15 kcal/gm-mole: Thus, for an appreciable sorbed layer to exist in equilibrium with a gas at pressures below about 10^{-6} torr, it must be chemisorbed.

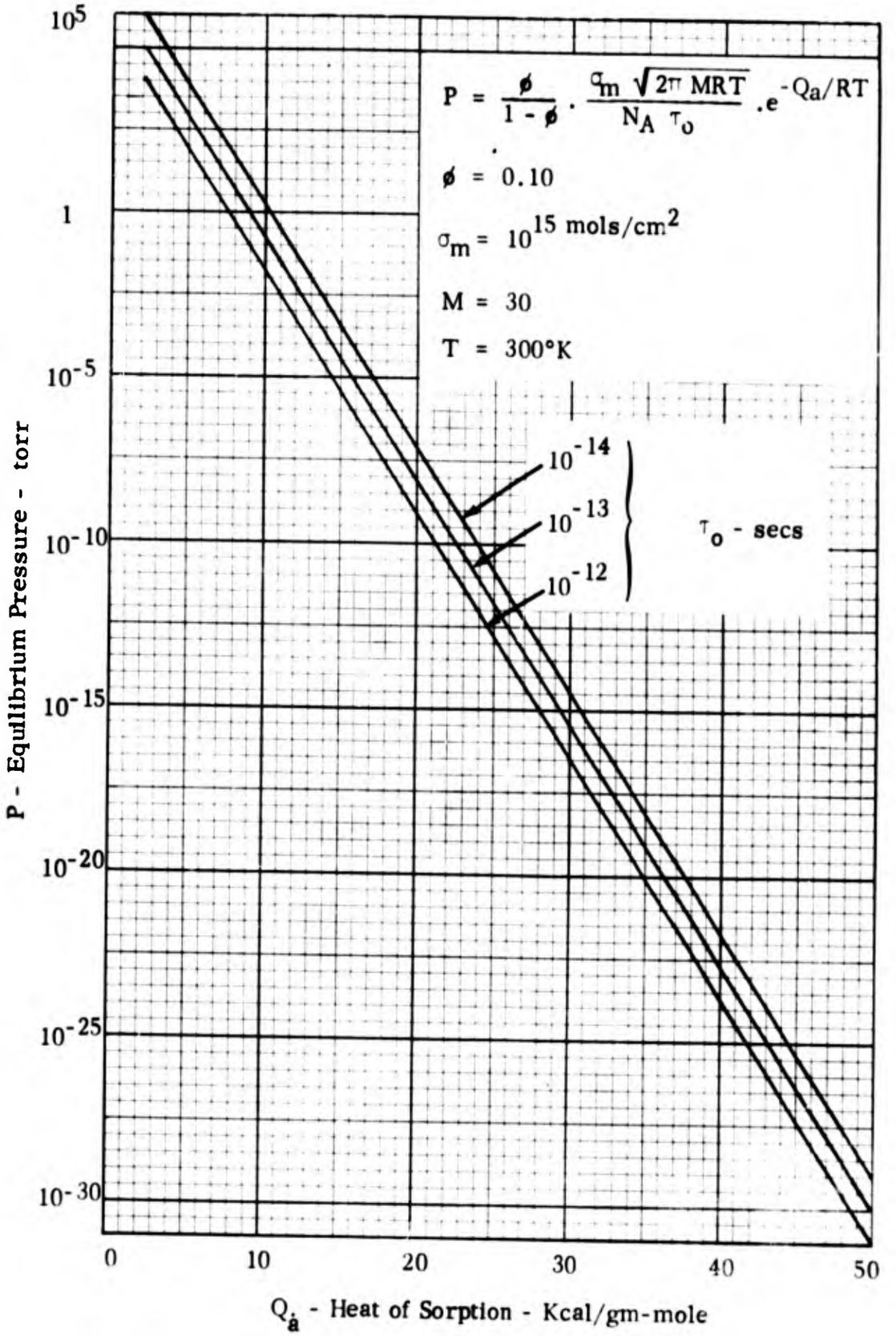

FIGURE B-2 EQUILIBRIUM PRESSURE FOR 10% SURFACE COVERAGE VS HEAT OF SORPTION

BLANK PAGE

V. DIFFUSION OF A SORBABLE GAS

A. BASIC EQUATIONS

Since sorbed molecules move about the surface of the sorbent during the time of sorption, a gas can diffuse through a porous medium by a combination of molecular motion in the gas phase and in the sorbed phase. In some cases, surface migration can become the controlling mechanism for diffusion. However, it can be shown that for most cases of interest, with powders of 10 particle size or larger, surface migration does not have a significant effect. In the analysis that follows, we will use equation (4), the gaseous diffusion equation, to describe the diffusion process; hence, the results will not be applicable to cases where surface migration controls diffusion.

In view of equation (9), equation (4) may be written

$$K \frac{\partial^2 n}{\partial x^2} = \epsilon \frac{\partial n}{\partial t} + S \frac{\partial \sigma}{\partial t} \tag{11}$$

(7) and (11) comprise a system of two partial differential equations with n and σ as dependent variables and x and t as independent variables. In principle, for appropriate initial and boundary conditions, they could be solved simultaneously to determine n and σ as functions of x and t. An analytical solution is not possible, however, because equation (7) is non-linear due to the term $\frac{\alpha n \bar{v}}{4} \cdot \frac{\sigma}{\sigma_m}$. It becomes expeditious, therefore, to consider cases where the fractional surface coverage, $\frac{\sigma}{\sigma_m}$, is small, i.e.

$$\frac{\sigma}{\sigma_m} << 1$$

Then equation (7) becomes

$$\frac{\partial \sigma}{\partial t} = \frac{\alpha n \bar{v}}{4} - \xi \sigma \tag{12}$$

which is linear.

The boundary and initial conditions of interest are

$$\frac{\partial n}{\partial x} (0, t) = 0 \tag{13}$$

$$n (x,o) = n_1 \tag{14}$$

$$\sigma\ (x,\ o) = \sigma_i \tag{15}$$

$$n\ (L,\ t) = n_L \tag{16}$$

Analytical solutions to equations (12) and (11) with the boundary conditions (13), (14), (15) and (16) have been obtained. Before describing the solution, it is convenient to write the equations and boundary conditions in dimensionless form. We define

$$R_1 \equiv \frac{\alpha \bar{v} S}{4 \epsilon \xi}$$

$$R_2 \equiv \frac{4k}{\alpha \bar{v} S L^2}$$

$$y \equiv \frac{x}{L}$$

$$\theta \equiv \xi\ t$$

$$\bar{n} \equiv \frac{n}{n_i}$$

and

$$\bar{\sigma} \equiv \frac{\sigma}{\sigma_i}$$

Then (12) becomes

$$\frac{\partial \bar{\sigma}}{\partial \theta} + \bar{\sigma} - \frac{\alpha \bar{v} n_i}{4 \epsilon \sigma_i} \cdot \bar{n} = 0 \tag{17}$$

and (11) becomes

$$R_2 \frac{\partial^2 n}{\partial y^2} - \frac{1}{R_1} \frac{\partial \bar{n}}{\partial \theta} - \frac{4 \epsilon \sigma_i}{\alpha \bar{v} n_i} \cdot \frac{\partial \sigma}{\partial \theta} = 0 \tag{18}$$

For most cases of interest the interstitial gas and the sorbed phase may be considered initially at equilibrium so that from (12)

$$\frac{\alpha n_i \bar{v}}{4} = \sigma_i$$

or

$$\frac{\alpha n_i \bar{v}}{4\sigma_i} = 1$$

Then (17) and (18) become

$$\frac{\partial \bar{\sigma}}{\partial \theta} + \bar{\sigma} - \bar{n} = 0 \tag{19}$$

and

$$R_2 \frac{\partial^2 n}{\partial y^2} - \frac{1}{R_1} \frac{\partial \bar{n}}{\partial \theta} - \frac{\partial \bar{\sigma}}{\partial \theta} = 0 \tag{20}$$

with boundary and initial conditions

$$\frac{\partial \bar{n}}{\partial y} (0, \theta) = 0 \tag{21}$$

$$\bar{n} (y, o) = 1 \tag{22}$$

$$\bar{\sigma} (y, 0) = 1 \tag{23}$$

and

$$\bar{n} (1,\theta) = \frac{n_L}{n_i} \bar{n}_L \tag{24}$$

B. EXACT SOLUTION TO EQUATIONS

The exact solutions for $\bar{n}$ and $\bar{\sigma}$ as functions of y and θ are

$$\bar{n} = (1-\bar{n}_L) \sum_{m_{odd}} (-1)^{\frac{m-1}{2}} \frac{4}{m\pi} \left[\frac{\lambda_m (1-u_m) e^{-u_m \theta} - u_m (1-\lambda_m) e^{-\lambda_m \theta}}{\lambda_m - u_m} \right] \cos \frac{m\pi y}{2} + \bar{n}_L \tag{25}$$

and

$$\bar{\sigma} = (1-\bar{n}_L) \sum_{m_{odd}} (-1)^{\frac{m-1}{2}} \frac{4}{m\pi} \left[\frac{\lambda_m e^{-\mu_m \theta} - \mu_m e^{-\lambda_m \theta}}{\lambda_m - \mu_m} \right] \cos \frac{m\pi y}{2} + \bar{n}_L \tag{26}$$

where

$$\lambda_m, \mu_m = \frac{1}{2} \left[\frac{m^2\pi^2}{4} R_1 R_2 + R_1 + 1 \pm \sqrt{\left(\frac{m^2\pi^2}{4} R_1 R_2 + R_1 + 1\right)^2 - m^2\pi^2 R_1 R_2} \right] \tag{27}$$

The solution is sufficiently complicated that it is not easy to gain physical insight into the problem by its inspection. However, calculations for several cases of interest using (25), (26) and (27) have shown that certain terms may frequently be neglected. An approximate solution which gives accurate results for many cases of interest and whose simplified form enables some insight into the physical process is described below.

C. APPROXIMATE SOLUTION TO EQUATIONS

To obtain an approximate solution, we examine the order of magnitude of terms in the differential equations (19) and (20) for cases of interest. For example, consider the evacuation of a 1-cm thick layer of powder with 10μ particle size, with 10% of the particle surface area initially covered by a sorbed layer (i.e., $\frac{\sigma}{\sigma_m}$ - = 0.1) in equilibrium with the interstitial gas. Assume the gas is water vapor, the sorbed layer is physically adsorbed and the temperature of the medium is 300°K. Then

$$L = 1 \text{ cm}$$

$$S \simeq 10^4 \text{ cm}^{-1}$$

$$\epsilon \simeq 0.4$$

$$\bar{v} = 5.9 \times 10^4 \frac{\text{cm}}{\text{sec.}}$$

$$Q_a \simeq 10 \frac{\text{kcal}}{\text{gm mole}} ; \quad \frac{Q_a}{RT} = \frac{10 \times 10^3}{1.986 \times 300} = 16.8$$

For $\tau_o = 10^{-13}$ secs. (an average value)

$$\xi = \frac{1}{o} e^{-Q_a/RT} = (10^{-13})\, e^{-16.8} = 5.05 \times 10^5 \text{ sec.}^{-1}$$

From equation (2):

$$K = 0.6\frac{\epsilon^2 \bar{v}}{S} = 0.6\,\frac{(0.16)\ (5.9 \times 10^4)}{10^4} = 0.566\,\frac{\text{cm}^2}{\text{sec.}}$$

Finally, we will take $\alpha = 1$.

From the above values,

$$R_1 = \frac{\alpha \bar{v} S}{4\epsilon\xi} = \frac{(1)\ (5.9 \times 10^4)\ (10^4)}{4\ (0.4)\ (5.05 \times 10^3)} = 731$$

$$R_2 = \frac{4k}{\alpha \bar{v} S L^2} = \frac{4\ (0.566)}{(1)\ (5.9 \times 10^4)\ (10^4)\ (1)} = 3.84 \times 10^{-9}$$

so that

$$R_1 >> 1$$

and

$$R_2 << 1$$

In equations (19) and (20) we may consider $\bar{n}$ and $\bar{\sigma}$ of the order unity. Then from (20) considering the orders of R_1 and R_2 above,

$$\frac{\partial \bar{\sigma}}{\partial \theta} << 1$$

and from (19)

$$\bar{\sigma} \simeq \bar{n} \tag{28}$$

Using this result, (20) may be written

$$R_2 \frac{\partial^2 n}{\partial y^2} - \frac{1}{R_1}\frac{\partial \bar{n}}{\partial \theta} - \frac{\partial \bar{n}}{\partial \rho} = 0$$

in which it is evident that the second term can be neglected. Thus

$$R_2 \frac{\partial^2 n}{\partial y^2} \simeq \frac{\partial n}{\partial \rho} \tag{29}$$

The solution to (29) with the boundary conditions (21) through (24) is

$$\bar{n} = \frac{n}{n_i} = \left(1-\frac{n_L}{n_i}\right) \sum_{m_{odd}} (-1)^{\frac{m-1}{2}} \frac{4}{m\pi} \left(e^{\frac{-m^2\pi^2 R_2}{4}\theta} \right) \cos\frac{m\pi y}{2} + \frac{n_L}{n_i} \tag{30}$$

According to (28), the variation of $\bar{\sigma}$ with y and θ is also given by (30). This approximate solution may be applied when $R_1 >> 1$ and $R_2 << 1$. These conditions will generally be met by layers of fine powders (10-100μ or less) of 1 cm or more, and gases with heats of adsorption greater than 10 $^{kcal}/_{gm\text{-}mole}$. Before applying (30) to a particular case, however, one should make sure that $R_1 >> 1$ and $R_2 << $. In all the examples to be discussed subsequently, (30) has been found to be applicable. In (30) an evacuation process is one in which $\frac{n_L}{n_i} < 1$ while pressurization is represented by $\frac{n_L}{n_i} > 1$. The form of (30) is convenient for the evacuation process but is somewhat misleading for a pressurization process in which, for example, $n_i = 0$. A more appropriate form for the pressurization process is obtained by multiplying (30) by $\frac{n_i}{n_L}$ and rearranging, viz.

$$\frac{n}{n_L} = 1-\left(1-\frac{n_i}{n_L}\right) \sum_{m_{odd}} (-1)^{\frac{m-1}{2}} \frac{4}{m\pi} \left(e^{\frac{-m^2\pi^2 R_2 \theta}{4}} \right) \cos\frac{m\pi y}{2} \tag{31}$$

BLANK PAGE

VI. THE CHARACTERISTIC TIME

In discussing evacuation and pressurization processes described by (30) or (31), it is convenient to define a characteristic time, t_c, such that

$$\frac{\pi^2 R_2}{4} \rho_c = \frac{\pi^2 R_2}{4} \varrho t_c = 1$$

or

$$t_c = \frac{\alpha \bar{v} S L^2 \tau_o}{\pi^2 K} e^{Q_{a/RT}}$$

At such time, the magnitude of the second term in the series of (30) or (31) (corresponding to m = 3) will be about $\frac{1}{3} e^{-8} \simeq \frac{1}{9000}$ times the magnitude of the first term; each subsequent term will be correspondingly smaller. Hence, at time t_c (or any greater time) the solution may be closely approximated by only the first term of the series. Thus, at $t = t_c$ for an evacuation process

$$\frac{n}{n_i} \simeq \left(1 - \frac{n_L}{n_i}\right)\left(\frac{4}{\pi e}\right) \cos \frac{\pi y}{2} + \frac{n_L}{n_i}$$

and for a pressurization process

$$\frac{n}{n_L} \simeq 1 - \left(1 - \frac{n_i}{n_L}\right)\left(\frac{4}{\pi e}\right) \cos \frac{\pi y}{2}$$

The distributions of $\frac{n}{n_i}$ and $\frac{\sigma}{\sigma_i}$ for pressurization process, at time $t = t_c$ are shown in Figure B-3. The characteristic time may be considered as one in which a substantial part of the response to the pressure change at the boundary y = 1 has been accomplished. The characteristic time for the example of Appendix B, Section V, paragraph C, but for various heats of sorption, is shown in Figure B-4.

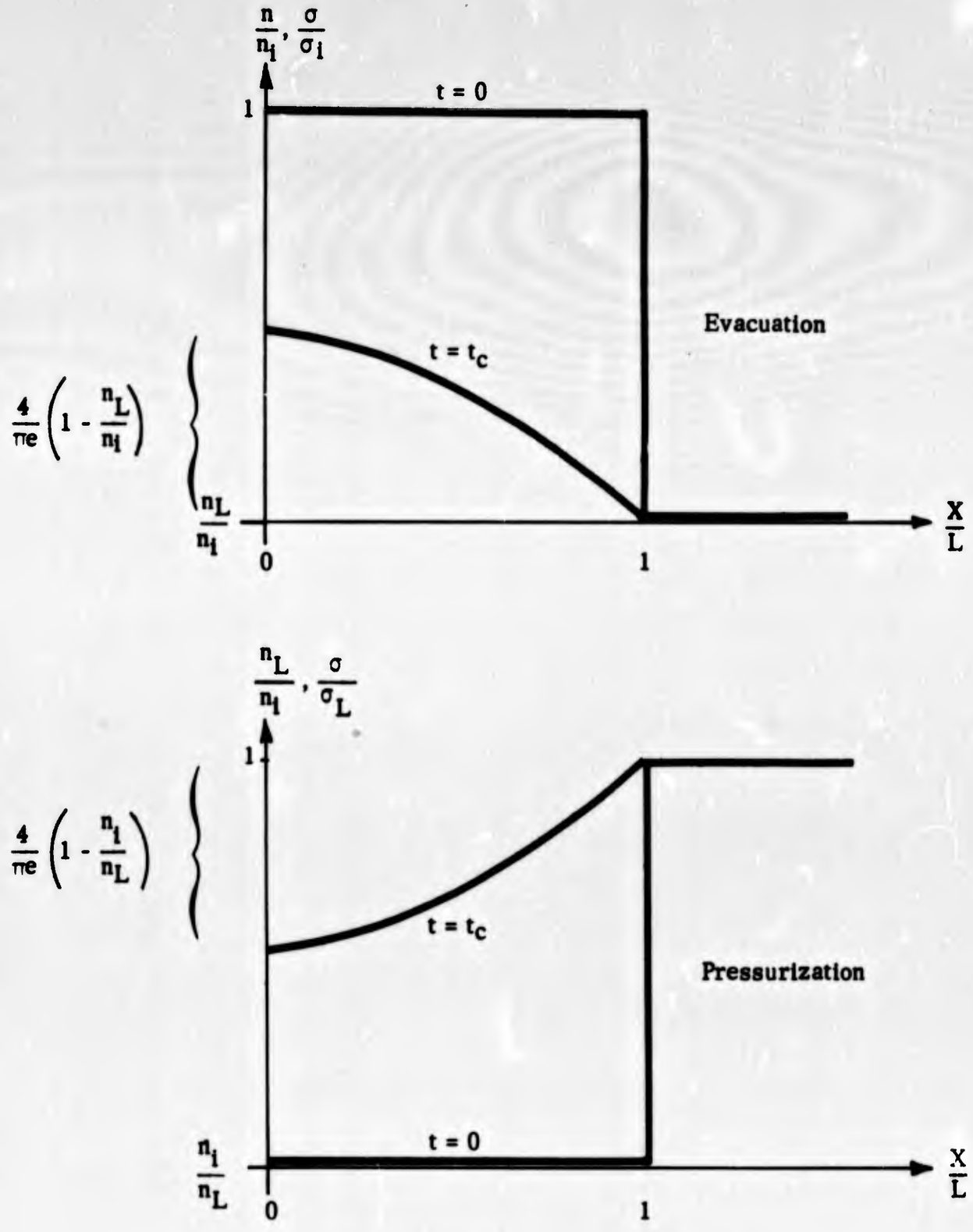

FIGURE B-3 CONDITIONS AT THE CHARACTERISTIC TIME

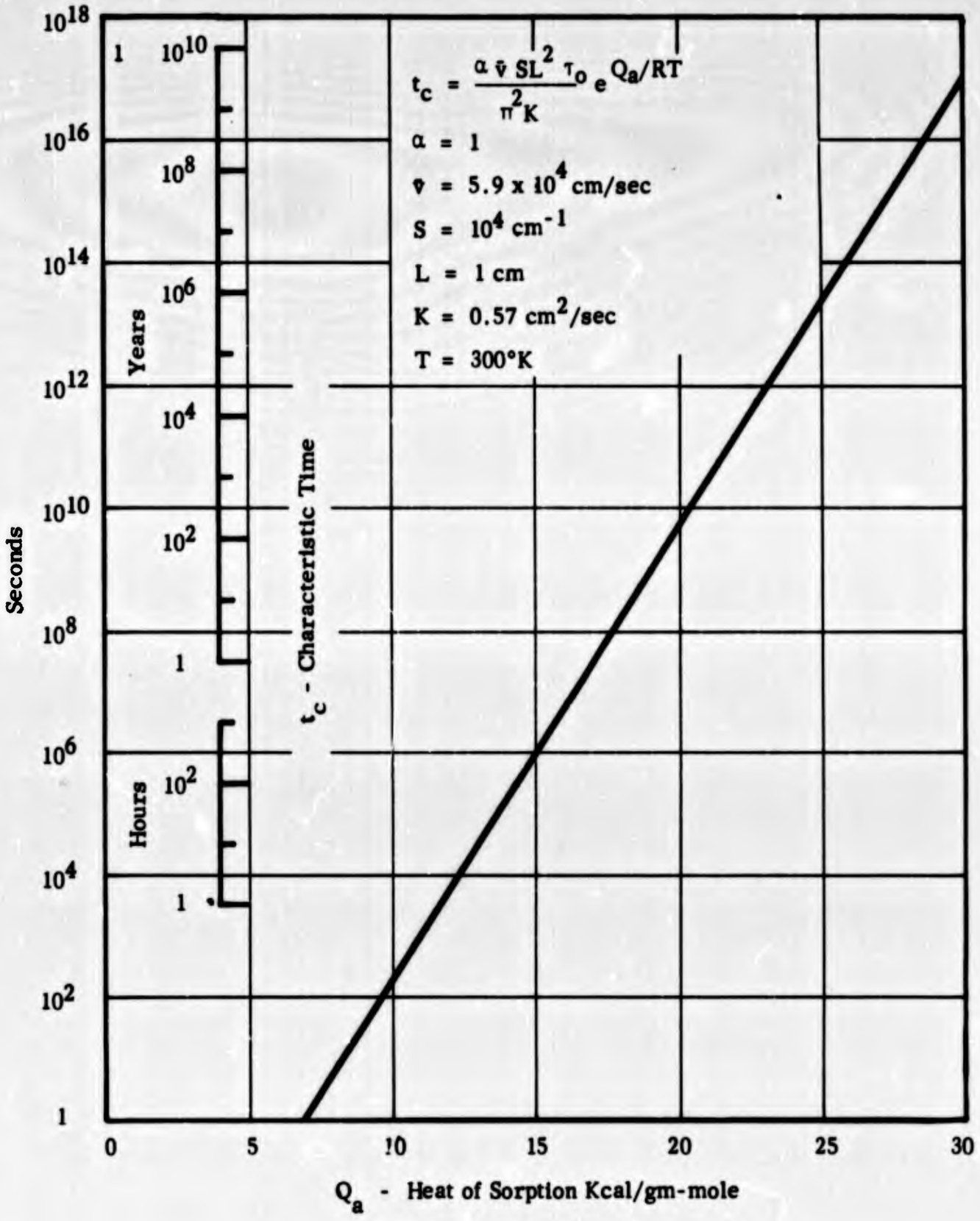

FIGURE B-4 CHARACTERISTIC TIME VS HEAT OF SORPTION

BLANK PAGE

VII. ILLUSTRATIVE CASES

A. EFFECT OF DISPOSITION OF POWDER ON DEGASSING ITS SURFACE

If a fine powder is spread out so that essentially all its surface is exposed and the surrounding pressure drops to and remains at zero (or a very low value), the surface coverage of a particular gas specie would decrease according to

$$\frac{\partial \sigma}{\partial t} = -\xi\sigma$$

i.e., equation (7) with n = 0. Thus

$$\frac{\sigma}{\sigma_i} = e^{-\xi t}$$

would describe the time decay of σ. Now if the powder is disposed in a layer with only one boundary exposed to a region where the pressure drops to and remains at zero, such as in Figure B-1, and we assume the gas and powder to be such that equation (30) can be applied, the time decay of σ for times comparable to t_c, is described by

$$\frac{\sigma}{\sigma_i} \simeq \frac{4}{\pi} e^{\frac{-\pi^2 R_2 \xi t}{4}} \cos \frac{\pi y}{2}$$

The time scale of the surface coverage decay for the layer of powder is $\frac{\pi^2 R_2}{4}$ times that for the completely exposed powder. R_2 may be written as

$$R_2 = 4 \frac{K/L^2}{\alpha \bar{v} S}$$

$\frac{K}{L^2}$ is a kind of rate constant for the gas diffusion process while $\alpha\bar{v}S$ describes the rate at which re-adsorption takes place. Thus,

$$R_2 = \frac{\text{Rate of diffusion}}{\text{Rate of re-adsorption}}$$

For fine powders (10-100μ) in layers of nominal thickness (say 1 cm) R_2 is very small. In the example of Section V-C, R_2 was of the order of 10^{-8}. To reach a certain value of $\frac{\sigma}{\sigma_i}$, would take 10^8 times as long as if the powder surface was all directly exposed to a very low pressure. Hence, the dispostion of the powder in a layer, where a desorbed molecule can be readsorbed many times before it diffuses out of the bed, greatly reduces the rate at which the surfaces will degas in vacuo.

B. CONTAMINATION OF A CLEAN POWDER

Suppose the 1-cm thick powder layer described in Section V-C has initially uncontaminated surfaces and is then exposed to a gas pressure of 10^{-9} torr. From Figure B-2, and noting that for low surface coverage $p \propto \phi$, only gases with heats of sorption greater than about 18 $^{kcal}/_{gm\text{-}mole}$ could form sorbed layers of $\phi \geq 0.01$. The time to form a 1% sorbed unimolecular layer on a surface directly exposed to the low pressure may be estimated from

$$t = \frac{\phi \sigma_m}{\alpha n \bar{v}/4}$$

For a pressure of 10^{-9} torr, $n = 3.7 \times 10^7$ $^{mol}/_{cm^3}$ and

$$t = \frac{4(.01)\ (10^{15})}{(1)\ (3.7 \times 10^7)(5.9 \times 10^4)} \simeq 18 \text{ secs.}$$

However, Figure B-4 shows that the characteristic time for a 1-cm layer and $Q_a = 18$ $^{kcal}/_{gm\text{-}mole}$ is about 10^8 secs. (over 3 years). For larger Q_a the characteristic time can be significantly higher.

Thus, although the surfaces directly exposed to even the low pressure of 10^{-9} torr can quickly become contaminated by strongly sorbed gases, the powder beneath the exposed boundary of the layer will remain uncontaminated for a long time. The same mechanisms which make the surface degassing of strongly held molecules from a powder layer exceedingly slow (as discussed in the previous section) also greatly retard contamination.

C. EFFECTS OF TEMPERATURE

The influence of temperature on both equilibrium and dynamic conditions is felt chiefly through its effect on the quantity ξ, the desorption rate constant, which is exponentially dependent on $Q_{a/RT}$. The abscissas of Figures B-2 and B-4 could have been $Q_{a/RT}$ rather than just Q_a, so the equilibrium conditions and the characteristic time for a gas with Q_{a_1} at some temperature other than 300°K (for which the figures are drawn) can be roughly ascertained by considering it to have a Q_a of $Q_{a_1} \frac{(300)}{T}$

If a powder layer contains sorbed gases with heats of sorption over about 15 $^{kcal}/_{gm\text{-}mole}$, Figure B-4 shows that exposure to vacuum at 300°K is not an effective means for degassing the surface in any reasonable time. By elevating the temperature to 600°K, gases with Q_a up to about 24 $^{kcal}/_{gm\text{-}mole}$ can be desorbed from the powder layer in vacuum in the order of 10 hours.

On the other hand, an initially uncontaminated powder layer at 600°K in a vacuum of 10^{-9} torr will not form an appreciable equilibrium sorbed layer of any gas with Q_a less than about 36 $^{kcal}/_{gm\text{-}mole}$ and will resist contamination by gases with $Q_a > 36$ $^{kcal}/_{gm\text{-}mole}$ for long periods of time.

APPENDIX C

DEVELOPMENT OF EXPRESSIONS USED IN LINE HEAT SOURCE ERROR ANALYSIS

I. BASIC EQUATIONS

The temperature distribution in an isotropic medium satisfies the well know diffusion equation.

$$\nabla^2 T - \frac{1}{\alpha}\frac{dT}{dt} = \frac{q_v}{k} \tag{1}$$

with the boundary conditions

$$k_1 \frac{\partial T_1}{\partial \vec{n}} - k_2 \frac{\partial T_2}{\partial \vec{n}} = 0 \tag{2}$$

$$T_1 + \frac{k_1}{h}\frac{\partial T_1}{\partial \vec{n}} - T_2 = 0 \tag{3}$$

at any interface. $\frac{\partial}{\partial \vec{n}}$ is the derivative normal to the boundary; T_1 and T_2 are the temperatures at the boundary in the first and second mediums, respectively. The variable h, the "transfer coefficient" at the interface, is essentially an empirical constant introduced to account for surface effects.

Equation (1) can be shown to be satisfied in infinite regions by functions of the form

$$T(\vec{r},t) = \frac{1}{2\pi k}\int_{-\infty}^{t}\int_{v}\frac{q_v(r',\tau)\exp[-(r-r')^2/4\alpha(t-\tau)]}{4(a\pi)^{1/2}(t-\tau)^{3/2}}\,dv'd\tau \tag{4}$$

(see for example Carslaw and Jaeger, 1959). $\vec{r}$ is the position vector of the point of observation and r' that of the volume element v'. In the event that a bounded region is being investigated a correction term for the effects of boundaries must be included. If we consider an infinite line source of heat lying along the z axis to which power is supplied at the rate qe per unit length such that

$$\begin{aligned} q(t) &= 0 \qquad & t < 0 \\ q(t) &= q \qquad & t \geq 0 \end{aligned} \tag{5}$$

then Equation (4) may be written

$$T(r,t) = \frac{1}{2\pi k} \int_0^t \int_{-\infty}^{\infty} \frac{q \exp\left[-(r^2+z'^2)/4\alpha(t-\tau)\right]}{4(\alpha\pi)^{1/2}(t-\tau)^{3/2}} \, dz' \, d\tau \tag{6}$$

For simplicity, it is appropriate to introduce the dimensionless variables

$$\begin{aligned} \bar{T} &= 4\pi k\, T/q & \bar{t} &= 4\alpha t/r^2 \\ \zeta &= z'/r & \bar{\tau} &= 4\alpha\tau/r^2 \end{aligned} \tag{7}$$

into Equation (6) resulting in

$$\bar{T}(\bar{t}) = \frac{1}{\sqrt{\pi}} \int_0^{\bar{t}} \int_{-\infty}^{\infty} \frac{\exp\left[-(1+\zeta^2)/(\bar{t}-\bar{\tau})\right]}{(\bar{t}-\bar{\tau})^{3/2}} \, d\zeta \, d\bar{\tau} \tag{8}$$

$$= \int_0^{\bar{t}} \frac{\exp\left[-1/(\bar{t}-\bar{\tau})\right]}{(\bar{t}-\bar{\tau})} \, d\bar{\tau} \tag{9}$$

Let

$$\bar{t} - \bar{\tau} = \frac{1}{u} \tag{10}$$

Then

$$\bar{T}(\bar{t}) = \int_{1/\bar{t}}^{\infty} \frac{\exp\left[-u\right]}{u} \, du \tag{11}$$

The terms on the right are of course the negative of the well known exponential integral whose argument is $-(1/\bar{t})$, hence, we may write

$$\bar{T}(\bar{t}) = Ei(-1/t) \tag{12}$$

It is worth noting that when the source function is of the form given by Equation (5), the variables $(t - \tau)$ and $(\bar{t} - \tau)$ in the integrand (6 et seq.) may be replaced by τ and $\bar{\tau}$, respectively, with no change in the value of the integral.

BLANK PAGE

II. FINITE LINE SOURCE IN AN INFINITE MEDIUM

In the event that the line source is not infinite but terminates at a distance $\pm\ell/2$ from the point $z = 0$ the temperature distribution may be found by setting the limits of integration of (8) at

$$\zeta = \pm \ell/2r \equiv \pm\lambda/2 \tag{13}$$

Thus, the temperature at $z = 0$ is given by

$$\bar{T} = \frac{1}{\pi^{1/2}} \int_0^{\bar{t}} \int_{\lambda/2}^{\lambda/2} \frac{\exp\left[- (1 + \zeta^2)/(\bar{t} - \bar{\tau})\right]}{(\bar{t} - \bar{\tau})^{3/2}} \, d\zeta \, d\bar{\tau} \tag{14}$$

$$= \frac{2}{\pi^{1/2}} \int_0^{\bar{t}} \int_0^{\lambda/2} \frac{\exp\left[- (1 + \zeta^2)/\bar{\tau}\right]}{\bar{\tau}^{3/2}} \, d\zeta \, d\bar{\tau} \tag{15}$$

$$= \frac{2}{\pi^{1/2}} \int_0^{\bar{t}} \int_0^{\infty} \frac{\exp\left[- (1 + \zeta^2)/\bar{\tau}\right]}{\bar{\tau}^{3/2}} \, d\zeta \, d\bar{\tau} \tag{16}$$

$$- \frac{2}{\pi^{1/2}} \int_0^{\bar{t}} \int_{\lambda/2}^{\infty} \frac{\exp\left[- (1 + \zeta^2)/\bar{\tau}\right]}{\bar{\tau}^{3/2}} \, d\zeta \, d\bar{\tau}$$

The second term on the right of Equation (16) represents the difference between the infinite line source and that of the finite line source. To evaluate this term, we may write

$$I = - \frac{2}{\pi^{1/2}} \int_0^{\bar{t}} \int_{\lambda/2}^{\infty} \frac{\exp\left[- (1 + \zeta^2)/\bar{\tau}\right]}{\bar{\tau}^{3/2}} \, d\zeta \, d\bar{\tau} \tag{17}$$

Now, by defining

$$\phi^2 = \zeta^2/\bar{\tau} \quad , \quad d\zeta = \bar{\tau}^{1/2}\, d\phi \tag{18}$$

Equation (17) becomes

$$I = -\frac{2}{\pi^{1/2}} \int_0^{\bar{t}} \frac{\exp[-1/\tau]}{\bar{\tau}}\, d\bar{\tau} \int_{\lambda/2\,\bar{\tau}^{1/2}}^{\infty} \exp[-\phi^2]\, d\phi \tag{19}$$

Integrating by parts

$$\int_{\lambda/2\,\bar{\tau}^{1/2}}^{\infty} \exp[-\phi^2]\, d\phi = \left[-\frac{\exp[-\phi^2]}{2\phi} - \int \frac{\exp[-\phi]^2}{2\phi^2}\, d\phi \right]_{\lambda/2\,\bar{\tau}^{1/2}}^{\infty} \tag{20}$$

For larger values of $\lambda/2\bar{\tau}^{1/2}$ the error introduced by neglecting the second term will be small.

Let us define

$$I' = -\frac{2}{\pi^{1/2}} \int_0^{\bar{t}} \frac{\exp[-(1+\lambda^2/4)/\bar{\tau}]}{\lambda\tau^{1/2}}\, d\bar{\tau} \tag{21}$$

By comparing Equation (19) with Equation (21) it is obvious that $|I'| > |I|$.

Now let us substitute

$$\begin{aligned} \bar{\tau} &= (1+\lambda^2/4)/u^2 \,, \\ d\bar{\tau} &= [-2(1+\lambda^2/4)/u^3]\, du \\ \bar{t} &= (1+\lambda^2/4)/u_o^2 \end{aligned} \tag{22}$$

into Equation (21) to yield

$$I' = -\frac{4}{\pi^{1/2}} \frac{(1+\lambda^2/4)^{1/2}}{\lambda} \int_{u_o}^{\infty} \frac{\exp[-u^2]}{u^2} \, du$$

$$= -\frac{4}{\pi^{1/2}} \frac{(1+\lambda^2/4)^{1/2}}{\lambda} \left\{ \left[-\frac{\exp[-u^2]}{2u^3} \right]_{u_o}^{\infty} - \frac{3}{2} \int_{u_o}^{\infty} \frac{\exp[-u^2]}{u^4} \, du \right\} \tag{23}$$

Now if we define

$$I'' = -\frac{4}{\pi^{1/2}} \frac{(1+\lambda^2/4)^{1/2}}{\lambda} \frac{\exp[-(1+\lambda^2/4)/\bar{t}]}{2[(1+\lambda^2/4)/\bar{t}]^{3/2}} \tag{24}$$

$$= -\frac{2\bar{t}^{3/2} \exp[-(1+\lambda^2/4)/\bar{t}]}{\pi^{1/2} \lambda (1+\lambda^2/4)} \tag{25}$$

Then

$$|I|'' > |I'| > |I|$$

and, thus, I" provides an upper bound for the error caused by neglecting the finite length of the wire.

BLANK PAGE

III. FINITE SOURCE IN A FINITE MEDIUM

In order to investigate the effects of finite dimensions of the heater and thermocouple wires we shall make use of the model shown in Figure VIII-3. A heater wire of length ℓ and radius a contains heat sources of strength q per unit length distributed evenly throughout the volume. The wire lies along the z axis with its center at the point $z = 0$. The temperature at $z = \pm\ell/2$ is held constant, both at the ends of the heater wire and at the ends of the sample. Contact resistance between the wire and the sample is assumed to be negligible.

The solution to this problem is best handled with the Laplace transform. As a detailed treatment of the method is available in many elementary texts as well as in standard works on heat flow (see, for example, Carslaw and Jaeger, 1959), only the main features need be summarized here.

The Laplace transform pair is defined by the relationships:

$$f(t) = \frac{1}{2\pi i} \int_{\delta - i\infty}^{\delta + i\infty} f^*(p)\, e^{pt}\, dp \tag{26}$$

$$f^*(p) = \int_0^{\infty} e^{-pt} f(t)\, dt \tag{27}$$

We can designate the transform operator $L\{\ \}$ as

$$f^*(p) = L\{ f(t) \} \tag{28}$$

Then defining new transformed variables as

$$T^* = L\{T\} \qquad \bar{T}^* = L\{\bar{T}\}$$
$$q^* = L\{q\} \tag{29}$$

and substituting them into Equation (1), Equation (1) reduces to

$$\nabla^2 T^* - \frac{p}{\alpha} T^* = \frac{q^*}{k} \tag{30}$$

Equations (2) and (3) remain the same after transformation except for the substitution of T* for T.

In circular cylindrical co-ordinates where there is symmetry about the z axis Equation (30) becomes

$$\frac{1}{r}\frac{\partial}{\partial r}\left(r\frac{\partial T^*}{\partial r}\right) + \frac{\partial^2 T^*}{\partial z^2} - \frac{p}{\alpha}T^* = -\frac{q_v^*}{k_1} \tag{31}$$

The appropriate boundary conditions are

$$\left.\begin{aligned} k_1\frac{\partial T_1^*}{\partial r} &= k_2\frac{\partial T_2^*}{\partial r} \\ T_1^* &= T_2^* \end{aligned}\right\} \quad \text{at } r = a \tag{32}$$

$$T^* = 0 \quad \text{at } z = \pm l/2 \tag{33}$$

$$q_v = q/\pi a^2 \tag{34}$$

Upon transformation, Equation (34) yields

$$\begin{aligned} q_v^* &= \frac{1}{\pi a^2}\int_0^\infty q\, e^{-pt}\, dt \\ &= q/\pi a^2 p \end{aligned} \tag{35}$$

Solutions of the homogeneous part of Equation (31) may be obtained by writing

$$T^* = R(r)Z(z) \tag{36}$$

and, hence,

$$\frac{1}{R}\frac{1}{r}\frac{\partial}{\partial r}\left(r\frac{\partial R}{\partial r}\right) + \frac{1}{Z}\frac{\partial^2 Z}{\partial Z^2} - \frac{p}{\alpha} = 0 \tag{37}$$

We may now define

$$\frac{1}{Z}\frac{\partial^2 Z}{\partial Z^2} = -b^2 \tag{38}$$

which has solutions

$$Z = C_1 \sin bx + C_2 \cos bx \tag{39}$$

and since $Z = 0$ at $z = \pm \ell/2$

$$b = (2n + 1)\pi/\ell \tag{40}$$

and

$$Z = \cos[(2n + 1)\pi/\ell] \tag{41}$$

From Equations (37) and (38)

$$\frac{1}{r}\frac{\partial}{\partial r}\left(r\frac{\partial R}{\partial r}\right) - \left[(2n + 1)^2\frac{\pi^2}{\ell^2} + p/\alpha\right] R = 0 \tag{42}$$

which is immediately recognizable as a form of Bessel's equation with solutions

$$R = a_m I_o(\beta_m^n r) + b_m K_o(\beta_m^n r) \tag{43}$$

where

$$\beta_m^n = \left[(2m + 1)^2\frac{\pi^2}{\ell^2} + \frac{p}{\alpha_n}\right]^{1/2} \tag{44}$$

a_n and b_n are arbitrary constants.

If we look for a particular solution of Equation (31) we see that the function

$$T^* = \frac{q_v^* \alpha_1}{kp}\left[1 - \frac{e^{\gamma z} + e^{-\gamma z}}{e^{\gamma \ell/2} + e^{-\gamma \ell/2}}\right] \tag{45}$$

where

$$\gamma = [p/\alpha_1]^{1/2} \tag{46}$$

satisfies the equation as well as the requirements of symmetry and boundary temperatures within the heater wire.

Since the temperature must remain finite both at $r = 0$ and as $r \to \infty$

$$T_1^* = \sum_{m=0}^{\infty} a_m I_o(\beta'_m r) \cos(\mu_m z) + \frac{q_v^* \alpha_1}{k_1 p} \left[1 - \frac{\cosh \gamma z}{\cosh(\gamma \ell/2)} \right] \tag{47}$$

$$T_2^* = \sum_{m=0}^{\infty} b_m K_o(\beta_m^2 r) \cos(\mu_m z) \tag{48}$$

where

$$\mu_m \equiv (2m + 1)\pi/\ell \tag{49}$$

In order to evaluate the constants a_m and b_m the second term of Equation (47) must be expanded in a Fourier series in the region $x = \pm\ell/2$.

To do this we write

$$1 - \frac{\cosh \gamma z}{\cosh \gamma \ell} \equiv \sum_{m=0}^{m} c_m \cos(\mu_m z) \tag{50}$$

Multiplying both sides by $\cos(\mu_n z)$ and integrating from $z = -\ell/2$ to $z = +\ell/2$ results in

$$\frac{2(-1)^m}{\mu_m} \left(\frac{\gamma^2}{\gamma^2 + \mu_m^2} \right) = c_m \ell/2 \tag{51}$$

or

$$c_m = \frac{4(-1)^m}{(2m+1)\pi} \left(\frac{\gamma^2}{\gamma^2 + \mu_m^2} \right) \tag{52}$$

Now if we define

$$d_m = \frac{q_v^* \alpha_1}{k_1 p} \left\{ \frac{4(-1)^m}{\pi(2m+1)} \left(\frac{\gamma^2}{\gamma^2 + \mu_m^2} \right) \right\} \tag{53}$$

and substitute this into Equation (47) we get

$$T_1^* = \sum_{m=0}^{\infty} [a_m I_o(\beta_m^1 r) + dm] \cos(\mu_m z) \tag{54}$$

Introducing the boundary condition (3) for the case of no contact resistance.

$$\sum_{m=0}^{\infty} [a_m I_o(\beta_m^1 a) - b_m K_o(\beta_m^2 a) + d_m] \cos(\mu_m z) = 0 \tag{55}$$

Since this must hold for all values of z and m

$$a_m I_o(\beta_m^1 a) - b_m K_o(\beta_m^2 a) = -d_m \tag{56}$$

Boundary condition (2) becomes

$$\left[k_1 \frac{\partial T_1^*}{\partial r} - \frac{k_2 \partial T_2^*}{\partial r} \right]_{r=a} = 0 \tag{57}$$

and substituting for T_1^* and T_2^* in Equation (57) yields

$$\sum_{m=0}^{\infty} [k_1 \; a_m \beta_m^1 \; I_1 (\beta_m^1 a) + k_2 \; b_m \beta_m^2 K_1 (\beta_m^2 a)] \cos (\mu_m z) = 0 \tag{58}$$

Therefore,

$$a_m k_1 \beta_m^1 I_1 (\beta_m^1 a) + b_m k_2 \beta_m^2 K_1 (\beta_m^2 a) = 0 \tag{59}$$

Solving Equations (56) and (59) for b_m results in

$$b_m = d_m \frac{k_1 \beta_m^1 I_1 (\beta_m^1 a)}{k_2 \beta_m^2 I_o (\beta_m^1 a) K_1 (\beta_m^2 a) + k_1 \beta_m^1 I_1 (\beta_m^1 a) K_o (\beta_m^2 a)} \tag{60}$$

Since we are interested in the dimensionless temperature we may rewrite Equation (48) as

$$\bar{T}_2^* \equiv \frac{4\pi K_2}{q} \sum_{m=0}^{\infty} b_m K_o (\beta_m^2 r) \cos (\mu_m z) \tag{61}$$

$$= \sum_{m=0}^{\infty} \bar{b}_m K_o (\beta_m^2 r) \cos (\mu_m z) \tag{62}$$

From Equations (60), (53), and (35)

$$\bar{b}_m = \frac{16\,\alpha_1}{\pi p^2 a^2} \frac{(-1)^m}{(2m+1)} \left(\frac{\gamma^2}{\gamma^2 + \mu_m^2}\right) \beta_m^1 I_1(\beta_m^1 a) \Big/$$

$$\left[\beta_m^2 I_o(\beta_m^1 a) K_1(\beta_m^2 a) + \frac{k_1}{k_2} \beta_m^1 I_1(\beta_m^1 a) K_o(\beta_m^2 a)\right] \tag{63}$$

Substitution of Equation (63) into Equation (62) yields the transform of the dimensionless temperature for the most general case. Fortunately, for many special cases this can be reduced considerably. If we consider only the temperature at the mid-point of the wire, Equation (62) reduces to

$$\bar{T}_2^* = \sum_{m=0}^{\infty} \bar{b}_m K_o(\beta_m^2 r) \tag{64}$$

For the remainder of this discussion we shall consider only the temperature at this point.

BLANK PAGE

IV. INFINITELY LONG HEATER WIRE OF FINITE RADIUS

As

$$\begin{aligned} &\ell \to \infty \\ &\beta_m^n \to [p/\alpha_n]^{1/2} \\ &\equiv \beta^{11} \end{aligned} \tag{65}$$

and

$$\bar{T}_2^* \to \frac{16\alpha_1}{\pi p^2 a^2}\left[\sum_{m=0}^{\infty}\frac{(-1)^m}{(2m+1)}\right] \beta^1 I_1(\beta_a^1) K_0(\beta^2 r)/$$

$$\left[\beta^2 I_0(\beta^1 a) K_1(\beta^2 a) + \frac{k_1}{k_2}\beta^1 I_1 K_0(\beta^2 a)\right] \tag{66}$$

$$= \frac{4\alpha_1}{p^2 a^2} \beta^1 I_1(\beta^1 a) K_0(\beta^2 r)/$$

$$\left[\beta^2 I_0(\beta^1 a) K_1(\beta^2 a) + \frac{k_1}{k_2}\beta^1 I_1(\beta^1 a) K_0(\beta^2 a)\right] \tag{67}$$

If we make the further restriction that a is very small but not infinitesimal we may make use of the asymptotic values of the Bessel functions

$$\begin{aligned} I_0(x) &\sim 1 & K_0(x) &\sim -\log x \\ I_1(x) &\sim x/2 & K_1(x) &\sim 1/x \end{aligned} \tag{68}$$

causing Equation (67) to reduce to

$$\bar{T}_2^* = \frac{\frac{2}{p} K_0(r\sqrt{p/\alpha_2})}{1 + \frac{k_1}{2k_2}\frac{pa^2}{\alpha_1} K_0(a\sqrt{p/\alpha_2})} \tag{69}$$

This may be further specialized in several ways.

If $a \to 0$

$$\bar{T}^{*} \rightarrow \frac{2}{p} K_o (r\sqrt{p/\alpha}) \tag{70}$$

and thus from Equation (12)

$$L \left\{ - E_i (- 1/\bar{t}) \right\} = \frac{2}{p} K_o (r\sqrt{p/\alpha}) \tag{71}$$

It should be noted that the difference between Equations (69) and (70) is mostly due to the thermal properties of the wire rather than the geometrical effects of the heat being liberated closer to the measuring point. The proof of this is that if we let the conductivity of the wire get very large and the specific heat become very small the second term of the denominator vanishes.

V. HEAT LEAKS AT END OF SAMPLE

For the very thin wire in a finite sample, the denominator of Equation (63) disappears in the same manner as it did in Equation (70), resulting in

$$\bar{T}_2^* = \frac{8}{\pi p} \sum_{m=0}^{\infty} \frac{(-)^m}{(2m+1)} K_o(\beta_m^2 r) \tag{72}$$

Now, if we let

$$p = \eta - (2m+1)^2 \frac{\pi^2}{l^2} \alpha_2 \tag{73}$$

$$\equiv \eta - C_m$$

$$\beta_m^2 = r\sqrt{\eta/\alpha_2} \tag{74}$$

Then, Equation (72) becomes

$$\bar{T}_2^* = \frac{8}{\pi} \sum_{m=0}^{\infty} \frac{(-1)^m}{2m+1} \left\{ \frac{K_o(r\sqrt{\eta/\alpha_2})}{\eta - C_m} \right\} \tag{75}$$

From Equation (26)

$$\bar{T}_2 = \frac{8}{\pi} \sum_{m=0}^{\infty} \frac{(-1)^m}{(2m+1)} \exp(-C_m t) \left\{ \frac{1}{2\pi} \int_{C_m+\delta-\infty}^{C_m+\delta\infty} \frac{K_o(r\sqrt{\eta/\alpha_2})\exp(\eta t)}{\eta - C_m} d\eta \right\} \tag{76}$$

Now, the portion in the braces { } is obviously the function whose transform is

$$K_o(r\sqrt{\eta/\alpha_2})/(\eta - C_m) \tag{77}$$

If we take η as a new transform variable

$$L\{\exp(C_m t)\} = 1/(\eta - C_m) \tag{78}$$

and $$L\left\{ \exp(-r^2/4\alpha t)/2t \right\} = K_o(r\sqrt{\eta/\alpha_2}) \tag{79}$$

Now making use of the well known theorem for Laplace transforms

$$f^*(p)\, g^*(p) = L\left\{ \int_0^t f(t-s)\, g(s)\, ds \right\} \tag{80}$$

$$\bar{T}_2 = \frac{4}{\pi} \sum_{m=0}^{\infty} \frac{(-1)^m}{(2m+1)} \int_0^t \frac{\exp\left[C_m(-s) - r^2/4\alpha_2 s\right] ds}{s} \tag{81}$$

If we make the substitution

$$u = r^2/4\alpha_2 s \tag{82}$$

Equation (81) becomes

$$\bar{T}_2 = \frac{4}{\pi} \sum_{m=0}^{\infty} \frac{(-1)^m}{2m+1} \int_{1/\bar{t}}^{\infty} \frac{\exp\left[-(C_m r^2/4\alpha_2 u) - u\right]}{u} du \tag{83}$$

VI. HEAT LEAKS OUT THE WIRE

To estimate whether the effects of heat leaks out the wire should be important we must remember that for the materials studied

$$\alpha_1 >> \alpha_2 \tag{84}$$

Thus in the range where the sample boundaries may be neglected,

$$\beta^2_m \approx \sqrt{p/\alpha_2} \tag{85}$$

but α_1 may be large enough that

$$\beta^1_m \approx (2m+1)\pi/\ell \tag{86}$$

In this case, for small a, Equations (64) and (63) become

$$\bar{T}_2^* \approx \frac{8}{\pi p} K_o(r\sqrt{p/\alpha_2}) \sum_{m=0}^{\infty} \frac{(-1)^m}{2m+1} \Bigg/ \left(1 + \frac{k_1}{2k_2}\left[(2m+1)\frac{\pi a}{\ell}\right]^2 K_o\left[(2m+1)\frac{\pi a}{\ell}\right]\right) \tag{87}$$

To evaluate the strictly geometrical effects of the finite radius of the probe we may replace it by a boundary at r = a through which the heat flow per unit time per unit length is q after time t = 0. Then Carslaw and Jaeger (1959, p. 338) have shown that for this case

$$\bar{T} = \frac{4}{\pi a}\int_0^{\infty}\left[\frac{1 - \exp(-\alpha_2 u^2 t)}{u^2}\right]\left\{\frac{J_o(ur)\,Y_1(ua) - Y_o(ur)\,J_1(ua)}{(J_1^2(ua) + Y_1^2(ua))}\right\} du \tag{88}$$

We may rewrite this as

$$\bar{T} = -2\int_0^\infty \left[\frac{1 - \exp(-\alpha_2 u^2 t)}{u}\right] J_o(ur)$$

$$\left\{\left[-\frac{2}{\pi ua}\left(\frac{Y_1(ua) - Y_o(ur)J_1(ua)/J_o(ur)}{J_1^2(ua) + Y_1^2(ua)}\right) - 1\right] + 1\right\} du \tag{89}$$

and then define ϵ such that

$$T \equiv -2\int_0^\infty \left[\frac{1 - \exp(-\alpha_2 u^2 t)}{u}\right] J_o(ur)(\epsilon + 1)\, du \tag{90}$$

The exact evaluation of Equation (90) is difficult but it is obvious that the value of the integral is very strongly affected by the portion of the integrand in brackets, which passes through a maximum for some value of u and then decreases rapidly towards zero. Calculating the value of ϵ in the neighborhood of that maximum should provide an estimate of the total error introduced.

To find the maximum we differentiate with respect to u and set the result equal to zero:

$$\frac{d}{du}\left[\frac{1 - \exp(\alpha_2 u^2 t)}{u}\right] = -\frac{1}{u^2} + \left(\frac{1}{u^2} + 2\alpha_2 t\right)\exp(-\alpha_2 u^2 t) = 0 \tag{91}$$

which has roots

$$u = 1.12/\sqrt{\alpha_2 t}$$

$$= 2.24/r\sqrt{t} \tag{92}$$

At this value of u

$$ur = 2.24/\sqrt{t} \tag{93}$$

and $$ua = 2.24\, a/r\sqrt{t} \tag{94}$$

If ua is small then we may make the approximations

$$J_1(ua) \sim ua/2$$

$$Y_1(ua) \sim -2/\pi ua \tag{95}$$

hence

$$J_1^2(ua) + Y_1^2(ua) \sim 4/\pi^2 u^2 a^2 \tag{96}$$

and

$$\epsilon \sim \frac{\pi u^2 a^2}{4} \quad \frac{Y_o(ur)}{J_o(ur)} \tag{97}$$

$$\sim \frac{2.25\,\pi}{4} \quad \frac{a^2}{r^2 \bar{t}} \quad \frac{Y_o(2.24/\sqrt{\bar{t}})}{J_o(2.24/\sqrt{\bar{t}})} \tag{98}$$

$$\sim 1.76 \frac{a^2}{r^2 \bar{t}} \quad \frac{Y_o(2.24/\sqrt{\bar{t}})}{J_o(2.24/\sqrt{\bar{t}})} \tag{99}$$

This approximation will lose its validity where $2.24/\sqrt{\bar{t}}$ approaches 2.4, the first root of the Bessel function, i.e., when $\bar{t}$ becomes as small as 1.

APPENDIX D

GLOSSARY OF SYMBOLS

I. INTRODUCTION

This Appendix provides separate lists of symbols and specific nomenclature applicable to each section or appendix of the report. Because various sections of this report contain technical descriptions pertaining to different scientific disciplines and because the scientists in these fields sometimes use common symbols to represent different meanings, symbols in one section or appendix of this report may not have the same meaning in another section. No attempt has been made to eliminate this condition because it would have been confusing to use symbols for particular nomenclature other than those commonly accepted by these scientists.

II. NOMENCLATURE FOR SECTION I

SYMBOL	NOMENCLATURE
k	Polytropic constant
p	Pressure
ρ	Density

III. NOMENCLATURE FOR SECTION IV

SYMBOL	NOMENCLATURE
S_o	Speed of the leak (volume/time)
S_i	Effective orifice "speed" (volume/time)
P_o	Supply pressure of hydrogen
P_1	Discharge space pressure
dq/dt	Mass blow rate (pressure-volume/time): $dq/dt = S_1 p_1 = S_o p_o$

IV. NOMENCLATURE FOR SECTION V

SYMBOL	NOMENCLATURE
A	Contact area
F	Force
a	Acceleration
d	Diameter
f	Normal Force
g	Acceleration due to gravity

V. NOMENCLATURE FOR SECTION VI

SYMBOL	NOMENCLATURE
A	Proportionality constant: $A = \pi^2 q^2 C$
A'	Propostionality constant: $A' = 251\ (\pi q e \alpha)^2$
C	Parameter: $C = 3/4\ E\alpha^2$
E	Characteristic energy
F	Force of attraction
U	Potential Energy of Interaction
c	Velocity of light
e	Charge of an electron
f	Force of attraction per unit area
h	Distance between spheres
$\hbar$	Planck's constant
k	Proportionality constant
n	Optical index of refraction
q	Number of atoms per unit volume
r	Distance between atoms
u	Potential energy per unit area
α	Polarizability
λ_o	Characteristic wavelength
ρ	Radius of sphere
$\Psi(n)$	Tabulated function on page 6: $\Psi(n) = 0.35$ for $n \leq 2.0$

BLANK PAGE

VI. NOMENCLATURE FOR SECTION VIII AND APPENDIX C

Note: Those symbols such as η, C_m, U, and S which have no physical significance and which appear only locally as dummy variables or variables of integration are not included in this list.

SYMBOL	NOMENCLATURE
A	$-\gamma_e - \ln \frac{r^2}{4\alpha}$
C	Heat capacity
Ei(x)	Exponential integral of x
$I_n(x)$	Modified Bessel function of first kind of order n
$J_n(x)$	Bessel function of order n
$K_n(x)$	Modified Bessel function of the second kind of order n
$Y_n(x)$	Bessel function of the second kind of order n
T	Temperature
$\bar{T}$	Dimensionless temperature $\bar{T} = \frac{4\pi kT}{q}$
a	Radius of wire
c	Specific heat
k	Thermal conductivity
k_g	Gas thermal conductivity
k_s	Solid thermal conductivity
n	Subscript applied to thermal parameters indicates n^{th} medium; for example α_1 and α_2 are diffusivity of wire and sample respectively.
p	Transform variable with dimensions 1/t
q	Power supplied to heater wire per unit length
q_v	Power supplied per unit volume
r	Radial distance from line heat source to point of observation

SYMBOL	NOMENCLATURE
s	Distance from heater wire to radial boundary of sample
t	Time since initial application of power to heater
$\bar{t}$	Dimensionless time: $\bar{t} = 4\alpha t/r^2$
z	Axial coordinate
α	Thermal diffusivity
β_m^n	$= \left[(2m+1)^2 \frac{\pi^2}{\ell^2} + \frac{p}{\alpha_n}\right]^{\frac{1}{2}}$
γ	$= (p/\alpha_1)^{\frac{1}{2}}$
γ_e	Euler's constant: $\gamma_e = 0.57221 \ldots$
ϵ	Error term
ζ	Dimensionless variable: $\zeta = z/r$
λ	Dimensionless length: $\lambda = \ell/r$
μ_m	$(2m+1)\pi/\ell$
ρ	Density
τ	Dummy variable with dimensions of t
$\bar{\tau}$	Dummy variable with dimensions of $\bar{t}$
$*$	Indicates Laplace transform - for example $f^*(p)$ is the transform of $f(t)$
$L[f(t)]$	Laplace transform operator of $f(t)$
ℓ	Length of wire

VII. NOMENCLATURE FOR APPENDIX B

SYMBOL	NOMENCLATURE
A	- Cross section area of medium normal to flow -cm^2
a	- Inter atomic distance in the surface structure of a solid particle -cm
K	- Diffusion coefficient for flow through a porous medium -cm^2/sec
k	- Boltzmann constant $^{kcal}/_{molecule} - {}^{o}K$
L	- Thickness of layer of porous medium -cm
M	- Molecular weight - $^{gms}/_{gm\text{-}mole}$
N	- Molecular flow rate - $^{molecules}/_{sec}$
N_A	- Avogadro's constant - 6.02×10^{23} $^{molecules}/_{gm\text{-}mole}$
n	- Molecular density of gas in the interstices - $^{molecules}/_{cm^3}$
n_i	- Initial value of n - $^{molecules}/_{cm^3}$
n_L	- Value of n at X = L - $^{molecules}/_{cm^3}$
$\bar{n}$	- Dimensionless n : $\bar{n} = {}^{n}/_{n_i}$
$\bar{n}_L$	- Dimensionless n_L : $\bar{n}_L = {}^{n_L}/_{n_i}$
P	- Pressure of gas in the interstices - $dyne/cm^2$ (Torr in some places)
Q_a	- Heat of sorption of a gas on the surface of the particles in the medium - $^{kcal}/_{gm\text{-}mole}$
Q'_a	- Heat of activation for surface motion - $^{kcal}/_{gm\text{-}mole}$
R	- Molar gas constant $^{-kcal}/_{gm\text{-}mole} - {}^{o}K$
S	- Surface area per unit volume of the medium - cm^{-1}
T	- Absolute temperature - ^{o}K
t	- Time - secs.

t_c - Characteristic time - secs.

$\bar{t}$ - Average time for a molecule to pass through a capillary tube - secs.

$\bar{v}$ - Average molecular speed - $^{cm}/sec.$

X - Coordinate describing position in the medium - cm

y - Dimensionless x : $y = {}^{x}/L$

α - Fraction of incident molecules that are adsorbed (i.e., not reflected)

γ - Net gas flow per unit area from surfaces of the medium particles - $^{molecules}/sec\text{-}cm^2$

δ_o/k' - Dimensionless factor relating free molecule flow to pressure drop.

ϵ - Void fraction of medium

θ - Dimensionless time: $\theta = \xi t$

R_1 - Dimensionless ratio: $R_1 = {}^{\alpha\bar{v}S}/4\epsilon\xi$

R_2 - Dimensionless ratio: $R_2 = {}^{4K}/\alpha\bar{v}SL^2$
(Ratio of diffusion rate constant to re-adsorption rate constant)

σ - Concentration of sorbed molecules on surface - $^{molecules}/cm^2$

σ_i - Initial value of σ - $^{molecules}/cm^2$

σ_m - Value of σ corresponding to a complete unimolecular sorbed layer - $^{molecules}/cm^2$

$\bar{\sigma}$ - Dimensionless σ : $\bar{\sigma} = \sigma/\sigma_i$

τ - Time of adsorption - secs.

τ_o - Time of oscillation of molecules in the sorbed state perpendicular to the surface - secs.

τ' - Time between movements of sorbed molecules along the surface, halting time - secs.

τ'_o - Time of oscillation of molecules in the sorbed state along the surface - secs.

ϕ - Fraction of sorption sites covered: $\phi = \sigma / \sigma_m$

ξ - Desorption rate coefficient: $\xi = \frac{1}{\tau_o} e^{-Q_a/RT}$

APPENDIX E

BIBLIOGRAPHY

Aberdeen, J. and Laby, T. H. (1926), "Conduction of Heat Through Powders and Its Dependence on Pressure and Conductivity of the Gaseous Phase", Proc. Royal Soc., London, A 113, 459.

Baldwin, R. B. (1949), "The Face of the Moon", Univ. of Chicago Press.

Baldwin, R. B. (1962), "The Measure of the Moon", Univ. of Chicago Press.

Barnett, C. F., Stier, P. N., and Evans, G. E. (1953), "Pig Ion Source", Review of Scientific Instruments, 24, 394.

Bell, E. E., and Eisner, L. (1956), "Infrared Radiation from the White Sands at White Sands National Monument, New Mexico", J. Opt. Soc. Am., 46, 303-304.

Benjamin, P., and Weaver, C. (1963), "The Adhesion of Metals to Crystal Faces", Proceedings of the Royal Society, A 274, 267-273.

Bernett, E. C., Wood, H. L., Jaffee, L. D., and Martens, H. E. (1963), "Thermal Properties of a Simulated Lunar Material in Air and in Vacuum", AIAA Journal, 1, No. 6, 1402.

Bethe, H., and Ashkin, S. (1953), Experimental Nuclear Physics, E. Segre, Ed., I.

Bjork, E. L. (1961), "Analysis of the Formation of Meteor Crater Arizona, A Preliminary Report", J. Geophys. Res., 66, 3379-3387.

Black, I. A., Fowle, A. A., and Glaser, P. E. (1959), "The Single Guarded Cold Plate Apparatus for Thermal Conductivity Tests at Low Temperatures", Proceedings Xth Int. Congress of Refrigeration, Int. Institute of Refrigeration, Paris.

Bohr, N. (1948), Kgl., Danske Vid. Selskab., Mat.-pys, Medd., 18, 8.

Bowden, F. P., and Tabor, D. (1950), "The Friction and Lubrication of Solids", Oxford: Clarendon Press, London.

Bradley, R. S. (1932), "The Cohesive Force Between Solid Surfaces and the Surface Energy of Solids", Phil. Mag., 13, 853-862.

Brandt, J. C. (1960), "Density of the Lunar Atmosphere", Science, 131, 1606-1671.

Brawn, E. W. (1959), Data as recorded on the pictorial "Map of the Moon", Aerospace Laboratories, Missile Div., North American Aviation, Inc.

Bryant, J. (1962), "Cohesion of Clean Surfaces and the Effect of Adsorbed Gase ', 1962 Transactions of the Ninth Vacuum Symposium, American Vacuum Society, October 31-November 2, 1962, Los Angeles, California, published by MacMillan Co., New York, 311-313.

Burns, E. A. (1962), "Background for Thermal Emissivity Studies", Appendix C in Evaluation of Infrared Spectrophotometry for Compositional Analysis of Lunar and Planetary Soils (see reference to Lyon, 1962).

Burns, E. A., and Lyon, R. J. P. (1964), "Feasibility of Remote Compositional Mapping of the Lunar Surface", in the Lunar Surface Layer, J. W. Salisbury and P. E. Glaser, eds., Academic Press, New York, p. 469.

Carman, P. C. (1956), "Flow of Gases through Porous Media", Academic Press, Inc., New York.

Carslaw, H. S., and Jaeger, J. C. (1959), "Conduction of Heat in Solids", Clarendon Press, Oxford, England.

Casimir, H. B. G., and Polder, D. (February 15, 1948), "The Influence of Retardation on the London-van der Walls' Forces", Physical Review 73, (4), 360-372.

Chapman, D. R., and Larson, H. K. (1963), "On the Lunar Origin of Tektites", J. Geophys. Res., 68, No. 14, 4305-4358.

Chen, J. and Churchill, S. W. (1963), "Radiant Heat Transfer in Packed Beds", A.I.Ch.E. Journal, 9, 35-41.

Coblentz, W. W. (1906), "Investigations of Infrared Spectra", Part III: Infrared Transmission Spectra; Part IV: Infrared Reflection Spectra, Carnegie Institute of Washington, Publication 65.

Coblentz, W. W. (1908), "Supplementary Investigations of Infrared Spectra", Part V: Infrared Reflection Spectra, Part VI: Infrared Transmission Spectra, Part VII: Infrared Emission Spectra, Carnegie Institute of Washington, Publication 97.

Coffman, M. L. (1963), "Charging Grains of Dust", Jour. Geophys. Res., 8, 1565-1566.

Cohen, A. J. (1960), "Trace Element Relationships and Terrestrial Origin of Tektites", Nature, 188, 653-654.

Costain, C. H., Ellsmore, B., and Whitfield, G. R. (1955), "Radio Observations of a Lunar Occultation of the Crab Nebula", M.N., 116, 380-385.

Crawford, J. H. and Wittels, M. C. (1956), Proc. Int. Conf. Peaceful Uses of Atomic Energy, 7, 654.

Cudaback, D. (1963), "Moon Dust and Cotton Candy", Lecture Univ. of Calif., Berkeley, May.

De Boer, J. H. (1936), "The Influence of van der Waals' Forces and Primary Bonds on Binding Energy, Strength and Orientation, with Special Reference to Some Artificial Resins", Trans. Faraday, 32, 10-28.

De Boer, J. H. (1953), "The Dynamical Character of Adsorption", The Clarendon Press, Oxford.

Deissler, R. G., and Boegli, J. S. (1958), "An Investigation of Effective Thermal Conductivities of Powders in Various Gases", Trans. ASME, 80, 1417-1425.

Deissler, R. G., and Eian, C. S. (1952), "An Investigation of Effective Thermal Conductivities of Powders", NACA RME52C05, June 24.

De Nee, P. (1963), Oak Ridge National Laboratory, Personal Communication.

Derjaguin, B. V., Abrikossova, I. I., and Lifshitz, E. M. (1956), "Direct Measurement of Molecular Attraction Between Solids Separated by a Narrow Gap", Quarterly Reviews (London) 10, 295-329.

Derjaguin, B. V., and Abrikossova, I. I. (1958), "Direct Measurements of Molecular Attraction of Solids", J. of Physical and Chem. Solids, 5, 1-10.

Dienes, G. J., and Vineyard, G. H. (1957), "Radiation Effects in Solids", Interscience, New York.

Ditchburn, G. H., et.al., (1955), "Reports Bristol Conf. on Defects in Crystals, Phys. Soc. (London), 92-107.

Dollfus, A. (1952), "Nouvelle Recherche d'une Atmosphere au Voisinage de la Lune", C.R., 234, 2046-2049.

Donn, B., and Sears, G. W. (1963), "Planets and Comets: Role of Crystal Growth in Their Formation", Science, 140, 1208.

Dushman-Lafferty, (1962), "Scientific Foundations of Vacuum Technique", p. 324.

Dzyaloshinskii, I. E., Lifshitz, E. M., and Pitaevskii, L. P. (1961), "The General Theory of van der Waals' Forces", Advances in Physics, 10, 165-209.

Edwards, W. F., and Borst, L. G. (1958), "Possible Sources of a Lunar Atmosphere", Science, 127, 325-328.

Ellsmore, B., and Whitfield, G. R. (1955), "Lunar Occultation of a Radio Star and the Derivation of an Upper Limit for the Density of the Lunar Atmosphere", Nature, 176, 457-458.

Evans, J. V. (1962), "Radio-Echo Observations of the Moon at 3.6 cm Wavelength" Technical Report No. 256, Lincoln Laboratory, Massachusetts Institute of Technology.

Everest, A., Glaser, P. E., and Wechsler, A. E. (1963), "On the Thermal Conductivity of Powder Insulations", Proceedings of the XIth International Congress of Refrigeration, Munich, Germany, August 27.

Firsoff, V. A. (1961), "Surface of the Moon", Hutchinson & Co. Ltd., London.

Gault, D. E., Shoemaker, E. M., and Moore, H. J. (1963), "Spray Ejected from the Lunar Surface by Meteoroid Impact", NASA Technical Note, D-1767.

Gibson, J. E. (1962), "Lunar Surface Characteristics Indicated by the March 1960 Eclipse and Other Observations", Astrophys. J., 133, 1072-1080.

Glaser, P. E. (1961), "Heat Transfer Mechanisms in Evacuated Powders", Proceedings 1961 ASME Int. Heat Transfer Conference, Boulder, Colorado, Part IV, 829-837.

Goeffrion, A. R., Korner, M., and Sinton, W. M. (1960), "Isothermal Contours of the Moon", Lowell Observatory Bul. No. 106, 15 pp.

Gold, T. (1959), "Dust on the Moon" in Vistas in Astronautics, M. Alper, ed., 2, 261-266, Pergamon Press, New York, N.Y.

Gold, T. (1962), "Processes on the Lunar Surface", Proceedings of the I.A.U. Pulkovo Meeting, December 1960 (Z. Kopal and Z. Michailova, eds).

Goldstein, M. (1961), "Effect of Solid Conduction on Thermal Conductivity", Internal Memorandum, Arthur D. Little, Inc., Cambridge, Mass.

Gorring, R. L., and Churchill, S. W. (1961), "Thermal Conductivity of Heterogeneous Materials", Chem. Eng. Progress, 57, 53-59.

Grannis, P. D. (1961), "Electrostatic Erosion Mechanisms on the Moon", Jour. Geophys. Res., 66, 4293-4299.

Green, J. (1960), "Geophysics as Applied to Lunar Exploration", Final Report under Contract AF19(604)-5886, AFCRL-TR-60-409.

Green, J. (1961), "The Geology of the Lunar Base", North American Aviation Space and Information Systems Division, Report 61-358.

Hamaker, H. C. (1937), "The London-van der Waals' Attraction Between Spherical Particles", Physics 4, 1058.

Hamaker, H. C. (1947), "Radiation and Heat Conduction in Light Scattering Materials", Philips Research Reports, 2, 55-67, 103-111, 112-125, 420-425.

Hapke, B. W. (1963), "A Theoretical Photometric Function for the Lunar Surface", J. Geophys. Res., 68, No. 15, 4571-4585.

Hapke, B. W., and Van Horn, H. (1963), "Photometric Studies of Complex Surfaces with Applications to the Moon", J. Geophys. Res. 68, No. 15, 4545-4570.

Hawkins, G. S. (1960), "Tektites and the Earth", Nature, 185, 300-301.

Hibbs, A. R. (1963), "The Physical Nature of Lunar Surface Material", Proc. Lunar and Planetary Exploration Colloquium, North American Aviation, Inc., Vol. III, No. 3, 23-24.

Hill, F. B. and Wilhelm, R. H. (1959), "Radiative and Conductive Heat Transfer in a Quiescent Gas-Solid Bed of Particles; Theory and Experiment", AICHE Journal 5, 486-496.

Hines, R. L. (1957), "Radiation Effect of Positive Ion Bombardment on Glass", J. of Appl. Phys., 28, 587.

Hooper, F. C. and Lepper, F. R. (1950), "Transient Heat Flow Apparatus for the Determination of Thermal Conductivities", ASHVE Journal 56, 309.

Hunt, J. H., Wishered, M. P. and Bonhan, L. C. (1950), "Absorption Spectra of Silicates", Analyt. Chem., 22, 1478.

Jaeger, J. C. and Harper, A. F. A. (1950), "Nature of the Surface of the Moon", Nature 166, 1026.

Johnston, R., Knapton, D., and Lull, D. (1963), "Meteoroid Bumper Protection for Space Vehicles - Tentative Design Criteria", Report No. 65008-05-01, Arthur D. Little, Inc., under NASA Contract NAS5-664.

Kannuluik, W. G., and Martin, L. H. (1933), "Conduction of Heat in Powders", Proc. Royal Society, London, A 141, 144.

Kerr, P. F. (1959), "Optical Mineralogy" McGraw Hill Book Co., N.Y., 257-259.

Kistler, S. S. (1935), "The Relation Between Heat Conductivity and Structure in Silica Aerogel", J. Phys. Chem. 39, 79.

Kitchener, J. A., and Prosser, A. P. (November 5, 1957), "Direct Measurement of the Long-range van der Waals' Forces", Proceedings of the Royal Society, A 242 (1230), 403-409.

Kock, J. (1949), Nature, 164, 19.

Kopal, Z. (1959), "Does the Moon Possess a Magnetic Field?" Space J., 2, No. 1, 3-8.

Kopal, Z. (1960), "The Moon", Academic Press, New York.

Kopal, Z., et.al., (1961), "Studies in Lunar Topography", GRD Research Notes, No. 67.

Kozyrev, N. A. (1959), "Observation of a Volcanic Process on the Moon", Sky and Telescope, 18, 184-186.

Krotikov, V. D. and Shchuko, O. B. (1963), "The Heat Balance of the Lunar Surface Layer during a Lunation", Soviet Astronomy - AJ., 7, 228.

Krotikov, V. D. and Troitskii, V. S. (1963), "Thermal Conductivity of Lunar Material from Precise Measurement of Lunar Radio Emission", Soviet Astronomy - AJ., 7, 119.

Lander, J. J., Gobeli, G. W., and Morrison, J. (August 1963), "Structural Properties of Cleaved Silicon and Germanium Surfaces", J. Applied Physics, 34 (8), 2298-2306.

Larkin, B. K., and Churchill, S. W. (1959), "Heat Transfer by Radiation Through Porous Insulations", AICHE Journal, 5, 467-474.

Leidenfrost, W., (1955), "Uber die Warmedammwirkung feinkorniger Pulver in verdunnten Gasen", VDI-Zeitschrift, 97, 1235.

Levy, A. and Dienes, G. J. (1955), Reports of Bristol Conf. on Defects in Crystals, Phys. Soc. (London), 256-260.

Lifshitz, E. M. (1955), "The Theory of Molecular Attractive Forces Between Solids", J. Exp. Theo. Phys., U.S.S.R., 29, 94.

Liu, N. and Dobar, W. I. (1964), "The Nature of the Lunar Surface: The Thermal Conductivity of Dust and Pumice", in the Lunar Surface Layer, J. W. Salisbury and P. E. Glaser, eds., Academic Press, New York, 381.

London, F., Z. Phys., 60, 491 (1930), Z. Phys., 63, 245 (1930), Z. Physik. Chem., 11, 222 (1931), Trans. Faraday Soc. 33, 8 (1937), "On Centers of van der Waals' Attraction", Journal of Phys. Chem., 46, 305-315 (1942).

Lowman, P. D. Jr., (1963), "The Relation of Tektites to Lunar Igneous Activity", Icarus, 2, 35-48.

Lyon, R. J. P. (1962), "Evaluation of Infrared Spectrophotometry for Compositional Analysis of Lunar and Planetary Soils", Final Report under NASA Contract No. NAS-49(04), Stanford Research Institute Project No. PSU-3943.

Lyon, R. J. P., and Burns, E. A. (1962), "Infrared Spectral Analysis of the Lunar Surface from an Orbiting Spacecraft", Proceedings of the Second Symposium on Remote Sensing of Environment, University of Michigan, October 16.

MacDonald, G. J. F. (1961), "Interior of the Moon", Science 133, 1045-1050.

MacDonald, G. J. F. (1962), "On the Internal Constitution of the Inner Planets", J. Geophys. Res. 67, 2945-2974.

Margenau, H., (1939), "Van der Waals' Forces", Rev. Mod. Phys. 11, 1.

Masamune, S. and Smith, J. M. (1963), "Thermal Conductivity of Beds of Spherical Particles", Ind. and Eng. Chem. Fundamentals, 2, 136.

Medd, W. J. and Broten, N. W. (1961), "Lunar Temperature Measurements at 3200 mc/s", Planetary and Space Science, 5, 307-313.

Mezger, P. S., and Strassl, H. (1959), "The Thermal Radiation of the Moon at 1420 mc/s", Planetary and Space Sci., 1, 213-226.

Mitchell, E. W. J., and Paige, E. G. S. (1955), Proc. Phys. Soc. (London), B68, 223.

Mitra, S. K. (1952), "The Upper Atmosphere", The Asiatic Society Monography Series, 85.

Moore, H. J., Gault, D. E., and Lugn, R. V. (1962), "Impact Craters in Basalt", Abstract in Pacific Southwest Mineral Conference of AIME, San Francisco, p. 17.

Murray, B. C., and Wildey, R. L. (1963), "Stellar and Planetary Observations at 10 Microns", The Astrophysical Journal, 137, 692-693.

O'Keefe, J. A. and Cameron, W. S. (1962), "Evidence from the Moon's Surface Features for the Production of Lunar Granites", Icarus, VI, No. 3, 271-285.

Opik, E. J., and Singer, S. F. (1960), "Escape of Gases from the Moon", J. Geophys. Res., 65, 3065-3070.

Overbeek, J. Th. G. and Sparnaay, M. J. (1954), "I. Classical Coagulation London-van der Waals' Attraction Between Microscopic Objects", Disc. Faraday Society 18, 12-24.

Pinson, W. H., Jr. (1962), "Chemical and Physical Studies of Tektites", Report AFCRL-62-221.

Riemann, G. G. M. W. (1919), "Die Partielle Differential - Gleichung der Mathematischen Physik", Band 1, F. Vieweg u. Sohn, Braunschweig, 474.

Russell, A. W. (1935), "Principles of Heat Flow in Porous Insulators", Journal Am. Ceram. Soc., 19, 1-5.

Saari, J. M., and Shorthill, R. W. (1963), "Isotherms of Crater Regions on the Illuminated and Eclipsed Moon", Icarus, 2, 115-136.

Salisbury, J. W. (1962), "The Lunar Environment in Space and Planetary Environments", Air Force Surveys in Geophysics, AFCRL-62-270, No. 139.

Salisbury, J. W. and Smalley, V. G. (1964), "The Lunar Surface Layer", in The Lunar Surface Layer, J. W. Salisbury and P. E. Glaser, eds., Academic Press, New York, 411.

Salisbury, J. W., Glaser, P. E., Stein, B. A., and Vonnegut, B. (1964), "Adhesive Behavior of Silicate Powders in Ultrahigh Vacuum", Journ. Geoph. Res., 69, 235-242.

Schleiermacher, A. L. E. F. (1888), "Uber die Waermeleitung der Gase", Annalen de Physik, U. Chemie, 34, 623.

Schotte, W. (1960), "Thermal Conductivity of Packed Beds", AICHE Journal 6, 63-67.

Schumann, T. E. W. and Voss, V. (1934), "Heat Flow Through Granulated Materials", Fuel, 13, 249-256.

Seitz, F. (1949), Disc. of Faraday Soc. 18, No. 5, 1.

Shoemaker, E. M. (1962a), "Exploration of the Moon's Surface", American Scientist, 50, 99-130.

Shoemaker, E. M. (1962b), "Interpretation of Lunar Craters", in Physics and Astronomy of the Moon, edited by Z. Kopal, Academic Press.

Simon, I. (1951), "Spectroscopy in Infrared by Reflection and Its Use for Highly Absorbing Substances", J. Opt. Soc. Am. 41, 336-345.

Singer, S. F. and Walker, E. H. (1962a), "Photoelectric Screening of Bodies of Interplanetary Space", Icarus, 1, 7-12.

Singer, S. F. and Walker, E. H. (1962b), "Electrostatic Dust Transport on the Lunar Surface", Icarus, 1, 112-120.

Smithsonian Physical Tables (1954), 9th Ed.

Smoluchowski, M. (1910), "Sur la Conductibilite Calorifique des Corps Pulverises", Bull Int. de L'Academie des Sciences de Cracovie, A. 129.

Sparnaay, M. J. (1957), Nature 180, 334.

Spock, L. E. (1953), "Guide to the Study of Rocks", Harper and Bros., N.Y., 82-83.

Stalhane, B. and Pyk, S. (1931), "A New Method for Determining the Coefficients of Thermal Conductivity", Teknisk Tidskift, 61, 389.

Stein, B. A., and Johnson, P. C. (1964), "Investigation of Soil Adhesion Under High Vacuum", in the Lunar Surface Layer, J. W. Salisbury and P. E. Glaser, eds., Academic Press, New York, 93.

Strong, H. M., Bundy, F. P., and Bovenkirk, H. P. (1960), "Flat Panel Vacuum Thermal Insulation", Journal Appl. Phys. 31, 39-50.

Sytinskaya, N. N. (1959), "New Data on the Meteoric Slag Theory of the Formation of the Outer Layer of the Lunar Surface", Soviet Astronomy-A.J. 3, 310-314.

Timoshenko, S. (1945), "Strength of Materials", D. Van Nostrand Co., Inc., New York.

Tsao, G. T. (1961), "Thermal Conductivity of Two-Phase Materials", Ind. and Eng. Chem. 53, 395-397.

Urey, H. C. (1952), "The Planets", Yale Univ. Press, 245 pp.

Urey, H. C. (1962), in "The Moon", Academic Press, New York, p. 20.

Urey, H. C. and Craig, H. (1953), Geochim. et Cosmochim. Acta, 4, 36-82.

Van der Held, E. M. F. and Van Drunen, F. G. (1949), "A Method of Measuring the Thermal Conductivity of Liquids", Physica, 15, 865.

Verschoor, J. D. and Greebler, P. (1952), "Heat Transfer by Gas Conduction and Radiation in Fibrous Insulation", Trans. ASME, 961-968.

Walker, E. H. (1962), Comments on a paper by P. D. Grannis, "Electrostatic Erosion Mechanisms on the Moon", Jour. Geophys. Res. 67, 2586-2587.

Watson, F. G. (1941), "Between the Planets", Blakiston Co., Philadelphia.

Watson, J., Murray, B. C., and Brown, H. (1951), "The Behavior of Volatiles on the Lunar Surface", J. Geophys. Res. 66, 3033.

Watson, J., Murray, B., and Brown, H. (1961), "On the Possible Presence of Ice on the Moon", Journal of Geophysical Research, 66, 1598-1600.

Wechsler, A. E. et al (1963), Unpublished data obtained at Arthur D. Little, Inc., Cambridge, Mass., under Contract AF19(628)-421, for Air Force Cambridge Research Laboratories, Bedford, Mass.

Wechsler, A. E., and Glaser, P. E. (1961), "Investigation of Materials for Vacuum Insulation up to 4000°F", Final Report to WADD, Contract No. AF33(616)-6816.

Wechsler, A. E., Glaser, P. E., and Allen, R. V. (1963), "Investigation of the Thermal Conductivity of Non-Metallic Materials", Summary Report prepared for NASA George C. Marshall Space Flight Center by Arthur D. Little, Inc., under Contract No. NAS8-1567.

Wehner, G. K. (1961), "Sputtering Effects on the Moon's Surface", Amer. Rocket Society Journal, 31, 438.

Weil, H., and Barasch, M. L. (1963), "A Theoretical Lunar Ionosphere", Icarus, 1, No. 4, 346-350.

Whipple, F. L. (1961), "The Dust and Cloud About the Earth", Nature 189, 127-8.

Whipple, F. L. (1962), "Dust and Meteorites", Astronautics, 7, No. 8, 40-42.

Whipple, F. L. (1963), "On Meteoroids and Penetration", J. Geophys. Res., 68, 4929-4940.

Wilhelm, R. H., Johnson, W. C., Wynkoop, R., and Collier, D. W. (1948), Chem. Eng. Prog., 44, 105.

Woodside, W. and Messmer, J. (1961), "Thermal Conductivity of Porous Media - I. Consolidated Sands", J. Appl. Physics, 32, No. 9, 1688.

SPECIAL REPORTS

No. 1. Today's Meteorological Rocket Network and Atmospheric Problems of Aerospace Vehicles, *Norman Sissenwine, May 1964 (REPRINT).*

No. 2. Ferrimagnetic Resonance Relations for Magnetocrystalline Anisotropy in Cubic Crystals, *Hans Roland Zapp, April 1964.*

No. 3. Worldwide Collection and Evaluation of Earthquake Data, Final Report on Evaluation of 1960 Seismicity, *R.L. Fisher, R.G. Baker, and R.R. Guidroz, June 1964.*

No. 4. Visual Observations Beneath a Developing Tornado, *Ralph J. Donaldson, Jr., and William E. Lamkin, August 1964 (REPRINT).*

No. 5. Bibliography of Rock Deformation, *R.E. Riecker, 1/Lt, USAF, September 1964.*

No. 6. The Modification of Electromagnetic Scattering Cross Sections in the Resonant Region, A Symposium Record, Volume I, *J.K. Schindler, 1/Lt, USAF, R.B. Mack, Editors, September 1964.*

No. 6. The Modification of Electromagnetic Scattering Cross Sections in the Resonant Region (U), A Symposium Record, Volume II, *J.K. Schindler, 1/Lt, USAF, R.B. Mack, Editors, September 1964(SECRET).*

No. 7. The Natural Environment for the Manned Orbiting Laboratory System Program (MOL), *25 October 1964.*

No. 8. The Vertical Transfer of Momentum and Heat At and Near the Earth's Surface, *Morton L. Barad, October 1964 (REPRINT).*

No. 9. Bibliography of Lunar and Planetary Research–196[illegible] *J.W. Salisbury, R.A. VanTassel, J.E.M. Adler, R.T. Dodd, Jr., and V.G. Smalley, November 1964.*

No. 10. Hourly Rawinsondes for a Week (Part II), *Arnold A. Barnes, Jr., and Henry A. Salmela, November 1964.*

No. 11. An Appraisal of Rayleigh, *John Howard, Editor, November 1964 (REPRINT).*

No. 12. Communication by Electroencephalography, *E.M. Dewan, November 1964.*

No. 13. Proceedings of AFCRL Workshop on 20 July 1963 Solar Eclipse, *J.A. Klobuchar and R.S. Allen, Editors, December 1964.*

No. 14. Continuous Zone Refining, *John K. Kennedy and N. Grier Parke,III, December 1964.*

No. 15. Applications of Lasers, *C. Martin Stickley, November 1964.*

No. 16. On the Physical Necessity for General Covariance in Electromagnetic Theory, *E.J. Post, December 1964.*

No. 17. A Compendium of Papers in the Fields of Wave Propagation and Geotechnics Prepared at AFCRL During 1963, *Owen W. Williams, December 1964.*

No. 18. A Compendium of Papers in the Fields of Geodesy and Planetary Geometry Prepared at AFCRL During 1963, *Owen W. Williams, Editor, January 1965.*

No. 19. Study of Ferrimagnetic Crystals by Parallel Pumping, *James C. Sethares and Frank A. Olson, January 1965.*

No. 20. Studies of the Characteristics of Probable Lunar Surface Materials, *John W. Salisbury and Peter E. Glaser, Editors, January 1964.*

Unclassified
Security Classification

DOCUMENT CONTROL DATA - R&D

(Security classification of title, body of abstract and indexing annotation must be entered when the overall report is classified)

1. ORIGINATING ACTIVITY *(Corporate author)* Hq AFCRL, OAR (CRF) United States Air Force Bedford, Massachusetts	2a. REPORT SECURITY CLASSIFICATION Unclassified 2b. GROUP -

3. REPORT TITLE

Studies of the Characteristics of Probable Lunar Surface Materials

4. DESCRIPTIVE NOTES *(Type of report and inclusive dates)*

5. AUTHOR(S) *(Last name, first name, initial)*

Salisbury, John W., and Glaser, Peter E., Editors

6. REPORT DATE January 1964	7a. TOTAL NO. OF PAGES 330	7b. NO. OF REFS 150 (Bibliographic)
8a. CONTRACT OR GRANT NO. AF19(628)-421 b. PROJECT NO. 8602-02 c. ~~XXX~~ DOD element 61445014 d. DOD subelement 681311	9a. ORIGINATOR'S REPORT NUMBER(S) AFCRL-64-970 9b. OTHER REPORT NO(S) *(Any other numbers that may be assigned this report)* AFCRL-64-970	

10. AVAILABILITY/LIMITATION NOTICES Qualified requestors may obtain copies of this report from DDC. Other persons or organizations should apply to the U.S. Department of Commerce, Office of Technical Services, Washington, D.C. 20230

11. SUPPLEMENTARY NOTES -	12. SPONSORING MILITARY ACTIVITY Hq AFCRL, OAR (CRF) United States Air Force Bedford, Massachusetts

13. ABSTRACT This report presents the findings of a cooperative effort by scientists of the Lunar Planetary Research Branch of the Air Force Cambridge Research Laboratories and of Arthur D. Little, Inc., on theoretical and experimental studies to determine the nature and most probable physical form of materials on the lunar surface. To accomplish these goals, the following efforts were performed: (1) installation of an ultra-high-vacuum system to simulate the probable lunar environment, (2) selection of material samples to simulate the probable lunar surface, (3) experimentation on and analysis of these materials in a high vacuum, (4) studies of the behavior of clean surfaces in a high vacuum, (5) measurements of electrostatic phenomena in a high vacuum, (6) measurement of thermal properties in a high vacuum, and (7) spectroscopic studies.

DD FORM 1 JAN 64 1473

Unclassified
Security Classification

Unclassified

Security Classification

14. KEY WORDS	LINK A		LINK B		LINK C	
	ROLE	WT	ROLE	WT	ROLE	WT
Lunar Surface Lunar Surface Materials Lunar Environment						

INSTRUCTIONS

1. ORIGINATING ACTIVITY: Enter the name and address of the contractor, subcontractor, grantee, Department of Defense activity or other organization *(corporate author)* issuing the report.

2*a*. REPORT SECURITY CLASSIFICATION: Enter the overall security classification of the report. Indicate whether "Restricted Data" is included. Marking is to be in accordance with appropriate security regulations.

2*b*. GROUP: Automatic downgrading is specified in DoD Directive 5200.10 and Armed Forces Industrial Manual. Enter the group number. Also, when applicable, show that optional markings have been used for Group 3 and Group 4 as authorized.

3. REPORT TITLE: Enter the complete report title in all capital letters. Titles in all cases should be unclassified. If a meaningful title cannot be selected without classification, show title classification in all capitals in parenthesis immediately following the title.

4. DESCRIPTIVE NOTES: If appropriate, enter the type of report, e.g., interim, progress, summary, annual, or final. Give the inclusive dates when a specific reporting period is covered.

5. AUTHOR(S): Enter the name(s) of author(s) as shown on or in the report. Enter last name, first name, middle initial. If military, show rank and branch of service. The name of the principal author is an absolute minimum requirement.

6. REPORT DATE: Enter the date of the report as day, month, year, or month, year. If more than one date appears on the report, use date of publication.

7*a*. TOTAL NUMBER OF PAGES: The total page count should follow normal pagination procedures, i.e., enter the number of pages containing information.

7*b*. NUMBER OF REFERENCES: Enter the total number of references cited in the report.

8*a*. CONTRACT OR GRANT NUMBER: If appropriate, enter the applicable number of the contract or grant under which the report was written.

8*b*, 8*c*, & 8*d*. PROJECT NUMBER: Enter the appropriate military department identification, such as project number, subproject number, system numbers, task number, etc.

9*a*. ORIGINATOR'S REPORT NUMBER(S): Enter the official report number by which the document will be identified and controlled by the originating activity. This number must be unique to this report.

9*b*. OTHER REPORT NUMBER(S): If the report has been assigned any other report numbers *(either by the originator or by the sponsor)*, also enter this number(s).

10. AVAILABILITY/LIMITATION NOTICES: Enter any limitations on further dissemination of the report, other than those imposed by security classification, using standard statements such as:

(1) "Qualified requesters may obtain copies of this report from DDC."

(2) "Foreign announcement and dissemination of this report by DDC is not authorized."

(3) "U. S. Government agencies may obtain copies of this report directly from DDC. Other qualified DDC users shall request through

_____."

(4) "U. S. military agencies may obtain copies of this report directly from DDC. Other qualified users shall request through

_____."

(5) "All distribution of this report is controlled. Qualified DDC users shall request through

_____."

If the report has been furnished to the Office of Technical Services, Department of Commerce, for sale to the public, indicate this fact and enter the price, if known.

11. SUPPLEMENTARY NOTES: Use for additional explanatory notes.

12. SPONSORING MILITARY ACTIVITY: Enter the name of the departmental project office or laboratory sponsoring *(paying for)* the research and development. Include address.

13. ABSTRACT: Enter an abstract giving a brief and factual summary of the document indicative of the report, even though it may also appear elsewhere in the body of the technical report. If additional space is required, a continuation sheet shall be attached.

It is highly desirable that the abstract of classified reports be unclassified. Each paragraph of the abstract shall end with an indication of the military security classification of the information in the paragraph, represented as *(TS), (S), (C), or (U).*

There is no limitation on the length of the abstract. However, the suggested length is from 150 to 225 words.

14. KEY WORDS: Key words are technically meaningful terms or short phrases that characterize a report and may be used as index entries for cataloging the report. Key words must be selected so that no security classification is required. Identifiers, such as equipment model designation, trade name, military project code name, geographic location, may be used as key words but will be followed by an indication of technical context. The assignment of links, rules, and weights is optional.

Unclassified

Security Classification

BLANK PAGE